# TRAJECTORY DESIGN BETWEEN CISLUNAR SPACE AND SUN-EARTH LIBRATION POINTS IN A FOUR-BODY MODEL

by

**Kenza K. Boudad**

**A Dissertation**

*Submitted to the Faculty of Purdue University*

*In Partial Fulfillment of the Requirements for the degree of*

**Doctor of Philosophy**


School of Aeronautics and Astronautics

West Lafayette, Indiana

May 2022

# THE PURDUE UNIVERSITY GRADUATE SCHOOL
# STATEMENT OF COMMITTEE APPROVAL

**Dr. Kathleen C. Howell, Chair**

School of Aeronautics and Astronautics

**Dr. Caroline E. Frueh**

School of Aeronautics and Astronautics

**Dr. Aaron N.K. Yip**

Department of Mathematics

**Dr. Diane C. Davis**

a.i. solutions, Inc.

**Approved by:**

Dr. Gregory A. Blaisdell

Pour Mamie et Jedda

# ACKNOWLEDGMENTS

I would like to express my deepest gratitude to my advisor, Professor Kathleen Howell. I have thoroughly enjoyed taking your classes, but I have enjoyed working in your research group far more. Thank you for this amazing opportunity. Your guidance, expertise, and commitment have been instrumental to my growth as a researcher and as a person over the last six years.

I would also like to express my gratitude and appreciation to Dr. Diane Davis from a.i. solutions, for her guidance during the research and writing of our many papers together. It was quite the ride, and I have learned so much from you. Thank you for your patience! Many thanks to Professor Carolin Frueh and Professor Nung Yip for their valuable feedback and insights throughout this investigation.

For providing funding for my studies, I would like to thank the School of Aeronautics and Astronautics. Support provided by the NASA Cooperative Agreement 80NSSC18M0122, and the Purdue Bilsland Dissertation Fellowship were greatly appreciated.

I am incredibly grateful for the support of my friends. Camille Briquet, Thomas Maimbourg, and Emily Spreen: thank you for letting me talk through my troubles and thank you even more for the silly conversations that remind me not to take life so seriously. I would also like to thank past and present members of the Purdue Multi-Body Dynamics Research Group for their friendship, including Andrew Cox, Bonnie Prado Pino, and Robert Pritchett for their mentorship, Maaninee Gupta and Nick LaFarge for the coffee relief, and Brian McCarthy for going through all the steps of grad school together.

Maman, Papa, Jaffar et Zakia, merci de votre amour et vos encouragements au cours des six dernières années. Votre soutien inconditionel m'a permis de traverser à la fois les bons et mauvais moments de cette aventure. Merci aussi à ma cousine Marie de ton support et de m'avoir montré la voie de l'ingénierie.

Last but certainly not least, I would like to thank my partner, Zachary McClure. Your (and Lucy's) love and support have been crucial over the last few years. Thank you especially for always believing in me when I do not. You are the kindest and most patient person I know; I am so grateful to have you at my side for whatever comes next. We did it!

# TABLE OF CONTENTS

# LIST OF TABLES

# LIST OF FIGURES

# LIST OF SYMBOLS

| | |
|---|---|
| $B_1$ | E-M barycenter |
| $B_2$ | E-M-S barycenter |
| $t$ | E-M nondimensional independent time variable |
| $\underline{t}$ | Sun-$B_1$ nondimensional independent time variable |
| $x,\ y,\ z$ | E-M nondimensional spacecraft position coordinates, E-M rotating frame |
| $\dot{x},\ \dot{y},\ \dot{z}$ | E-M nondimensional spacecraft velocity coordinates, E-M rotating frame |
| $\ddot{x},\ \ddot{y},\ \ddot{z}$ | E-M nondimensional spacecraft acceleration coordinates, E-M rotating frame |
| $\underline{x},\ \underline{y},\ \underline{z}$ | Sun-$B_1$ nondimensional spacecraft position coordinates, Sun-$B_1$ rotating frame |
| $\underline{\dot{x}},\ \underline{\dot{y}},\ \underline{\dot{z}}$ | Sun-$B_1$ nondimensional spacecraft velocity coordinates, Sun-$B_1$ rotating frame |
| $\underline{\ddot{x}},\ \underline{\ddot{y}},\ \underline{\ddot{z}}$ | Sun-$B_1$ nondimensional spacecraft acceleration coordinates, Sun-$B_1$ rotating frame |
| $\bar{r}_{\mathrm{i}}$ | E-M nondimensional position vector from $B_1$ to body i, E-M rotating frame |
| $\bar{r}_{\mathrm{i\text{-}sc}}$ | E-M nondimensional position vector from body i to the spacecraft, E-M rotating frame |
| $\underline{\dot{x}},\ \underline{\dot{x}},\ \underline{\dot{x}}$ | Sun-$B_1$ nondimensional spacecraft velocity coordinates, Sun-$B_1$ rotating frame |
| $\underline{\bar{r}}_{\mathrm{i}}$ | Sun-$B_1$ nondimensional position vector from $B_2$ to body i, Sun-$B_1$ rotating frame |
| $\underline{\bar{r}}_{\mathrm{i\text{-}sc}}$ | Sun-$B_1$ nondimensional position vector from body i to the spacecraft, Sun-$B_1$ rotating frame |
| $\mu$ | mass parameter of the E-M CR3BP |
| $n$ | E-M nondimensional mean motion of the primaries in the E-M CR3BP |
| $U^*$ | pseudo-potential function of the E-M CR3BP |
| $C$ | Jacobi constant of the E-M CR3BP |
| $\mathrm{L_i}$ | $\mathrm{i^{th}}$ equilibrium points of the E-M CR3BP |
| $\mu_{\mathrm{s}}$ | E-M nondimensional mass of the Sun |
| $a_{\mathrm{s}}$ | E-M nondimensional distance to the Sun from $B_1$ |
| $\theta$ | Sun angle, i.e., epoch variable in the BCR4BP, E-M formulation |
| $\underline{\theta}$ | Moon angle, i.e., epoch variable in the BCR4BP, Sun-$B_1$ formulation |
| $\omega$ | E-M nondimensional angular rate of the Sun, E-M rotating frame |

| | |
|---|---|
| $\underline{\omega}$ | Sun-$B_1$ nondimensional angular rate of the Earth and the Moon, Sun-$B_1$ rotating frame |
| $\Upsilon^*$ | pseudo-potential function of the BCR4BP, E-M formulation |
| $\underline{\Upsilon^*}$ | pseudo-potential function of the BCR4BP, Sun-$B_1$ formulation |
| $\mathcal{N}$ | number of bodies in the $\mathcal{N}$-body problem |
| $N$ | number of celestial bodies included in the $N$-body ephemeris model |
| $\mathbf{A}$ | Jacobian matrix associated with a set of equations of the motion |
| $\mathbb{P}$ | period |
| $\phi$ | Lyapunov exponent |
| $\lambda$ | eigenvalue |
| $\bar{\nu}$ | eigenvector |
| $\alpha_{\mathrm{s/u}}$ | six-dimensional angle between stable and unstable eigenvectors |
| $\mathbf{\Phi}$ | state-transition matrix |
| $\bar{\mathfrak{X}}$ | design variables vector |
| $\bar{\mathcal{F}}$ | constraint vector |
| $\mathrm{D}\bar{\mathcal{F}}$ | Jacobian matrix of the constraints vector with respect to the design variables vector |
| $\bar{\mathcal{G}}$ | augmented constraints vector for pseudo-arclength continuation |
| $W_{loc}$ | local manifolds |
| $W$ | global manifolds |

# ABBREVIATIONS

| | |
|---|---|
| AEP | Artificial Equilibrium Point |
| BCR4BP | Bicircular Restricted Four-Body Problem |
| CR3BP | Circular Restricted Three-Body Problem |
| ECI | Earth-Centered Inertial |
| ESA | European Space Agency |
| E-M | Earth-Moon |
| E-M-S | Earth-Moon-Sun |
| JWST | James Webb Space Telescope |
| LEO | Low Earth Orbit |
| LGA | Lunar Gravity Assist |
| NASA | National Aeronautics and Space Administration |
| NPC | Natural Parameter Continuation |
| NRHO | Near Rectilinear Halo Orbit |
| NRST | Nancy Roman Space Telescope |
| S-$B_1$ | Sun-$B_1$ |
| ZVSs | Zero Velocity Surfaces |
| ZACs | Zero Acceleration Contours |

# ABSTRACT

Many opportunities for frequent transit between the lunar vicinity and the heliocentric region will arise in the near future, including servicing missions to space telescopes and proposed missions to various asteroids and other destinations in the solar system. The overarching goal of this investigation is the development a framework for periodic and transit options in the Earth-Moon-Sun system. Rather than overlapping different dynamical models to capture the dynamics of the cislunar and heliocentric region, this analysis leverages a four-body dynamical model, the Bicircular Restricted Four-Body Problem (BCR4BP), that includes the dynamical structures that exist due to the combined influences of the Earth, the Moon, and the Sun. The BCR4BP is an intermediate step in fidelity between the CR3BP and the higher-fidelity ephemeris model. The results demonstrate that dynamical structures from the Earth-Moon-Sun BCR4BP provide valuable information on the flow between cislunar and heliocentric spaces.

Dynamical structures associated with periodic and bounded motion within the BCR4BP are successfully employed to construct transfers between the 9:2 NRHO and locations of interest in heliocentric space. The framework developed in this analysis is effective for transit between any cislunar orbit and the Sun-Earth libration point regions; a current important use case for this capability involves departures from the NRHOs, orbits that possess complex dynamics and near-stable properties. Leveraging this methodology, one-way trajectories from the lunar vicinity to a destination orbit in heliocentric space are constructed, as well as round-trip trajectories that returns to the NRHO after completion of the objectives in heliocentric space. The challenges of such trajectory design include the phasing of the trajectory with respect to the Earth, the Moon, the Sun, on both the outbound and inbound legs of the trajectory. Applications for this trajectory include servicing missions to a space telescope in heliocentric space, where the initial and final locations of the mission is the Gateway near the Moon. Lastly, the results of this analysis demonstrate that the properties and geometry of the periodic orbits, bounded motion, and transfers that are delivered from the BCR4BP are maintained when the trajectories are transitioned to the higher-fidelity ephemeris model.

# 1. INTRODUCTION

## 1.1 Motivation

As evidenced by the Global Exploration Roadmap [1], international interest exists in a new era of human exploration of the solar system. Such an effort is commencing with the examination of options for maintaining a facility—at times crewed—in an orbit near the Moon. The proposed Gateway concept is the current framework for the NASA development of this space facility. From a baseline trajectory in a Near Rectilinear Halo Orbit (NRHO), the Gateway is intended to serve as a proving ground for deep space technologies and as a staging location for missions beyond low Earth orbit. While the NRHOs are identified in cislunar space in terms of the Earth-Moon Circular Restricted Three-Body Problem (CR3BP), the impact of the solar gravity generally cannot be ignored when considering departure from the Earth-Moon region.

Many opportunities for frequent transit between the lunar vicinity and the heliocentric region will arise in the near future. Servicing missions from the Gateway to space telescopes and observatories in Sun-Earth $L_1$ and $L_2$ libration point orbits, including NASA's James Webb Space Telescope (JWST) [2], successfully launched earlier this year, and the Nancy Roman Space Telescope (NRST) [3], scheduled to launch in 2027, as well as ESA's Euclid telescope [4] and ISRO's Aditya-L1 solar observatory [5], may occur during their operational lifetimes. Other opportunities include departure of spacecraft and probes to destinations beyond the Earth-Moon vicinity, and the safe disposal of various objects from the proposed Gateway facility. A common characteristic for these diverse mission scenarios is that the combined gravitational influences of the Earth, the Moon, and the Sun are considered at some stage of the trajectory design process. Transit trajectories between the Gateway orbit in cislunar space and these Sun-Earth libration point orbits present many advantages; the time of flight and the $\Delta V$ budget are generally lower than those associated with transfers initiated in Low-Earth Orbit (LEO). Note that part of this cost is often assumed by the launch vehicle. However, regular access to heliocentric space need not rely on such expensive departure scenarios.

Preliminary designs for trajectories in the Earth-Moon-Sun system often rely on approaches that overlap different dynamical models. A model describing the Earth-Moon system, often the Earth-Moon CR3BP, is leveraged to describe the dynamics close to these two primaries. A second model, for instance, the Sun-Earth CR3BP, is employed to represent the dynamics when the Sun's gravitational influence is significant. One of the main challenges of this approach is appropriate selection of the transition point between the two models. Additionally, overlapping models inherently lack the framework to describe dynamical structures that exist due to the combined influences of the Earth, the Moon, and the Sun. Thus, a dynamical model that includes the gravitational influences of all three bodies of interest on an object is useful to design trajectories in such complex dynamical environment. By furthering the understanding of dynamical structures of the Earth-Moon-Sun system in a unified model, periodic orbits and transit trajectories that leverage the dynamical flow are constructed.

### 1.2 Previous Contributions

Multi-body dynamical models have been available for centuries to predict the motion of celestial bodies and, more recently, design trajectories for manufactured objects. In particular, three-body models attempt to model dynamical systems where Keplerian mechanics are limited or inadequate. The Circular Restricted Three-Body Problem (CR3BP) [6] is a common model to design trajectories in the Sun-Earth and Earth-Moon systems. In the Sun-Earth system, missions like SOHO [7] in 1995, GENESIS [8] in 2001 or Gaia [9] in 2013 have successfully flown trajectories leveraging structures from the CR3BP. In the Earth-Moon system, the spacecraft ARTEMIS P-1 as part of the THEMIS mission [10] was the first spacecraft to fly between Earth-Moon libration points orbits in 2011. As of January 2022, the satellite Queqiao, part of the Chinese Chang'e-4 mission [11], is the only spacecraft orbiting an Earth-Moon libration point.

Four-body dynamical models are currently an active area of research. In 1960, Huang [12] derived the equations of motion in a problem now termed the Bicircular Restricted Four-Body Problem (BCR4BP), and published them in a technical note titled *The Very Restricted*

*Four-Body Problem.* Since then, four-body models have been defined and investigated by a number of researchers. Examples of such work include the development by Scheeres [13] and Olikara[14] of the restricted Hill four-body problem, which was employed to explore the motion near the Sun-perturbed $L_4$ and $L_5$ equilibrium points of the Earth-Moon system. Additionally, coherent four-body models, i.e., models where the Moon's motion is a solution of the Sun-Earth CR3BP, have been developed. Andreu [15] developed a Sun-perturbed, coherent bicircular four-body model, denoted the quasi-bicircular problem, to investigate the phase space in the vicinity of the $L_1$ and $L_2$ points. Another coherent four-body model describing a Moon-perturbed Sun-Earth system was derived by Guzmàn [16] and employed to construct transfers to Sun-Earth libration point orbits leveraging lunar gravity assists. Comparisons between non-coherent and coherent bicircular four-body models have been discussed extensively [17]–[19]. The four-body model that is employed in this investigation is the BCR4BP [20], [21]. Periodic and quasi-periodic motion associated with the phase space near the collinear[22] and triangular [20], [23] Earth-Moon equilibrium points are an active field of research. Note that four-body models are not restricted to the Sun-planet-moon-spacecraft configurations described in the previous contributions; Scheeres and Bellerose [24] describe the motion of a spacecraft under the influence of a sun and a binary system of asteroids. Lower-fidelity models capture behaviors from the ephemeris model; the numerous four-body models mentioned in the previous contributions each capture various aspects of this higher-fidelity model.

Four-body models have been successfully employed for trajectory design in recent years. One preeminent problem that is examined within the context of the four-body dynamical models is the design of low-energy transfers [25]–[28] from the Earth to the Moon leveraging the gravitational influence of the Sun. An exhaustive list of optimal two-impulse Earth-Moon transfers computed in the BCR4BP is provided by Topputo [29]. Three-impulse transfers that include Lunar Gravity Assists (LGA) are constructed within the context of the bicircular restricted four-body problem [30], [31] and the bielliptic restricted four-body problem [32]. Recent contributions [33]–[35] have explored the design of low-energy lunar transfers with low-thrust propulsion methods.

This investigation leverages the Earth-Moon NRHOs as the hub orbit in cislunar space. The NRHOs are a subset of the halo family of orbits and are defined within the context of the CR3BP. Previous contributions demonstrate that an infinity of periodic orbits exists in the CR3BP [36], [37]. Howell [36] demonstrated the existence of the halo family of periodic orbits. Zimovan et al. [38] employed the linear stability properties of the Earth-Moon halo orbits to define the boundaries of the NRHO subsets. An NRHO baseline is available as a SPICE SPK-type [39] file on the JPL website [40]. The baseline spans 15 years from January 2020 to February 2035 and possesses small discontinuities in velocity near apolune that allow the orbit to be maintained [41]. Additionally, Zimovan-Spreen [42], [43] identified multiple related families of periodic orbits in the close vicinity of the $L_2$ NRHOs. Previous authors also investigated the transition of the NRHOs to higher-fidelity dynamical models, including Boudad et al. [44] in the BCR4BP and Vutukuri [45] in the ephemeris force model.

### 1.3 Research Objectives and Document Overview

The overarching goal of this investigation is the development of a framework for periodic and transit options in the Earth-Moon-Sun system. To enable frequent transit between the cislunar and the heliocentric region, further understanding of the fundamental dynamical structures in the Earth-Moon-Sun system is necessary. Expanding the understanding of this complex dynamical environment increases the number of options for a mission scenario and facilitates the trajectory design process. Rather than relying on an overlapping models approach, the current investigation employs a four-body model, the Bicircular Restricted Four-Body Problem (BCR4BP). The proposed framework is articulated in terms of the following objectives:

1. *Develop a catalog of dynamical structures in an Earth-Moon-Sun multi-body model*
   Dynamical structures, such as equilibrium solutions, periodic orbits and their associated manifolds, as well as forbidden regions are investigated within the context of the BCR4BP. The relationships between these dynamical structures and the lower-fidelity natural flows existing in the CR3BP are explored.

2. *Develop a framework for transfer design in the Earth-Moon-Sun system that employs the dynamical structures and techniques from dynamical system theory*

   The dynamical structures explored in the BCR4BP are the foundations of this transfer design framework. Tools from dynamical system theory, such as mapping techniques, differential corrections, and continuation schemes are employed such that the natural flow and low-energy pathways emerge between the structures in the cislunar space and the heliocentric region.

3. *Demonstrate the use of dynamical structures and tools to design end-to-end transfers between the cislunar and heliocentric regions*

   The applicability of the proposed framework to practical trajectory design scenarios is verified. The proposed framework is employed to design end-to-end trajectories for two sample mission scenarios. End-to-end transfers between the Gateway in an Earth-Moon NRHO and a Sun-Earth halo orbit are constructed. Two types of transfers are constructed: one-way transfers to heliocentric space as well as round-trip trajectories that return to the lunar orbit after completion of the objectives in heliocentric space. The trajectory design is then validated in the full ephemeris model.

The present investigation is focused on trajectory design in the Earth-Moon-Sun system, with the Gateway orbit as the orbit of interest in the cislunar region. However, the proposed framework is applicable to other planet-moon-sun systems, and other orbits in cislunar space. The document is organized as follow:

**Chapter 2 - Dynamical Models** The three dynamical models employed in this investigation are presented. The Circular Restricted Three-Body Problem (CR3BP) is an autonomous model approximating the Earth-Moon dynamics. The Bicircular Restricted Four-Body Problem (BCR4BP) is a time-dependent, periodic model describing the motion of a spacecraft in the Earth-Moon-Sun regime. Two formulations of the BCR4BP are leveraged. The first formulation is defined in the Earth-Moon rotating frame and corresponds to a *Sun-perturbed* Earth-Moon CR3BP. The second formulation describes a *Moon-perturbed* Sun-Earth CR3BP and is defined in the Sun-$B_1$

rotating frame, where $B_1$ is the Earth-Moon barycenter. The BCR4BP is an intermediate step between the CR3BP and a high-fidelity, time-dependent, non-periodic ephemeris model. This $N$-body model based on ephemeris data provides high-fidelity analysis for particular mission scenarios.

**Chapter 3 - Trajectory Building and Numerical Schemes** Nonlinear dynamical systems, such as models developed in the first chapter, are complex and challenging to analyze. Methods from dynamical systems theory facilitate the investigation of these complex systems. In contrast to linear systems, nonlinear systems cannot be decomposed into parts, solved separately and recombined to deliver a final assessment; the superposition principle does not apply to nonlinear systems. Thus, the goal of any application of dynamical systems theory is not to supply a solution to this complex, nonlinear problem, but to offer insight concerning the dynamical space in the vicinity of a specific trajectory. First, linear behavior characteristics are obtained through the state-transition matrix. Differential corrections schemes then leverage this information to adjust the characteristics of a certain trajectory. Continuation strategies then expand these solutions into a family of trajectories sharing similar features. Finally, the algorithms employed to numerically integrate the differential equations of motion, as well as the trajectory design tools employed for verification of these integrations, are introduced.

**Chapter 4 - Dynamical Structures in the BCR4BP** In this chapter, various dynamical structures that exist within the context of the BCR4BP are defined. Instantaneous equilibrium solutions exist in the BCR4BP, as non-autonomous counterparts of the time-invariant Lagrange points in the CR3BP. Instantaneous, or pulsating, zero velocity surfaces (ZVSs) appear in the BCR4BP to add perspective for the dynamical behavior. The ZVSs enclose forbidden regions that limit the motion of an object in space and are defined as a function of the energy along a trajectory. Two energy-like quantities are defined within the BCR4BP: the Earth-Moon energy-like value and the Sun-$B_1$ energy-like value. Energy-like plots offer a binary check to record possible transit into and out of cislunar space at a certain epoch along a path. Precisely periodic

orbits that possess orbital periods in resonance with the Earth-Moon-Sun period, i.e., the synodic period, are accessible in both the Earth-Moon and the Sun-$B_1$ rotating frames. Bounded motion is also available and constructed for transitioning orbits that do not possess a resonance with the synodic period. Lastly, invariant manifolds provide a useful approximation to the nonlinear dynamical behavior in the vicinity of a reference solution. Strategies to compute global invariant manifolds associated with periodic orbits and bounded motion are introduced.

**Chapter 5 - Cislunar-to-Heliocentric Transfers** A comprehensive knowledge of the dynamical structures identified in the BCR4BP simplifies the preliminary design process for transfers between the Earth-Moon system and the Sun-$B_1$ system. The transfer framework between cislunar and heliocentric space is described. Natural motion to and from the lunar vicinity is explored using an approximate manifold from the BCR4BP halo orbits. Perilune transfer families are then constructed to extend the pool of available initial guesses for the end-to-end transfer between the Earth-Moon NRHO and the Sun-$B_1$ LPO and are summarized in perilune transfer maps. Various methods to select an initial guess among the collection of available arcs for a transfer to/from the 9:2 synodic resonant $L_2$ NRHO, given certain desired transfer characteristics, are introduced. The selected initial guess is then corrected using a differential corrections scheme, resulting in a continuous end-to-end trajectory. To illustrate the trajectory design framework, multiple families of round-trip transfers between the Earth-Moon 9:2 synodic resonant BCR4BP NRHO and $\underline{L}_1/\underline{L}_2$ halo LPOs are constructed. The transfers represent a range of departure and arrival epochs along the Earth-Moon NRHO, as well as a variety of the geometries near the Moon and in heliocentric space. Finally, the trajectories constructed in the BCR4BP are validated in the higher-fidelity ephemeris model. To facilitate the transition between dynamical models, a novel transformation strategy is developed to transition an end-to-end transfer from the BCR4BP to a suitable initial guess for a transfer in the ephemeris model.

**Chapter 6 - Concluding Remarks** A summary of the results is presented and recommendations for future work are offered.

Portions of this work have been presented at various conferences and published elsewhere prior to incorporation into this document. The original papers are available in References [21], [44], [46]–[52].

# 2. DYNAMICAL MODELS

Three dynamical models are employed in this investigation. The Circular Restricted Three-Body Problem (CR3BP) is an autonomous model approximating the Earth-Moon dynamics. The Bicircular Restricted Four-Body Problem (BCR4BP) is a time-dependent, periodic model describing the motion of a spacecraft in the Earth-Moon-Sun regime. Two formulations of the BCR4BP are leveraged. The first formulation is defined in the Earth-Moon rotating frame and corresponds to a *Sun-perturbed* Earth-Moon CR3BP. The second formulation describes a *Moon-perturbed* Sun-Earth CR3BP and is defined in the Sun-$B_1$ rotating frame, where $B_1$ is the Earth-Moon barycenter. The BCR4BP is an intermediate step between the CR3BP and a high-fidelity, time-dependent, non-periodic ephemeris model. This $N$-body model based on ephemeris data provides high-fidelity analysis for particular mission scenarios. Note that these three lower-fidelity dynamical models are specific cases of the general $\mathcal{N}$-body problem[1].

## 2.1 The Circular Restricted Three-Body Problem

The first lower-fidelity model employed in this analysis is the CR3BP. In the CR3BP, the motion of a massless spacecraft is subject to the influence of two primary gravitational bodies, for example, the Earth and the Moon or the Sun and the Earth. The model assumes that the two primaries are point masses in circular orbits about their common center of mass; this assumption yields an autonomous dynamical system. The motion of the spacecraft under the influence of the two primaries is described relative to a rotating frame moving at a fixed rate consistent with the circular rotation of the primaries. By convention, the differential equations governing the CR3BP are nondimensional. The characteristic quantities include: (i) the distance between the primaries; (ii) the sum of the primary masses; (iii)

[1]↑See Appendix A for a discussion on the $\mathcal{N}$-body problem.

a characteristic time such that the nondimensional gravitational constant $\tilde{G}$ equals unity[2]. The nondimensional equations of motion are then

$$\ddot{x} = 2\dot{y} + \frac{\partial U^*}{\partial x}, \quad \ddot{y} = -2\dot{x} + \frac{\partial U^*}{\partial y}, \quad \ddot{z} = \frac{\partial U^*}{\partial z} \tag{2.1}$$

where $x, y, z$ (respectively, $\dot{x}, \dot{y}, \dot{z}$) are the position (respectively, the velocity) components of the spacecraft expressed in the Earth-Moon rotating coordinates and derivatives as viewed by an observer in the rotating frame. The associated pseudo-potential function $U^*$ is defined for the Earth-Moon CR3BP as

$$U^* = \frac{1}{2}(x^2 + y^2) + \frac{\mu}{r_{\text{e-sc}}} + \frac{1-\mu}{r_{\text{m-sc}}} \tag{2.2}$$

The quantities $r_{\text{e-sc}}$ and $r_{\text{m-sc}}$ are the distances between the spacecraft and the primaries, and $\mu = {}^{m_{\text{m}}}/_{(m_{\text{e}}+m_{\text{m}})}$ is the mass parameter for the Earth-Moon CR3BP system.

The equations of motion in the CR3BP do not admit a closed-form solution. However, five equilibrium solutions, the libration points, exist and are denoted $L_1$ through $L_5$. The CR3BP allows a single integral of the motion, the Jacobi constant, evaluated as

$$C = 2U^* - \left(\dot{x}^2 + \dot{y}^2 + \dot{z}^2\right) \tag{2.3}$$

This energy-like quantity limits the motion of the spacecraft to regions where the magnitude of the rotating velocity is real and not a complex quantity. These regions are bounded by Zero Velocity Surfaces (ZVSs). Detailed derivation of the equations of motion, equilibrium points, and ZVSs of the CR3BP are available in Boudad, 2018 [21].

## 2.2 The Bicircular Restricted Four-Body Problem

In scenarios where the gravitational influence of the Sun is non-negligible, a higher-fidelity model is necessary to accurately describe the spacecraft behavior. The BCR4BP incorporates the gravitational effect of three massive bodies, for instance, the Earth, the Moon and the

[2]↑See Appendix B for the characteristic quantities associated with various CR3BP systems.

Sun, on the motion of a spacecraft [17], [20], [21]. The mass of the spacecraft is assumed to be negligible in comparison to the masses of the other bodies.

### 2.2.1 Earth-Moon Frame Formulation

In this model, the Earth and the Moon are assumed to move in circular orbits around their common barycenter, denoted $B_1$, while the Sun and $B_1$ move in circular orbits with respect to the Earth-Moon-Sun barycenter, labeled $B_2$. Note that this adaptation of the BCR4BP assumes the Sun moves in the Earth-Moon plane of motion. While versions of BCR4BP with different orbital planes for the primaries exist [21], the coplanar assumption is adequate for the variety of applications considered in this analysis. The BCR4BP is not a coherent model: the perturbing acceleration from the Sun does not influence the motion of the Earth and the Moon, thus, the motion of the Moon is not a solution to the Sun-Earth CR3BP. When viewed in the Earth-Moon rotating frame, the Sun moves in a circular orbit around the Earth-Moon barycenter $B_1$, as apparent in Figure 2.1. The period of the orbit of the Sun in this frame is equal to the synodic month, that is, approximately 29.5 days. The equations of the motion for the Earth-Moon CR3BP, in Equation (2.1), are extended to include the solar gravitational influence as follows[3],

$$\ddot{x} = 2\dot{y} + \frac{\partial \Upsilon^*}{\partial x}, \quad \ddot{y} = -2\dot{x} + \frac{\partial \Upsilon^*}{\partial y}, \quad \ddot{z} = \frac{\partial \Upsilon^*}{\partial z} \tag{2.4}$$

where $\Upsilon^*$ is the pseudo-potential function in the BCR4BP

$$\Upsilon^* = U^* + \frac{\mu_\mathrm{s}}{r_\text{s-sc}} - \frac{\mu_\mathrm{s}}{a_\mathrm{s}^3}(x_\mathrm{s}\, x + y_\mathrm{s}\, y + z_\mathrm{s}\, z) \tag{2.5}$$

Then, $\mu_\mathrm{s} = \frac{m_\mathrm{s}}{m_\mathrm{e}+m_\mathrm{m}}$ is the nondimensional mass of the Sun and $a_\mathrm{s} = \frac{r_\mathrm{s}}{r_\text{e-m}}$ is the nondimensional distance between the Earth-Moon barycenter and the Sun. The variables $x_\mathrm{s}, y_\mathrm{s}, z_\mathrm{s}$ are the

[3]↑A detailed derivation of the equations of motion is available in Appendix C.1.

position components of the Sun, originating at $B_1$, and expressed in terms of the Earth-Moon rotating frame,

$$\begin{bmatrix} x_s \\ y_s \\ z_s \end{bmatrix} = a_s \begin{bmatrix} \cos(\theta) \\ \sin(\theta) \\ 0 \end{bmatrix} = \begin{bmatrix} \cos(\omega\, t + \theta_0) \\ \sin(\omega\, t + \theta_0) \\ 0 \end{bmatrix} \tag{2.6}$$

where the Sun angle $\theta$ is measured from the rotating $\hat{x}$ axis to the Sun position vector as defined in Figure 2.1, and $\omega = -0.9253$ is the nondimensional angular velocity of the Sun as viewed in the Earth-Moon rotating frame. This angular velocity is computed as the difference between the nondimensional mean motion of the Sun in the inertial frame centered at the Earth-Moon barycenter, that is, $n_s = \sqrt{(1+\mu_s)/a_s^3}$, and the nondimensional mean motion of the Earth-Moon system with respect to the same observer, $n$, that is, the value one. Since the nondimensional mean motion of the Sun is less than nondimensional mean motion of the Earth-Moon system, $\omega$ is negative and the Sun appears to move clockwise in the Earth-Moon rotating frame.

Observe that the independent time variable, $t$, expressed in Earth-Moon nondimensional units, explicitly appears in the BCR4BP pseudo-potential expression through the terms that include the position of the Sun. Therefore, the BCR4BP is time-dependent and does not

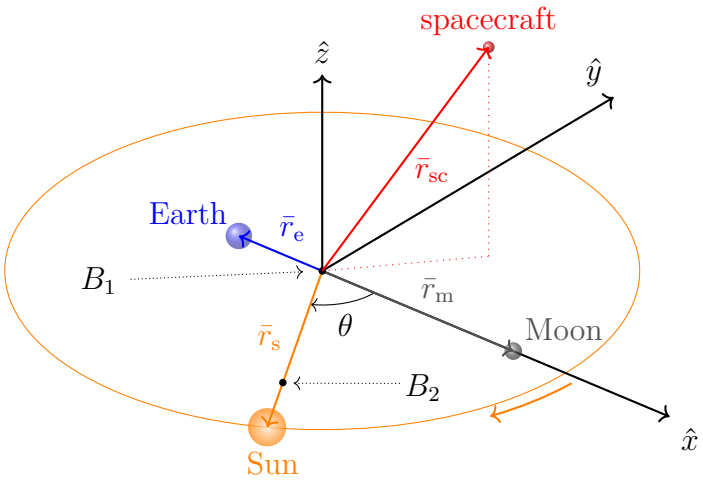


**Figure 2.1.** BCR4BP in the Earth-Moon rotating frame

admit an integral of the motion. However, an energy-like function is defined to be consistent with the Jacobi constant in the CR3BP, i.e.,

$$H(\theta) = 2\Upsilon^* - \left(\dot{x}^2 + \dot{y}^2 + \dot{z}^2\right) \tag{2.7}$$

Similar to the Jacobi constant, this energy-like quantity instantaneously limits the motion of the spacecraft to regions where the magnitude of the rotating velocity is real and not a complex quantity. Note that this energy-like function, $H$, is defined as a scaled multiple of the Hamiltonian function [6], [53] in the BCR4BP as formulated in the Earth-Moon rotating frame, $\mathcal{H}$, such that $H = -2\mathcal{H}$.

### 2.2.2 Sun-$B_1$ Frame Formulation

In scenarios where the spacecraft departs the Earth-Moon vicinity, its trajectory may be more insightful when represented in the Sun-$B_1$ rotating frame. The BCR4BP equations of motion are, therefore, also derived in this frame. In the $B_2$-centered Sun-$B_1$ rotating frame, the Sun and $B_1$ are fixed, while the Earth and the Moon are in circular orbits about their common barycenter $B_1$, as illustrated Figure 2.2. The positions of the Earth and the Moon are uniquely described by the Moon angle, $\underline{\theta}$, defined as the angle between the rotating $\hat{\underline{x}}$ axis and the position vector from $B_1$ to Moon, labeled $\bar{\underline{r}}_{B_1\mathrm{m}}$. Note that underlined variables denote quantities in the Sun-$B_1$ rotating frame, while non-underlined variables describe quantities in the Earth-Moon rotating frame. The equations of motion for the BCR4BP in the Sun-$B_1$ rotating frame are[4],

$$\ddot{\underline{x}} = 2\dot{\underline{y}} + \frac{\partial \underline{\Upsilon^*}}{\partial \underline{x}}, \quad \ddot{\underline{y}} = -2\dot{\underline{x}} + \frac{\partial \underline{\Upsilon^*}}{\partial \underline{y}}, \quad \ddot{\underline{z}} = \frac{\partial \underline{\Upsilon^*}}{\partial \underline{z}} \tag{2.8}$$

where $\underline{\Upsilon^*}$ is the pseudo-potential function defined in the Sun-$B_1$ rotating frame,

$$\underline{\Upsilon^*} = \frac{1}{2}(\underline{x}^2 + \underline{y}^2) + \frac{1 - \frac{1}{\mu_\mathrm{s}+1}}{\underline{r}_{\text{s-sc}}} + \frac{\frac{1-\mu}{\mu_\mathrm{s}+1}}{\bar{\underline{r}}_{\text{e-sc}}} + \frac{\frac{\mu}{\mu_\mathrm{s}+1}}{\underline{r}_{\text{m-sc}}} \tag{2.9}$$

[4]↑A detailed derivation of the equations of motion is available in Appendix C.2.

The equations of motion in the BCR4BP, as formulated in the Sun-$B_1$ rotating frame in Equation (2.8) represent the same dynamics as the equations of motion for the BCR4BP in the Earth-Moon rotating frame in Equation (2.4). Consistent with the equations of motion in the CR3BP and the equations of motion for the BCR4BP as formulated in the Earth-Moon rotating frame, the equations of motion describing the BCR4BP dynamics in the Sun-$B_1$ rotating frame are nondimensional. The characteristic quantities include: (i) the Sun-$B_1$ distance; (ii) the sum of the Sun, Earth and Moon masses; (iii) a characteristic time such that the nondimensional gravitational constant $\underline{\tilde{G}}$ equals unity[5]. The position vectors of the Earth and the Moon with respect to the system barycenter, $B_2$, are then defined as,

$$\begin{aligned}
\bar{\underline{r}}_{\mathrm{e}} &= \bar{\underline{r}}_{B_1} + \bar{\underline{r}}_{B_1\mathrm{e}} = \begin{bmatrix} 1 - \frac{1}{\mu_{\mathrm{s}}+1} \\ 1 - \frac{1}{\mu_{\mathrm{s}}+1} \\ 0 \end{bmatrix} + \begin{bmatrix} -\frac{\mu}{a_{\mathrm{s}}} \cos(\underline{\theta}) \\ -\frac{\mu}{a_{\mathrm{s}}} \sin(\underline{\theta}) \\ 0 \end{bmatrix} \\
\bar{\underline{r}}_{m} &= \bar{\underline{r}}_{B_1} + \bar{\underline{r}}_{B_1\mathrm{m}} = \begin{bmatrix} 1 - \frac{1}{\mu_{\mathrm{s}}+1} \\ 1 - \frac{1}{\mu_{\mathrm{s}}+1} + \\ 0 \end{bmatrix} + \begin{bmatrix} \frac{1-\mu}{a_{\mathrm{s}}} \cos(\underline{\theta}) \\ \frac{1-\mu}{a_{\mathrm{s}}} \sin(\underline{\theta}) \\ 0 \end{bmatrix}
\end{aligned} \tag{2.10}$$

[5] ↑See Appendix B for the characteristic quantities associated with the Sun-$B_1$ CR3BP.

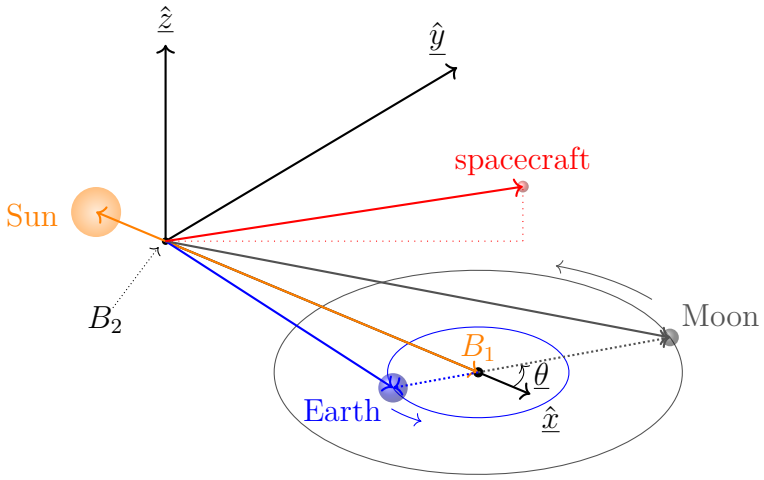


**Figure 2.2.** BCR4BP in the Sun-$B_1$ rotating frame.

where $\underline{\theta} = \boldsymbol{\pi} - \theta = \underline{\omega}\,\underline{t} + \underline{\theta}_0$ is the Moon angle, and $\underline{\omega} = \frac{|\omega|}{1-|\omega|}$ is the nondimensional angular rate of the Earth and the Moon in their motion around their common barycenter $B_1$. Note that $\underline{t}$ is the independent time variable expressed in terms of Sun-$B_1$ nondimensional quantities. Alignment of the Sun, Earth, and Moon occurs every synodic period, that is, approximately 29.5 days. Similar to the BCR4BP formulated in the Earth-Moon rotating frame, the Sun-$B_1$ BCR4BP is a non-autonomous, periodic system.

An energy-like quantity is defined in the Sun-$B_1$ frame formulation of the BCR4BP. Recall that the BCR4BP is a time-dependent system. In the Earth-Moon rotating frame, the independent time variable, $\underline{t}$ explicitly appears in the BCR4BP pseudo potential in Equation (2.9) through the positions of the Earth and the Moon, defined in Equation (2.10). Thus, the BCR4BP does not admit an integral of the motion. However, a scaled version of the Hamiltonian function in the BCR4BP is defined to be consistent with the Jacobi constant in the CR3BP. In the Sun-$B_1$ rotating frame, this energy-like value is

$$\underline{H}(\underline{\theta}) = 2\underline{\Upsilon^*} - \sqrt{(\underline{\dot{x}}^2 + \underline{\dot{y}}^2 + \underline{\dot{z}}^2)} \tag{2.11}$$

Equations (2.11) relate nondimensional position and velocity states. Thus, similar to the Jacobi constant in the CR3BP, the $\underline{H}$ value, is a nondimensional energy-like metric.

### 2.2.3 Transformation Between the Two Formulations

The equations of motion for the BCR4BP as viewed in the Earth-Moon frame in Equation (2.4), and the formulation in the Sun-$B_1$ rotating frame in Equation (2.8), describe the same dynamical system. A combination of scaling and rotating transformations is employed to transition states from one formulation to the other. First, the transformation from the Earth-Moon frame formulation to the Sun-$B_1$ frame is described in terms of the following steps:

1. Compute the epoch in the Sun-$B_1$ formulation, Moon angle $\underline{\theta}$ from the epoch in the Earth-Moon rotating frame, i.e., the Sun angle $\theta$

2. Rotate each state from the Earth-Moon rotating frame to the Sun-$B_1$ rotating frame using the Moon angle $\underline{\theta}$
3. Dimensionalize the state components using the Earth-Moon characteristic quantities
4. Nondimensionalize the resulting state components using the Sun-$B_1$ characteristic quantities
5. Shift the origin of the position components[6] of the state vector from $B_1$ to $B_2$

The relationship between the Sun angle and the Moon angle is

$$\underline{\theta} = \boldsymbol{\pi} - \theta \tag{2.12}$$

Thus, a Sun-Earth-Moon configuration occurs at $\theta = 180°$, or equivalently, $\underline{\theta} = 0°$ and from the perspective of the Earth, a full Moon is observed. Conversely, for $\theta = 0°$ or $\underline{\theta} = 180°$, an Earth-Moon-Sun configuration occurs, and a new Moon is observed from Earth. Steps 2 through 5 of the transformation are summarized in two equations as

$$\begin{aligned}
\begin{bmatrix} \underline{x} & \underline{y} & \underline{z} \end{bmatrix} &= \frac{1}{a_\mathrm{s}} \left( \begin{bmatrix} x & y & z \end{bmatrix} \cdot \mathcal{C} \right) + \begin{bmatrix} 1 - \frac{1}{\mu_\mathrm{s}+1} & 0 & 0 \end{bmatrix} \\
\begin{bmatrix} \dot{\underline{x}} & \dot{\underline{y}} & \dot{\underline{z}} \end{bmatrix} &= \sqrt{\frac{a_\mathrm{s}}{\mu_\mathrm{s}+1}} \left( \begin{bmatrix} \dot{x} & \dot{y} & \dot{z} \end{bmatrix} \cdot \mathcal{C} + \begin{bmatrix} x & y & z \end{bmatrix} \cdot \dot{\mathcal{C}} \right)
\end{aligned} \tag{2.13}$$

where the direction cosine matrix from the Earth-Moon rotating frame to the Sun-$B_1$ rotating frame and its first derivative with respect to time are

$$\mathcal{C} = \begin{bmatrix} \cos\underline{\theta} & \sin\underline{\theta} & 0 \\ -\sin\underline{\theta} & \cos\underline{\theta} & 0 \\ 0 & 0 & 1 \end{bmatrix}, \quad \dot{\mathcal{C}} = \underline{\omega} \begin{bmatrix} -\sin\underline{\theta} & \cos\underline{\theta} & 0 \\ -\cos\underline{\theta} & -\sin\underline{\theta} & 0 \\ 0 & 0 & 0 \end{bmatrix}, \tag{2.14}$$

[6]↑The relative velocity of $B_1$ with respect to $B_2$ is zero. Thus, the velocity components of the state vector do not need to be shifted.

To transform states from the Sun-$B_1$ frame formulation to the Earth-Moon formulation, steps 2 to 5 are simply accomplished in reverse order. The corresponding operations are summarized in the following equations

$$\begin{aligned}\begin{bmatrix} x & y & z \end{bmatrix} &= a_{\mathrm{s}} \left( \begin{bmatrix} \underline{x} & \underline{y} & \underline{z} \end{bmatrix} - \begin{bmatrix} 1 - \frac{1}{\mu_{\mathrm{s}}+1} & 0 & 0 \end{bmatrix} \right) \cdot \mathcal{C}^T \\ \begin{bmatrix} \dot{x} & \dot{y} & \dot{z} \end{bmatrix} &= \sqrt{\frac{\mu_{\mathrm{s}}+1}{a_{\mathrm{s}}}} \left( \begin{bmatrix} \underline{\dot{x}} & \underline{\dot{y}} & \underline{\dot{z}} \end{bmatrix} \cdot \mathcal{C} + \begin{bmatrix} \underline{x} & \underline{y} & \underline{z} \end{bmatrix} \cdot \dot{\mathcal{C}}^T \right)\end{aligned} \tag{2.15}$$

where the $\mathcal{X}^T$ operator denotes the transpose of the matrix $\mathcal{X}$. The transformations in Equations (2.13)–(2.15) offer a useful way to transition states from one formulation of the BCR4BP to the other and eliminate the need to numerically integrate both sets of differential equations in Equations (2.4) and (2.8).

### 2.3 The $N$-Body Ephemeris Model

For applications in mission scenarios where high-fidelity modeling accuracy is required, the $N$-Body differential equations and planetary ephemerides are employed. The $N$-body dynamics describe the motion of a particle of interest (e.g., a spacecraft), labeled $P_{\mathrm{i}}$, subject to the gravitational influence of a central body, $P_c$, and $N$ perturbing bodies $P_1, P_2, \ldots, P_N$, all assumed to be modeled as particles. The position state vector, $\bar{\rho}$ , for each of the bodies is expressed in inertial coordinates relative to the central body $P_c$, as denoted in Figure 2.3. The equations of motion for the body of interest are

$$\ddot{\bar{\rho}}_{c\mathrm{i}} = -G\left(\frac{m_{\mathrm{i}} + m_c}{\|\bar{\rho}_{c\mathrm{i}}\|^3}\right)\bar{\rho}_{c\mathrm{i}} + G\sum_{\substack{k=1 \\ k\neq \mathrm{i},c}}^{N} m_k \left(\frac{\bar{\rho}_{ck} - \bar{\rho}_{c\mathrm{i}}}{\|\bar{\rho}_{ck} - \bar{\rho}_{c\mathrm{i}}\|^3} - \frac{\bar{\rho}_{ck}}{\|\bar{\rho}_{ck}\|^3}\right) \tag{2.16}$$

where $G$ is the gravitational constant and $m_\gamma$ is the mass of the $P_\gamma$ body. Note that the state vector for the $P_k$ perturbing body with respect to the central body $P_c$, that is, $\bar{\rho}_{ck}$, is accessed using the Jet Propulsion Laboratory DE430 ephemerides via the SPICE toolkit [39], [54]. The ephemeris formulation in the current investigation includes the Earth, the Moon, the Sun, and Jupiter. The equilibrium points derived in the lower-fidelity models, such as the $\mathrm{L_i}$ libration points in the CR3BP, do not exist in the ephemeris model. However,

quasi-periodic motion in the vicinity of these points remains available in the higher-fidelity ephemeris model.

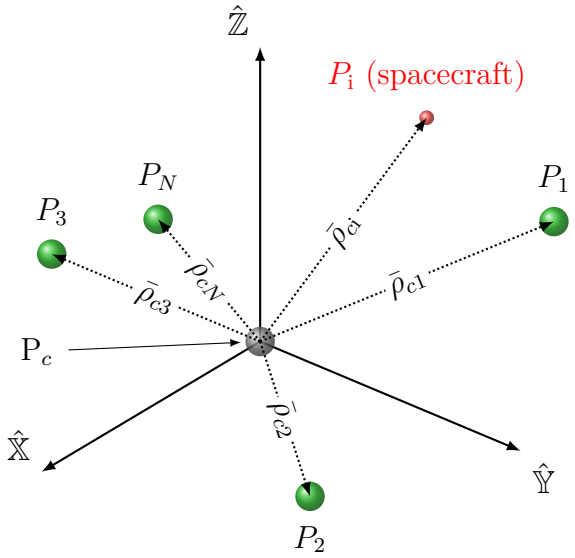


**Figure 2.3.** $N$-Body ephemeris model as defined in the $P_c$-centered inertial frame.

# 3. TRAJECTORY BUILDING AND NUMERICAL SCHEMES

Nonlinear dynamical systems, such as the CR3BP or the BCR4BP, are complex and analysis can be challenging. Methods from dynamical systems theory facilitate the investigation of these complex systems. In contrast to linear systems, nonlinear systems cannot be decomposed into parts, solved separately and recombined to deliver a final assessment; the superposition principle does not apply to nonlinear systems [55]. Thus, the goal of any application of dynamical systems theory is not to supply a solution to this complex, nonlinear problem, but to offer insight concerning the dynamical space in the vicinity of a specific trajectory. First, linear behavior characteristics are obtained through the state-transition matrix. Differential corrections schemes then leverage this information to adjust the characteristics of a certain trajectory. Continuation strategies then expand these solutions into a family of trajectories sharing similar features. Finally, the algorithms employed to numerically integrate the differential equations of motion, as well as the trajectory design tools employed for verification of these integrations, are introduced.

## 3.1 State-Transition Matrix

The equations of motion for the CR3BP in Equation (2.1), for the BCR4BP in Equations (2.4) and (2.8), and the $N$-body ephemeris models in Equation (2.16) are nonlinear. Nonlinear systems of equations are expressed in terms of a vector differential equation in the form

$$\dot{\bar{\mathcal{X}}}(\mathcal{T}) = \bar{\mathcal{F}}\left(\bar{\mathcal{X}}(\mathcal{T})\right) \tag{3.1}$$

where $\bar{\mathcal{X}}$, the state vector and $\bar{\mathcal{F}}$, the vector of nonlinear functions depend on the time $\mathcal{T}$. The perturbation along a given trajectory, $\delta\bar{\mathcal{X}}(\mathcal{T})$, is defined

$$\delta\bar{\mathcal{X}}(\mathcal{T}) = \bar{\mathcal{X}}(\mathcal{T}) - \bar{\mathcal{X}}_R(\mathcal{T}) \tag{3.2}$$

where $\bar{\mathcal{X}}_R(\mathcal{T})$ is the reference state and $\bar{\mathcal{X}}(\mathcal{T})$ is the actual state at any time along the path. Using the perturbation defined in Equation (3.2), Equation (3.1) is rewritten as a function of a reference state $\bar{\mathcal{X}}_R(\mathcal{T})$ and a perturbation $\delta\bar{\mathcal{X}}(\mathcal{T})$.

$$\dot{\bar{\mathcal{X}}}_R(\mathcal{T}) + \delta\dot{\bar{\mathcal{X}}}(\mathcal{T}) = \bar{\mathcal{F}}\left(\bar{\mathcal{X}}_R(\mathcal{T}) + \delta\bar{\mathcal{X}}(\mathcal{T})\right) \tag{3.3}$$

Then, a first-order Taylor series expansion yields

$$\dot{\bar{\mathcal{X}}}_R(\mathcal{T}) + \delta\dot{\bar{\mathcal{X}}}(\mathcal{T}) \approx \bar{\mathcal{F}}\Big(\bar{\mathcal{X}}_R(\mathcal{T})\Big) + \left.\frac{\partial\bar{\mathcal{F}}}{\partial\bar{\mathcal{X}}}\right|_{\bar{\mathcal{X}}_R(\mathcal{T})} \delta\bar{\mathcal{X}}(\mathcal{T}) + \text{H.O.T.} \tag{3.4}$$

The terms of order 2 or higher are denoted as Higher Order Terms, or H.O.T. Equation (3.4) is reduced to a linear relationship between $\delta\dot{\bar{x}}(t)$ and $\delta\bar{\mathcal{X}}(\mathcal{T})$ by recognizing that $\dot{\bar{\mathcal{X}}}_R(\mathcal{T}) = \bar{\mathcal{F}}\Big(\bar{\mathcal{X}}_R(\mathcal{T})\Big)$ and ignoring the H.O.T. Thus, Equation (3.4) is reduced to

$$\delta\dot{\bar{\mathcal{X}}}(\mathcal{T}) \approx \left.\frac{\partial\bar{\mathcal{F}}}{\partial\bar{\mathcal{X}}}\right|_{\bar{\mathcal{X}}_R(\mathcal{T})} \delta\bar{\mathcal{X}}(\mathcal{T}) = \mathbf{A}(\mathcal{T})\ \delta\bar{\mathcal{X}}(\mathcal{T}) \tag{3.5}$$

The $\mathbf{A}(\mathcal{T})$ matrix is the Jacobian matrix for the vector differential equation $\bar{\mathcal{F}}$ evaluated on $\bar{\mathcal{X}}_R(\mathcal{T})$. For instance, by defining $\delta\bar{\mathcal{X}} = \begin{bmatrix}\delta x & \delta y & \delta z & \delta\dot{x} & \delta\dot{y} & \delta\dot{z}\end{bmatrix}^T$, the linear variational equations of motion for the BCR4BP as defined in the Earth-Moon rotating frame are

$$\begin{bmatrix}\delta\dot{x}\\ \delta\dot{y}\\ \delta\dot{z}\\ \delta\ddot{x}\\ \delta\ddot{y}\\ \delta\ddot{z}\end{bmatrix} = \begin{bmatrix} 0 & 0 & 0 & 1 & 0 & 0\\ 0 & 0 & 0 & 0 & 1 & 0\\ 0 & 0 & 0 & 0 & 0 & 1\\ \Upsilon^*_{xx} & \Upsilon^*_{xy} & \Upsilon^*_{xz} & 0 & 2 & 0\\ \Upsilon^*_{yx} & \Upsilon^*_{yy} & \Upsilon^*_{yz} & -2 & 0 & 0\\ \Upsilon^*_{zx} & \Upsilon^*_{zy} & \Upsilon^*_{zz} & 0 & 0 & 0\end{bmatrix}\begin{bmatrix}\delta x\\ \delta y\\ \delta z\\ \delta\dot{x}\\ \delta\dot{y}\\ \delta\dot{z}\end{bmatrix} \tag{3.6}$$

where $\Upsilon^*$ is the pseudo-potential function for the BCR4BP in the Earth-Moon rotating frame, as defined in Equation (2.5). Similarly, the linear variational equations of motion

for the BCR4BP as defined in the Sun-$B_1$ rotating frame are obtained by denoting $\delta\bar{\mathcal{X}} = \begin{bmatrix} \delta\underline{x} & \delta\underline{y} & \delta\underline{z} & \delta\underline{\dot{x}} & \delta\underline{\dot{y}} & \delta\underline{\dot{z}} \end{bmatrix}^T$ and appear in the form

$$\begin{bmatrix} \delta\underline{\dot{x}} \\ \delta\underline{\dot{y}} \\ \delta\underline{\dot{z}} \\ \delta\underline{\ddot{x}} \\ \delta\underline{\ddot{y}} \\ \delta\underline{\ddot{z}} \end{bmatrix} = \begin{bmatrix} 0 & 0 & 0 & 1 & 0 & 0 \\ 0 & 0 & 0 & 0 & 1 & 0 \\ 0 & 0 & 0 & 0 & 0 & 1 \\ \underline{\Upsilon^*_{xx}} & \underline{\Upsilon^*_{xy}} & \underline{\Upsilon^*_{xz}} & 0 & 2 & 0 \\ \underline{\Upsilon^*_{yx}} & \underline{\Upsilon^*_{yy}} & \underline{\Upsilon^*_{yz}} & -2 & 0 & 0 \\ \underline{\Upsilon^*_{zx}} & \underline{\Upsilon^*_{zy}} & \underline{\Upsilon^*_{zz}} & 0 & 0 & 0 \end{bmatrix} \begin{bmatrix} \delta\underline{x} \\ \delta\underline{y} \\ \delta\underline{z} \\ \delta\underline{\dot{x}} \\ \delta\underline{\dot{y}} \\ \delta\underline{\dot{z}} \end{bmatrix} \tag{3.7}$$

where $\underline{\Upsilon^*}$ is the pseudo-potential function for the BCR4BP in the Earth-Moon rotating frame, as defined in Equation (2.9). Linear variational equations for the BCR4BP are derived employing a first-order Taylor series approximation.

A general solution of the linear variational equations is produced by integrating Equation (3.5) from time $\mathcal{T}_0$ to time $\mathcal{T}$. Recall that the $\mathbf{A}$ matrix relates the time derivative of the variational vector, $\dot{\bar{\mathcal{X}}}(\mathcal{T})$ to the variational vector itself, and is generally a function of time. Thus, a general solution of the linear variational vector equation is

$$\delta\bar{\mathcal{X}}(\mathcal{T}) = \mathbf{\Phi}(\mathcal{T}, \mathcal{T}_0)\ \delta\bar{\mathcal{X}}(\mathcal{T}_0) \tag{3.8}$$

where $\mathbf{\Phi}(\mathcal{T}, \mathcal{T}_0)$ is the State-Transition Matrix (STM) such that

$$\begin{aligned} \mathbf{\Phi}(\mathcal{T}, \mathcal{T}_0) &= \exp\left(\mathbf{A}(\mathcal{T} - \mathcal{T}_0)\right) \\ &= \frac{\partial\bar{\mathcal{X}}(\mathcal{T})}{\partial\bar{\mathcal{X}}(\mathcal{T}_0)} \end{aligned} \tag{3.9}$$

The State-Transition Matrix or *sensitivity matrix* relates perturbations in an initial state $\bar{\mathcal{X}}(\mathcal{T}_0)$ to the perturbations in a state downstream $\bar{\mathcal{X}}(\mathcal{T})$. This matrix is essentially a linear

map between the initial perturbation $\delta\bar{\mathcal{X}}(\mathcal{T}_0)$ and the perturbation at a later time $\bar{\mathcal{X}}(\mathcal{T}_0)$. The STM possesses many useful properties, including

$$\mathbf{\Phi}(\mathcal{T}_0, \mathcal{T}_0) = \mathbf{I} \tag{3.10}$$

$$\mathbf{\Phi}(\mathcal{T}_2, \mathcal{T}_0) = \mathbf{\Phi}(\mathcal{T}_2, \mathcal{T}_1)\,\mathbf{\Phi}(\mathcal{T}_1, \mathcal{T}_0) \tag{3.11}$$

$$\mathbf{\Phi}(\mathcal{T}_0, \mathcal{T}_1) = \mathbf{\Phi}^{-1}(\mathcal{T}_1, \mathcal{T}_0) \tag{3.12}$$

Substituting the general solution from Equation (3.8) into the differential equation in Equation (3.5) yields the following system of differential equations, here presented in matrix form, for $\mathbf{\Phi}(t, t_0)$:

$$\dot{\mathbf{\Phi}}(\mathcal{T}, \mathcal{T}_0) = \mathbf{A}\,\mathbf{\Phi}(\mathcal{T}, \mathcal{T}_0) \tag{3.13}$$

This system of differential equations is numerically integrated along with the equations of the motion, where Equation (3.10) identifies the initial conditions, i.e., $\mathbf{\Phi}(\mathcal{T}_0, \mathcal{T}_0)$. In regimes that admit no closed-form solution, such as the CR3BP or the BCR4BP, the sensitivity information from the STM offers useful predictions (in the linear sense) of the dynamical behavior.

### 3.2 Differential Corrections Schemes

The goal of the differential corrections process is the determination of a set of variables, collected into the design variable vector $\bar{\mathcal{X}}$, such that a collection of scalars and/or constraints, in a constraint vector $\bar{\mathcal{F}}$, is satisfied. The $n$ elements in the design variable vector, $\bar{\mathcal{X}}$, can be states, angles (for instance, Sun angle or Moon angle), time-of-flight or another variable of interest. The design variable vector is then formed as

$$\bar{\mathcal{X}} = \begin{bmatrix} \mathcal{X}_1 & \mathcal{X}_2 & \dots & \mathcal{X}_n \end{bmatrix}^T \tag{3.14}$$

Since the role of $\bar{\mathcal{X}}$ is essentially to 'control' the values in the constraint vector, $\bar{\mathcal{X}}$ is also termed the *control variables vector*. The $m$ elements of the constraint vector, $\bar{\mathcal{F}}$, are functions of one or more variables

$$\bar{\mathcal{F}} = \begin{bmatrix} \mathcal{F}_1 & \mathcal{F}_2 & \dots & \mathcal{F}_m \end{bmatrix}^T \tag{3.15}$$

The constraints are satisfied when a desired final state is computed such that the two-norm of the constraint vector evaluated at the design variable vector $\bar{\mathcal{X}}^*$ is below a specified numerical tolerance e,

$$\|\bar{\mathcal{F}}(\bar{\mathcal{X}}^*)\|_2 =< \mathrm{e} \tag{3.16}$$

The elements of the design variable vector are not independent. Thus, a relationship between them exists and the determination of $\bar{\mathcal{X}}^*$ is an iterative process. A multi-dimensional Newton-Raphson scheme [56] is the basis for the update equation due to its versatility and straightforward implementation. Let $\bar{\mathcal{X}}_c$ be a design variable vector close to $\bar{\mathcal{X}}^*$. The constraint vector, $\bar{\mathcal{F}}(\bar{\mathcal{X}}^*)$, is expanded about $\bar{\mathcal{X}}^*$ in a first-order Taylor series such that

$$\bar{\mathcal{F}}(\bar{\mathcal{X}}^*) = \bar{\mathcal{F}}(\bar{\mathcal{X}}_c) + \mathrm{D}\bar{\mathcal{F}}(\bar{\mathcal{X}}_c)\left(\bar{\mathcal{X}}^* - \bar{\mathcal{X}}_c\right) \tag{3.17}$$

where $\mathrm{D}\bar{\mathcal{F}}(\bar{\mathcal{X}}_c)$ is the $m \times n$ Jacobian matrix such that the term in the $\mathrm{i}^{\mathrm{th}}$ row and the $\mathrm{j}^{\mathrm{th}}$ column is defined as $\frac{\partial \mathcal{F}_\mathrm{i}}{\partial \mathcal{X}_\mathrm{j}}$ and evaluated at $\bar{\mathcal{X}}_c$. For speed and efficiency, the higher-order terms are ignored. Recognizing that $\bar{\mathcal{X}}^*$ satisfies the constraints, Equation (3.17) is rewritten as

$$\bar{\mathcal{F}}(\bar{\mathcal{X}}_c) + \mathrm{D}\bar{\mathcal{F}}(\bar{\mathcal{X}}_c)\left(\bar{\mathcal{X}}^* - \bar{\mathcal{X}}_c\right) = \bar{0} \tag{3.18}$$

For nonlinear problems, an iterative process is required to solve for $\bar{\mathcal{X}}^*$. When replacing $\bar{\mathcal{X}}^*$ by the design variables vector at the current iteration, i.e., $\bar{\mathcal{X}}_\mathrm{i}$, and $\bar{\mathcal{X}}_c$ by the design variables vector at the previous iteration, that is, $\bar{\mathcal{X}}_c$, Equation (3.18) becomes

$$\bar{\mathcal{F}}(\bar{\mathcal{X}}_{\mathrm{i}-1}) + \mathrm{D}\bar{\mathcal{F}}(\bar{\mathcal{X}}_{\mathrm{i}-1})\left(\bar{\mathcal{X}}_\mathrm{i} - \bar{\mathcal{X}}_{\mathrm{i}-1}\right) = \bar{0} \tag{3.19}$$

The change in the control variable vector, $\delta\bar{\mathcal{X}} = \bar{\mathcal{X}}_\mathrm{i} - \bar{\mathcal{X}}_{\mathrm{i}-1}$, is produced by inverting and rearranging Equation (3.19). When the number of design variables $n$ is equal to the number

of constraints $m$, the Jacobian matrix $\mathrm{D}\bar{\mathcal{F}}$ is square. If $\mathrm{D}\bar{\mathcal{F}}$ is nonsingular, the change in the design variables is evaluated as

$$\delta\bar{\mathcal{X}} = -\left(\mathrm{D}\bar{\mathcal{F}}(\bar{\mathcal{X}}_{\mathrm{i}-1})\right)^{-1} \bar{\mathcal{F}}(\bar{\mathcal{X}}_{\mathrm{i}-1}) \tag{3.20}$$

If the number of design variables exceeds the number of constraints ($n > m$), an infinite number of solutions $\bar{\mathcal{X}}_{\mathrm{i}}$ to Equation (3.16) exists. From among many options, the approach in this work identifies an update closest to the reference $\bar{\mathcal{X}}_{\mathrm{i}-1}$, and leverages the minimum-norm solution via the update equation

$$\delta\bar{\mathcal{X}} = -\left(\mathrm{D}\bar{\mathcal{F}}(\bar{\mathcal{X}}_{\mathrm{i}-1})\right)^{T} \left(\mathrm{D}\bar{\mathcal{F}}(\bar{\mathcal{X}}_{\mathrm{i}-1}) \left(\mathrm{D}\bar{\mathcal{F}}(\bar{\mathcal{X}}_{\mathrm{i}-1})\right)^{T}\right)^{-1} \bar{\mathcal{F}}(\bar{\mathcal{X}}_{\mathrm{i}-1}) \tag{3.21}$$

In Equation (3.21), the Jacobian matrix is a non-square matrix. The higher-order terms are ignored in the Taylor expansion, and the update equations are approximations. Thus, a solution $\bar{\mathcal{X}}_{\mathrm{i}}$ is computed by iterating on Equation (3.20) or on Equation (3.21), until reaching a selected tolerance. If the number of constraints exceeds the number of control variables ($n < m$), the system is said to be 'overdetermined' and, in general, admits no solution[1]. In this scenario, an approximate solution is selected that minimizes the square of the error for each scalar constraint using the method of least squares [57].

A note on the convergence rate is relevant. The rate of convergence for the Newton-Raphson algorithm is quadratic. The proof for the one-dimensional Newton-Raphson rate of convergence follows; it is extendable to the multi-dimensional case as well [58]. For any scalar function $\mathcal{F}(\bar{\mathcal{X}})$ with a continuous second derivative, the second-order Taylor expansion about the point $\bar{\mathcal{X}}$ near a root $\bar{\mathcal{X}}_r$ of $\mathcal{F}(x)$ yields

$$\mathcal{F}(\bar{\mathcal{X}}_r) = \mathcal{F}(\bar{\mathcal{X}}) + \mathcal{F}'(\bar{\mathcal{X}})(\bar{\mathcal{X}}_r - \bar{\mathcal{X}}) + \frac{1}{2}\mathcal{F}''(\bar{\mathcal{X}}_r)(\bar{\mathcal{X}} - \bar{\mathcal{X}}_r)^2 \tag{3.22}$$

[1]↑Overdetermined systems do offer solutions if some of the constraints are linear functions of the others.

Recall that, since $\bar{\mathcal{X}}_r$ is a root, $\mathcal{F}(\bar{\mathcal{X}}_r) = 0$ and rearranging the terms, yields

$$\frac{\mathcal{F}(\bar{\mathcal{X}})}{\mathcal{F}'(\bar{\mathcal{X}})} + (\bar{\mathcal{X}}_r - \bar{\mathcal{X}}) = -\frac{\mathcal{F}''(\bar{\mathcal{X}}_r)}{2\,\mathcal{F}'(\bar{\mathcal{X}})}(\bar{\mathcal{X}}_r - \bar{\mathcal{X}})^2 \tag{3.23}$$

Thus, the update equation for a one-dimensional Newton-Raphson method is

$$\bar{\mathcal{X}}_{\mathrm{i}} = \bar{\mathcal{X}}_{\mathrm{i}-1} - \frac{\mathcal{F}(\bar{\mathcal{X}}_{\mathrm{i}-1})}{\mathcal{F}'(\bar{\mathcal{X}}_{\mathrm{i}-1})} \tag{3.24}$$

Combining Equations (3.22) and (3.24) yields:

$$\begin{aligned} \bar{\mathcal{X}}_r - \bar{\mathcal{X}}_{\mathrm{i}} &= -\frac{\mathcal{F}''(\bar{\mathcal{X}}_r)}{2\,\mathcal{F}'(\bar{\mathcal{X}}_{\mathrm{i}-1})}(\bar{\mathcal{X}}_r - \bar{\mathcal{X}}_{\mathrm{i}})^2 \\ \varsigma_{\mathrm{i}} &= -\frac{\mathcal{F}''(\bar{\mathcal{X}}_r)}{2\,\mathcal{F}'(\bar{\mathcal{X}}_{\mathrm{i}})}\,(\varsigma_{\mathrm{i}-1})^2 \end{aligned} \tag{3.25}$$

where $\varsigma_{\mathrm{j}}$ is the error at iteration j. It is apparent from Equation (3.25) that the error decreases quadratically when $\bar{\mathcal{X}}$ is in the vicinity of $\bar{\mathcal{X}}_r$.

### 3.2.1 Single Shooting

A straightforward application of a Newton-Raphson procedure involves path planning and targeting. The simplest implementation for targeting is a single shooting scheme. Consider a particle in the BCR4BP as defined in the Earth-Moon rotating frame, with a state at $t_0$ equal to $\bar{x}_0 = \left[\, x_0 \;\; y_0 \;\; z_0 \;\; \dot{x}_0 \;\; \dot{y}_0 \;\; \dot{z}_0 \,\right]^T$. Additionally, the epoch associated with the initial state is $\theta_0$. After propagation for a given time, $T$, the final state $\bar{x}_f = \left[\, x_f \;\; y_f \;\; z_f \;\; \dot{x}_f \;\; \dot{y}_f \;\; \dot{z}_f \,\right]^T$ is achieved at epoch $\theta_f = \theta_0 + \omega T$. Assume a scenario where the target is a predetermined position, defined as $\bar{r}_t = \left[\, x_t \;\; y_t \;\; z_t \,\right]^T$ that is different from the position components for $\bar{x}_f$. Assume that, in this scenario, the initial position is fixed but the velocity components are to be modified in both magnitude and direction. This scenario corresponds to a spacecraft at an initial location in space that would instantaneously implement a $\Delta\bar{V}$ maneuver at $t_0$ to modify its final position at $t_0 + T$. Thus, the design variable vector is

$$\bar{\mathcal{X}} = \begin{bmatrix} \dot{x}_0 & \dot{y}_0 & \dot{z}_0 \end{bmatrix}^T \tag{3.26}$$

The constraints include position components, and the variations are all equal to zero when the final state matches the desired final position. Then, the constraint vector is

$$\bar{\mathcal{F}}(\bar{\mathcal{X}}) = \begin{bmatrix} x_f - x_t & y_f - y_t & z_f - z_t \end{bmatrix}^T \tag{3.27}$$

In this example, the time of flight is not a design variable. In the BCR4BP, note that the Sun angle at the final state, $\theta_f$, is linearly related to the epoch associated with the initial state, $\theta_0$, and the time-of-flight, $T$. The time-of-flight and/or the Sun angle associated with the initial state may be incorporated into the design variables vector to allow a shift in final epoch. The Jacobian matrix $\mathrm{D}\bar{\mathcal{F}}$ relating the change in the initial values of the position design variables to the desired change in final states is evaluated such that,

$$\begin{aligned} \mathrm{D}\bar{\mathcal{F}}(\bar{\mathcal{X}}) = \frac{\partial \bar{\mathcal{F}}(\bar{\mathcal{X}})}{\partial \bar{\mathcal{X}}} &= \begin{bmatrix} \frac{\partial(x_f - x_t)}{\partial \dot{x}_0} & \frac{\partial(x_f - x_t)}{\partial \dot{y}_0} & \frac{\partial(x_f - x_t)}{\partial \dot{x}_0} \\ \frac{\partial(y_f - y_t)}{\partial \dot{x}_0} & \frac{\partial(y_f - y_t)}{\partial \dot{y}_0} & \frac{\partial(y_f - y_t)}{\partial \dot{z}_0} \\ \frac{\partial(z_f - z_t)}{\partial \dot{x}_0} & \frac{\partial(z_f - z_t)}{\partial \dot{y}_0} & \frac{\partial(z_f - z_t)}{\partial \dot{z}_0} \end{bmatrix} \\ &= \begin{bmatrix} \frac{\partial x_f}{\partial \dot{x}_0} - \frac{\partial x_t}{\partial \dot{x}_0} & \frac{\partial x_f}{\partial \dot{y}_0} - \frac{\partial x_t}{\partial \dot{y}_0} & \frac{\partial x_f}{\partial \dot{z}_0} - \frac{\partial x_t}{\partial \dot{z}_0} \\ \frac{\partial y_f}{\partial \dot{x}_0} - \frac{\partial y_t}{\partial \dot{x}_0} & \frac{\partial y_f}{\partial \dot{y}_0} - \frac{\partial y_t}{\partial \dot{y}_0} & \frac{\partial y_f}{\partial \dot{z}_0} - \frac{\partial y_t}{\partial \dot{z}_0} \\ \frac{\partial z_f}{\partial \dot{x}_0} - \frac{\partial z_t}{\partial \dot{x}_0} & \frac{\partial z_f}{\partial \dot{y}_0} - \frac{\partial z_t}{\partial \dot{y}_0} & \frac{\partial z_f}{\partial \dot{z}_0} - \frac{\partial z_t}{\partial \dot{z}_0} \end{bmatrix} \end{aligned} \tag{3.28}$$

Since the target states $\bar{r}_t = \begin{bmatrix} x_t & y_t & z_t \end{bmatrix}^T$ are not an explicit function of the initial velocity $\bar{v}_0 = \begin{bmatrix} \dot{x}_0 & \dot{y}_0 & \dot{z}_0 \end{bmatrix}^T$, all the partial derivatives corresponding to the target state with respect to the initial velocity components are equal to zero. Thus, Equation (3.28) simplifies to

$$\mathrm{D}\bar{\mathcal{F}}(\bar{\mathcal{X}}) = \frac{\partial \bar{\mathcal{F}}(\bar{\mathcal{X}})}{\partial \bar{\mathcal{X}}} = \begin{bmatrix} \frac{\partial(x_f)}{\partial \dot{x}_0} & \frac{\partial(x_f)}{\partial \dot{y}_0} & \frac{\partial(x_f)}{\partial \dot{x}_0} \\ \frac{\partial(y_f)}{\partial \dot{x}_0} & \frac{\partial(y_f)}{\partial \dot{y}_0} & \frac{\partial(y_f)}{\partial \dot{z}_0} \\ \frac{\partial(z_f)}{\partial \dot{x}_0} & \frac{\partial(z_f)}{\partial \dot{y}_0} & \frac{\partial(z_f)}{\partial \dot{z}_0} \end{bmatrix} = \begin{bmatrix} \Phi_{41} & \Phi_{42} & \Phi_{43} \\ \Phi_{51} & \Phi_{52} & \Phi_{53} \\ \Phi_{61} & \Phi_{62} & \Phi_{63} \end{bmatrix} \tag{3.29}$$

where $\Phi_{ij}$ is the element on the i$^{th}$ row and the j$^{th}$ column of the state transition matrix $\boldsymbol{\Phi}(t_f, t_0)$, as defined in Equation (3.9). The Jacobian matrix $\mathrm{D}\bar{\mathcal{F}}(\bar{\mathcal{X}})$ is square, therefore, a unique solution to this targeting problem exists. The initial velocity is updated using

Equation (3.20) until the final state position matches the target position to the required tolerance, i.e., until Equation (3.16) is satisfied.

### 3.2.2 Multiple Shooting

The single shooting approach to targeting is powerful. However, for more complex path planning applications, e.g., an array of nonlinear constraints or, simply, a longer time interval, a more sophisticated targeting concept is warranted. For example, correcting trajectories in the vicinity of the primaries is generally challenging. Terms in the equations of motion, in the CR3BP, the BCR4BP, or the $N$-body ephemeris model, are inversely proportional to the distance from the primaries or celestial bodies. Whenever the spacecraft is close to a primary, these terms grow extremely large. Thus, the sensitivities in the region near the primaries are high; slight changes in the initial state result in large differences in the final, propagated state. A single shooting algorithm, based on the linear variational equations of motion, can struggle to converge in this regime. To mitigate these convergence issues, extending the single shooting strategy to a multiple shooting scheme is often successful. In a multiple shooting strategy, the trajectory is decomposed into segments, or *discretized*, as illustrated schematically in Figure 3.1(a). The initial state along the segment $k$ at time $t_k$, $\bar{x}_{k,\mathrm{i}}$, is propagated for a time $T_k$, and the final time at $t_k + T_k$ is defined as $\bar{x}_{k,f}$. A differential corrections scheme corrects the discontinuities in position, velocity and time between consecutive segments, as apparent in Figure 3.1(b).

As an illustration, a multiple shooting scheme enforcing continuity between consecutive arcs is derived for the BCR4BP, Earth-Moon frame formulation[2]. First, note that the design variable vector, $\bar{\mathfrak{X}}$, may be defined in many different ways. A patch point is a break point between two consecutive segments along the trajectory. In the schematic representation in Figure 3.1, the patch points are $\bar{x}_{1,\mathrm{i}}$, $\bar{x}_{2,\mathrm{i}}$, $\ldots$, $\bar{x}_{\beta-1,\mathrm{i}}$, $\bar{x}_{\beta,\mathrm{i}}$, where $\beta$ is the number of patch points. In this example, the design variable vector is defined as the collection of the states

[2]↑This scheme is extendable to the Sun-$B_1$ formulation of the BCR4BP, or to other dynamical models such as the CR3BP or the $N$-body ephemeris model.

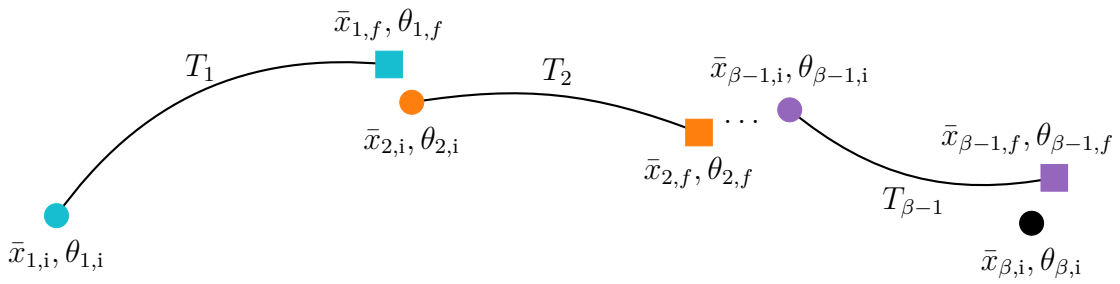


(a) Discretized segments before the correction

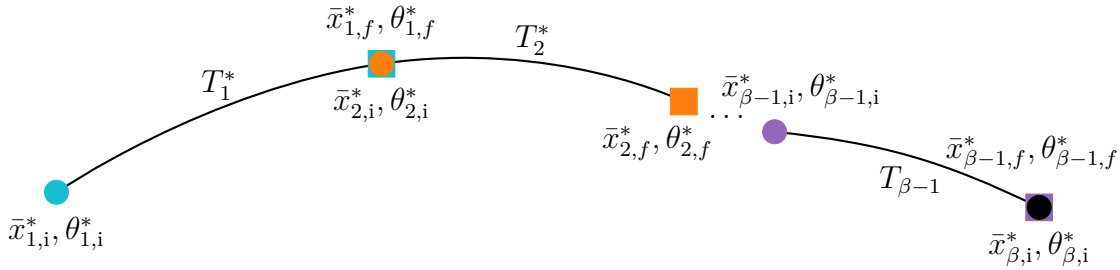


(b) Discretized segments after the correction

**Figure 3.1.** Definition of the segments in the multiple shooting algorithm

associated with the patch points, $\bar{\mathcal{X}}_{\mathrm{pv}}$, and the epoch associated with each consecutive patch points, $\bar{\mathcal{X}}_{\theta}$, as follows

$$\begin{aligned} \bar{\mathcal{X}} &= \begin{bmatrix} \bar{\mathcal{X}}_{\mathrm{pv}} & \bar{\mathcal{X}}_{\theta} \end{bmatrix}^T \\ &= \begin{bmatrix} \bar{x}_{1,\mathrm{i}} & \bar{x}_{2,\mathrm{i}} & \dots & \bar{x}_{\beta,\mathrm{i}} & \dots & \theta_{1,\mathrm{i}} & \theta_{2,\mathrm{i}} & \dots & \theta_{\beta,\mathrm{i}} \end{bmatrix}^T \end{aligned} \tag{3.30}$$

The minimum number of constraints to produce a continuous trajectory between $\bar{x}_{1,\mathrm{i}}$ and $\bar{x}_{\beta,\mathrm{i}}$ is $7\beta$. Each propagated arc endpoint, $\bar{x}_{k,f}$, must be continuous with the consecutive patch point state $\bar{x}_{k+1,\mathrm{i}}$ in the three position components and the three velocity components. Thus, the $6(\beta \times 1)$ position and velocity constraint vector is

$$\bar{\mathcal{F}}_{\mathrm{pv}}(\bar{\mathcal{X}}) = \begin{bmatrix} \bar{x}_{2,\mathrm{i}} - \bar{x}_{1,f} \\ \bar{x}_{3,\mathrm{i}} - \bar{x}_{2,f} \\ \vdots \\ \bar{x}_{\beta,\mathrm{i}} - \bar{x}_{\beta-1,f} \end{bmatrix} \tag{3.31}$$

In the BCR4BP, the continuity in epoch must also be maintained. Thus, for a continuous trajectory, the Sun angle at the end of a propagated arc is equal to the Sun angle associated with the next patch point. The $(\beta \times 1)$ epoch constraint vector is defined as

$$\bar{\mathcal{F}}_\theta(\bar{\mathcal{X}}) = \begin{bmatrix} \theta_{2,\mathrm{i}} - \theta_{1,f} \\ \theta_{3,\mathrm{i}} - \theta_{2,f} \\ \vdots \\ \theta_{\beta,\mathrm{i}} - \theta_{\beta-1,f} \end{bmatrix} \tag{3.32}$$

The complete constraint vector is then expressed as

$$\bar{\mathcal{F}}(\bar{\mathcal{X}}) = \begin{bmatrix} \bar{\mathcal{F}}_{\mathrm{pv}} \\ \bar{\mathcal{F}}_\theta \end{bmatrix} \tag{3.33}$$

In this application, both the design variable vector and the constraint vector possess $7\beta$ elements. Thus, the Jacobian matrix is a square $(7\beta \times 7\beta)$ matrix that is decomposed into the following submatrices

$$\mathrm{D}\bar{\mathcal{F}}(\bar{\mathcal{X}}) = \begin{bmatrix} \mathrm{D}\bar{\mathcal{F}}_{\mathrm{pv,pv}} & \mathrm{D}\bar{\mathcal{F}}_{\mathrm{pv},\theta} \\ \mathrm{D}\bar{\mathcal{F}}_{\theta,\mathrm{pv}} & \mathrm{D}\bar{\mathcal{F}}_{\theta,\theta} \end{bmatrix} \tag{3.34}$$

The first submatrix, $\mathrm{D}\bar{\mathcal{F}}_{\mathrm{pv,pv}}$ is defined by the partial derivatives of the position and velocity constraints with respect to the initial position and velocity variables

$$\mathrm{D}\bar{\mathcal{F}}_{\mathrm{pv,pv}} = \begin{bmatrix} \frac{\partial(\bar{x}_{2,\mathrm{i}} - \bar{x}_{1,f})}{\partial \bar{x}_{1,\mathrm{i}}} & \frac{\partial(\bar{x}_{2,\mathrm{i}} - \bar{x}_{1,f})}{\partial \bar{x}_{2,\mathrm{i}}} & \cdots & \frac{\partial(\bar{x}_{2,\mathrm{i}} - \bar{x}_{1,f})}{\partial \bar{x}_{\beta-1,\mathrm{i}}} \\ \frac{\partial(\bar{x}_{3,\mathrm{i}} - \bar{x}_{2,f})}{\partial \bar{x}_{1,\mathrm{i}}} & \frac{\partial(\bar{x}_{3,\mathrm{i}} - \bar{x}_{2,f})}{\partial \bar{x}_{2,\mathrm{i}}} & \cdots & \frac{\partial(\bar{x}_{3,\mathrm{i}} - \bar{x}_{2,f})}{\partial \bar{x}_{\beta-1,\mathrm{i}}} \\ \vdots & \vdots & \ddots & \vdots \\ \frac{\partial(\bar{x}_{\beta,\mathrm{i}} - \bar{x}_{\beta-1,f})}{\partial \bar{x}_{1,\mathrm{i}}} & \frac{\partial(\bar{x}_{\beta,\mathrm{i}} - \bar{x}_{\beta-1,f})}{\partial \bar{x}_{2,\mathrm{i}}} & \cdots & \frac{\partial(\bar{x}_{\beta,\mathrm{i}} - \bar{x}_{\beta-1,f})}{\partial \bar{x}_{\beta-1,\mathrm{i}}} \end{bmatrix} \tag{3.35}$$

Recognizing that the final state $\bar{x}_{k,f}$ is only a function of the initial state $\bar{x}_{k,\mathrm{i}}$ associated with the same patch point, and that $\frac{\partial \bar{x}_{k,\mathrm{i}}}{\partial \bar{x}_{k,\mathrm{i}}}$ is equal to the $(6\times 6)$ identity matrix $\mathbf{I}$, Equation (3.35) simplifies to the following form

$$\mathrm{D}\bar{\mathcal{F}}_{\mathrm{pv,pv}} = \begin{bmatrix} -\mathbf{\Phi}_1(\theta_2,\theta_1) & \mathbf{I} & \mathbf{0} & \mathbf{0} & \mathbf{0} \\ \mathbf{0} & -\mathbf{\Phi}_2(\theta_3,\theta_2) & \mathbf{I} & \mathbf{0} & \mathbf{0} \\ \vdots & \vdots & \ddots & \vdots & \vdots \\ \mathbf{0} & \mathbf{0} & \mathbf{0} & -\mathbf{\Phi}_{\beta-1}(\theta_\beta,\theta_{\beta-1}) & \mathbf{I} \end{bmatrix} \tag{3.36}$$

Note that the STM elements in Equation (3.36) are written as function of Sun angles rather than times as in Equation (3.9). The $\mathrm{D}\bar{\mathcal{F}}_{\theta,\theta}$ submatrix, which relates the epoch continuity constraints to the initial epoch design variables is defined as

$$\mathrm{D}\bar{\mathcal{F}}_{\theta,\theta} = \begin{bmatrix} \frac{\partial(\theta_{2,\mathrm{i}}-\theta_{1,f})}{\partial\theta_{1,\mathrm{i}}} & \frac{\partial(\theta_{2,\mathrm{i}}-\theta_{1,f})}{\partial\theta_{2,\mathrm{i}}} & \cdots & \frac{\partial(\theta_{2,\mathrm{i}}-\theta_{1,f})}{\partial\theta_{\beta,\mathrm{i}}} \\ \frac{\partial(\theta_{3,\mathrm{i}}-\theta_{2,f})}{\partial\theta_{1,\mathrm{i}}} & \frac{\partial(\theta_{3,\mathrm{i}}-\theta_{2,f})}{\partial\theta_{2,\mathrm{i}}} & \cdots & \frac{\partial(\theta_{3,\mathrm{i}}-\theta_{2,f})}{\partial\theta_{\beta,\mathrm{i}}} \\ \vdots & \vdots & \ddots & \vdots \\ \frac{\partial(\theta_{\beta,\mathrm{i}}-\theta_{\beta-1,f})}{\partial\theta_{1,\mathrm{i}}} & \frac{\partial(\theta_{\beta,\mathrm{i}}-\theta_{\beta-1,f})}{\partial\theta_{2,\mathrm{i}}} & \cdots & \frac{\partial(\theta_{\beta,\mathrm{i}}-\theta_{\beta-1,f})}{\partial\theta_{\beta,\mathrm{i}}} \end{bmatrix} \tag{3.37}$$

Since there is a linear relationship between Sun angle and time, the final epoch along a propagated arc is written as a function of the initial epoch and the propagation time $T_k$

$$\theta_{k,f} = \theta_{k,\mathrm{i}} + \omega T_k \tag{3.38}$$

where $k$ is the index of the patch point. Leveraging this relationship, Equation (3.37) becomes

$$\mathrm{D}\bar{\mathcal{F}}_{\theta,\theta} = \begin{bmatrix} -1 & 1 & 0 & \dots & 0 \\ 0 & -1 & 1 & \dots & 0 \\ \vdots & \vdots & \vdots & \ddots & \vdots \\ 0 & 0 & \dots & -1 & 1 \end{bmatrix} \tag{3.39}$$

The $\mathrm{D}\bar{\mathcal{F}}_{\mathrm{pv},\theta}$ submatrix includes the dependencies of the propagated position and velocity states with respect to the initial epoch design variables. The elements of this matrix are

estimated using a finite difference scheme [59], or by integrating additional terms for the state/epoch dependencies[3] along with the equations of motion. Finally, the $\mathrm{D}\bar{\mathcal{F}}_{\theta,\mathrm{pv}}$ submatrix is equal to a $(\beta \times 6\beta)$ matrix of zeros, since the epoch constraints do not depend on the position and velocity design variables. The design variable vector is iteratively updated using Newton's method and Equation (3.20), until the norm of the total constraint vector falls below a specified tolerance. The multiple shooting method is a powerful approach for targeting trajectories with long times-of-flight and/or close approaches to the primaries.

## 3.3 Continuation Schemes

Once a trajectory is constructed, a continuation scheme delivers a set, or *family*, of trajectories or arcs that reflect the solutions over the variation of some system parameter. Families of periodic orbits, quasi-periodic orbits, trajectories, or equilibrium solutions can all be constructed using a continuation scheme. Although many types of continuation approaches are available, two specific continuation schemes are employed in this analysis. Natural parameter continuation (NPC) steps along a physical parameter to produce new arcs or orbits. As an alternative, pseudo-arclength continuation (PALC), steps along a nonphysical parameter. Natural parameter continuation is very insightful to clarify the impact of a change in a physical parameter. Pseudo-arclength can evolve a family when physical insight is lacking.

### 3.3.1 Natural Parameter Continuation

Natural parameter continuation is a scheme where a variation in a physical parameter is employed to step along a family of solutions. This physical parameter is, for instance, a position, a velocity, a time-of-flight, an energy level or a mass parameter. First, a reference solution is converged using a single shooting or multiple shooting algorithm. Then, the variation in some physical parameter is introduced. This perturbed state does not satisfy the set of constraints or characteristics as defined for the reference solution. However, if the variation in a physical parameter is sufficiently small, a new solution is obtained by correcting the perturbed solution. This new converged solution satisfies the constraints/characteristics

[3]↑See Appendix D for a derivation of the state/epoch dependencies in the BCR4BP.

requirements and is, therefore, a viable option and a member of the family of solutions. The same process is repeated by perturbing the latest member of the family.

### 3.3.2 Pseudo-arclength continuation

Natural parameter continuation is simple to implement and is an efficient continuation scheme for many problems. However, limitations do exist. At fold points that occur during the continuation scheme, a Newton-Raphson process does not consistently converge [60]. Difficulties in convergence can also occur if the physical parameter or the step size is poorly selected, for example. To mitigate such convergence issues, prior knowledge of the family evolution is often required. Thus, a more robust continuation scheme under such conditions is required for certain applications.

The pseudo-arclength continuation (PALC) strategy employs steps along a nonphysical direction to construct a family. This scheme requires no prior knowledge of the family evolution and is more flexible for complex continuation paths. The illustration in Figure 3.2, adapted from Bosanac [61], schematically demonstrates the difference between the NPC and PALC algorithms. Figure 3.2(a) represents the natural parameter continuation process in $p - \bar{\mathcal{X}}$ space, with $p$ as the continuation parameter and $\bar{\mathcal{X}}$ in its role as the design variable vector (a scalar in this schematic). The blue line is $\bar{\mathcal{X}}^*$, the design variable vector for

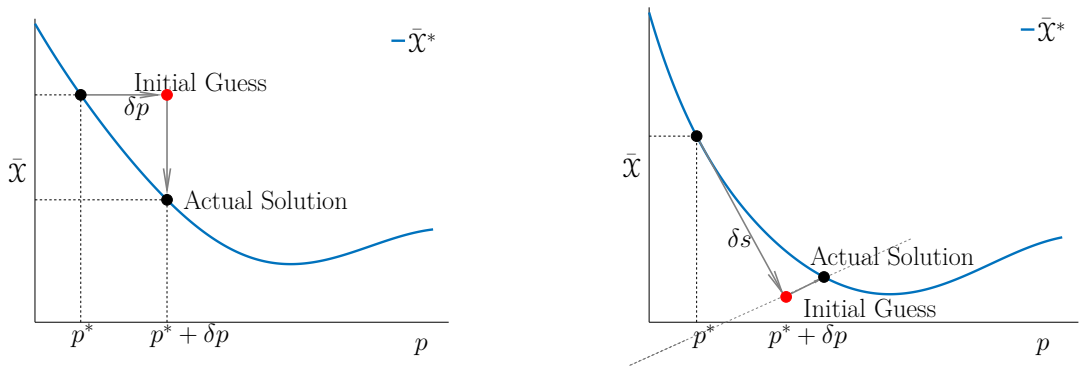


(a) NPC

(b) PALC, adapted from [61]

**Figure 3.2.** Comparison between (a) the natural parameter continuation and (b) the pseudo-arclength continuation in $p - \bar{\mathcal{X}}$ space

the members of the family over the range of the continuation parameter. From an initial, converged family member at $p^*$, a step of size $\delta p$ is introduced, resulting in an initial guess for the continuation $p^* + \delta p$, marked by a red dot. The quality of the initial guess is a function of the step size, $\delta p$, and the slope of $\bar{\mathcal{X}}^*$ at the previous family member.

In the pseudo-arclength continuation scheme, the continuation parameter is not a physical parameter associated with the system. Rather, the step $\delta s$ leverages the tangent slope at $p^*$, as apparent in Figure 3.2(b). Thus, for some applications, the quality of the step is generally better than the initial guess supplied by a step in a natural parameter. The tangential direction to $\bar{\mathcal{X}}$ at $p^*$ is the nullspace of the $\mathrm{D}\bar{\mathcal{F}}$ matrix. Since this family is evolving along one degree of freedom, $p$, the nullspace must be one-dimensional. Thus, the $\mathrm{D}\bar{\mathcal{F}}$ matrix must possess one more column than rows, i.e., if there are $n$ design variables, there must be $n-1$ constraints. A PALC algorithm typically proceeds using the following procedure:

1. Compute the first family member. Its design variable vector is $\bar{\mathcal{X}}_0^*$.

2. Compute the nullspace $\Delta\bar{\mathcal{X}}_0^*$ of the matrix $\mathrm{D}\bar{\mathcal{F}}$ evaluated at $\bar{\mathcal{X}}_0^*$.

3. The initial guess for the next member of the family, $\bar{\mathcal{X}}_k$, is constructed by stepping in the direction of $\Delta\bar{\mathcal{X}}_k^*$

$$\bar{\mathcal{X}}_k = \bar{\mathcal{X}}_{k-1}^* + s\ \Delta\bar{\mathcal{X}}_{k-1}^* \tag{3.40}$$

   where $s$ is a scaling term that determines the size of the step along the nullspace.

4. Differentially correct this initial guess:

   (a) To ensure that the update for the design variable vector projects onto the nullspace direction, an additional constraint is added. The augmented constraint vector is

$$\bar{\mathcal{G}}(\bar{\mathcal{X}}_k) = \begin{bmatrix} \bar{\mathcal{F}}(\bar{\mathcal{X}}_k) \\ \left(\bar{\mathcal{X}}_k - \bar{\mathcal{X}}_{k-1}^*\right)^T \Delta\bar{\mathcal{X}}_{k-1}^* - s \end{bmatrix} \tag{3.41}$$

   where $\bar{\mathcal{F}}(\bar{\mathcal{X}}_k)$ is the $n-1$ constraint vector that includes the constraints necessary for the design variable vector to be defined as a member of the family.

(b) The augmented Jacobian matrix $\mathrm{D}\bar{\mathcal{G}}(\bar{\mathcal{X}}_k)$ is evaluated at $\bar{\mathcal{X}}_k$. The partial derivative of the additional constraint with respect to $\bar{\mathcal{X}}_k$ simplifies to the nullspace vector, $\Delta\bar{\mathcal{X}}^*_{k-1}$, that is

$$\mathrm{D}\bar{\mathcal{G}}(\bar{\mathcal{X}}_k) = \begin{bmatrix} \mathrm{D}\bar{\mathcal{F}}(\bar{\mathcal{X}}_k) \\ \left(\Delta\bar{\mathcal{X}}^*_{k-1}\right)^T \end{bmatrix} \tag{3.42}$$

The Jacobian matrix, $\mathrm{D}\bar{\mathcal{F}}$, is an $(n-1\times n)$ matrix. With the additional row, $\Delta\bar{\mathcal{X}}^*_{k-1}$, with $n$ elements, the augmented Jacobian matrix $\mathrm{D}\bar{\mathcal{G}}(\bar{\mathcal{X}}_k)$ is a square $(n\times n)$ matrix. Thus, Equation (3.20) for square matrices is applied to update the design variable vector, using the augmented constraint vector and the augmented Jacobian matrix.

$$\delta\bar{X}_k = -\left(\mathrm{D}\bar{\mathcal{G}}(\bar{\mathcal{X}}_k)\right)^{-1}\bar{\mathcal{G}}(\bar{\mathcal{X}}_k) \tag{3.43}$$

(c) Iterations on Equation (3.43) are repeated until the constraints are satisfied, i.e., until $\|\bar{\mathcal{G}}(\bar{\mathcal{X}}_k)\| < \mathrm{e}$, where e is the specified tolerance.

5. The new member of the family is characterized by a design variables vector $\bar{\mathcal{X}}^*_k$. The nullspace $\Delta\bar{\mathcal{X}}^*_k$ of the (non-augmented) Jacobian matrix $\mathrm{D}\bar{\mathcal{F}}$ is evaluated at $\bar{\mathcal{X}}^*_k$. To compute the next family member, the process is restarted at step 3.

Pseudo-arclength continuation is a robust continuation process that steps in a nonphysical direction to move along a family of solutions. While comparatively more versatile than the natural parameter scheme, its implementation is not as straightforward as the NPC implementation, and the nonphysical step direction is not usually as insightful as a physical step. Thus, the pseudo-arclength continuation is a powerful alternative for problems where the natural parameter continuation process struggles.

## 3.4 Transition between Dynamical Models

Methods for transitioning solutions, including periodic orbits and trajectories, between the CR3BP and the BCR4BP are introduced. First, a scheme that transitions trajectories between the Earth-Moon CR3BP and the BCR4BP is implemented by artificially scaling the mass of the Sun. Second, a method for evolving a solution from the Sun-$B_1$ CR3BP to

the BCR4BP. For this method, a parameter is employed to scale the orbital radii associated wit the Earth and Moon when represented in the Sun-$B_1$ rotating frame. Both methods are successfully employed in this analysis to construct precisely periodic orbits in the Earth-Moon-Sun BCR4BP.

### 3.4.1 Earth-Moon CR3BP to/from BCR4BP

To construct a BCR4BP trajectory from a CR3BP solution, the most successful strategy employs a natural parameter continuation process. One effective continuation parameter is a coefficient that scales the mass of the Sun [20]. This coefficient is varied between zero, corresponding to the Earth-Moon CR3BP, and unity, reflecting the Earth-Moon-Sun BCR4BP. To transition between the models, the pseudo-potential $\Upsilon^*$ from Equation (2.5) is rewritten as

$$\Upsilon^*(\epsilon, \theta) = U^* + \epsilon\, \mu_\mathrm{s} \left( \frac{1}{r_{\text{s-sc}}(\theta)} - \frac{1}{{a_\mathrm{s}}^3} \left( x_\mathrm{s}(\theta) x + y_\mathrm{s}(\theta) y + z_\mathrm{s}(\theta) z \right) \right) \tag{3.44}$$

such that $\epsilon$ is the coefficient that scales the mass of the Sun, i.e., $\mu_\mathrm{s}$. Note that for $\epsilon = 0$, the updated pseudo-potential $\Upsilon^*$ is equivalent to the CR3BP pseudo-potential, introduced in Equation (2.2). Conversely, for $\epsilon = 1$, Equation (3.44) is equivalent to the BCR4BP pseudo-potential, in Equation (2.5).

This transition method is employed to transition periodic orbits from the CR3BP to the BCR4BP. Transition of the periodic orbit between the models is achieved using one step in $\epsilon$, i.e., one jump from zero to one, or by decomposing the continuation procedure into multiple steps. The results from an example of the latter strategy appear in Figure 3.3. In this example, the initial orbit is the 3:1 synodic resonant NRHO in the CR3BP, and it appears in light blue in Figure 3.3. Its orbital period is exactly one third of the synodic period. Therefore, the orbital period of the BCR4BP periodic solution is a single synodic period. To transition a trajectory from the CR3BP to a higher-fidelity model involves a straightforward targeting scheme. Three revolutions of the 3:1 synodic resonant NRHO in the CR3BP are stacked to form the initial guess. (Note that more sophisticated targeting strategies that accommodate constraints and alternative goals are also available. But the simplified

approach is sufficient in this example). The solution is then discretized into patch points to facilitate the convergence process. While a single-shooting algorithm is an acceptable alternative, the BCR4BP periodic orbits typically possess longer periods and more 'loops' than their CR3BP counterparts. Thus, a parallel-shooting scheme [56] is typically more robust for this type of scenario. At each step, represented by the evolving value of the mass parameter, $\epsilon$, the solution is propagated and corrected for continuity between consecutive patch points as well as for periodicity. Once a solution for a given $\epsilon$ value is computed, it is employed as the initial guess for the next step in the continuation procedure. For the example in Figure 3.3(a), 25 equally-spaced steps between $\epsilon = 0$ and $\epsilon = 1$ are introduced, and the converged, periodic solution for each step is plotted. The solution corresponding to $\epsilon = 1$, colored in purple in Figure 3.3(b), reflects the Earth-Moon-Sun BCR4BP periodic solution. In this investigation, each BCR4BP periodic orbit is constructed using this method, in which a synodic resonant CR3BP orbit serves as the initial guess for a continuation process with the Sun's mass as the continuation parameter. A modified pseudo-potential function and a natural parameter continuation in nondimensional Sun mass are employed to transition a trajectory from the CR3BP to the BCR4BP.

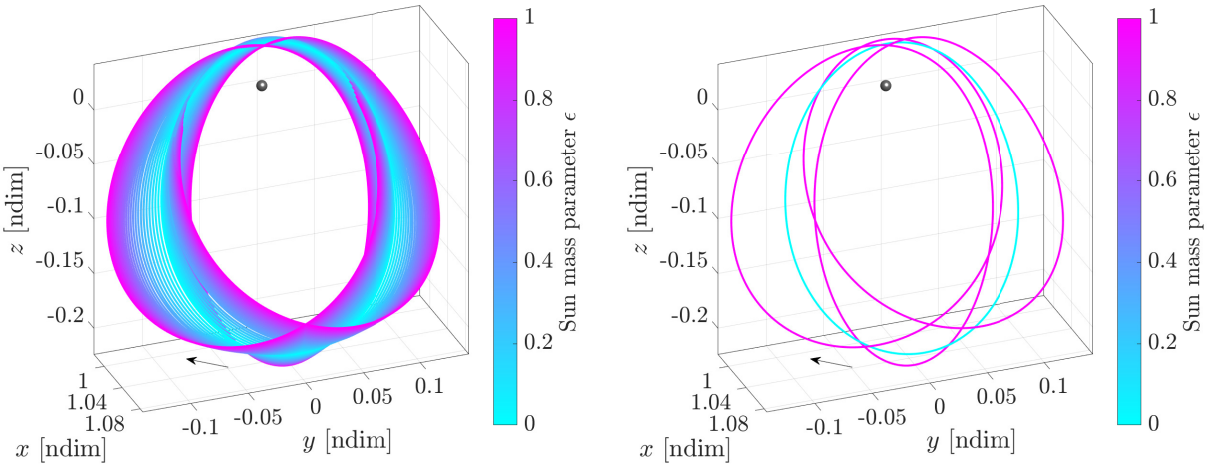


**Figure 3.3.** Continuation orbits between the CR3BP 3:1 resonant NRHO and its BCR4BP periodic counterpart (a). The initial orbit in the CR3BP, in blue, and the final orbit in the BCR4BP, in pink (b).

### 3.4.2 Sun-$B_1$ CR3BP to/from BCR4BP

A continuation process between the Sun-$B_1$ CR3BP and the BCR4BP as formulated in the Sun-$B_1$ rotating frame is introduced. Recall that the Sun-$B_1$ CR3BP is also the representation of a CR3BP where the second body is a fictitious body located at the Earth-Moon barycenter and with mass equal to the sum of the masses of the Earth and the Moon [62]. To transition between the Sun-$B_1$ CR3BP and the BCR4BP as formulated in the Sun-$B_1$ rotating frame, the relative positions of the Earth and the Moon with respect to their common barycenter $B_1$ is varied in the equations of motion in Equations (2.8) and (2.9). The continuation parameter, $\gamma$, is introduced and Equation (2.10) is rewritten as,

$$\begin{aligned}
\bar{\underline{r}}_{\mathrm{e}}(\gamma, \underline{\theta}) &= \bar{\underline{r}}_{B_1} + \gamma\, \bar{\underline{r}}_{B_1\mathrm{e}}(\underline{\theta}) = \begin{bmatrix} 1 - \frac{1}{\mu_{\mathrm{s}}+1} \\ 1 - \frac{1}{\mu_{\mathrm{s}}+1} \\ 0 \end{bmatrix} + \gamma \begin{bmatrix} -\frac{\mu}{a_{\mathrm{s}}} \cos(\underline{\theta}) \\ -\frac{\mu}{a_{\mathrm{s}}} \sin(\underline{\theta}) \\ 0 \end{bmatrix} \\
\bar{\underline{r}}_{m}(\gamma, \underline{\theta}) &= \bar{\underline{r}}_{B_1} + \gamma\, \bar{\underline{r}}_{B_1\mathrm{m}}(\underline{\theta}) = \begin{bmatrix} 1 - \frac{1}{\mu_{\mathrm{s}}+1} \\ 1 - \frac{1}{\mu_{\mathrm{s}}+1} \\ 0 \end{bmatrix} + \gamma \begin{bmatrix} \frac{1-\mu}{a_{\mathrm{s}}} \cos(\underline{\theta}) \\ \frac{1-\mu}{a_{\mathrm{s}}} \sin(\underline{\theta}) \\ 0 \end{bmatrix}
\end{aligned} \tag{3.45}$$

When $\gamma$ is equal to zero, $\bar{\underline{r}}_{\mathrm{e}}(0, \underline{\theta}) = \bar{\underline{r}}_{m}(\underline{\theta}) = \bar{\underline{r}}_{B_1}(\underline{\theta})$, i.e., the Earth and the Moon are located at $B_1$, creating a fictitious body of mass equal to the sum of the masses of the Earth and the Moon. This case corresponds to the Sun-$B_1$ CR3BP. When $\gamma$ is equal to one, Equation (2.10) and Equation (3.45) are identical, and the BCR4BP, as expressed in the Sun-$B_1$ rotating frame, emerges. For instance, consider the transition of the 2:17 $\underline{\mathrm{L}}_2$ synodic resonant Lyapunov orbit from the CR3BP to the BCR4BP in Figure 3.4. The minimal period of the 2:17 resonant Lyapunov orbit in the CR3BP is $^{17}/_{2}$, or 8.5 synodic periods. However, the period associated with periodic solutions in the BCR4BP must be equal to an integer multiple of the synodic period[20]. Thus, two revolutions of the CR3BP orbit are stacked to form the initial guess for the BCR4BP periodic orbit. The transition process to an orbit in the BCR4BP includes a targeting scheme[44]. The trajectory is discretized into patch points, and a parallel-shooting scheme[56] is employed to mitigate the potential

convergence issues arising from the long period of the orbit. At each step, represented by the evolving value of the continuation parameter, $\gamma$, the solution is propagated and corrected for continuity between consecutive patch points as well as for periodicity. Once a solution for a given $\gamma$ value is computed, it is employed as the initial guess for the next step in the continuation procedure. For the example in Figure 3.4(a), 50 equally-spaced steps between

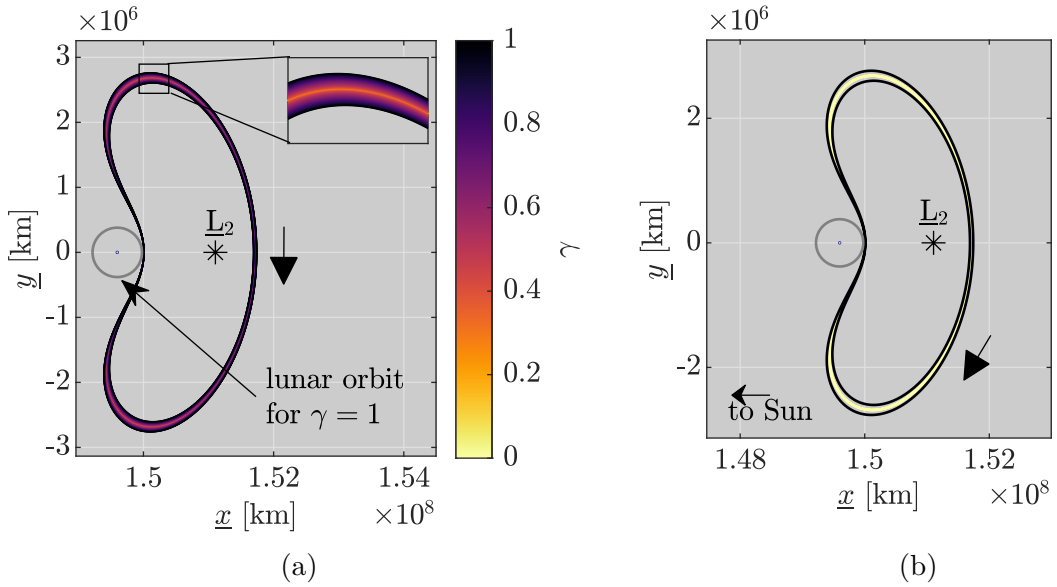


**Figure 3.4.** Continuation orbits between the Sun-$B_1$ CR3BP 2:17 Lyapunov and its BCR4BP periodic counterpart (a). The initial orbit in the CR3BP, in yellow, and the final orbit in the BCR4BP, in black (b).

$\gamma = 0$ and $\gamma = 1$ are introduced, and the converged, periodic solution for each step is plotted. The solution corresponding to $\gamma = 1$, colored in black in Figure 3.4(b), reflects the Earth-Moon-Sun BCR4BP periodic solution. In this investigation, each BCR4BP periodic orbit is constructed using this method, in which a synodic resonant Sun-$B_1$ CR3BP orbit serves as the initial guess for a continuation process with the relative distance of the Earth and the Moon as the continuation parameter.

## 3.5 Numerical Integration and Trajectory Design Tools

Numerical integration is employed to evaluate the nonlinear equations of motion and differential equations governing the STM for the CR3BP (Equation (2.1)), the BCR4BP

(Equations (2.4) and (2.8)), or the $N$-body ephemeris model (Equation (2.16)). Throughout this investigation, trajectories are propagated using the Boost C++ library [63], version 1.68.0. Specifically, the numerical integration scheme (or 'stepper' in Boost) that is employed is a Runge-Kutta Fehlberg 78. The details of this method are available from the Boost documentation [64]:

> "The Runge-Kutta Fehlberg 78 method is a standard method for high-precision applications. The method is explicit and fulfills the Error Stepper concept. Step size control is provided but continuous output is not available for this method."

To minimize numerical error along the integration, the absolute and relative tolerances are both set to $10^{-12}$. This value is equivalent in the Earth-Moon system to a tolerance of approximately $4 \cdot 10^{-4}$ meters in position and $1 \cdot 10^{-9}$ m/s in velocity.

The remainder of the analysis (aside from the integration) is performed in MATLAB [65]. The numerical integration from C++ is included, or 'mexxed' in MATLAB using MEX file functions [66]. From the MATLAB documentation [66]:

> "A MEX file is a function, created in MATLAB, that calls a C/C++ program or a Fortran subroutine. A MEX function behaves just like a MATLAB script or function."

A MEX file allows the user to combine the benefits of both the C++ language and MATLAB. For this investigation, C++ is employed for the propagation as it typically runs faster than the MATLAB integration implementation. For instance, consider Figure 3.5. The integration times between the Runge-Kutta Fehlberg 78 method in C++ and a similar method in MATLAB, i.e., `ode78`, are compared for 600 periodic orbits in the Earth-Moon CR3BP .The absolute and relative tolerances are set to $10^{-12}$ in both languages. The numerical integration in C++ using the Boost library takes on average 0.0004 seconds, while 0.04 seconds are required on average to numerically integrate in MATLAB. Thus, the numerical integration in C++ is approximately 100 times faster than the integration in MATLAB for this illustration. While the performance improvement varies from application to application, the integration in C++ is generally at least an order of magnitude faster than the integration in MATLAB.

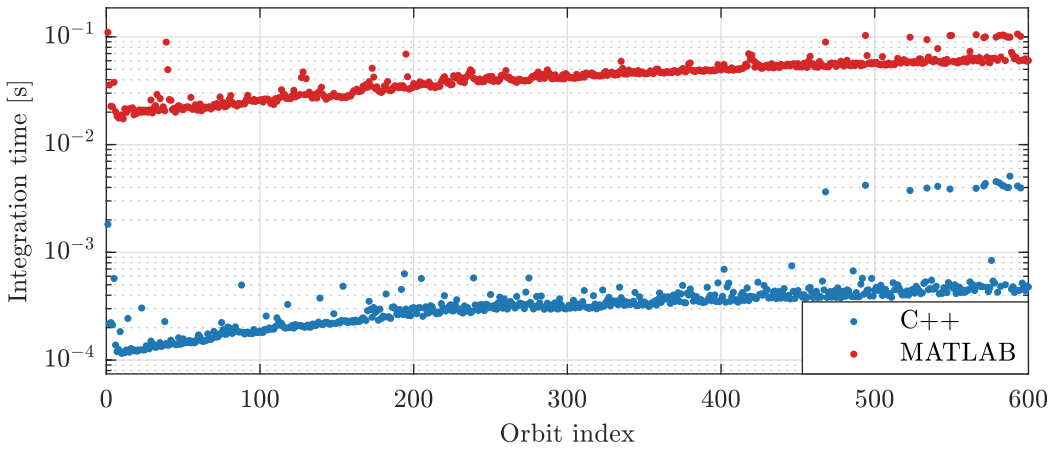


**Figure 3.5.** Comparison between the MATLAB and C++ integration of 600 members of $L_1$ Lyapunov family of periodic orbits in Earth-Moon CR3BP.

Two trajectory design software packages are employed to verify the results and the trajectories constructed in this investigation. An open-source software system, GMAT [67], for space mission design, optimization, and navigation, is employed to verify the numerical propagation of trajectories in the $N$-body ephemeris model. Additionally, the differential corrections schemes employed in the $N$-body ephemeris model are compared to the corrections schemes available in the Adaptive Trajectory Design (ATD) software. Adaptive Trajectory Design (ATD) is a multi-body trajectory design tool [68] developed at Purdue University and NASA Goddard Space Flight Center. In this investigation, the `atd-core` Java library from ATD v2 [69] is employed to verify the propagation and corrections in the $N$-body ephemeris model. The results of this investigation are generated using integration and analysis scripts written by the author; the results are then verified using the two off-the-shelf trajectory design software packages.

# 4. DYNAMICAL STRUCTURES IN THE BCR4BP

Various dynamical structures that exist within the context of the BCR4BP are defined. Instantaneous equilibrium solutions exist in the BCR4BP, as non-autonomous counterparts of the time-invariant Lagrange points in the CR3BP. Instantaneous, or pulsating, zero velocity surfaces (ZVSs) appear in the BCR4BP to add perspective for the dynamical behavior. The ZVSs enclose forbidden regions that limit the motion of an object in space and are defined as a function of the energy along a trajectory. Two energy-like quantities are defined within the BCR4BP: the Earth-Moon energy-like value and the Sun-$B_1$ energy-like value. Energy-like plots offer a binary check to record possible transit into and out of cislunar space at a certain epoch along a path. Precisely periodic orbits that possess orbital periods in resonance with the Earth-Moon-Sun period, i.e., the synodic period, are accessible in both the Earth-Moon and the Sun-$B_1$ rotating frames. Bounded motion is also available and constructed for transitioning orbits that do not possess a resonance with the synodic period. Lastly, invariant manifolds provide a useful approximation to the nonlinear dynamical behavior in the vicinity of a reference solution. Strategies to compute global invariant manifolds associated with periodic orbits and bounded motion are introduced.

## 4.1 Instantaneous Equilibrium Points

Due to the time-dependent nature of the model, the equations of motion for the BCR4BP, in Equations (2.4) and (2.8) do not admit invariant equilibrium solutions. However, instantaneous equilibrium solutions may exist for a given epoch, that is, for a given Sun angle in the Earth-Moon rotating frame or a given Moon angle in the Sun-$B_1$ rotating frame. These instantaneous equilibrium points are related to the concept of *Artificial Equilibrium Points* (AEPs). Under the presence of a perturbing force, AEPs extend the discrete Lagrange points to a continuum of points that form level surfaces parametrized by the perturbing force. The AEPs are straightforwardly employed within the context of solar sail [70] as well as low-thrust [69], [71] trajectory design. The instantaneous equilibrium points in this analysis exist due to the addition of the gravitational action of the Sun, rather than the acceleration due to thrust or solar radiation pressure.

The relationship between the epoch-dependent instantaneous, equilibrium points in the BCR4BP and the autonomous libration point solutions from the CR3BP is explored. The locations of the five Earth-Moon CR3BP Lagrange points, labeled $L_1$ through $L_5$, and the five Sun-$B_1$ CR3BP equilibrium points, labeled $\underline{L}_1$ through $\underline{L}_5$, appear in Figure 4.1. The instantaneous equilibrium points of the BCR4BP, as formulated in the Earth-Moon rotating frame, correspond to the $L_i$ points perturbed by the gravitational influence of the Sun. Conversely, the instantaneous equilibrium solutions of the BCR4BP, as formulated in the Sun-$B_1$ rotating frame, correspond to the Lagrange points of the Sun-$B_1$ CR3BP, i.e., $\underline{L}_i$, under the perturbations due to the individual motions of the Earth and the Moon along their orbits.

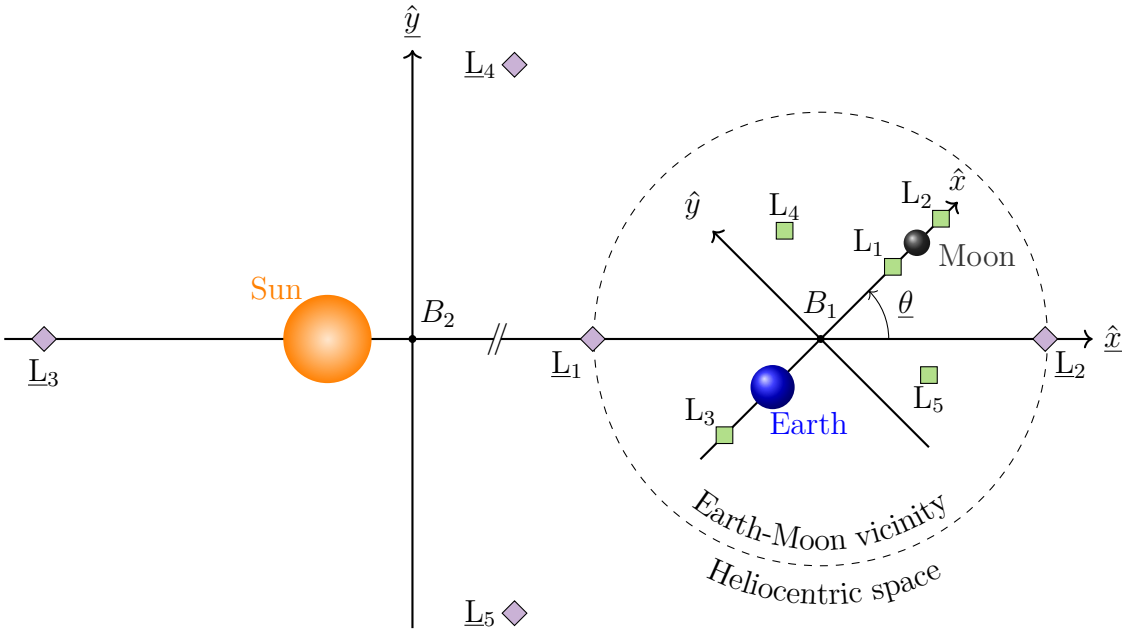


**Figure 4.1.** Locations of the equilibrium points of the Sun-$B_1$ CR3BP (purple diamonds) and the Earth-Moon CR3BP (green diamonds), not to scale

### 4.1.1 Derivation

The derivation of the algorithms employed to compute the instantaneous equilibrium points is detailed. For conciseness, only the derivation for the instantaneous equilibrium points in the Earth-Moon frame formulation of the BCR4BP is offered here. The derivation

for the equilibrium points in the Sun-$B_1$ frame formulation of the BCR4BP is produced by substituting the appropriate variables and functions. By definition, the velocity and acceleration associated with an equilibrium point are equal to zero. Setting the velocity and acceleration in the equations of motion in Equation (2.4) yields, for a given Sun angle $\theta$,

$$\frac{\partial \Upsilon^*}{\partial x} = 0, \qquad \frac{\partial \Upsilon^*}{\partial y} = 0, \qquad \frac{\partial \Upsilon^*}{\partial z} = 0 \tag{4.1}$$

that is rewritten as the vector expression

$$\bar{\nabla}_{\bar{r}} \Upsilon^*(\bar{r}, \theta) = \bar{0} \tag{4.2}$$

where $\bar{\nabla}_{\bar{r}}$ denotes the gradient with respect to the vector $\bar{r} = [\, x \;\; y \;\; z \,]^T$. The point or collection of points that satisfy Equation (4.2) are denoted the instantaneous equilibrium points in the BCR4BP. For clarity, the notation introduced by Cox [69], [71] is adapted to label these points. From this point forward, $\mathrm{E}_{\mathrm{i}}^{\mathrm{j}}(\theta)$ denotes the BCR4BP instantaneous equilibrium point, where

- The subscript i refers to the corresponding Lagrange point $\mathrm{L}_{\mathrm{i}}$.
- The argument $\theta$ is the epoch corresponding to this instantaneous equilibrium point.
- The superscript j is introduced when multiple equilibrium solutions exist at certain epochs. When multiple solutions exist, they are numbered from lowest energy (highest $H$) to highest energy (lowest $H$).

For instance, $\mathrm{E}_1(45°)$ reflects the instantaneous equilibrium point in the BCR4BP for a Sun angle of 45°corresponding to the first Lagrange point in the Earth-Moon CR3BP. The notation $\mathbb{E}_{\mathrm{i}}$ denotes the Zero Acceleration Contour (ZAC) [69], that is, the collection of equilibrium points over a synodic month.

A differential corrections scheme is implemented to solve for the position of the instantaneous equilibrium point for a given epoch. The design variables are the position components of the equilibrium point

$$\bar{\mathfrak{X}} = \begin{bmatrix} x & y & z \end{bmatrix}^T \tag{4.3}$$

and the constraints vector variable as given by Equation (4.2), i.e.,

$$\bar{\mathcal{F}}\left(\bar{r},\theta\right) = \bar{\nabla}_{\bar{r}}\Upsilon^{*}(\bar{r},\theta) \tag{4.4}$$

Then, the Jacobian matrix $\mathrm{D}\bar{\mathcal{F}}$ is expressed as

$$D\bar{\mathcal{F}}\left(\bar{\mathcal{X}},\theta\right) = \frac{\partial\bar{\mathcal{F}}}{\partial\bar{\mathcal{X}}} = \begin{bmatrix} \frac{\partial^2\Upsilon^*}{\partial^2 x} & \frac{\partial^2\Upsilon^*}{\partial x\partial y} & \frac{\partial^2\Upsilon^*}{\partial x\partial z} \\ \frac{\partial^2\Upsilon^*}{\partial y\partial x} & \frac{\partial^2\Upsilon^*}{\partial^2 y} & \frac{\partial^2\Upsilon^*}{\partial y\partial z} \\ \frac{\partial^2\Upsilon^*}{\partial z\partial x} & \frac{\partial^2\Upsilon^*}{\partial z\partial y} & \frac{\partial^2\Upsilon^*}{\partial^2 z} \end{bmatrix} \tag{4.5}$$

Since the matrix is square, i.e., there are three design variables and three independent constraints, a unique solution is numerically produced iteratively using the update expression from Equation (3.20). The initial guess is selected as the position of the closest Lagrange point in the Earth-Moon CR3BP. For instance, to compute $\mathrm{E}_2(\theta)$, the design variable vector is initially set to $\bar{\mathcal{X}} = \begin{bmatrix} x_{\mathrm{L}_1} & 0 & 0 \end{bmatrix}^T$. A straightforward differential corrections scheme is then employed to solve for the position of the instantaneous equilibrium points in the BCR4BP.

Once the first instantaneous equilibrium point is computed, a natural parameter continuation scheme is employed to construct the BCR4BP ZAC corresponding to each of the Lagrange points of the Earth-Moon CR3BP. The parameter selected for the continuation parameter is the Sun angle $\theta$. The design variable for the first converged equilibrium point is $\bar{\mathcal{X}}_1^*$; the associated equilibrium point corresponds to the epoch $\theta_1$. The epoch associated with the second point on the ZAC is $\theta_2 = \theta_2 + \Delta\theta$, where $\Delta\theta$ is the natural parameter step. The constraints are generally not satisfied for the combination $(\bar{\mathcal{X}}_1^*, \theta_2)$. Thus, the differential corrections scheme described in Equations (4.3)–(4.5) is repeated, for the epoch $\theta_2$ and with $\bar{\mathcal{X}}_1^*$ as the initial guess, until $\bar{\mathcal{X}}_2^*$ is obtained. The process is repeated until the complete ZAC is obtained, that is, until equilibrium points are obtained for each epoch between 0 and $2\boldsymbol{\pi}$. A natural parameter continuation scheme stepping in Sun angle is an option to construct the BCR4BP ZACs corresponding to each of the Lagrange points of the Earth-Moon CR3BP.

Pseudo-arclength continuation is a second option to construct the BCR4BP ZACs. While the natural parameter continuation scheme delivers the majority of the instantaneous equilibrium points, it fails to produce the complete $\mathbb{E}_3$ ZAC for the Earth-Moon frame formulation

of the BCR4BP. Fold points exist along the $\mathbb{E}_3$ continuation evolution,, that impede the convergence along the natural parameter continuation scheme. Thus, an alternative strategy to compute the ZAC in the BCR4BP is introduced. The design variables vector from Equation (4.3) is augmented with the Sun angle:

$$\bar{\mathcal{X}}' = \begin{bmatrix} x & y & z & \theta \end{bmatrix}^T \tag{4.6}$$

Thus, in this formulation of the continuation scheme, the Sun angle is a free variable rather than a continuation parameter. The constraints vector is the same as the one defined in Equation (4.4), that is, $\bar{\mathcal{F}}(\bar{r}, \theta) = \bar{\nabla}_{\bar{r}} \Upsilon^*(\bar{r}, \theta)$. Then, the Jacobian matrix of the constraint vector is,

$$D\bar{\mathcal{F}}\left(\bar{\mathcal{X}}'\right) = \frac{\partial \bar{\mathcal{F}}}{\partial \bar{\mathcal{X}}'} = \begin{bmatrix} \frac{\partial^2 \Upsilon^*}{\partial^2 x} & \frac{\partial^2 \Upsilon^*}{\partial x \partial y} & \frac{\partial^2 \Upsilon^*}{\partial x \partial z} & \frac{\partial^2 \Upsilon^*}{\partial x \partial \theta} \\ \frac{\partial^2 \Upsilon^*}{\partial y \partial x} & \frac{\partial^2 \Upsilon^*}{\partial^2 y} & \frac{\partial^2 \Upsilon^*}{\partial z \partial z} & \frac{\partial^2 \Upsilon^*}{\partial y \partial \theta} \\ \frac{\partial^2 \Upsilon^*}{\partial z \partial x} & \frac{\partial^2 \Upsilon^*}{\partial z \partial y} & \frac{\partial^2 \Upsilon^*}{\partial^2 z} & \frac{\partial^2 \Upsilon^*}{\partial z \partial \theta} \end{bmatrix} \tag{4.7}$$

Note that the matrix is no longer square: there are more design variables than constraints. The first point along the ZAC is computed using Equations (4.4), (4.6) and (4.7) along with the minimum norm update from Equation (3.21). Similar to the natural parameter continuation scheme, the pseudo-arclength continuation process is initialized with the position of the closest CR3BP Lagrange point and a specified epoch. Let $\bar{\mathcal{X}}_0'^*$ be the first converged point along the ZAC. In the pseudo-arclength continuation method, the initial guess for the second point along the ZAC is represented as

$$\bar{\mathcal{X}}_1' = \bar{\mathcal{X}}_0'^* + s\Delta\bar{\mathcal{X}}_0'^* \tag{4.8}$$

where $\Delta\bar{\mathcal{X}}_0'^*$ is the null space of the D$\bar{\mathcal{F}}$ matrix evaluated at $\bar{\mathcal{X}}_0'^*$. Additionally, $s$ is the nondimensional parameter defining the arclength of the step along the null space direction. As defined in Equation (3.41), an additional scalar constraint ensures that the solution is

perpendicular to the projection of the null space direction. Thus, the constraint vector is augmented as follows

$$\bar{\mathcal{G}}(\bar{\mathcal{X}}'_1) = \begin{bmatrix} \bar{\mathcal{F}}(\bar{\mathcal{X}}'_1) \\ \left(\bar{\mathcal{X}}'_1 - \bar{\mathcal{X}}'^{*}_0\right)^T \Delta\bar{\mathcal{X}}'^{*}_0 - s \end{bmatrix} \tag{4.9}$$

and the Jacobian of the augmented constraint vector is then

$$\mathrm{D}\bar{\mathcal{G}}(\bar{\mathcal{X}}'_1) = \begin{bmatrix} \mathrm{D}\bar{\mathcal{F}}(\bar{\mathcal{X}}'_1) \\ \left(\Delta\bar{\mathcal{X}}'^{*}_0\right)^T \end{bmatrix} \tag{4.10}$$

The augmented problem $(\bar{\mathcal{X}}'_1, \bar{\mathcal{G}}(\bar{\mathcal{X}}'_1))$ yields a square matrix. The update is, thus, computed using Equation (3.20) along with Equations (4.9) and (4.10). After a second solution that satisfies the constraints is obtained, i.e., $\bar{\mathcal{X}}'^{*}_1$, the initial guess for the third result is generated using the null space of the $\mathrm{D}\bar{\mathcal{F}}$ matrix evaluated at $\bar{\mathcal{X}}'^{*}_1$. The process is repeated until the complete ZAC is constructed, that is, until a set of instantaneous equilibrium points is produced between epochs 0 and $2\boldsymbol{\pi}$. A note on the direction of the computed null space is relevant here. The vectors $\Delta\bar{\mathcal{X}}'^{*}_k$ and $-\Delta\bar{\mathcal{X}}'^{*}_k$ are both kernels associated with the $\mathrm{D}\bar{\mathcal{F}}$ matrix at the converged solution $\bar{\mathcal{X}}^{*}_k$. Therefore, an additional step is generally required to ensure that consecutive steps along the continuation process are in the same direction, preventing the continuation scheme to simply oscillate back and forth between two solutions. For a sufficiently small step size $s$, the dot product between two consecutive null space vectors is positive. Thus, Equation (4.8) is generalized for the steps $k > 1$

$$\bar{\mathcal{X}}'_{k+1} = \bar{\mathcal{X}}'^{*}_k + s\,\mathrm{sgn}\left(\Delta\bar{\mathcal{X}}'^{*}_k \cdot \Delta\bar{\mathcal{X}}'^{*}_{k-1}\right)\Delta\bar{\mathcal{X}}'^{*}_k \tag{4.11}$$

where sgn is the sign function. The pseudo-arclength continuation scheme, as detailed in Equations (4.6)–(4.11), successfully delivers all of the instantaneous equilibrium points in the BCR4BP, including the complete $\mathbb{E}_3$ ZAC for the Earth-Moon frame formulation.

### 4.1.2 Stability

The linear stability of a solution is evaluated consistent with the Lyapunov definition. The Lyapunov stability, in the linear sense, of a solution leverages the roots of the characteristic equation, or eigenvalues, of the **A** matrix. Recall, from Equation (3.5), that the **A** matrix is the Jacobian matrix of the equations of the motion of the system. For a constant equilibrium solution, the **A** matrix is constant. The stability properties, in the *linear* sense, for the equilibrium points are defined as follows

- If the eigenvalues of **A** are real, the equilibrium solution is stable if all the roots are negative. If any root is positive, the equilibrium point is unstable. Note that this is valid even if certain roots are repeated.

- If the eigenvalues of **A** are purely imaginary, the equilibrium point is stable and oscillatory motion in its vicinity exists. However, if any of the eigenvalues is repeated, the linearized motion in the vicinity of the equilibrium point has periodic and secular terms, and the equilibrium solution is unstable.

- If the eigenvalues are complex, the stability is a function of the sign of the real part of the root.

  - If all the eigenvalues possess negative real parts, the equilibrium solution is stable.
  - If one or more eigenvalues has a positive real part, the equilibrium solution is determined to be unstable.

  Note that for the complex eigenvalues, these statements are still valid if any of the roots is repeated.

These properties are employed to determine the stability (in the linear sense) of the instantaneous equilibrium points of the BCR4BP.

The eigenvalue equation associated with the **A** matrix possesses real coefficients; the eigenvalues thus occur in complex conjugate pairs [72]. In the CR3BP and the BCR4BP, the three pairs of eigenvalues determine the three linear *modes*. The modes are characterized as follows:

- If a pair of eigenvalues is real, i.e., $\mathrm{Im}\,\lambda_i = 0$, the associated mode is a saddle mode. In the linearized model, perturbations along the unstable and the stable directions grow exponentially in positive and negative time, respectively.

- If a pair of eigenvalues is purely imaginary, i.e., oscillatory motion exists in the vicinity of the equilibrium point, the associated mode is a center mode.

- If a pair of eigenvalues is complex and $\mathrm{Re}\,\lambda_i \neq 0$, $\mathrm{Im}\,\lambda_i \neq 0$, a mixed mode is associated with the equilibrium point. This mode involves both the oscillatory and the exponentially growing motions in the vicinity of the equilibrium point, in the linearized model.

Following Cox's naming convention [69], each equilibrium point is described by a string $S^{n_s} \times C^{n_c} \times M^{n_m}$, where $S$, $C$, and $M$ denote a saddle mode, a center mode, and a mixed mode, respectively. The superscripts $n_s$, $n_c$, and $n_m$ denote the dimensions of the subspaces associated with each mode. The sum of the dimensions is equal to the dimensions of the phase space, which is six for both the CR3BP and the BCR4BP. For instance, $S^2 \times C^4$ denotes an equilibrium point with a two-dimensional saddle mode and a four-dimensional center mode. In addition to the binary stable/unstable property, an equilibrium point is described by its associated modes.

### 4.1.3 Earth-Moon Instantaneous Equilibrium Points

In the Earth-Moon vicinity, the instantaneous equilibrium solutions correspond to the perturbed, or oscillating, counterparts from the Earth-Moon CR3BP, and are denoted $\mathrm{E}_1$ through $\mathrm{E}_5$. The collections of these instantaneous equilibrium points over a synodic month form the Zero Acceleration Contours (ZACs), which are labeled $\mathbb{E}_1$ through $\mathbb{E}_2$. The $\mathbb{E}_1$ and $\mathbb{E}_2$ ZACs are plotted in the Earth-Moon rotating frame in Figure 4.2. The distance between the CR3BP $\mathrm{L}_1$ equilibrium point and the BCR4BP instantaneous equilibrium $\mathrm{E}_1$ ranges from 200 km to 650 km in Figure 4.2(a), while the range from $\mathrm{L}_2$ to $\mathrm{E}_2$ in Figure 4.2(b) varies between 400 km and 1700 km. Note that the set of instantaneous equilibrium points,

$E_i$, as plotted in Figure 4.2 are not trajectories; rather, they are a collection of points that instantaneously possess zero velocity and zero acceleration.

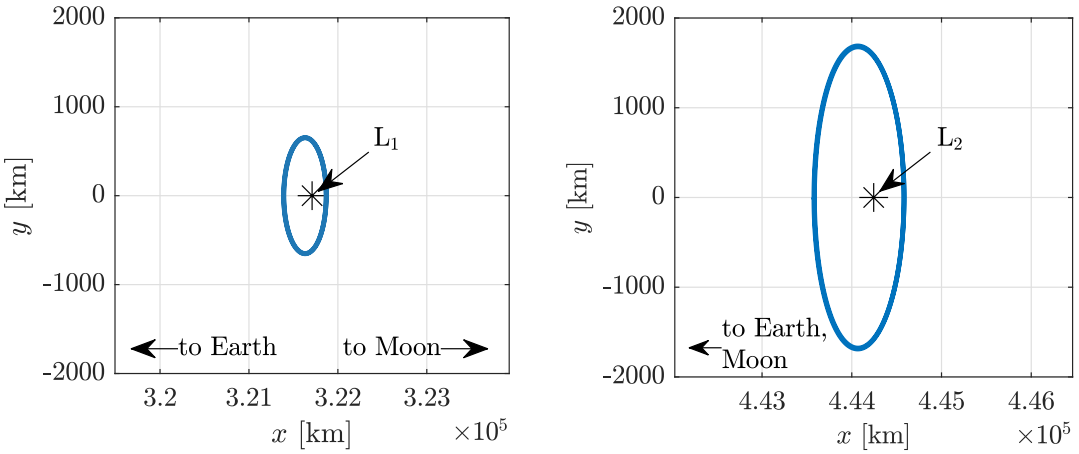


(a) $\mathbb{E}_1$ (b) $\mathbb{E}_2$

**Figure 4.2.** $\mathbb{E}_1$ and $\mathbb{E}_2$ ZACs in the Earth-Moon frame. The Earth-Moon CR3BP equilibrium points are denoted by black asterisks.

The ZACs encircle the Earth-Moon Lagrange points twice: the two cycles are indistinguishable at the scale of Figure 4.2. To visualize the two cycles, the instantaneous equilibrium points are plotted for half of a synodic month and colored by Sun angle in Figure 4.3. The instantaneous points are collinear with the Earth-Moon rotating $\hat{x}$ axis for $\theta = {}^{k\pi}/_{2},\ k = 1, \ldots, 4$. For all other epochs, the instantaneous equilibrium points are located off the rotating $\hat{x}$ axis; the maximum excursions from the Earth-Moon line occur for $\theta = {}^{(2k+1)\pi}/_{4},\ k = 1, \ldots, 4$. The relative geometry of the Earth, Moon, and Sun, evaluated by the Sun angle $\theta$ determines the orientation and distance of the instantaneous equilibrium points with respect to their CR3BP counterpart.

The Zero Acceleration Contour is a subset of the Zero Acceleration *Surfaces* (ZASs). The ZASs are parametrized by the Sun angle and the Sun distance $a_s$. Thus, the ZACs correspond to 'slices' of the ZASs for a particular Sun distances $a_s$[1]. While the value of $a_s$ is evaluated as constant in the BCR4BP, it is actually a function of time. Thus, the selection of $a_s$ value impacts the dynamics of the Earth-Moon-Sun BCR4BP. (The evolution

[1]↑An analogous framework relates the Zero Velocity Contours (ZVCs) to the Zero Velocity Surfaces (ZVSs).

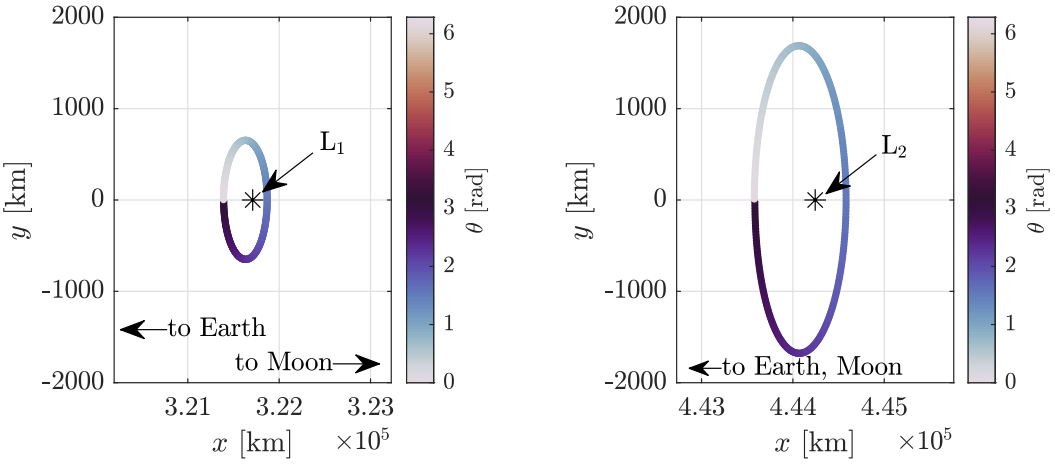


(a) $\mathrm{E}_1(\theta), 0 \leq \theta < \pi$




(b) $\mathrm{E}_2(\theta), 0 \leq \theta < \pi$

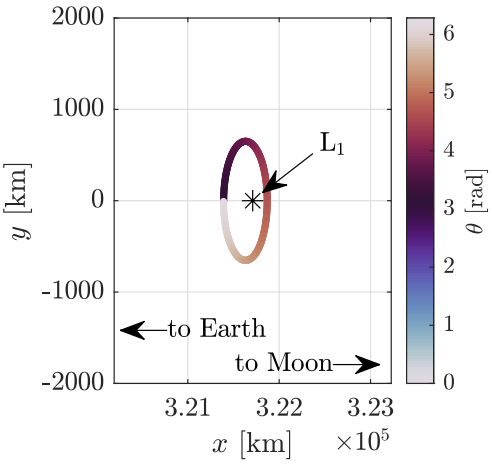


(c) $\mathrm{E}_1(\theta), \pi \leq \theta < 2\pi$

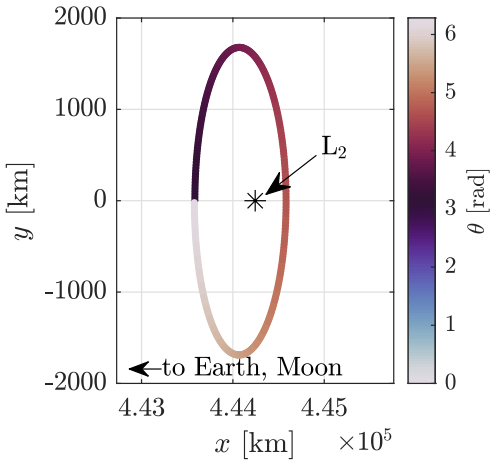


(d) $\mathrm{E}_2(\theta), \pi \leq \theta < 2\pi$

**Figure 4.3.** $\mathrm{E}_1(\theta)$ and $\mathrm{E}_2(\theta)$ instantaneous equilibrium solutions in the BCR4BP, Earth-Moon frame formulation. The Earth-Moon CR3BP equilibrium point is denoted by black asterisks.

of the Sun nondimensional distance obtained from the ephemerides [39] for the years 2022 through 2024 is presented in Appendix B). The ZASs corresponding to $\mathbb{E}_1$ and $\mathbb{E}_2$ appear in Figure 4.4. The surface is colored as a function of the value of $a_\mathrm{s}$; lighter shades correspond to large values of the nondimensional distance while dark shades values reflected small $a_\mathrm{s}$ values. The 'slices' of the ZVS corresponding to the mean value of $a_\mathrm{s}$ that is employed in this analysis are plotted in white. As expected, the distance of the ZACs relative to their corresponding Lagrange points is inversely proportional to the Sun distance. At the limit

$a_s \to \infty$, the BCR4BP simplifies into the Earth-Moon CR3BP and the ZACs collapses to the Lagrange points. Note that the nondimensional Sun distance is a function of both the

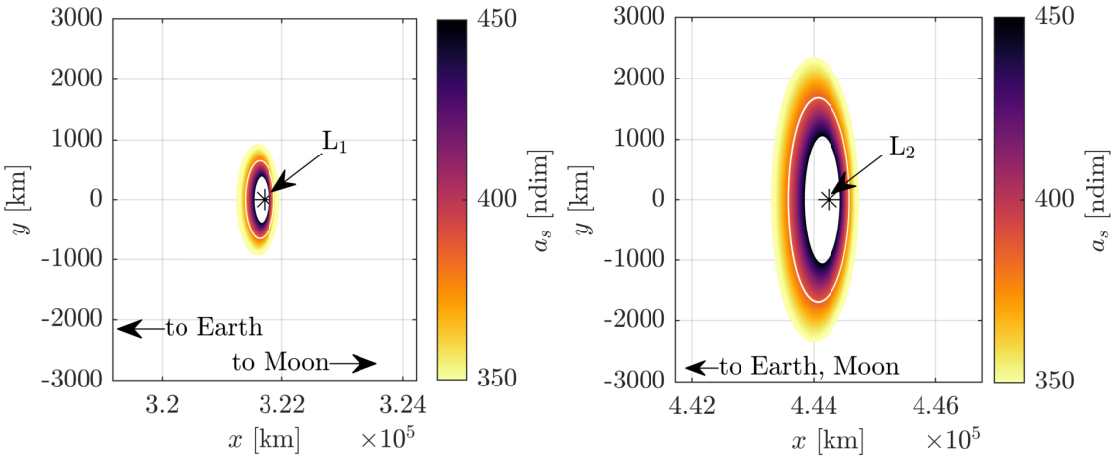


(a) $\mathbb{E}_1$ (b) $\mathbb{E}_2$

**Figure 4.4.** Zero Acceleration Surfaces (ZASs) associated with $\mathbb{E}_1$ and $\mathbb{E}_2$ in the BCR4BP, Earth-Moon frame formulation, colored as a function of the nondimensional Sun distance. The Zero Acceleration Contours (ZACs) for $a_s = 389.1725$ ndim value are plotted in white. The Earth-Moon CR3BP equilibrium points are denoted by black asterisks.

Earth-Moon and the Sun-$B_1$ distances. For instance, increasing the value of $a_s$ correlates to a decrease in the Earth-Moon distance and/or an increase in the Sun-$B_1$ distance. For the purposes of Figure 4.4(a), the Earth-Moon distance is assumed constant and the variations of $a_s$ only correspond to the changes in Sun-$B_1$ distances. The one-dimensional (Sun angle) ZACs are a subset of the two-dimensional ZASs (Sun angle, Sun distance).

The stability of the instantaneous equilibrium solutions is assessed from the eigenvalues of the **A** matrix. The eigenvalues are evaluated at each instantaneous $E_1$ and $E_2$ equilibrium point. The range of values for these eigenvalues over the set of equilibrium solutions as well as the eigenvalues corresponding to the $L_1$ and $L_2$ points, are summarized in Table 4.1. Note that the eigenvalues corresponding to the BCR4BP equilibrium points are not constant and, thus, the minimum and maximum values along the set of instantaneous equilibrium points are included in Table 4.1. The BCR4BP instantaneous equilibrium points near the Moon, that is, $E_1$ and $E_2$, present stability characteristics similar to the CR3BP equilibrium

**Table 4.1**. Eigenvalues associated with the first and second equilibrium points in the Earth-Moon CR3BP and in the BCR4BP, Earth-Moon formulation

| Point | $\lambda_i$ in the CR3BP | $\lambda_i$ range in the BCR4BP |
|---|---|---|
| $L_1/E_1(\theta)$ | $\pm 2.932$ | $\pm 2.916 - \pm 2.940$ |
| | $\pm 2.334\,i$ | $\pm 2.324\,i - \pm 2.337\,i$ |
| | $\pm 2.269\,i$ | $\pm 2.258\,i - \pm 2.276\,i$ |
| $L_2/E_2(\theta)$ | $\pm 2.159$ | $\pm 2.137 - \pm 2.200$ |
| | $\pm 1.863\,i$ | $\pm 1.847\,i - \pm 1.887\,i$ |
| | $\pm 1.786\,i$ | $\pm 1.776\,i - \pm 1.811\,i$ |

points: one saddle mode, described by the real pair of eigenvalues, and two center modes, characterized by the two pairs of complex eigenvalues. Note that remains true for the range of Sun distances examined in Figure 4.4. The $\mathbb{E}_1$ and $\mathbb{E}_2$ ZACs of the BCR4BP in the Earth-Moon frame formulation remain in the vicinity of $L_1$ and $L_2$.

The BCR4BP instantaneous equilibrium points, corresponding to the Earth-Moon $L_3$ Lagrange point, are similarly explored. In contrast to $\mathbb{E}_1$ and $\mathbb{E}_2$, the ZAC in the vicinity of $L_3$ does not remain in close proximity of the Lagrange point, as evident from Figure 4.5(a). The insert in the figure highlights the contour formed by the collection of equilibrium points, which is not apparent at the scale of Figure 4.5(a). The distance between the instantaneous equilibrium and the underlying Lagrange point is plotted as a function of epoch in Figure 4.5(b). The distance ranges from approximately 800 to 371,000 kilometers. From Figure 4.5(b), it is also apparent that multiple solutions exist for certain Sun angle values. For epochs where multiple instantaneous equilibrium solutions exist, these solutions are labelled $E_3{}^j$, where j ranges from 1 to 3. The numbering follows the increasing energy (decreasing $H$) direction. The instantaneous equilibrium points corresponding to $L_3$ are not unique for certain Sun angle values.

The stability (in the linear sense) of the $\mathbb{E}_3$ collection of points is investigated. Since multiple equilibrium solutions exist at certain epochs, a direct comparison between the eigenvalues of $\mathbb{E}_3$ and $L_3$ is not compelling. Thus, the more relevant dimensions of the subspaces associated with each equilibrium point are compared. The Earth-Moon $L_3$ libration point possesses one real and two purely imaginary pairs of eigenvalues. Thus, a two-dimensional

saddle and a four-dimensional center mode emerges for $L_3$ and is denoted $S^2 \times C^4$. The linear stability properties for $\mathbb{E}_3$ are presented in Figure 4.6. Each instantaneous equilibrium point is colored as function of the characteristics of its subspaces: red point corresponds with similar eigenstructure to $L_3$ (two-dimensional saddle and four-dimensional center) while green points possess a six-dimensional center. In the plot in configuration space in Figure 4.6(a),

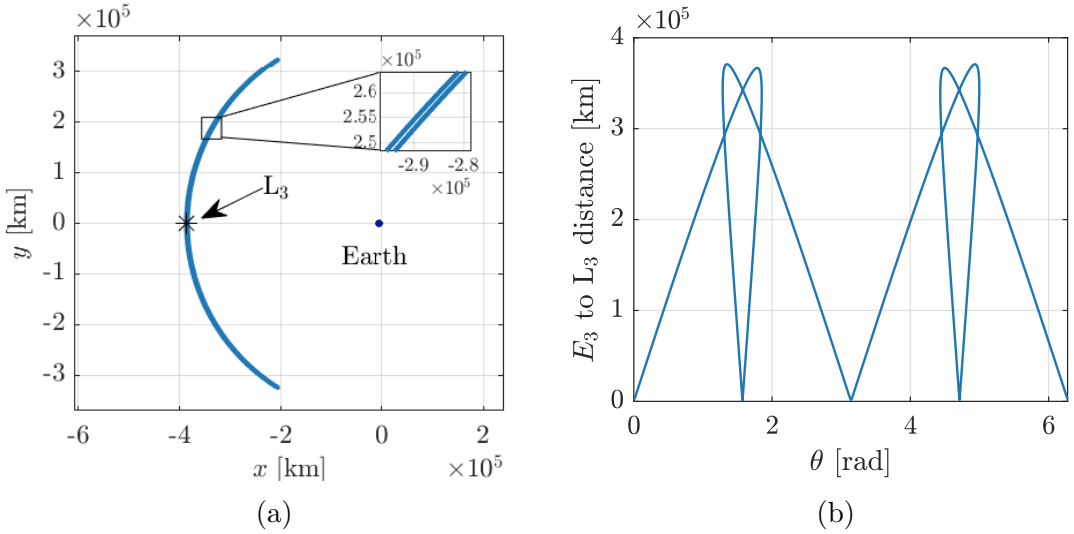


**Figure 4.5.** $\mathbb{E}_3$ in the BCR4BP, Earth-Moon formulation (a). Distance between the instantaneous equilibrium points and $L_3$ as a function of epoch (b).

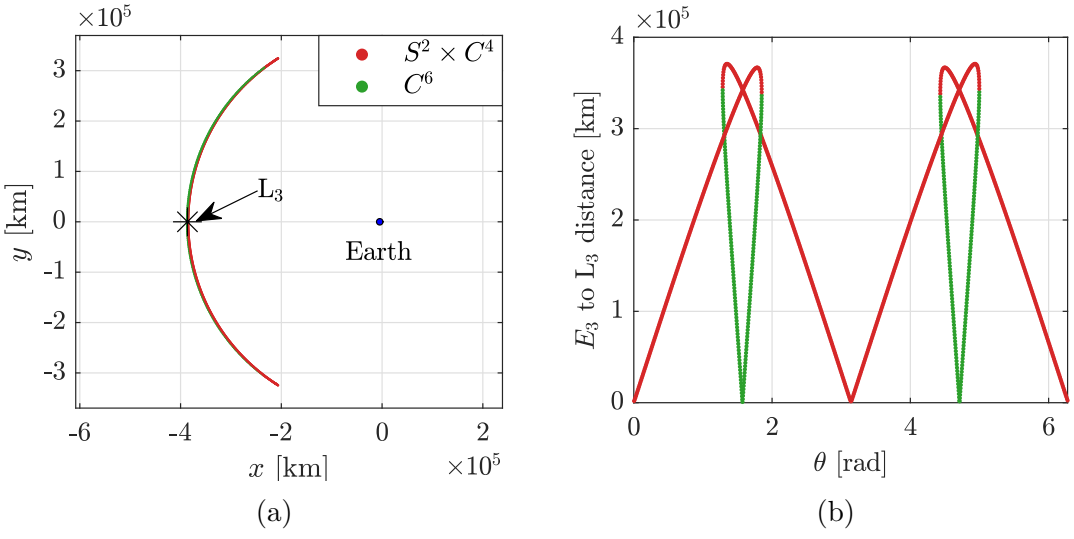


**Figure 4.6.** $\mathbb{E}_3$ in the BCR4BP, Earth-Moon formulation, as colored by the linear stability properties of the equilibrium instantaneous points. Red points denote $S^2 \times C^4$ points, while green points correspond to center $C^6$ points.

the points are close to indistinguishable due to the large dimensions of $\mathbb{E}_3$. However, note that the instantaneous equilibrium points with the $C^6$ characteristics compose the 'outer' part of the contour (furthest from the Earth) while the $S^2 \times C^4$ points form the 'inner' part of the contour. Reading Figure 4.6(b) from left to right offers insight into the dynamical evolution of $\mathbb{E}_3$. From $\theta = 0$ to $\theta = 1.286$ rad $= 73°$, only one $E_3$ instantaneous equilibrium point exists. At $\theta = 1.286$ rad $= 73°$, a *degenerate* [73] instantaneous equilibrium point appears. A saddle-node bifurcation [72] occurs and the instantaneous equilibrium points evolve in two directions: the $S^2 \times C^4$ equilibrium point plotted in red in Figure 4.6(b) and the $C^6$ equilibrium plotted in green. Between $\theta = 1.286$ rad $= 73°$ and $\theta = 1.849$ rad $= 106°$, three equilibrium solutions exist. Note that at $\theta = \pi/2$, the two $S^2 \times C^4$ equilibrium points are equidistant from $L_3$, at a distance of approximately 340,000 km, while the $C^6$ equilibrium point is located along the $\hat{x}$ axis, 800 km away from $L_3$. At $\theta = 1.849$ rad $= 106°$, the two additional equilibrium points collapse into the degenerate equilibrium point. Between $\theta = 1.849$ rad $= 106°$ and $\theta = \boldsymbol{\pi}$, the unique instantaneous equilibrium point possesses the same eigenstructure as $L_3$. A mirrored evolution of the equilibrium points occurs between $\theta = \boldsymbol{\pi}$ and $\theta = 2\boldsymbol{\pi}$. The linear stability properties of $\mathbb{E}_3$ differ significantly from the properties associated with the Earth-Moon $L_3$ Lagrange point.

Finally, the ZACs associated with the $L_4$ and $L_5$ points are examined in the Earth-Moon formulation of the BCR4BP. The two ZACs are plotted in the Earth-Moon rotating frame in Figure 4.7. The distance between the CR3BP $L_4$ equilibrium point and the BCR4BP instantaneous equilibrium $E_4$ ranges from 700 to 233,000 km. Note that the shape of $\mathbb{E}_5$ is the mirror of $\mathbb{E}_4$ across the Earth-Moon rotating $\hat{x}$ axis. Similar to the $\mathbb{E}_1$ and $\mathbb{E}_2$ ZACs, $\mathbb{E}_4$ and $\mathbb{E}_5$ encircle their associated Lagrange point twice. The two cycles are visualized by plotting the instantaneous equilibrium points for half of the synodic month, as in Figure 4.8. While the shape of the ZACs is mirrored across the rotating $\hat{x}$ axis, such is not the case for the evolution of the individual instantaneous equilibrium points. For a given epoch $\theta$, the $E_5(\theta)$ equilibrium point is generally not the mirror image of $E_5(\theta)$. From Figure 4.8 and the symmetry properties of the Earth-Moon-Sun frame, the two points mirror of each other when $\theta = k\boldsymbol{\pi}$, $k = 1, 2$. The relative geometry of the Earth, Moon, and Sun, evaluated

by the Sun angle $\theta$ determines the orientations of the $E_4$ and $E_5$ instantaneous equilibrium points.

The stability of the instantaneous equilibrium points associated with $\mathbb{E}_4$ and $\mathbb{E}_5$ is straightforwardly assessed. The eigenvalues associated with $L_4/L_5$ and the corresponding ranges in the associated eigenvalues in the BCR4BP are presented in Table 4.2. The $L_4/L_5$ points in the CR3BP are linearly stable, i.e., they possess a six-dimensional center mode. Their instantaneous counterparts in the BCR4BP are also stable, as apparent by the purely imaginary ranges of the eigenvalues in the second column of Table 4.2. However, note the different variations in the range of eigenvalues; the eigenvalues associated with the long-period motion [74], i.e., the eigenvalues with the smallest magnitude, reflect a larger variation than the eigenvalues associated with the short-period motion and the unit eigenvalues. The eigen-

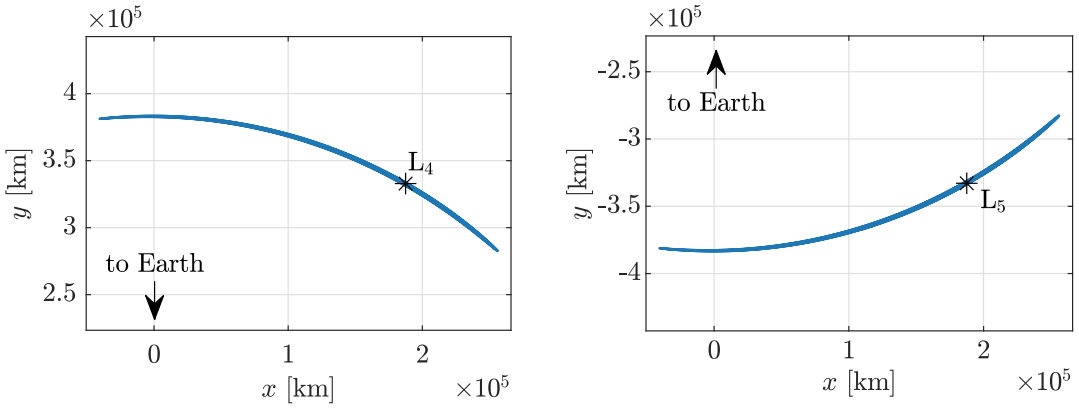


(a) $\mathbb{E}_4$ (b) $\mathbb{E}_5$

**Figure 4.7.** $\mathbb{E}_4$ and $\mathbb{E}_5$ ZACs in the Earth-Moon frame. The Earth-Moon CR3BP equilibrium points are denoted by black asterisks.

**Table 4.2**. Eigenvalues associated with the fourth and five equilibrium points in the Earth-Moon CR3BP and in the BCR4BP, Earth-Moon formulation

| $\lambda_i$ in the CR3BP | $\lambda_i$ range in the BCR4BP |
|---|---|
| $\pm 0.298\,i$ | $\pm 0.019\,i - \pm 0.460\,i$ |
| $\pm 0.955\,i$ | $\pm 0.881\,i - \pm 0.994\,i$ |
| $\pm 1.000\,i$ | $\pm 1.000\,i - \pm 1.010\,i$ |

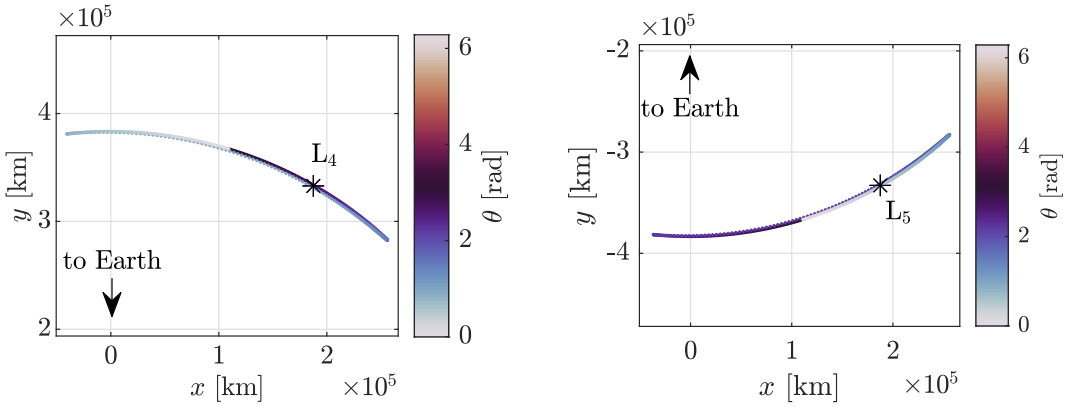


(a) $\mathrm{E}_4(\theta), 0 \leq \theta < \pi$ (b) $\mathrm{E}_5(\theta), 0 \leq \theta < \pi$

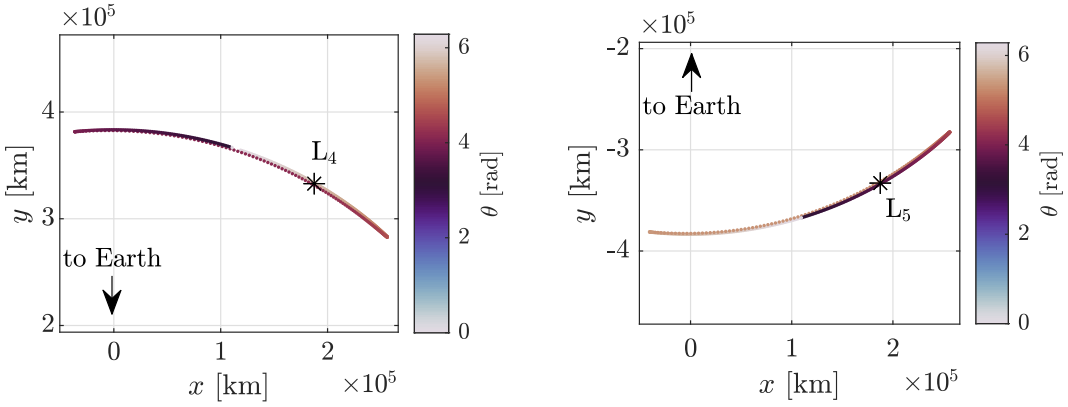


(c) $\mathrm{E}_4(\theta), \pi \leq \theta < 2\pi$ (d) $\mathrm{E}_5(\theta), \pi \leq \theta < 2\pi$

**Figure 4.8.** $\mathrm{E}_4(\theta)$ and $\mathrm{E}_5(\theta)$ instantaneous equilibrium solutions in the BCR4BP, Earth-Moon frame formulation. The Earth-Moon CR3BP equilibrium points are denoted by black asterisks.

structure of the $\mathrm{E}_3$ equilibrium points is analogous to that associated with the Earth-Moon $\mathrm{L}_3$ Lagrange point.

The ZASs associated with $\mathbb{E}_3$, $\mathbb{E}_4$, and $\mathbb{E}_5$ are examined. Recall that the ZAS is the collection of ZACs for a range of nondimensional Sun distances $a_s$. The ZASs associated with $\mathbb{E}_3$, $\mathbb{E}_4$, and $\mathbb{E}_5$ appear in Figure 4.9. Points colored in the darker shades of the color map correspond to a large nondimensional Sun distance $a_s$. Since the gravitational action from the Sun is inversely proportional to the nondimensional Sun distance, these points are

less influenced by the acceleration due the Sun than points colored in lighter shades. For nondimensional Sun distances greater than 381 ndim, three distinct ZACs exist, as evidenced by the purple-to-dark islands around $L_3$, $L_4$, $L_5$ in Figure 4.9. Conversely, the three ZACs merge for nondimensional Sun distances equal to or less than 381 ndim. The 'merged' ZACs form a horseshoe-shaped surface that encloses $L_3$, $L_4$, and $L_4$. For the average nondimensional Sun distance employed through this analysis, $a_s = 389.1725$ ndim, three distinct ZACs exist. However, this selected value is not far from the critical value that results in merged ZASs; from the ephemerides data in Appendix B, epochs with nondimensional Sun distances below the critical Sun distance occur commonly throughout the 2022-2025 period. Merged and separated sets of ZACs are observed when examining the ZASs associated with $\mathbb{E}_3$, $\mathbb{E}_4$, and $\mathbb{E}_5$.

The stability properties (in the linear sense) associated with $\mathbb{E}_3$, $\mathbb{E}_4$, and $\mathbb{E}_5$ are a function of the nondimensional Sun distance. For each set of instantaneous equilibrium point, the real and imaginary parts of the eigenvalues associated with $\mathbf{A}$, that is, the Jacobian matrix

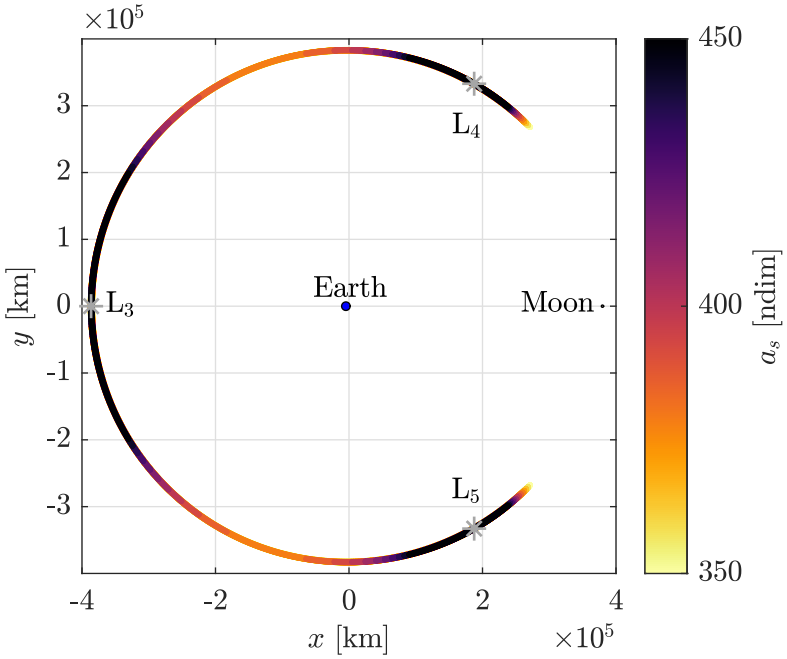


**Figure 4.9.** ZASs associated with $\mathbb{E}_3$, $\mathbb{E}_4$, and $\mathbb{E}_5$. The contours merge for $a_s < 381$ ndim. The Earth-Moon CR3BP equilibrium points are denoted by gray asterisks.

in Equation (2.4), are plotted as a function of Sun angle in Figure 4.10. Each point is colored as a function of the nondimensional Sun distance; darker shades denote larger $a_s$ values (Sun further away from $B_1$) while lighter shades represent smaller values of $a_s$ (Sun closer to $B_1$). The real part and the imaginary part of the eigenvalues of $\mathbf{A}$ are plotted on the left column and right column of Figure 4.10, respectively. Since all of the eigenvalues are either purely real or purely imaginary, i.e., there are no mixed modes, the left column represents the saddle modes for the instantaneous equilibrium points while the center modes are described in the right column. First, consider the stability characteristics associated with $\mathbb{E}_3$ in Figures 4.10(a) and 4.10(b). For descending values of $a_s$ between 450 and 441 ndim (black and dark purple points), there exist only one instantaneous equilibrium point for all epochs. Similar to the Earth-Moon $L_3$, these instantaneous equilibrium points are all associated with a two-dimensional saddle and a four-dimensional center. For $a_s$ less than 441 ndim, three distinct equilibrium solutions exist for a range of epochs, as observed in Figures 4.5 and 4.6. The range of epochs for which multiple counterparts to $L_3$ exist is a function of the Sun distance; the closer the Sun, the larger this range, as apparent from the concentric orange curves near $\theta = \pi/2$, $\boldsymbol{\pi}$ in Figure 4.10(a). The type of modes associated with the instantaneous equilibrium solutions is also a function of the Sun distance. For nondimensional Sun distances between 441 and 382, a $S^2 \times C^4$ equilibrium point exists at all epochs. Additionally, a second $S^2 \times C^4$ equilibrium point and a $C^6$ point exists for certain epochs. Note that the average Sun distance employed in this investigation is within this range of $a_s$; the stability properties associated with the ZACs at $a_s = 389.1725$ ndim are plotted in as a blue curve in Figures 4.10(a) and 4.10(b) over the darker hues. Finally, for nondimensional Sun distances between 350 and 382, two equilibrium points with a six-dimensional center mode exist for certain epochs, in addition to the $S^2 \times C^4$ equilibrium points that exist for all Sun angle values. A similar analysis is conducted for the ZASs corresponding to $\mathbb{E}_4$ and $\mathbb{E}_5$; the real and imaginary parts of the eigenvalues associated with the Jacobian matrix are plotted as functions of Sun angle and Sun distance in Figures 4.10(c) and 4.10(d). Similar to $\mathbb{E}_3$, the stability characteristics of $\mathbb{E}_4$ and $\mathbb{E}_5$ vary as a function of the Sun distance. For values of $a_s$ greater than 388 nondim, all of the instantaneous equilibrium points along the $\mathbb{E}_4$ and $\mathbb{E}_5$ ZACs present the same $C^6$ structure as the Earth-Moon $L_4$ and

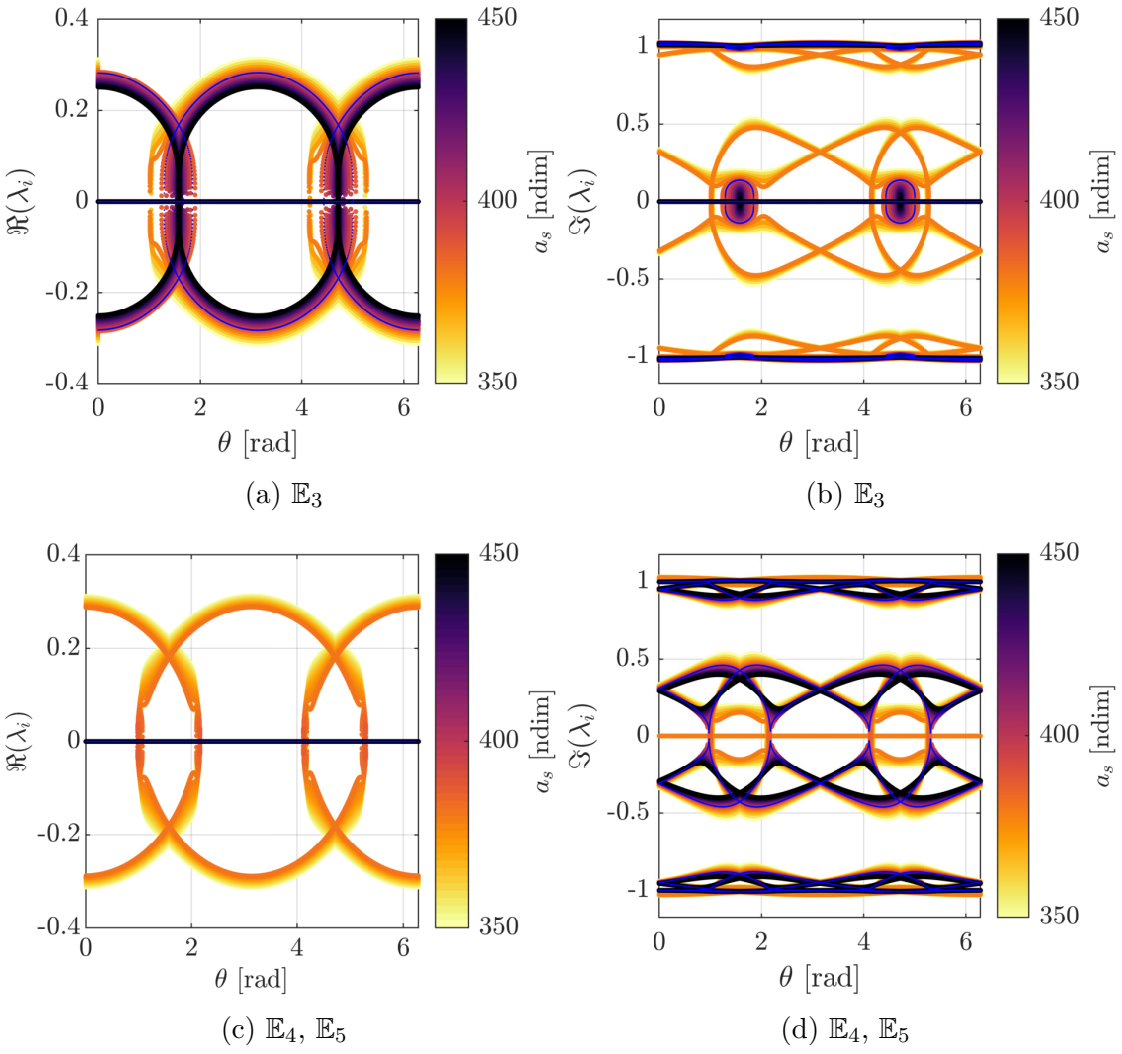


**Figure 4.10.** Linear stability properties associated with the $\mathbb{E}_3$, $\mathbb{E}_4$, and $\mathbb{E}_5$ ZACs colored as a function of the nondimensional Sun distance. Blue lines denote the stability properties for the average nondimensional Sun distance employed in this analysis, $a_s = 389.1725$ ndim.

$L_5$, i.e., the equilibrium points are stable in the linear sense. Note that this range includes the average $a_s$ value employed in this analysis; the eigenvalues associated with the ZAS at this Sun distance are again plotted in blue in Figures 4.10(c) and 4.10(d). For values of $a_s$ between 388 and 381, the instantaneous equilibrium points present a six-dimensional center mode over the majority of the synodic month, except for a small range of epochs for which the equilibrium points possess $S^2 \times C^4$ characteristics. These epochs are identifiable in Figure 4.10(c) by the small vertical lines colored in dark orange near $\theta = 1, 2, 4, 5$ rad.

Finally, for $a_s$ less than 381 ndim, the ZACs associated with $\mathbb{E}_3$, $\mathbb{E}_4$, and $\mathbb{E}_5$ merge. The $\mathbb{E}_3$ set retrieves its $C^6$ characteristics. Note the similarity of the orange-to-yellow curves between Figures 4.10(a) and 4.10(c), and between Figures 4.10(b) and 4.10(d); for these Sun distance values, the ZACs are merged. Various linear stability properties are observed as the two parameters (Sun angle, Sun distance) associated with the ZASs evolve.

### 4.1.4 Sun-$B_1$ Instantaneous Equilibrium Points

Time-dependent, or instantaneous equilibrium solutions also exist in the Sun-$B_1$ rotating frame. They are denoted $\underline{\mathrm{E}}_1(\underline{\theta})$ through $\underline{\mathrm{E}}_5(\underline{\theta})$ and correspond to the Sun-$B_1$ equilibrium solutions instantaneously perturbed by the motions of the Earth and the Moon along their respective orbits. The ZACs for the $\underline{\mathrm{E}}_1(\underline{\theta})$ and $\underline{\mathrm{E}}_2(\underline{\theta})$ instantaneous equilibrium points are plotted in Figure 4.11. The distance Sun-$B_1$ from the CR3BP equilibrium point to the BCR4BP instantaneous equilibrium points range from 600 to 2500 km for both $\underline{\mathrm{E}}_1(\underline{\theta})$ and $\underline{\mathrm{E}}_2(\underline{\theta})$. Recall that the set of instantaneous equilibrium points, $\underline{\mathrm{E}}_\mathrm{i}$, are not trajectories; rather, they are a collection of points that instantaneously possess zero velocity and zero acceleration in the appropriate equations of motion. The points in Figures 4.11(a) and 4.11(b) are colored as a function of the epoch, i.e., the Moon angle $\underline{\theta}$ for which they satisfy these conditions. For reference, the orbits of the Earth and the Moon are plotted in Figure 4.11(c). Note that the radius of the Earth's orbit has been scaled by a factor of 10 for visualizations purposes. The ZACs encircle the Earth-Moon Lagrange points twice. The shape of the cycle, and its distance from the Sun-$B_1$ Lagrange point, are determined by the location of the Moon and the Earth along their respective orbits. The distance between $\underline{\mathrm{E}}_\mathrm{i}$ and $\underline{\mathrm{L}}_\mathrm{i}$, as well as the rotating $\hat{\underline{y}}$ component associated with $\underline{\mathrm{E}}_\mathrm{i}$ are plotted for a synodic month in Figure 4.12. For instance, at $\underline{\theta} = 0$ and $\underline{\theta} = \pi$, the Sun, the Earth, $B_1$, and the Moon are aligned (not in the same order). As a consequence, the points on the $\underline{\mathrm{E}}_1$ and $\underline{\mathrm{E}}_2$ curves for these two epochs are also located on the Sun-$B_1$ rotating $\hat{\underline{x}}$ axis, i.e., their associated $\underline{y}$ component is equal to 0, as apparent in Figure 4.12(a). Furthermore, the instantaneous equilibrium points are also located on the rotating $\hat{\underline{y}}$ axis for an epoch shortly before or after $\pi/2$ and $3\pi/2$, as denoted by the black arrows in Figure 4.12(a). Figure 4.12(b) includes the distance from $\underline{\mathrm{E}}_\mathrm{i}$

to $\underline{\mathrm{L}}_{\mathrm{i}}$, i.e., the distance between the equilibrium points perturbed by the individual motions of the Earth and the Moon and the points unperturbed (Earth and Moon fixed at $B_1$). The minimum distances of $\underline{\mathrm{E}}_{\mathrm{i}}$ relative to $\underline{\mathrm{L}}_{\mathrm{i}}$ occur near $\underline{\theta} = \pi/2$ and $\underline{\theta} = 3\pi/2$, when the Earth-Moon line is nearly perpendicular to the rotating $\hat{x}$ axis. The $\mathbb{E}_1$ and $\mathbb{E}_2$ behaviors are influenced by the relative position of the Earth and the Moon along their respective orbits.

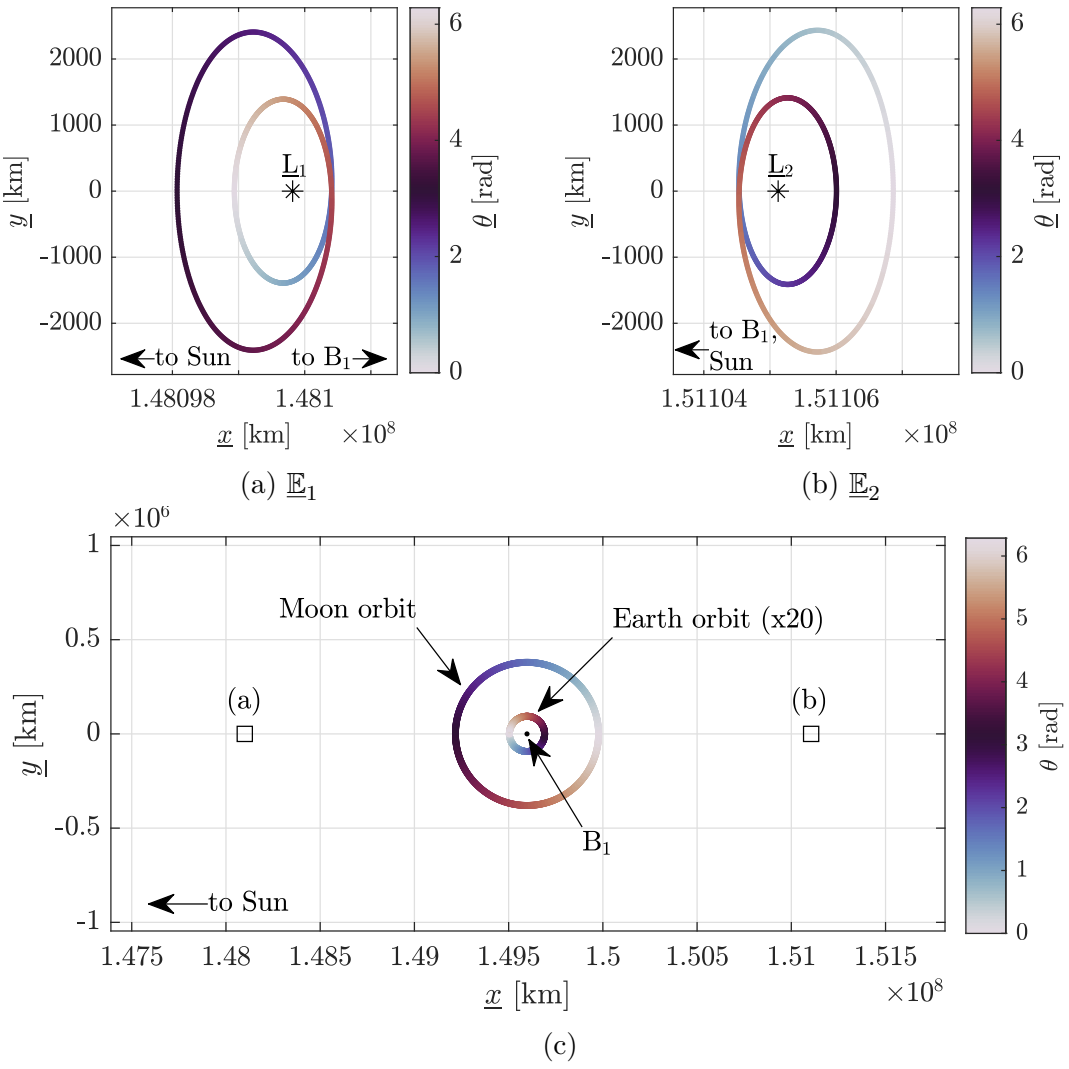


**Figure 4.11.** $\underline{\mathbb{E}}_1$ and $\underline{\mathbb{E}}_2$ ZACs in the Sun-$B_1$ frame, colored as a function of the epoch (a, b). The Sun-$B_1$ CR3BP equilibrium points are denoted by black asterisks. Moon and Earth orbits colored as a function of the epoch (c). Note that the radius of the Earth's orbit is at $\times 10$ scale.

The stability of the instantaneous equilibrium solutions is assessed from the eigenvalues of the **A** matrix in Equation (3.7). The eigenvalues are evaluated at each instantaneous $\underline{\mathrm{E}}_1$ and $\underline{\mathrm{E}}_2$ equilibrium point. The range of these eigenvalues over the set of equilibrium solutions as well as the eigenvalues corresponding to the $\underline{\mathrm{L}}_1$ and $\underline{\mathrm{L}}_2$ points, are summarized in Table 4.3. Both $\underline{\mathrm{L}}_1$ and $\underline{\mathrm{L}}_2$, as computed in the Sun-$B_1$ CR3BP, possess a two-dimensional saddle and a four-dimensional center, as evidenced by the real pair and two imaginary pairs of eigenvalues associated with Lagrange point. The instantaneous equilibrium points for the Sun-$B_1$ formulation of the BCR4BP possess the same eigenstructure as the CR3BP equilibrium points. The magnitude of the eigenvalues associated with $\underline{\mathbb{E}}_1$ and $\mathbb{E}_2$ vary as a

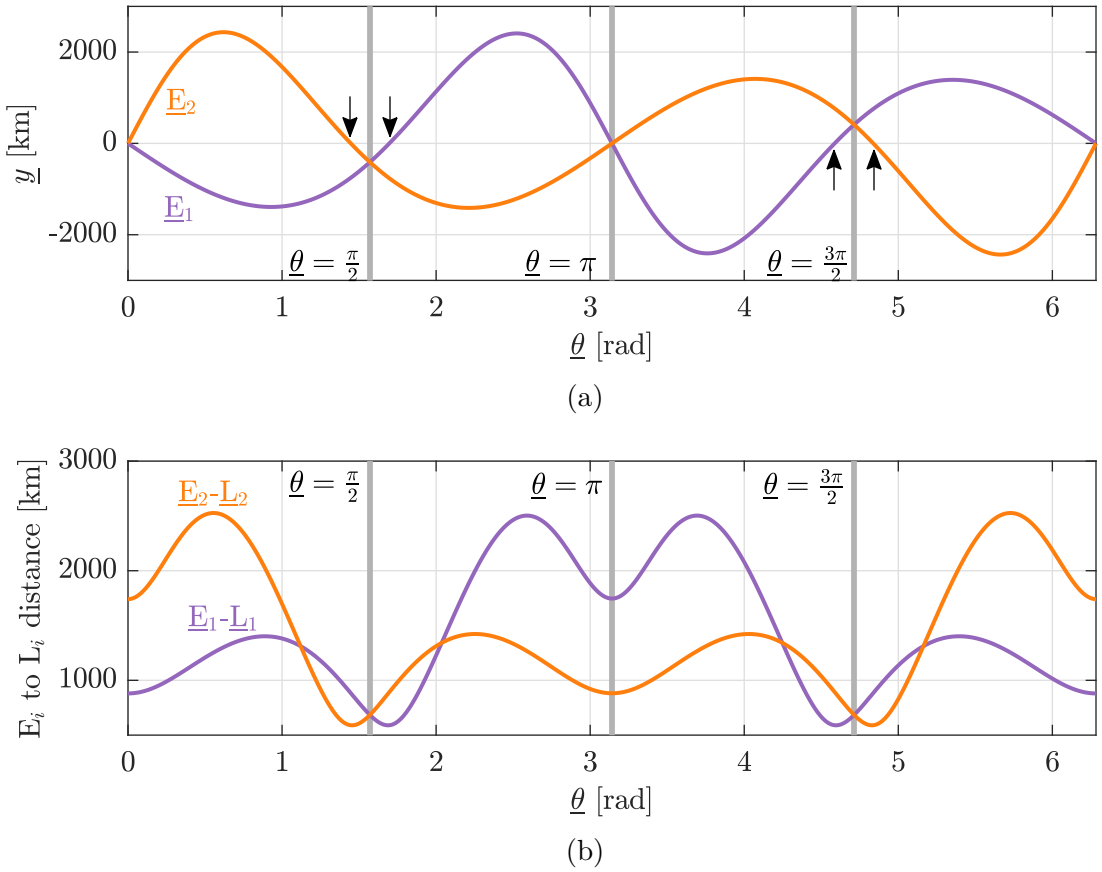


**Figure 4.12.** Distance between the $\underline{\mathrm{E}}_\mathrm{i}$ instantaneous equilibrium and the $\underline{\mathrm{L}}_\mathrm{i}$ Lagrange point (a). Sun-$B_1$ rotating $\hat{\underline{x}}$ component associated with the instantaneous equilibrium points (b).

function of the epoch. However, the variations are limited, as apparent in the second column in Table 4.3.

**Table 4.3**. Eigenvalues associated with the first and second equilibrium points in the Sun-$B_1$ CR3BP and in the BCR4BP, Sun-$B_1$ formulation

| Point | $\lambda_i$ in the CR3BP | $\lambda_i$ range in the BCR4BP |
|---|---|---|
| $\underline{L}_1$ /$\underline{E}_1(\underline{\theta})$ | $\pm 2.533$ | $\pm 2.531 - \pm 2.538$ |
| | $\pm 2.087$ i | $\pm 2.084$ i $- \pm 2.090$ i |
| | $\pm 2.015$ i | $\pm 2.015$ i $- \pm 2.018$ i |
| $\underline{L}_2$ /$\underline{E}_2(\underline{\theta})$ | $\pm 2.484$ | $\pm 2.483 - \pm 2.489$ |
| | $\pm 2.057$ i | $\pm 2.055$ i $- \pm 2.060$ i |
| | $\pm 1.985$ i | $\pm 1.985$ i $- \pm 1.988$ i |

Recall that a Zero Acceleration Contour is a subset of the Zero Acceleration Surfaces (ZASs). The ZASs are parametrized by the Moon angle $\underline{\theta}$ and the nondimensional Earth-Moon distance. Since the nondimensional parameter $a_s$ represents the ratio of the Sun-$B_1$ distance and the Earth-Moon distance, $1/a_s$ yields the nondimensional Earth-Moon distance. Assumed constant in the Earth-Moon CR3BP and the BCR4BP, this distance actually varies due to the eccentricity associated with the Moon's orbit around the Earth. Additionally, varying the nondimensional Earth-Moon distance is achieved by adjusting the dimensional Earth-Moon distance and maintaining the dimensional Sun-$B_1$ distance constant. The ZASs associated with $\underline{\mathbb{E}}_1$ and $\underline{\mathbb{E}}_2$ appear in Figure 4.13. The nondimensional Earth-Moon distance $1/a_s$ is varied between 0.0022 and 0.0029, corresponding to a range in the value of $a_s$ from 450 to 350 ndim. From Figure 4.13, the distance between $\underline{L}_i$ and $\underline{E}_i$ is a function of the nondimensional Earth-distance. For larger $1/a_s$ values, or equivalently, darker shades of the surfaces, the instantaneous equilibrium points are furthest from their Lagrange point counterpart. Conversely, for smaller Earth-Moon distances, the perturbations due to the motions of the Earth and the Moon are less significant, and the distances between $\underline{L}_i$ and $\underline{E}_i$ are smaller. Note that the limiting case is $1/a_s \to 0$, for which the Earth and the Moon are located at $B_1$, and the model is reduced to the Sun-$B_1$ CR3BP. The stability properties of $\mathbb{E}_1$ and $\mathbb{E}_2$ are maintained for the range of nondimensional Earth-Moon distance in Figure 4.13; all the points on the ZAS present a two-dimensional saddle mode and a four-dimensional

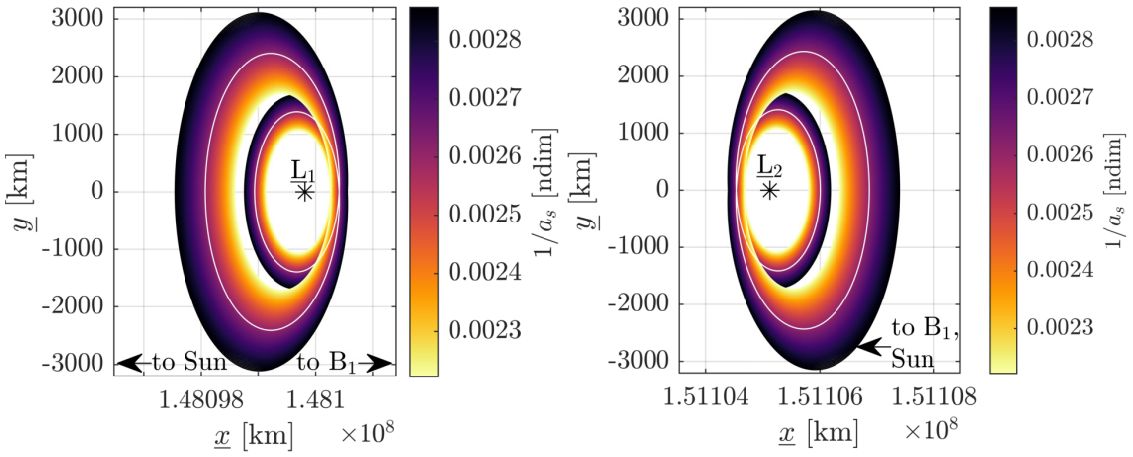


(a) $\underline{\mathbb{E}}_1$ (b) $\underline{\mathbb{E}}_2$

**Figure 4.13.** Zero Acceleration Surfaces (ZASs) associated with $\underline{\mathbb{E}}_1$ and $\underline{\mathbb{E}}_2$ in the BCR4BP, Sun-$B_1$ frame formulation, colored as a function of the nondimensional Earth-Moon distance. The Zero Acceleration Contours (ZACs) for $a_s = 389.1725$ ndim value are plotted in white. The Sun-$B_1$ CR3BP equilibrium points are denoted by black asterisks.

center mode. The Zero Acceleration Surfaces associated with $\mathbb{E}_1$ and $\mathbb{E}_2$ are parametrized by the nondimensional Earth-Moon distance.

The Sun-$B_1$ $\underline{L}_3$, $\underline{L}_4$, and $\underline{L}_5$ equilibrium points are not significantly affected by the motions of the Earth and the Moon along their respective orbits. Recall from Figure 4.1 that, while the Sun influences the locations of all of the Earth-Moon $L_i$ Lagrange points, the perturbations due to the Earth and Moon motions primarily influence the Sun-$B_1$ $\underline{L}_1$ and $\underline{L}_2$ points. The distances from the Sun-$B_1$ Lagrange points to the Earth-Moon barycenter in terms of the Earth-Moon distance $l^*$ are summarized in Table 4.4. The first and second Lagrange points are located less than $4l^*$ from the Earth-Moon barycenter; these two points are significantly perturbed by the motions of the Earth and the Moon, as evidenced in Figure 4.11. The $\underline{L}_3$ and $\underline{L}_4/\underline{L}_5$ Lagrange points are located $778.34\,l^* = 2\,\text{AU}$ and $389.17\,l^* = 1\,\text{AU}$ from the Earth-Moon barycenter $B_1$, respectively. At these distances, the motion of the Earth and Moon along their orbits can be ignored, and the $\mathbb{E}_i$ is well approximated by the Sun-$B_1$ CR3BP, and $\mathbb{E}_i = L_i$, for $i = 3, 4, 5$.

**Table 4.4**. Distances of the Sun-$B_1$ Lagrange points from the Earth-Moon barycenter $B_1$ in terms of the Earth-Moon distance $l^*$.

| | $\underline{\mathrm{L}}_1$ | $\underline{\mathrm{L}}_2$ | $\underline{\mathrm{L}}_3$ | $\underline{\mathrm{L}}_4/\underline{\mathrm{L}}_5$ |
|---|---|---|---|---|
| $\underline{\mathrm{L}}_\mathrm{i}$ to $B_1$ distance $[l^*]$ | 3.8960 | 3.9222 | 778.3442 | 389.1725 |

## 4.2 Instantaneous Zero Velocity Contours

In the CR3BP, some boundaries on the motion of the spacecraft are obtained from the Jacobi constant. The Jacobi constant expression from Equation (2.3) is rewritten as $\dot{x}^2 + \dot{y}^2 + \dot{z}^2 = 2U^* - C$. Since the velocity cannot be imaginary, the inequality $2U^* - C \geq 0$ defines boundaries on the motion. All the locations that do not satisfy this inequality and, therefore, yield an imaginary velocity, are labeled as part of the forbidden region. The collection of points satisfying the equality $2U^* = C$ form a surface, and therefore, yield a velocity relative to the rotating frame that is equal to zero, is labeled the set of zero velocity surfaces. The zero velocity surfaces offer great insight into the possible motion of the spacecraft, given a certain energy level. Cross sections of the ZASs at a given values of the out-of-plane $z$-component are denoted the Zero Velocity Contours (ZVCs). Illustrations and a discussion of the ZVSs and ZVCs as computed in the Earth-Moon CR3BP are included in Boudad [21].

Pulsating, or instantaneous, Zero Velocity Contours (ZVCs) exist in the BCR4BP [21]. Recall that for a given energy-like quantity, the ZVCs bound the regions of space where all the rotating velocity components are real numbers. In the CR3BP, the energy-like quantity, i.e., the Jacobi constant, remains at its constant value along a trajectory. However, in the BCR4BP, the energy-like quantity does not remain constant. Therefore, the ZVCs evolve, or pulsate, along the trajectory as a function of the states and the position of the Earth, the Moon, and the Sun. For example, consider the planar trajectory in Figure 4.14. This trajectory is propagated for 27 days using the BCR4BP equations of motion as formulated in the Earth-Moon rotating frame in Equation (2.4). The black circles represent the Earth and the Moon, and the black arrow originating at $B_1$ is consistently directed toward the Sun. The instantaneous equilibrium points are denoted by green squares. At the initial time,

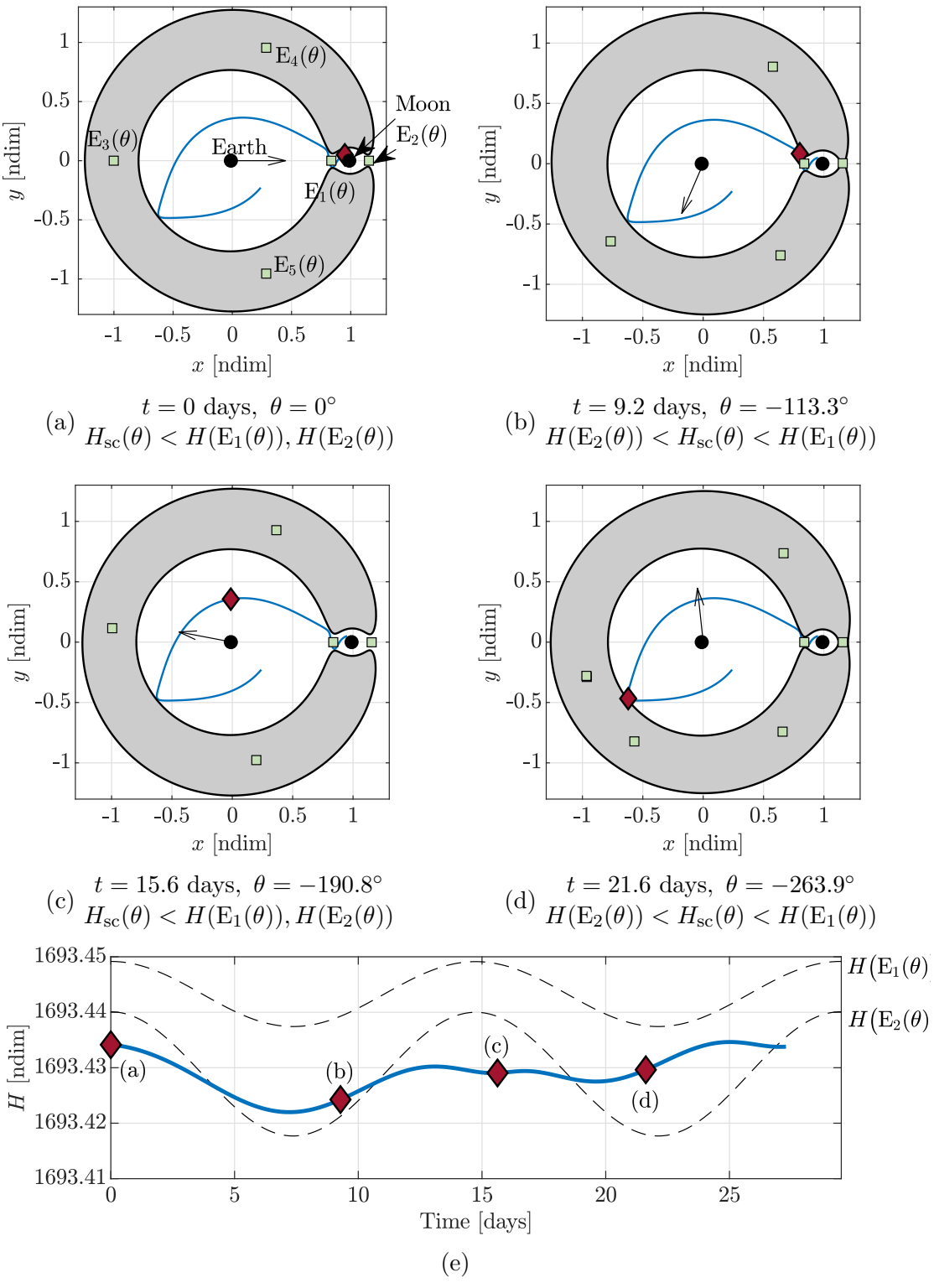


**Figure 4.14.** Instantaneous ZVCs over a planar BCR4BP trajectory as viewed in the Earth-Moon rotating frame (a)-(d). Earth-Moon energy-like value along the trajectory (e).

the spacecraft, identified by a maroon diamond, is located near the Moon, as apparent in Figure 4.14(a). The ZVCs are the black lines bounding the gray regions, i.e., the forbidden regions. Note that in Figure 4.14(a), the portals at $E_1$ and $E_2$ are open; the Earth, Moon, and the exterior region are connected. As the spacecraft departs the Moon vicinity, in Figure 4.14(b), the portal at $E_2$ closes and the exterior region is no longer accessible as the exterior and the Earth and Moon regions are no longer connected. As the trajectory evolves in time, the ZVCs continue pulsating; the $E_2$ portal opens, in Figure 4.14(c), and closes again, in Figure 4.14(d). While plotting the ZVCs at each time step along the trajectory offers valuable insight, it is not necessarily the most convenient representation of the flow information. Therefore, plots of the energy-like value, $H$, are introduced. In Figure 4.14(e), the Earth-Moon energy-like value is plotted against the time along the trajectory. For reference, the Earth-Moon energy-like values associated with the $E_1$ and $E_2$ instantaneous equilibrium points are also plotted as dashed lines. For energy-like values above the dashed line associated with the $E_1$ ZAC, the pulsating ZVCs form two closed regions around the Earth and the Moon. For energy-like values between the two dashed lines, the $E_1$ portal is open and transit between the Earth and the Moon is possible. Finally, for energy-like values below the values associated with $E_2$, the $E_2$ portal is also open, and the Earth, the Moon, and the exterior region are connected. Note that epoch, i.e., the Sun angle, along the ZAC and the trajectory must be consistent for appropriate comparisons of the energy-like values. The flow information described by the ZVCs in Figures 4.14(a)–4.14(d) is summarized in Figure 4.14(e). The diamonds labeled (a) and (c) in Figure 4.14(e) correspond to the plots in Figures 4.14(a) and 4.14(c); both portals near the Moon are open. Conversely, the $E_2$ portal is closed in Figures 4.14(b) and 4.14(d), as indicated by locations of the diamonds labeled (b) and (d) in Figure 4.14(e). The energy-like quantity $H$ plots are useful to assess the $E_i$ portal access, i.e., a binary check to record whether a portal is open at a certain time along the trajectory.

Similar to the BCR4BP as modeled in the Earth-Moon rotating frame, instantaneous Zero Velocity Contours exist in the BCR4BP as formulated in the Sun-$B_1$ rotating frame. Consider the planar trajectory presented in Figure 4.15. This trajectory is propagated for 27 days using the BCR4BP equations of motion as formulated in the Earth-Moon rotating

frame in Equation (2.8). The blue and the gray circles represent the Earth's orbit and the Moon's orbit, respectively. At the initial time, the spacecraft, identified by a magenta circle, is located near the Moon, as apparent in Figure 4.15(a). The ZVCs are the black lines bounding the gray regions, i.e., the forbidden regions. At the initial time along the trajectory, the portals at $\underline{E}_1$ and $\underline{E}_2$ are closed; the Earth-Moon region and the exterior regions are not connected as apparent in Figure 4.15(a). Additionally, the boundaries on the allowable flow are also apparent from the Sun-$B_1$ energy-like value plot in Figure 4.15(e), where the energy-like quantity, $\underline{H}$, as defined in Equation (2.11) associated with the spacecraft is initially above the ones associated with the Sun-$B_1$ portals. (Note that the energy-like values associated with the Sun-$B_1$ portals, i.e., the dashed lines in Figure 4.15(e), vary as a function of time, but their variations are indistinguishable at this scale.) As the spacecraft evolves along its trajectory, the energy-like quantity associated decreases, until it crosses the instantaneous value associated with the $\underline{E}_1$ equilibrium point. Thus, the portal at $\underline{E}_1$ open approximately 3.3 days after the initial time along the trajectory, as apparent in Figure 4.15(b). The portal at $\underline{E}_2$ opens approximately 2 hours later. As the value of the energy-like quantity continues to decrease, the ZVCs continue to recede and the portal open further, as apparent in Figure 4.15(c). Approximately 20 days after the initial time, the energy-like quantity along the trajectory reaches a plateau near $\underline{H} = 3.00051$, a value for which the instantaneous ZVCs do not exist in the vicinity of the Earth-Moon region. This plateau occurs when the spacecraft reaches a certain distance from the Earth-Moon system; as the distance to the Moon increases, the influence of the last term in Equation (2.9) becomes marginal and the dynamics of the system become well approximated by the Sun-Earth CR3BP. Energy-like quantity plots are useful to assess the $\underline{E}_i$ portal access, i.e., a binary check to record whether a portal is open at a certain time along the trajectory.

### 4.3 Periodic Orbits

A periodic orbit is an oscillatory solution that precisely repeat. Unlike periodic orbits generated in the Keplerian Two-Body model, periodic orbits constructed in multi-body models such as the CR3BP or the BCR4BP do not necessarily revolve around a celestial bodies.

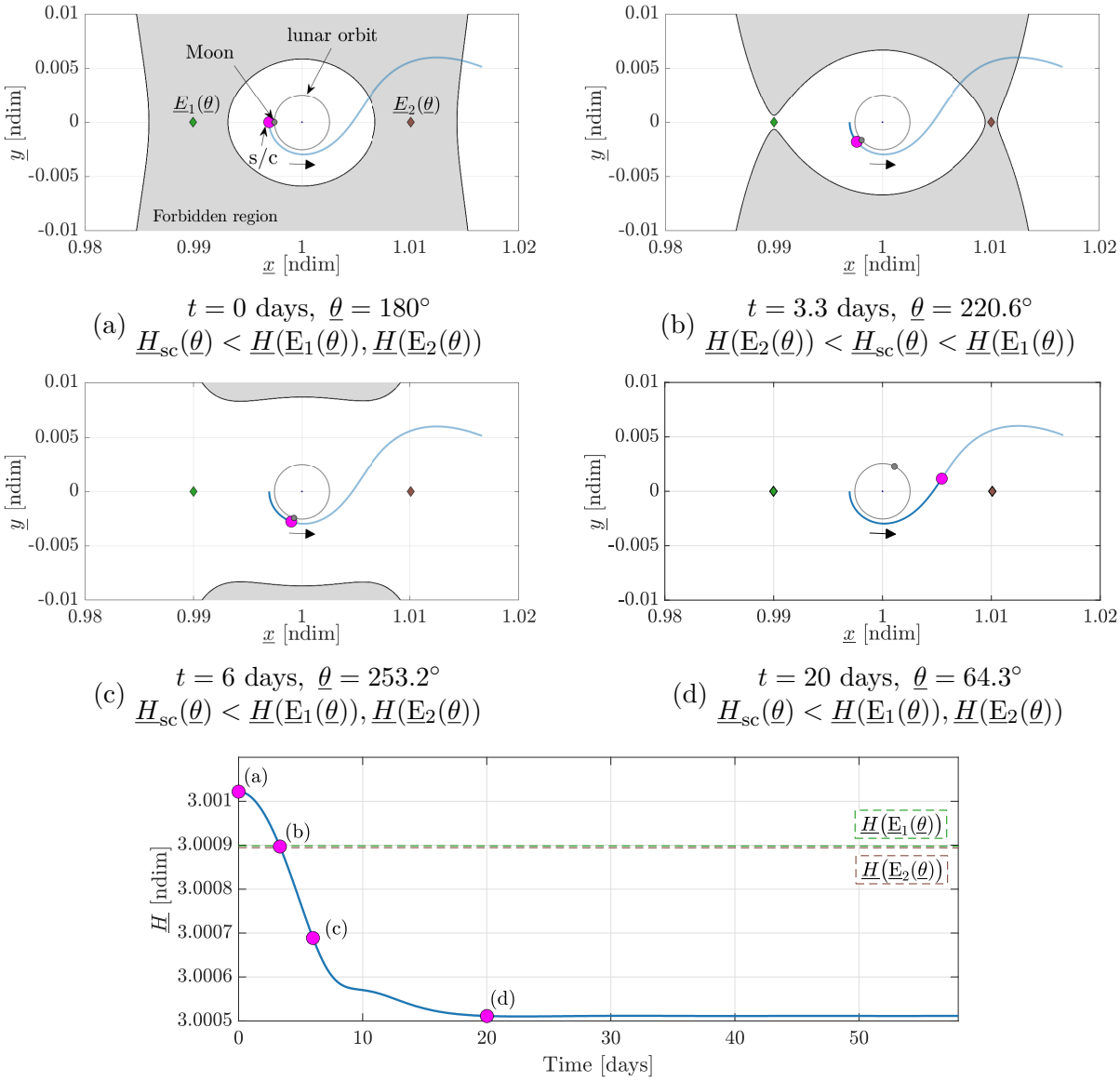


**Figure 4.15.** Instantaneous ZVCs over a planar BCR4BP trajectory as viewed in the Sun-$B_1$ rotating frame (a)-(d). Sun-$B_1$ energy-like value along the trajectory (e).

Periodic orbits are an essential component of the mission design process; they are used for departure, arrival, and/or intermediate stages of trajectories. This section focuses on the construction of periodic orbits within the context of the Earth-Moon-Sun BCR4BP.

### 4.3.1 Existence and Stability

Periodic orbits in the CR3BP are solutions that precisely repeat in all six position and velocity states ($x$, $y$, $z$, $\dot{x}$, $\dot{y}$ and $\dot{z}$) over every period. Previous contributions demonstrate that an infinity of periodic orbits exist in the CR3BP [37], [75]. Various numerical approaches to construct CR3BP periodic solutions include linearizing the equations of motion in the vicinity of the equilibrium points and then leveraging the symmetry properties in the system with the mirror theorem [53] and a targeting scheme.

The BCR4BP is formulated to represent a time-dependent, periodic system. Therefore, only isolated periodic orbits with specific periods exist rather than families with continuously varying periods [76]. While periodic solutions in the CR3BP only require periodicity in 6 states, periodic solutions in the BCR4BP require an additional condition, i.e., the epoch parameter, the Sun angle $\theta$ or the Moon angle $\underline{\theta}$ must also be commensurate with the periodic cycle over which the states repeat [20]. Thus, the period for any periodic orbit in the BCR4BP is a multiple of the Earth-Moon-Sun period, that is, approximately 29.5 days. As a consequence, all periodic solutions in the BCR4BP are isolated synodic resonant orbits.

Initial guess generation for periodic solutions in the BCR4BP is achieved by leveraging the synodic resonant orbits in the CR3BP. Across a family of orbits, the ratio of the orbital period to the synodic period, that is, $\mathbb{P}_{\text{orbital}}/\mathbb{P}_{\text{synodic}}$ is computed. Synodic resonant orbits are characterized by a rational quotient, denoted the resonance ratio. This ratio is represented as $P$:$Q$, where $P$ is the number of orbital periods and $Q$ is equal to the number of lunar synodic periods. Plotting the ratio across a family against another parameter, such as the perilune radius, uncovers the resonant family members. Sample resonance plots for the $L_1$ and the $L_2$ Earth-Moon CR3BP Lyapunov families of periodic orbits appear in Figure 4.16(a). Horizontal dashed lines indicate resonance ratios; intersections between these lines and the curve associated with the family of periodic orbits denote the existence of synodic resonant orbits. The synodic resonant 1:1 Lyapunov orbits, i.e., the Lyapunov orbits with orbital orbit precisely equal to the synodic period are highlighted by the circles in Figure 4.16(a). The corresponding orbits are plotted in thick lines along the representative members of the Lyapunov families of orbits in the Earth-Moon in Figure 4.16(b).

The BCR4BP is equivalently defined in both the Earth-Moon frame and the Sun-$B_1$ rotating frame. The equations of motion in the Earth-Moon rotating frame, in Equation (2.4), and in the Sun-$B_1$ rotating frame, in Equation (2.8) both describe a time-dependent, periodic system. Therefore, a periodic solution generated in one formulation is periodic in the alternative formulation. As an illustration, resonant Lyapunov orbits in the BCR4BP are explored. The Lyapunov orbits are families of periodic orbits in the CR3BP that evolve from investigation of the linear variational motion in the vicinity of the collinear equilibrium points [6]. Representative members from the Earth-Moon CR3BP $L_1$ and $L_2$ Lyapunov families are plotted in Figure 4.16(b). Recall that periodic orbits in the BCR4BP are in resonance with the lunar synodic period, that is, 29.5 days. Thus, the ratio of the synodic to orbital period across the Earth-Moon $L_1$ and $L_2$ Lyapunov families appears in Figure 4.16(a) to facilitate the identification of synodic resonant orbits. Dashed lines in Figure 4.16(a) highlight sample resonance ratios. For this example, the 1:1 synodic resonant $L_1$ and $L_2$ Lyapunov orbits are selected; they are identified by thick lines in Figure 4.16(b). These orbits possess an orbital period precisely equal to the synodic orbital period. Both orbits are transitioned from the Earth-Moon CR3BP to the Earth-Moon BCR4BP. The resulting orbits in the BCR4BP, plotted as viewed in the Earth-Moon rotating frame, appear in Figure 4.17(a), with the

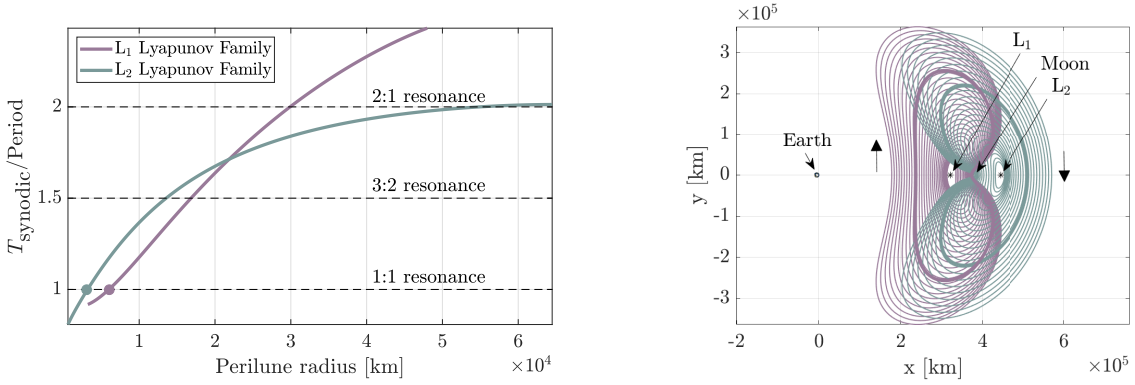


(a) (b)

**Figure 4.16.** Subset of the CR3BP Earth-Moon $L_1$ and $L_2$ Lyapunov families (a). Synodic resonance plot across the two families (b). The 1:1 resonant member of each family is denoted by thicker lines in (a) and by colored circles in (b).

initial guesses, that is, the periodic orbits in the CR3BP, denoted by dashed lines. The solar gravitational attraction tends to shift the $L_1$ and $L_2$ 1:1 synodic resonant Lyapunov orbits towards the libration points. The initial conditions for the periodic orbits in the Earth-Moon rotating frame are then rotated to the Sun-$B_1$ rotating frame, and the equations of the motion for the BCR4BP in this frame, Equation (2.8), are numerically propagated. The $L_1$ and $L_2$ 1:1 synodic resonant Lyapunov orbits as observed in the Sun-$B_1$ rotating frame are plotted in Figure 4.17(b), with the Earth and the Moon orbits indicated for reference. Although the orbits appear to intersect the lunar orbit multiple times, the phasing with the Moon is also significant. A single lunar flyby occurs along each periodic solution on the far-right side of the Earth orbit in Figure 4.17(b). Since both formulations of the BCR4BP in the Earth-Moon-Sun system share the same period, that is, the synodic period, periodic solutions remain periodic when rotated from one frame to the other.

Lagrange points from the Earth-Moon CR3BP are also employed as initial guesses for constructing periodic orbits in the BCR4BP. In the CR3BP, the Lagrange points are fixed points. Thus, the equilibrium points may also be considered periodic with an arbitrary period. Gómez [20] employed this method with an orbital period set to the synodic period to compute the BCR4BP periodic orbits corresponding to the triangular equilibrium points of

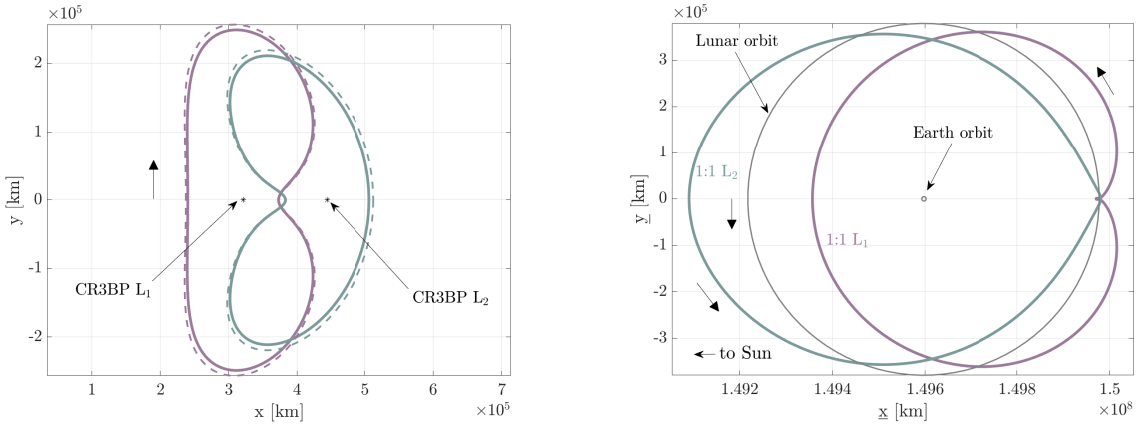


**Figure 4.17.** 1:1 $L_1$ and $L_2$ Lyapunov orbits in the BCR4BP (solid) and in the CR3BP (dashed), as seen in the Earth-Moon rotating frame (a). 1:1 $L_1$ and $L_2$ Lyapunov orbits in the BCR4BP, as observed in the Sun-$B_1$ rotating frame. The Moon and Earth orbits are indicated for reference.

the Earth-Moon CR3BP. The relationship between the dynamical structures of the BCR4BP and Earth-Moon and Sun-$B_1$ CR3BP are presented in Figure 4.18. The Lagrange points are transitioned to the Zero Acceleration Contours, as demonstrated in Section 4.1, or to periodic orbits, as detailed in Section 4.3.2. Periodic orbits in the BCR4BP are constructed from the synodic resonant periodic orbits or the Lagrange points of the Earth-Moon CR3BP.

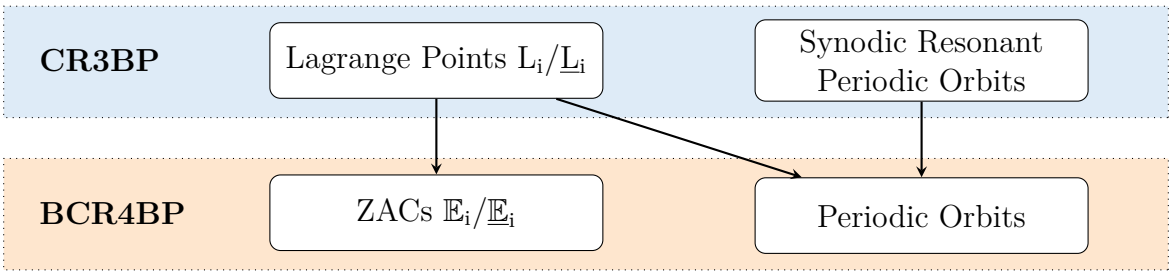


**Figure 4.18.** Relationship between the dynamical structures of the CR3BP and the BCR4BP

To evaluate the stability of a periodic solution, the state transition matrix, $\mathbf{\Phi}(t, t_0)$, is evaluated stroboscopically, after the precise period of the orbit. For a solution of period $\mathbb{P}$, the state-transition matrix after one revolution, $\mathbf{\Phi}(t_0 + \mathbb{P}, t_0)$, is labeled the *monodromy matrix*. The requirement for the stability of the solution is summarized as follows[77]: *A periodic solution is stable in the linear sense if and only if all the eigenvalues of the monodromy matrix have a magnitude smaller or equal to one.* From Lyapunov's theorem [78], if $\lambda_i$ is an eigenvalue of the monodromy matrix $\mathbf{\Phi}(t_0 + \mathbb{P}, t_0)$, then $\lambda_i^{-1}$ is also an eigenvalue. Thus, the real eigenvalues occur in reciprocal pairs, and the complex and purely imaginary occur in conjugate pairs. The stability requirement is rephrased as: *A periodic solution is stable in the linear sense if and only if all the eigenvalues of the monodromy matrix lie on the unit circle in the complex plane.* The stability of a periodic orbit is, thus, determined by the location of the eigenvalues of the monodromy matrix, $\mathbf{\Phi}(t_0 + \mathbb{P}, t_0)$ in the complex plane.

Rather than examining the eigenvalues, the Lyapunov exponents associated with the monodromy matrix are employed to assess the stability of a periodic solution. Note that metrics are available to determine stability, such as the stability index [79] or the Broucke stability diagram [76], [80]. The Lyapunov exponent is a convenient metric to assess the stability of a periodic solution and is directly obtained through the state-transition matrix

elements along the solution. The Lyapunov exponent is labeled $\phi_{\mathrm{i}}$, and is defined as the real part of the Floquet exponent, that is,

$$\phi_{\mathrm{i}} = \mathrm{Re}\left(\frac{\ln \lambda_{\mathrm{i}}}{\mathbb{P}}\right) \tag{4.12}$$

where $\mathbb{P}$ is the period of the orbit and $\lambda_{\mathrm{i}}$ is the i-th eigenvalue of the monodromy matrix associated with the periodic solution. Thus, the stability characteristics, i.e., the eigenvalues, are scaled by the orbital period for the Lyapunov exponents. The phase space in the CR3BP is six-dimensional, thus, the monodromy matrix corresponding to a periodic solution admits six eigenvalues, labeled $\lambda_1$ through $\lambda_6$. Recall, from the Lyapunov theorem [78], that eigenvalues occur in reciprocal pairs if they are real or in conjugate pairs if they are complex. A periodic solution in the CR3BP possesses a pair of eigenvalues equal to one due to the Jacobi constant and the time-autonomous nature of the CR3BP [6], [81]. These unit eigenvalues correspond to an absence of divergence if a perturbation is introduced along the direction of the periodic orbit. Thus, two of the Lyapunov exponents are equal to zero. They correspond to the absence of expansion (quantified by positive Lyapunov exponents), or contraction (quantified by negative Lyapunov exponents) when a perturbation is introduced along the direction of the trajectory. The sign of the remaining Lyapunov indices determines the stability (in the linear sense) of the periodic solution. The necessary condition for linear stability of a periodic orbit is that all the Lyapunov exponents must be equal to zero [6]. Similar to the equilibrium points, the three pairs of eigenvalues of the monodromy determine the three linear *modes* in the CR3BP and the BCR4BP. The modes are identified by the relationship between the eigenvalues of the monodromy matrix and the unit circle in the complex plane [73]. The modes are characterized as follows:

- If a pair of eigenvalues is real and not on the unit circle, i.e., $\mathrm{Im}\,\lambda_{\mathrm{i}} = 0$ and $\|\lambda_{\mathrm{i}}\| \neq 1$, the associated mode is a hyperbolic, or saddle, mode. In the linearized model, perturbations along the unstable subspace ($\|\lambda_{\mathrm{i}}\| > 1$) and the stable subspace ($\|\lambda_{\mathrm{i}}\| < 1$) grow exponentially in positive and negative time, respectively.

- If a pair of eigenvalues is on the unit circle ($\|\lambda_i\| = 1$) oscillatory motion exists in the vicinity of the periodic orbit and the associated mode is a center mode.

- If a pair of eigenvalues is not on the unit axis or the real axis $\mathrm{Re}\,\lambda_i \neq 0,\ \|\lambda_i\| \neq 1$, a mixed mode is associated with the periodic orbit. This mode involves both the oscillatory and the exponentially growing motions in the vicinity of the periodic orbit, in the linearized model.

Following Cox's naming convention [69], each periodic orbit is described by a string $S^{n_s} \times C^{n_c} \times M^{n_m}$, where $S$, $C$, and $M$ denote a saddle mode, a center mode, and a mixed mode, respectively. The superscripts $n_s$, $n_c$, and $n_m$ denote the dimensions of the subspaces associated with each mode. The sum of the dimensions is equal to the dimensions of the phase space, which is 6 for both the CR3BP and the BCR4BP. For instance, $S^2 \times C^4$ denotes an unstable periodic orbit with a two-dimensional saddle mode and a four-dimensional center mode. In addition to the binary stable/unstable property, a periodic orbit is described by its associated modes.

### 4.3.2 Earth-Moon Lagrange Orbits

The Earth-Moon Lagrange orbits are the dynamical counterparts in the BCR4BP of the Earth-Moon Lagrange points. While the $E_i$ instantaneous equilibrium points offer insight in the allowable motion through their relationship with the ZVCs, the dynamical evolution of the CR3BP libration points as the gravitational influence of the Sun is introduced is described by the Lagrange orbits. Lagrange orbits associated with $L_1$, $L_3$, and $L_4/L_5$as constructed in the BCR4BP are explored. The non-existence of the $L_2$ Lagrange orbit in the Earth-Moon-Sun BCR4BP is discussed.

#### $L_1$, $L_3$, and $L_4/L_5$ Orbits

Lagrange orbits associated with $L_1$, $L_3$, and $L_4/L_5$ exist within the context of the BCR4BP. Recall that these synodic resonant periodic orbits are constructed using the CR3BP libration points as the initial guess of the natural parameter continuation scheme in Sun mass

described in Section 3.4.1. The results of the continuation schemes for $L_1$, $L_3$, $L_4$, and $L_5$ are plotted in Figures 4.19(a), 4.20(a), 4.21(a) and 4.21(c), respectively. Each curve is a periodic orbit represented in the Earth-Moon rotating frame. The curves are colored as a function the nondimensional Sun mass parameter, $\epsilon$ which scales in the nondimensional mass of the Sun in Equation (3.44). Thus, each periodic orbit in the continuation scheme is a periodic in a BCR4BP with an artificial Sun mass that is generally not equal to the Sun mass employed in the Earth-Moon-Sun BCR4BP; these periodic orbits are used as steps along the continuation process between $\epsilon = 0$, i.e., the Earth-Moon CR3BP and $\epsilon = 1$, that is, the Earth-Moon-Sun BCR4BP. Recall that the property of symmetry with respect to the $\hat{y}$ axis is maintained in the BCR4BP. Thus, the $L_4$ and $L_5$ sets of orbits in Figures 4.21(a) and 4.21(c) are geometrically mirror of each other. As intuitively expected, the size of the periodic orbit increases as more Sun mass is introduced. While there appears to be a linear relationship between the size of the periodic orbit and the Sun mass for $L_1$ and $L_3$ in Figures 4.19(a) and 4.20(a), respectively, such is not the case for the continuation of the $L_4$ and $L_5$ libration points. As apparent from the insets in Figures 4.21(a) and 4.21(d), the periodic orbits remain relatively close to the Lagrange point for $\epsilon$ comprised between and 0 and 0.8. However, the size of the orbits grows significantly for $\epsilon$ between 0.8 and 1 as evidenced by the dark purple to black curves in Figures 4.21(a) and 4.21(c). A continuation scheme in Sun mass is employed to construct in the BCR4BP the Lagrange orbits corresponding the Earth-Moon $L_1$, $L_3$, and $L_4/L_5$ libration points.

Lagrange orbits associated with the Earth-Moon $L_1$, $L_3$, and $L_4/L_5$ libration points are obtained for $\epsilon = 1$. The resulting orbits are colored in blue in the Earth-Moon rotating frame in Figures 4.19(b), 4.20(b), 4.21(b) and 4.21(d). The orbital periods of these orbits are precisely equal to one synodic period. For reference, the CR3BP Lagrange points are indicated by the gray asterisks and the BCR4BP ZACs are denoted by the black contours. Note the different configurations between the Lagrange orbit and the ZACs. For instance, the $\mathbb{E}_1$ ZAC is enclosed within the $L_1$ periodic orbit in Figure 4.19(b). Conversely, the BCR4BP periodic orbit associated with $L_3$ has a much smaller size than the $\mathbb{E}_3$ ZAC plotted in Figure 4.5(a); a subset of the ZAC in the vicinity of the periodic orbit is included in Figure 4.20(b). The $L_4/L_5$ Lagrange orbits in Figures 4.21(b) and 4.21(d) have comparable

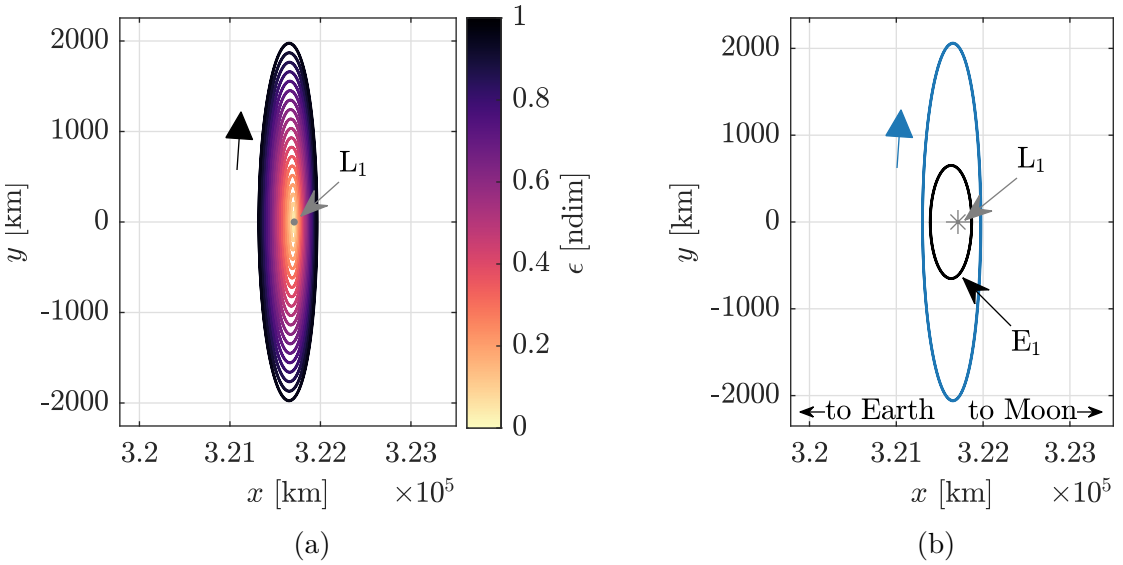


**Figure 4.19.** Continuation in Sun mass parameter $\epsilon$ of the Earth-Moon $L_1$ Lagrange point (a). Lagrange orbit associated with $L_1$, in blue, and $E_1$ instantaneous equilibrium solutions, in black (b).

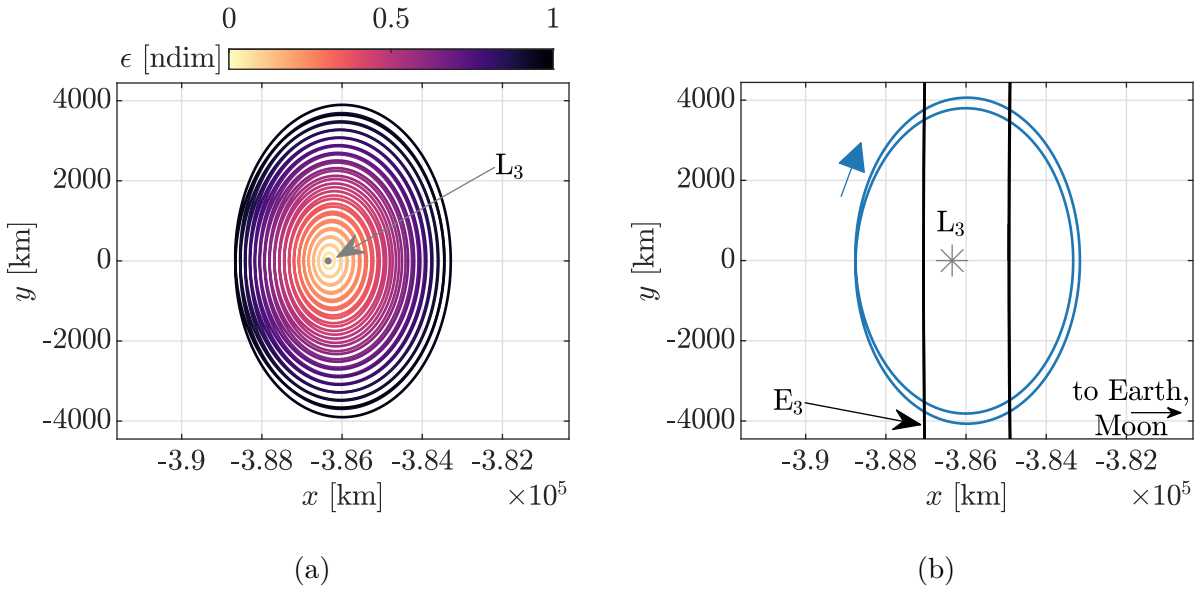


**Figure 4.20.** Continuation in Sun mass parameter $\epsilon$ of the Earth-Moon $L_2$ Lagrange point (a). Lagrange orbit associated with $L_2$, in blue, and $E_1$ instantaneous equilibrium solutions, in black (b).

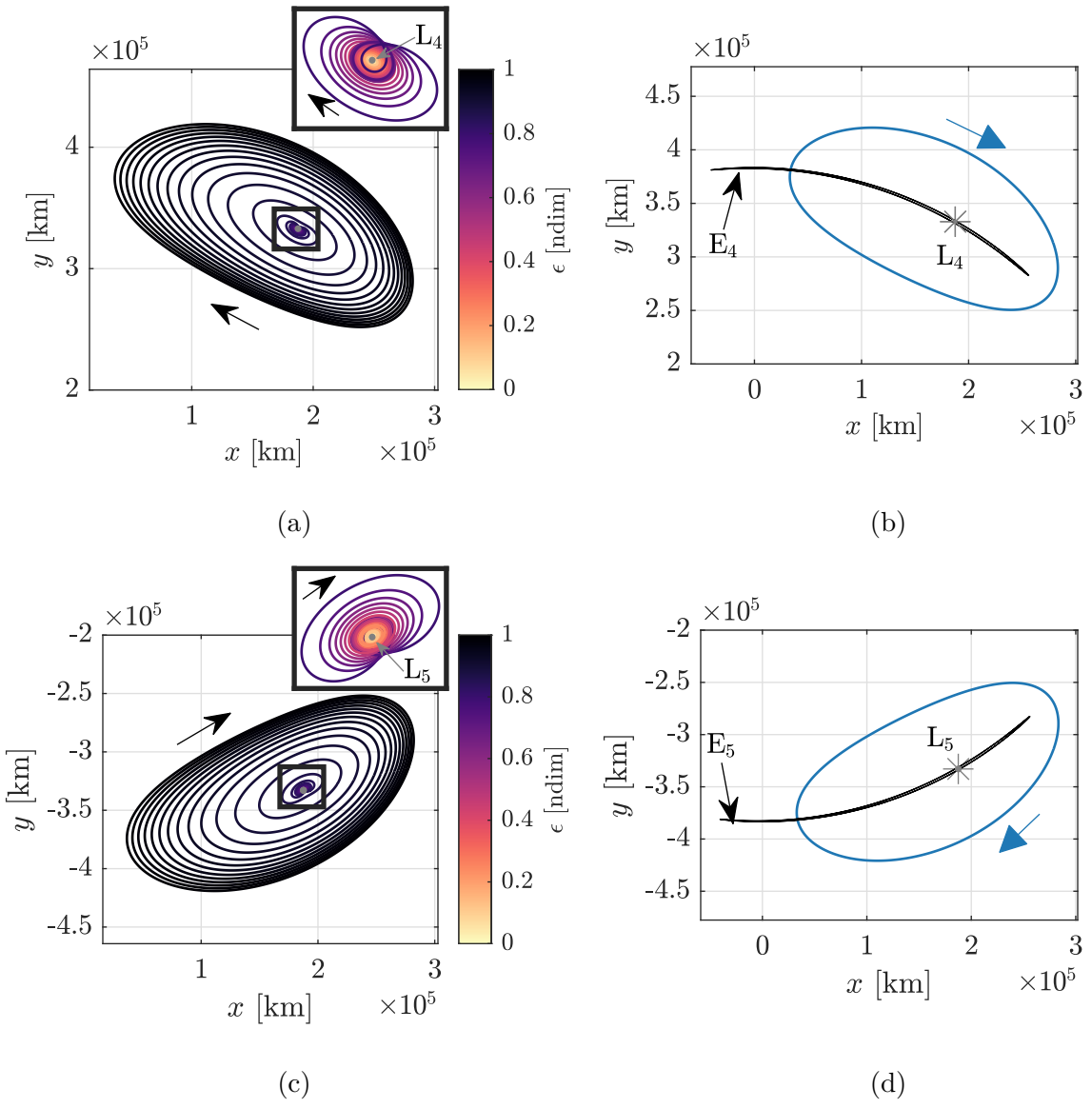


**Figure 4.21.** Continuation in Sun mass parameter $\epsilon$ of the Earth-Moon $L_4/L_5$ Lagrange point (a, c). Lagrange orbit associated with $L_4/L_5$, in blue, and $E_4/E_5$ instantaneous equilibrium solutions, in black (b, d).

dimensions with their associated ZACs. Unlike the Zero Acceleration Contours, the Lagrange periodic orbits are trajectories, that is, they satisfy the differential equations of motion in Equation (2.4).

The Lagrange periodic orbits instantaneously have a higher energy, or equivalently, a lower $H$ value, than the instantaneous equilibrium solution. For instance, consider the $L_1$ La-

grange periodic orbit and the $\mathbb{E}_1$ zero acceleration contours in Figure 4.22. In Figures 4.22(a)

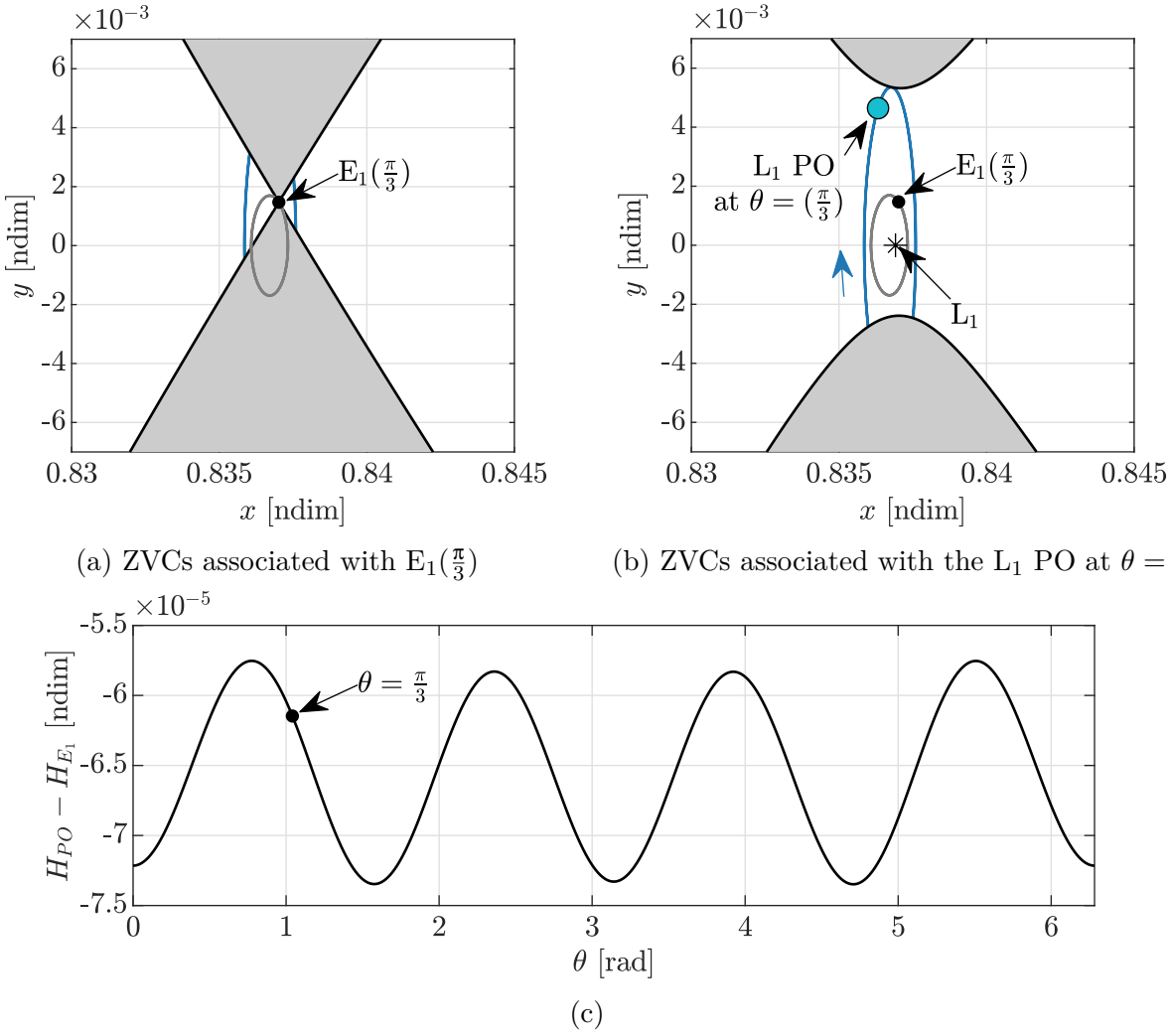


(a) ZVCs associated with $\mathrm{E}_1(\frac{\pi}{3})$

(b) ZVCs associated with the $\mathrm{L}_1$ PO at $\theta = \frac{\pi}{3}$

(c)

**Figure 4.22.** Forbidden regions (gray surfaces) bounded by the ZVCs (in black) for energy levels associated with the $\mathrm{L}_1$ periodic orbit (in blue) and the $\mathbb{E}_1$ (in gray) at $\theta = \frac{\pi}{3}$ (a,b). Difference in associated energy-like quantity $H$ between the Lagrange periodic orbit and the $\mathbb{E}_1$ ZAC.

and 4.22(b), the periodic orbit and the ZAC are plotted in blue and gray, respectively. Cyan and black dots denote the points corresponding to the $\theta = \frac{\pi}{3}$ epoch along each structure. The ZACs are evaluated for each of this point; the ZACs corresponding the instantaneous equilibrium point $\mathrm{E}_1(\frac{\pi}{3})$ are plotted in Figure 4.22(a) while the ZACs corresponding the state along the periodic orbit at the same epoch are plotted in Figure 4.22(b). As apparent in Figure 4.22(a), and consistently with the discussion in Section 4.2, the ZVCs associated with

the instantaneous equilibrium points act boundaries between various region of space. For an energy-like value consistent with the $\mathbb{E}_1$, the ZVCs between the Earth and the Moon regions are always closed and the point where the upper and lower parts of the ZACs meet traces the Zero Acceleration Contour, plotted in gray in Figure 4.22(a) (note that ZACs cannot violate the forbidden regions, as they are not solutions of the equations of motion). Now, consider the ZVCs associated with the Lagrange periodic orbit for $\theta = \frac{\pi}{3}$, plotted as the cyan marker in Figure 4.22(b). The associated $H$ value is lower or, equivalently, the energy along the orbit is higher than the one associated with the instantaneous equilibrium point. Thus, motion between the Earth and lunar region is possible. Note that the periodic orbit does not violate the forbidden regions, although the blue curve seems to be inside the gray region for negative $y$ values in Figure 4.22(b). Recall that the instantaneous ZVCs pulsate, or oscillate, as a function of epoch; as the cyan dot moves along the periodic orbit, the ZVCs recede. Another evidence of that the periodic orbit does not violate the forbidden region is available by the examining the energy-like quantity along the periodic orbit and the ZACs. The difference between the two energy-like quantities is plotted as a function of epoch in Figure 4.22(c); the $\theta = \frac{\pi}{3}$ epoch is denoted by a black dot. The difference is negative for all Sun angle values, i.e., the energy along the periodic orbit is always higher than the energy associated with the instantaneous equilibrium solutions. The Lagrange periodic orbits constructed in the BCR4BP do not violate the instantaneous Zero Velocity Curves.

The linear stability properties associated with the Lagrange point orbits are examined. Recall that the stability properties of periodic orbits by the relative position of the eigenvalues of the monodromy matrix with respect to the unit circle in the complex plane. The stability properties associated with the periodic orbits from Figures 4.19(a), 4.20(a), 4.21(a) and 4.21(c) are plotted in Figure 4.23. The horizontal axes represent the maximum distance from the Lagrange point along the periodic orbit (note the different scales for each plot); the vertical axis represent the nondimensional mass continuation parameter $\epsilon$ employed to construct each periodic orbit. The curves are colored as a function of the modes associated with the periodic orbits. For the $L_1$ and $L_3$ periodic orbits in Figures 4.23(a) and 4.23(b), the $S^2 \times C^4$ characteristics of the CR3BP Lagrange points are preserved along the continuation scheme. Similarly, the six-dimensional center associated with the $L_4/L_5$ Lagrange points is

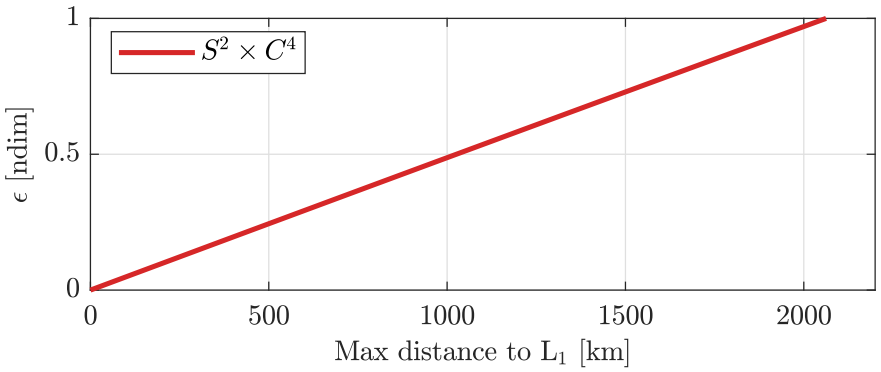


(a) $L_1$ periodic orbit from Figure 4.19(a)

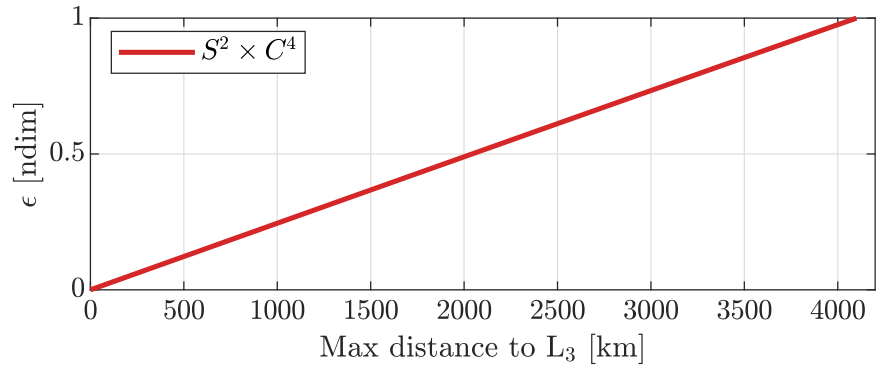


(b) $L_3$ periodic orbits from Figure 4.20(a)

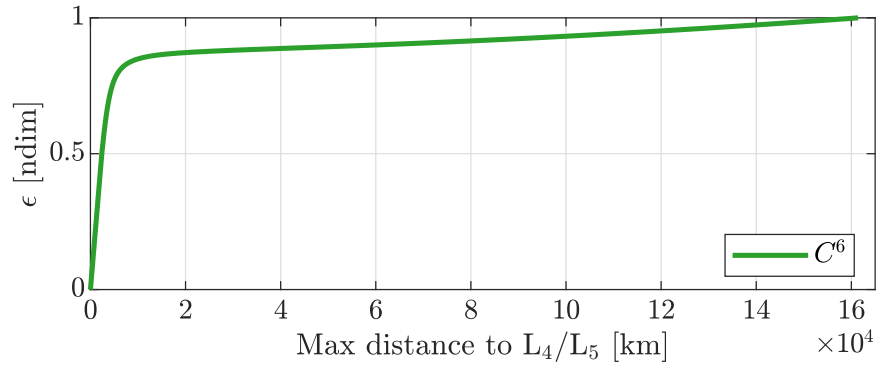


(c) $L_4/L_5$ periodic orbits from Figures 4.21(a) and 4.21(c)

**Figure 4.23.** Stability characteristics associated with the periodic orbits along the continuation in Sun mass parameter of the Earth-Moon $L_1$, $L_3$, and $L_4/L_5$ Lagrange points. Red points denote periodic orbits with $S^2 \times C^4$ modes, while green points correspond to periodic orbits with $C^6$ modes. Note the different scales for the horizontal axes.

maintained along the continuation from the CR3BP to the BCR4BP. However, while the relationship between the maximum distance between the periodic orbit and the Lagrange point is linear in Figures 4.23(a) and 4.23(b), such is not the case for the $L_3$ Lagrange orbit. From Figure 4.23(c), the maximum distance between the periodic orbits and the libration point increases at a fast rate for the mass parameter continuation $\epsilon$ between 0.8 and 1, which consistent with Figure 4.21(a). Additionally, bifurcations with no stability change occur along the continuation of the $L_4/L_5$ Lagrange points; see Gómez [20] for an analysis of the bifurcations associated with $L_4/L_5$ along the continuation in Sun mass. The $L_1$, $L_3$ and $L_4/L_5$ Lagrange periodic orbits in the BCR4BP possess the same stability characteristics as their respective underlying libration points.

### The $L_2$ Case

A Lagrange periodic orbit corresponding to the $L_2$ libration point does not exist in the Earth-Moon-Sun BCR4BP. Jorba-Cuscó et al. [17] demonstrate that a turning point occurs along the continuation in Sun mass of the $L_2$ point between the CR3BP and BCR4BP; an extension of this result is presented in this section. Consider the family of periodic solutions plotted in Figure 4.24(a). The horizontal and vertical axes represent the maximum distance from $L_2$ along the periodic orbit and the continuation parameter $\epsilon$, respectively. Each point along the curve is colored as a function of the linear stability properties; periodic orbits with two-dimensional saddle and four-dimensional center modes are colored in red while periodic solution with four-dimensional saddle and two-dimensional center are plotted in blue. It is apparent from Figure 4.24(a) that the evolution of the family is not monotonic; the Sun mass continuation parameter first decreases then increases. Thus, the natural parameter for the continuation scheme is updated to be the $x$ component of a $\hat{y}$-axis crossing along the periodic orbit [2]. Employing this natural parameter continuation scheme, the family first evolves in the direction of negative $\epsilon$ values. Recall this parameter scales the mass of the Sun in the pseudo-potential in Equation (3.44); while not possessing any physical meaning, a negative Sun mass yields a mathematically correct pseudo-potential function. A

[2]↑Alternatively, a pseudo-arclength continuation scheme may be employed.

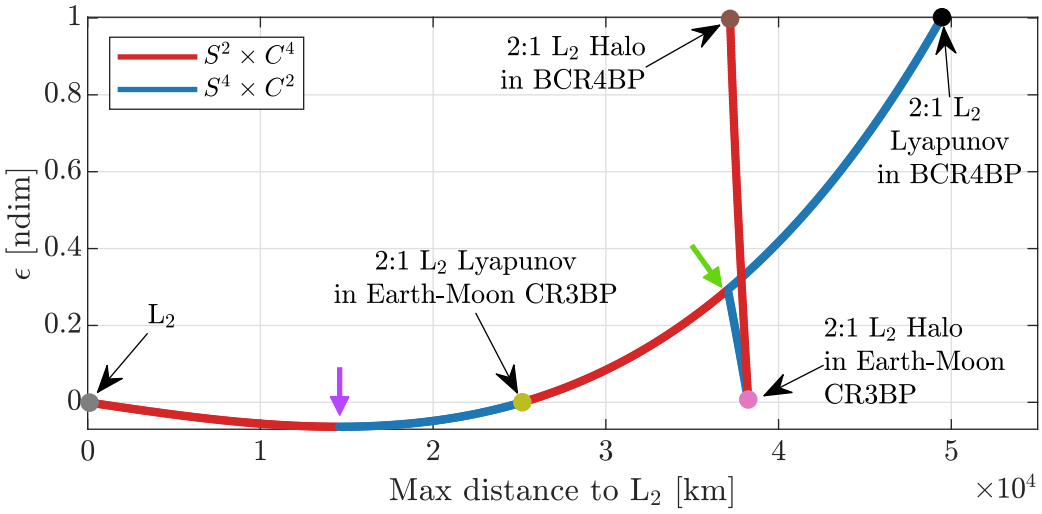


(a) Stability characteristics

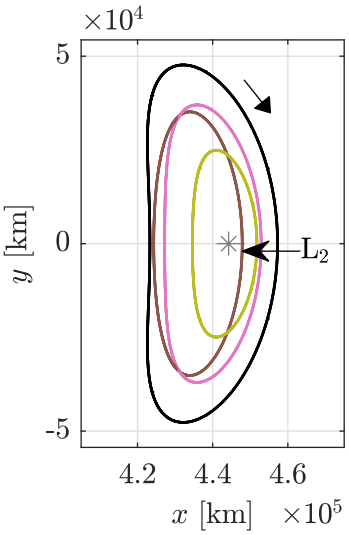


(b) $x - y$ view

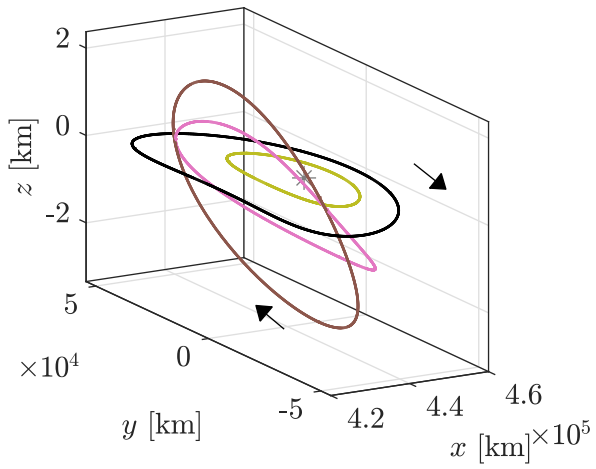


(c) Isometric view

**Figure 4.24.** Stability characteristics associated with the periodic orbits along the continuation in Sun mass parameter of the Earth-Moon $L_2$ Lagrange points (a). Selected periodic orbits as viewed in the Earth-Moon rotating frame (b, c).

minimum in Sun mass is then reached for $\epsilon \approx -0.06$. The $\mu$ reaches the 0 value again, at the location identified by an olive marker in Figure 4.24(a). The corresponding solution is the 2:1 synodic resonant $L_2$ Lyapunov orbit as computed in the Earth-Moon CR3BP. This orbit is then continued to $\epsilon = 1$, i.e., to the 2:1 $L_2$ Lyapunov orbit as computed in the BCR4BP, denoted by the black marker in Figure 4.24(a). Note that this orbit is not the dynamical

counterpart in the BCR4BP of the Earth-Moon $L_2$ Lagrange point. The 2:1 Lyapunov orbits computed in the CR3BP and BCR4BP are plotted as viewed in the Earth-Moon rotating frame in Figures 4.24(b) and 4.24(c). Due to a turning point along the continuation process, a Lagrange orbit corresponding to the $L_2$ Lagrange point is not obtained in the Earth-Moon CR3BP.

The changes in stability along the continuation in Sun mass of the $L_2$ Lagrange point are explored. Recall that each point in Figure 4.24(a) is colored as a function of the linear modes associated with the periodic orbit. Red points correspond to periodic with a two-dimensional hyperbolic manifold and a four-dimensional center; blue points represent periodic solution with a four-dimensional saddle mode and a two-dimensional center. Transitions from blue to red (or vice versa) denote a tangent bifurcation [73], [82] where the *order* of stability changes; both types correspond to unstable orbits but have different dimensions for the hyperbolic manifold. The first bifurcation along the family of periodic solutions in the direction of increasing maximum distance to $L_2$ is indicated by the purple arrow in Figure 4.24(a). This tangent bifurcation, which occurs at the turning point in Sun mass, is a cyclic-fold bifurcation. At cyclic-fold bifurcations, only the order of stability changes and no new periodic solutions emerge. Note that the location is of this cyclic-fold bifurcation is consistent with the evolution of the family as plotted in Figure 4.24(a), as single-parameter families exhibit a cyclic-fold bifurcation at the extremum of the varied parameter [83]. The second bifurcation along the family is a pitchfork bifurcation and is indicated by the green arrow in Figure 4.24(a). Following this bifurcation yields a new family of periodic solution; in one direction, the 2:1 $L_2$ halo orbit as computed in the Earth-Moon CR3BP is obtained . This orbit, denoted by the pink dot in Figure 4.24(a) is also a bifurcating orbit; following this bifurcation leads to the 2:1 $L_2$ halo orbit as computed in the Earth-Moon-Sun BCR4BP, represented by a brown dot. The periodic orbits constructed in the Earth-Moon CR3BP and the Earth-Moon-Sun BCR4BP are presented in Figures 4.24(b) and 4.24(c). The dynamics in the vicinity of the Earth-Moon $L_2$ point as the Sun mass is varied are complex, and a variety of bifurcations are available.

### 4.3.3 Earth-Moon Near Rectilinear Halo Orbits[3]

The proposed Gateway concept is the current framework for the NASA development of a space facility near the Moon with an option to return to the lunar surface [84], [85]. From a baseline trajectory in a Near Rectilinear Halo Orbit (NRHO), the Gateway is intended to serve as a proving ground for deep space technologies and as a staging location for missions beyond low Earth orbit. The NRHOs in the lunar vicinity are members of the $L_1$ or $L_2$ halo orbit families as defined within the context of the Circular Restricted Three-Body Problem (CR3BP), representing the Earth-Moon system. The NRHO subset of the halo family is characterized by favorable stability properties and relatively close approaches to the Moon. The NRHOs are defined as precisely periodic orbits in the CR3BP. However, when considering arrival and departure from the Earth-Moon region, the impact of solar gravity is significant. The Sun and its location in the Earth-Moon frame are also relevant when exploring the orbits for characteristics that translate to the higher-fidelity ephemeris model. The perturbing effects of the Sun on an orbit as it expands out from the lunar vicinity are crucial to any baseline trajectory. Thus, in this investigation, the Sun's gravitational impact is assessed in the Bicircular Restricted Four-Body Problem (BCR4BP) that incorporates solar gravity, reasonably represents the full range of starting epochs, and supports eventual transition to an ephemeris model. To successfully construct trajectories in this regime and offer meaningful analysis, the ability to translate the characteristics to higher-fidelity models is critical. This examination of potential baseline trajectories in the BCR4BP adds insight to the design process.

#### Definition in the CR3BP

The halo family and its subset, the Near Rectilinear Halo Orbits (NRHOs), are comprised of three-dimensional precisely periodic orbits as defined in the CR3BP. The halo family bifurcates from each family of planar Lyapunov orbits associated with the collinear libration points. For the $L_1$ and the $L_2$ equilibrium points in the Earth-Moon system, the halo family

[3]↑This chapter was published in Advances in Space Research, Vol 66, Boudad, Howell, Davis, Dynamics of Synodic Resonant Near Rectilinear Halo orbits in the Bicircular Four-Body Problem, Pages 2194-2214, © COSPAR (2020) [44].

originates in the $x$-$y$ plane from the bifurcation orbit in the Lyapunov family and evolves out of plane as the family of orbits approaches the Moon. Note that the halo family is mirrored across the $x$-$y$ plane: the northern family members possess a positive $z$ component over the majority of their orbit, while the southern family members are defined by a negative $z$ component. Representative southern $L_1$ and $L_2$ halo orbits in the Earth-Moon system appear in Figure 4.25.

Zimovan [38] define bounds on the NRHO subset for the $L_1$ and $L_2$ halo families by their linear stability properties. Recall that the Lyapunov exponents are the (linear) stability metric employed for periodic orbits in this analysis. The Lyapunov exponents along a portion of the $L_1$ and $L_2$ halo families are plotted as functions of the perilune distance in Figure 4.26. Zimovan [38] define the NRHO subset of the $L_1$ halo family as the orbits between the first and fourth stability changes along the family, in the direction of increasing perilune radius,

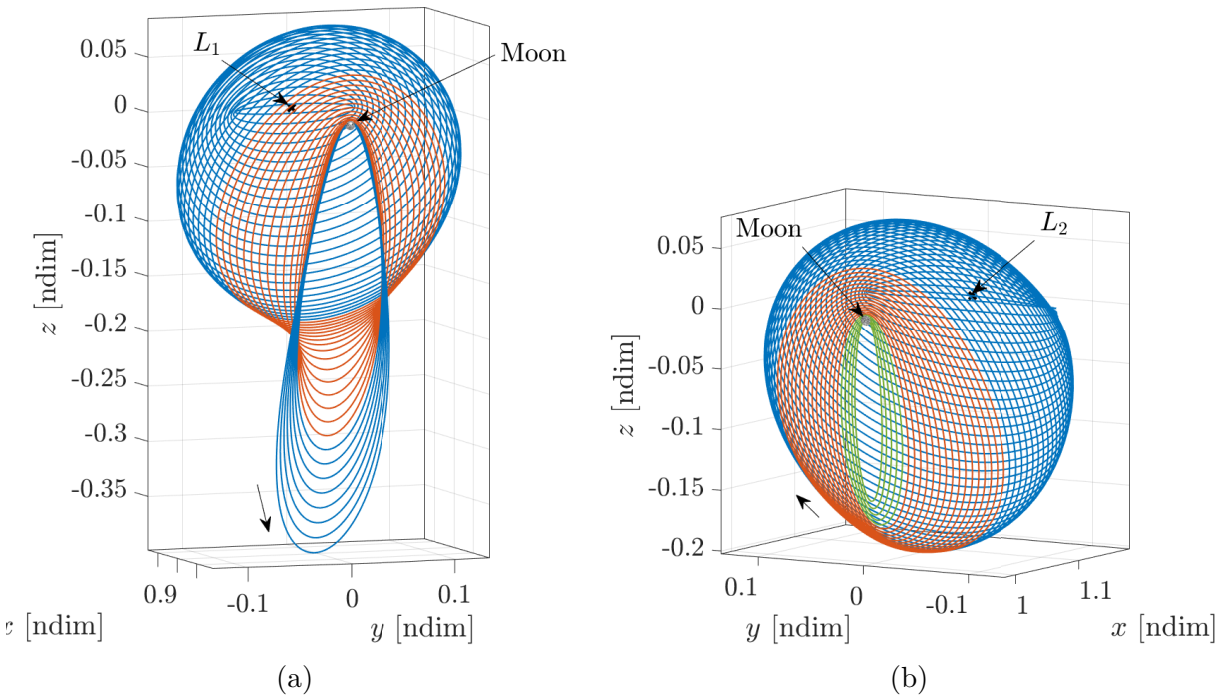


**Figure 4.25.** 3D view of the CR3BP Earth-Moon $L_1$ (a) and $L_2$ (b) halo families. Members of the NRHO subset as defined in this investigation are colored in orange. The NRHO+ subset, which only exists in the $L_2$ halo family, is colored in green.

as presented in Figure 4.26(a). Similarly, the NRHO subset of the $L_2$ halo family is defined as the group of orbits between the first and the third stability change, as plotted in Figure 4.26(b). The orbits on the left of the first stability change along the $L_1$ halo family, in Figure 4.26(a), present a rapidly increasing unstable mode as the perilune radius decreases. However, the orbits on the left of the first stability change along the $L_2$ halo family, colored in green in Figure 4.26(b), are stable (in the linear sense). The geometry associated with these orbits, also colored in green in Figure 4.25(b), is similar to geometry of the NRHOs. Therefore, this subset of stable, rectilinear orbits beyond the bounds of the $L_2$ NRHO region along the $L_2$ halo orbits is labeled the NRHO+ region. This subset only exists in the $L_2$ halo family. Note that the first stability change that serves as the original NRHO boundary occurs in an orbit with perilune above the lunar radius, as apparent in Figure 4.27. Recall that the Earth and the Moon are considered point masses in the CR3BP, thus, the model is unaware of the radius of the primaries. Some members of the NRHO+ subset also possess a perilune above the lunar surface. Members of the NRHO and the NRHO+ subsets of the $L_2$ halo family are considered in this investigation.

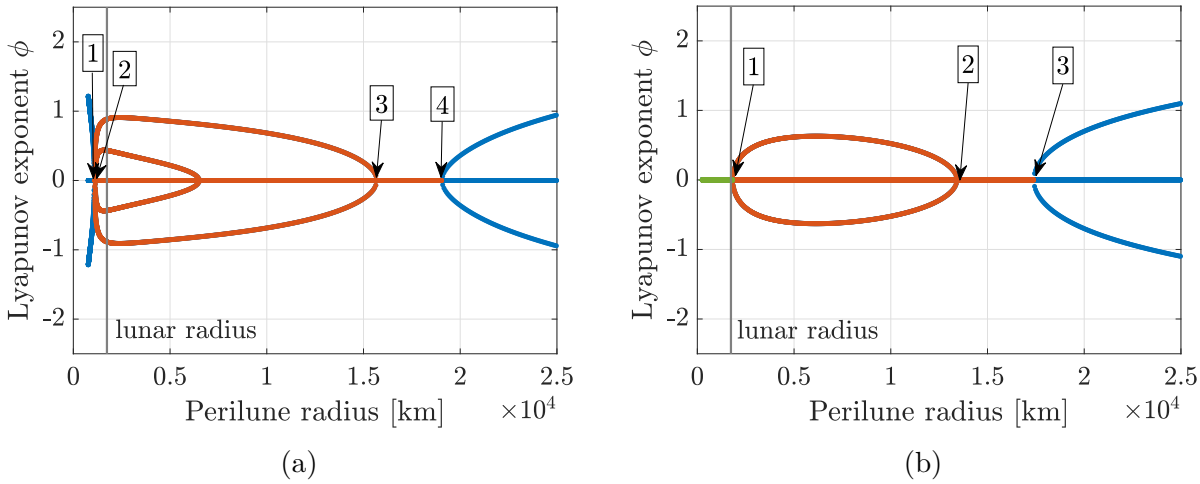


**Figure 4.26.** Lyapunov exponents across a portion of the $L_1$ (a) and $L_2$ (b) halo families. Members of the NRHO subset as defined in this investigation are colored in orange. Stability changes are denoted by arrows and numbered. The NRHO+ subset, which only exists in the $L_2$ halo family, is colored in green.

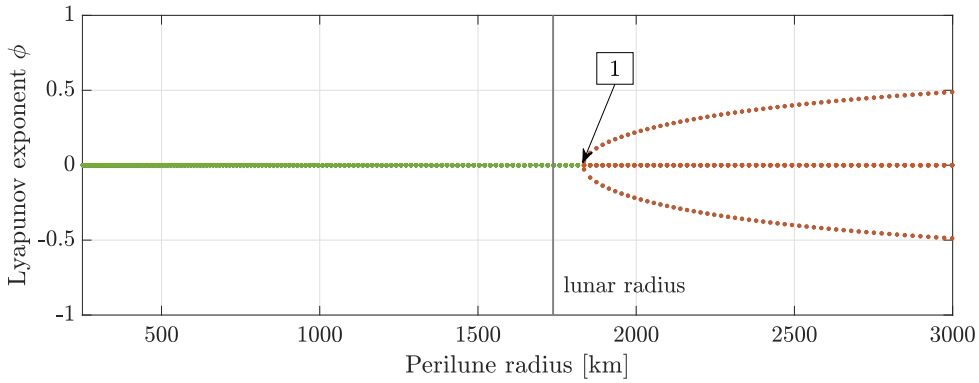


**Figure 4.27.** Close-up of the Lyapunov exponent along the $L_2$ halo family around the first stability change, as a function of the perilune radius.

Synodic resonant NRHOs in the Earth-Moon CR3BP are selected as initial guesses for constructing periodic orbits in the BCR4BP. Sample resonance plots for the $L_1$ and the $L_2$ Earth-Moon CR3BP halo families appear in Figure 4.28. Members of the NRHO subset along the halo family are colored in orange, and members of the NRHO+ subset are colored in green. Note that the evolution of the period is not monotonic for the $L_1$ family, in Figure 4.28(a). Thus, multiple orbits with the same resonance ratio may exist along the $L_1$ family; for instance, there are two 7:2 resonant $L_1$ NRHOs in the CR3BP Earth-Moon system. On the $L_2$ side, the orbital period monotonically decreases along the halo family as the perilune radius decreases, as apparent in Figure 4.28(b). Recall that the resonance ratio is inversely proportional to the orbital period. A larger range of period values exists in the $L_2$ NRHO subset as compared with $L_1$ NRHO subset, thus, more rational-quotient resonant members are observed in the $L_2$ halo family. However, note that the resonant orbits identified in Figures 4.28(a) and 4.28(b) comprise only a sample of the resonant NRHOs. Orbits possessing more complex resonance ratios, for instance, 61:17, are also synodic resonant orbits, although less obviously useful. While there is an infinity of synodic resonant NRHOs, this investigation generally focuses on NRHOs with simple resonant ratios. These synodic resonant NRHOs computed in the CR3BP serve as initial guesses for the generation of periodic NRHOs in the BCR4BP.

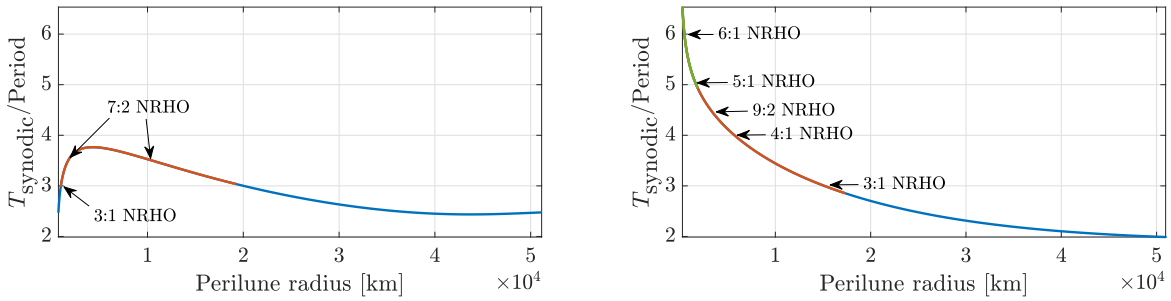


(a) $L_1$ (b) $L_2$

**Figure 4.28.** Synodic resonance across the CR3BP Earth-Moon $L_1$ (a) and $L_2$ (b) halo families. Members of the NRHO subset are colored in orange. NRHO+ orbits (in the $L_2$ halo family) are colored in green.

### Analogs in the BCR4BP

Four synodic resonant NRHOs from the CR3BP are transitioned to the BCR4BP using the updated pseudo-potential function in Equation (3.44) and a natural parameter continuation scheme. The four previous synodic resonant NRHOs and NRHO+ in the CR3BP are plotted together in Figure 4.29(a)[4]. Recall that they are selected for their periods: all four orbits are synodic resonant orbits with simple resonance ratios from the $L_2$ halo family. The four periodic orbits in Figure 4.29(a) are the basis for the construction of the solution in the BCR4BP via the continuation/corrections procedure, and the results appear in Figure 4.29(b). The $N$:1 synodic orbits are continued to $T_{\text{syn}}$-periodic orbits in the BCR4BP, and the 9:2 synodic NRHO is continued to a $2T_{\text{syn}}$-periodic orbit. The geometry and the apse distances to the Moon are maintained during the continuation procedure. The perturbing gravity from the Sun tends to stretch the NRHOs, mostly along the rotating $\hat{x}$ direction.

The selected BCR4BP NRHOs and NRHO+ are also periodic in the Sun-$B_1$ rotating frame, since they are $T_{\text{syn}}$-periodic orbits. The orbits are rotated from the Earth-Moon rotating frame to the Sun-$B_1$ rotating frame and appear in Figure 4.30, colored according to the scheme employed previously in Figure 4.29. The lunar and Earth orbits are represented by gray lines. When viewed in this particular frame, the BCR4BP synodic resonant NRHOs appear to wrap around the lunar orbit. Note that the crossings above the lunar orbit

[4]↑Initial conditions for these orbits are produced in Appendix E.1.

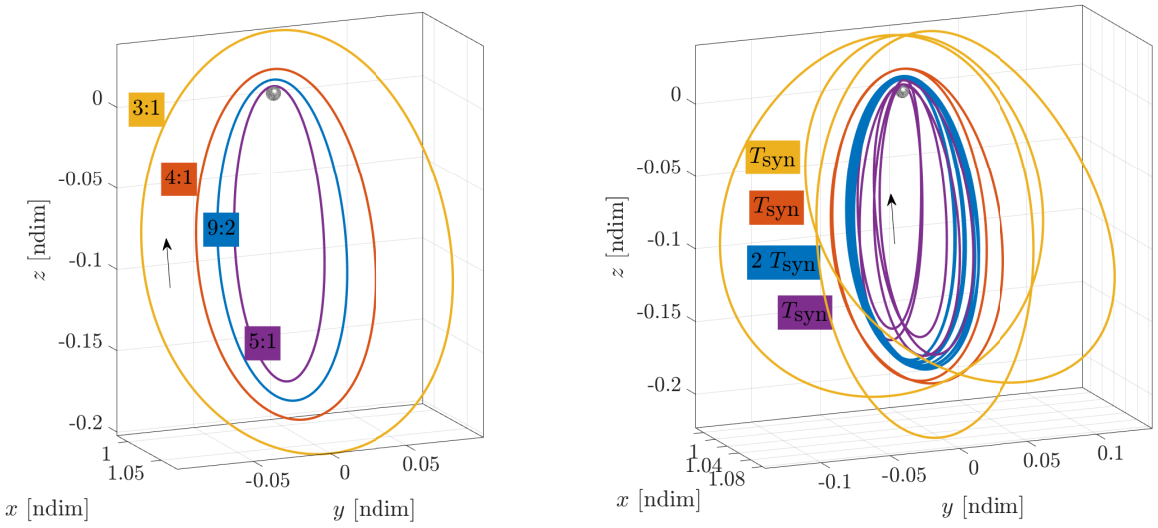


(a) (b)

**Figure 4.29.** Four synodic resonant NRHOs as viewed in the Earth-Moon rotating frame, computed in the Earth-Moon CR3BP (a) and in the Earth-Moon-Sun BCR4BP (b).

plane correspond to the perilunes along the periodic orbits. For instance, the BCR4BP periodic orbit corresponding to the 3:1 synodic, plotted in yellow in Figure 4.30, possesses three crossings above the lunar radius; these crossings correspond to the three perilunes of the BCR4BP periodic orbit, as seen in Figure 4.29(b). For the 2 $T_{\text{syn}}$-periodic orbit depicted in blue, the nine perilunes occur over two revolutions of Moon along its orbit. The BCR4BP NRHOs maintain their periodicity and characteristics when represented in the Sun-$B_1$ rotating frame.

### Eclipse-Avoidance Properties

Synodic resonant orbits may present favorable eclipse-avoidance properties. Recall that the orbital period for synodic resonant orbits is commensurate with the lunar synodic period, that is, the time between two consecutive alignments of the Sun, the Earth, and the Moon. Thus, the geometry of synodic resonant orbits repeats itself for a given Sun-Earth-Moon configuration, and long-term eclipse-avoidance is possible. For instance, consider the 9:2 NRHO. This synodic resonant orbit is a candidate location for the proposed Gateway facility

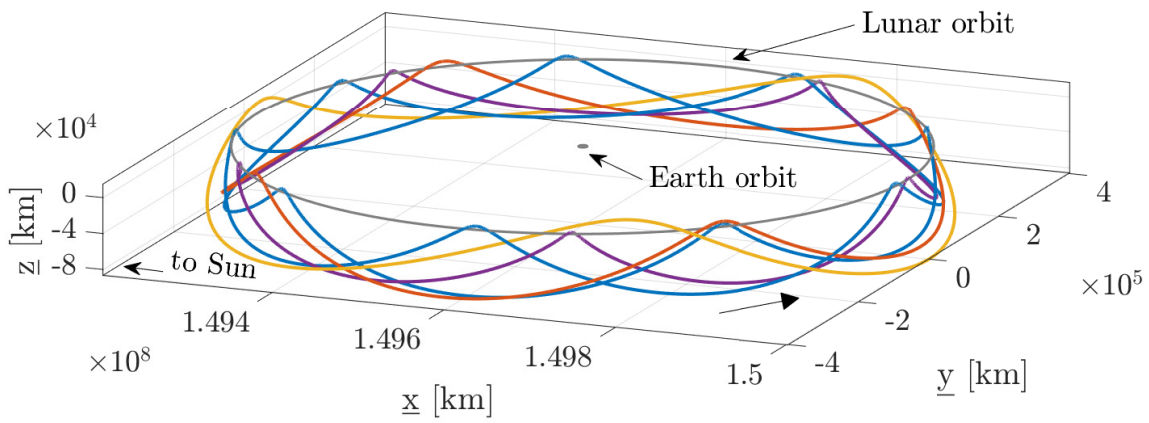


**Figure 4.30.** Four synodic resonant NRHOs as viewed in the Sun-$B_1$ rotating frame.

in cislunar space [38], [41], [86]. A 9:2 synodic resonant orbit computed in the BCR4BP that presents favorable Earth eclipse-avoidance properties is plotted in Figure 4.31(a). Recall that the Sun is seen as moving in the Earth-Moon frame. Thus, Earth eclipses are easier to identify in the Sun-$B_1$ rotating frame since the Sun is fixed and the motion of the Earth is fixed in that frame. The 9:2 NRHO in the BCR4BP is plotted in Figure 4.31(b), with the Earth penumbra cone [87] identified by the black cone. It is apparent that the penumbra cone does not intersect the trajectory in any location, thus, the trajectory is Earth eclipse-free.

Two spacecraft can fly concurrently in this eclipse-free synodic orbit. The synodic resonant 9:2 NRHO as computed in the BCR4BP is periodic over 2 synodic periods of the Moon, that is, two revolutions (4 $\pi$) in Moon angle $\underline{\theta}$ as presented in Figure 2.2. Thus, two spacecraft separated by a phase angle of $2\pi$ in $\underline{\theta}$ are flying in the NRHO simultaneously. To illustrate this concept of phasing along the orbit, consider two spacecraft: A, plotted as a red dot and B, plotted as a blue dot in Figure 4.31. It is apparent in Figure 4.31(c) that the two spacecraft are located at the same Moon angle, approximately equal to 120°. Recall that the BCR4BP is a non-autonomous model where the Sun angle and the Moon angle are linear functions of the independent time variable. While spacecraft A is approaching perilune, spacecraft B is getting closer to apolune, as apparent in Figures 4.31(a) and 4.31(b).

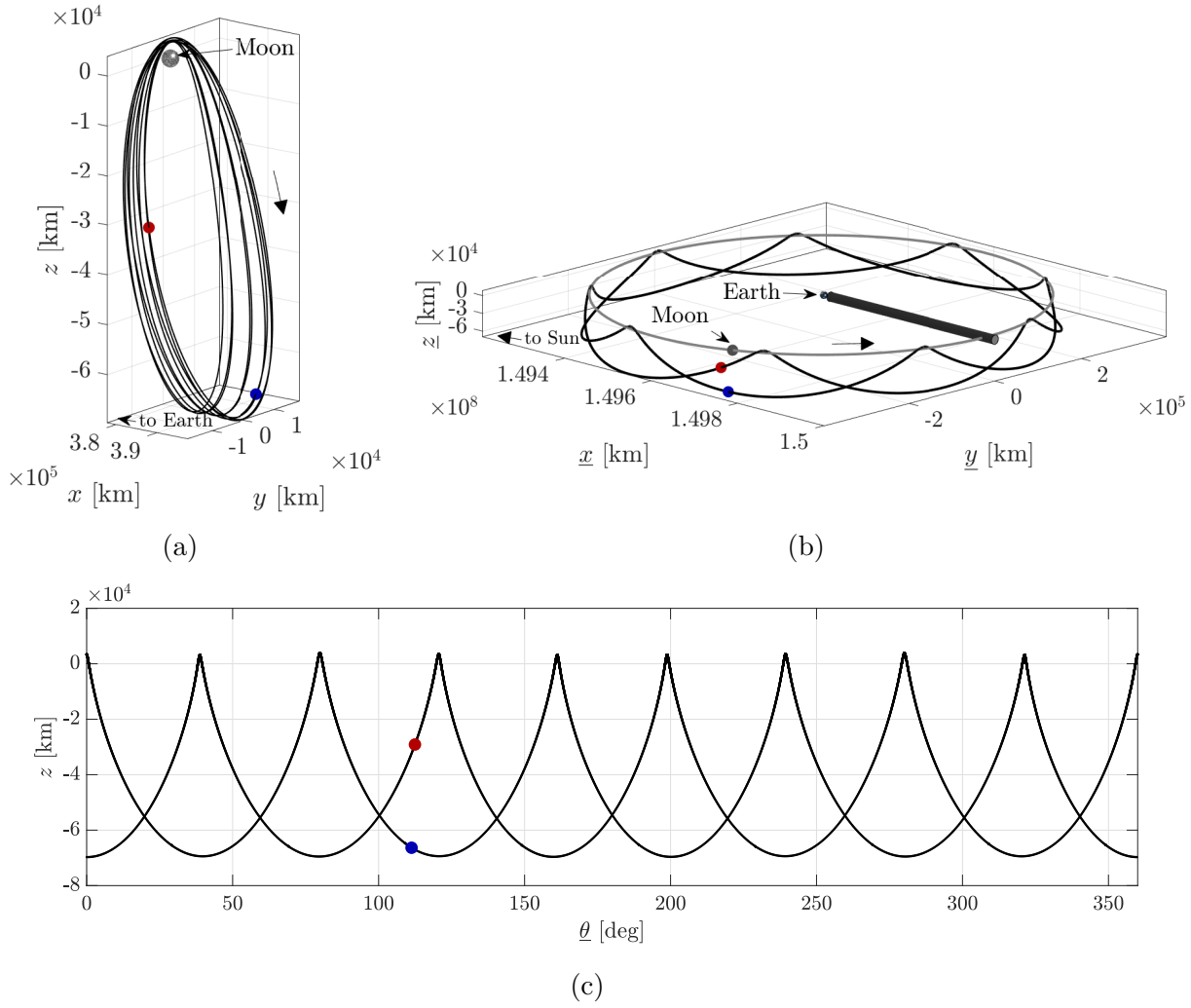


**Figure 4.31.** Synodic resonant 9:2 NRHO in the BCR4BP, as seen in the Earth-Moon rotating frame (a) and in the Sun-$B_1$ rotating frame (b). Evolution of the $z$ coordinate as a function of the Moon angle $\underline{\theta}$ (c). Spacecraft A is denoted by the red dot, spacecraft B by the blue dot.

Note that the orbit does not intersect itself as Figures 4.31(b) and 4.31(c) might suggest. The 'intersection' point corresponds to the closest approach between spacecraft A and B: the two spacecraft are then located at the same $z$ coordinate, but on different sides of the Earth-Moon rotating $x$ axis in Figure 4.31(a). Spacecraft A and B are contemporaneously flying in the Earth eclipse-free synodic resonant 9:2 NRHO as computed in the BCR4BP, without encountering each other.

### Energy Properties

An examination of the energy along the P:Q synodic resonant NRHOs is also insightful. In the CR3BP, the quantity evaluated for an energy-like assessment is the Jacobi constant $C$, defined in Eq. (2.3). A plot of Jacobi constant values is presented in Figure 4.32(a). The vertical axis is the Jacobi constant value and, since the CR3BP is time-autonomous and the Jacobi constant is conserved along natural arcs, the horizontal axis demonstrates that the $C$ value is constant against any other orbital parameter. Thus, the Jacobi constant value associated with each synodic resonant NRHO in the CR3BP is denoted by horizontal lines in Figure 4.32(a). The gray horizontal stripes represent the Jacobi constant range between each of the collinear libration points in the CR3BP: $L_1$, $L_2$ and $L_3$. Information about the flow is offered by the Jacobi constant values at the Lagrange points. Note that a decrease in the Jacobi constant value corresponds to an increase in energy. Thus, for Jacobi constant values above the one associated with $L_1$, no openings exist between the Earth and the Moon, that is, no path naturally passes near both primaries at such an energy level. A gateway, or portal, linking regions surrounding the two primaries opens when the energy is evaluated such that $C < C(L_1)$. As the energy increases, two more gateways open: first at $L_2$ when $C < C(L_2)$, then at $L_3$ when $C < C(L_3)$.

The $L_2$ halo family of orbits and its subsets, the NRHOs and the NRHO+s, are defined in the vicinity of the $L_2$ libration point. Therefore, the $L_2$ gateway is open, and the Jacobi constant associated with each of the synodic resonant NRHOs is below the value associated with $L_2$, that is, $C < C(L_2)$. The Jacobi constant associated with resonant NRHOs are linked to the perilune radius: the higher the perilune, the higher the energy along the orbit. Note that, in contrast to the orbital period, the evolution of the Jacobi constant across the $L_2$ halo family is not monotonic, as demonstrated in Figure 4.33. As the $L_2$ halo family evolves out-of-plane from the bifurcating, planar Lyapunov orbit, the energy along the family first increases and, correspondingly, the Jacobi constant decreases. A minimum value in Jacobi constant occurs as the Jacobi constant reaches the NRHO subset. Then, the energy increases as the perilune radius continues to decrease. The synodic resonant NRHOs in the CR3BP

possess relatively low Jacobi constant values, and the energy is inversely proportional to the perilune altitude.

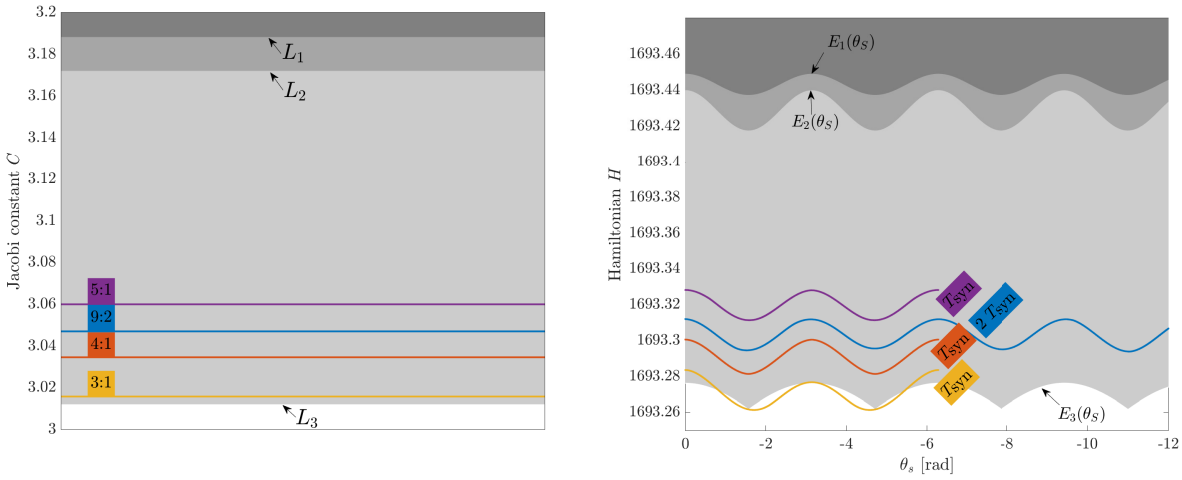


(a) (b)

**Figure 4.32.** Energy-like quantity along the synodic resonant NRHOs: Jacobi constant in the CR3BP (a) and Hamiltonian value in the BCR4BP (b).

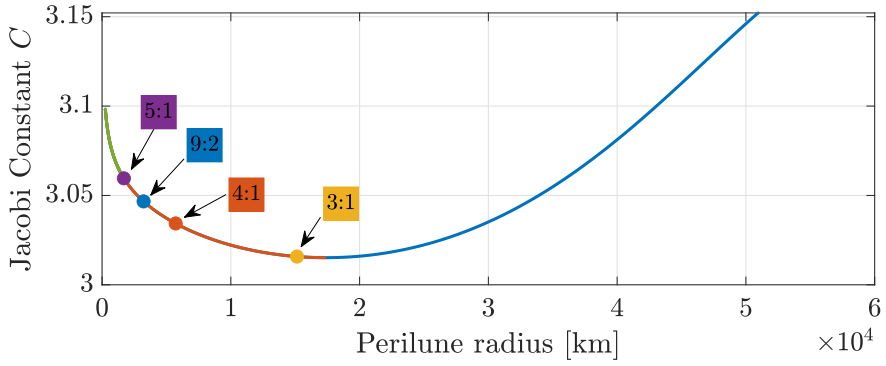


**Figure 4.33.** Jacobi constant across the CR3BP $L_2$ halo family. Members of the NRHO subset are colored in orange and NRHO+ orbits are colored in green. Synodic resonant orbits of interest are denoted by colored dots.

A similar analysis for the synodic-periodic NRHOs and NRHO+ in the BCR4BP yields further insight. Recall that the BCR4BP is time-dependent and does not possess an integral of the motion. The Hamiltonian value, defined in Eq. (2.7), is a function of the position of the Sun as viewed in the Earth-Moon rotating frame and, thus, is a function of time. A

Hamiltonian time history is plotted in Figure 4.32(b). The horizontal axis represents the Sun angle, i.e., $\theta$, which is a linear function of the independent time variable: $\theta = -\omega\, t + \theta_0$. The vertical axis corresponds to the Hamiltonian value. The Hamiltonian values associated with the instantaneous libration points $\mathrm{E}_1(\theta)$ through $\mathrm{E}_3(\theta)$ are also indicated. Since the libration points are oscillating, their associated Hamiltonian values are also time-varying. However, the Hamiltonian values cycle over one synodic period, as do the instantaneous equilibrium points in the BCR4BP. Note that the order of the openings of the gateways in the BCR4BP is consistent with the order of opening in the CR3BP: the Zero-Velocity Curves (ZVCs) in the Earth-Moon-Sun BCR4BP are not degenerated [12]. The Hamiltonian values along one period of each of the periodic orbits in the BCR4BP are denoted by colored lines. The order of the lines is consistent with the order of the Jacobi constant values in Figure 4.32(a). The Hamiltonian value along the $T_{\mathrm{syn}}$-periodic orbit in the BCR4BP continued from the 3:1 CR3BP NRHO, i.e., the yellow line in Figure 4.32(b), dips below the line associated with the Hamiltonian value of $\mathrm{E}_3(\theta)$ for certain values of $\theta$. Since the $\mathrm{E}_3(\theta)$ equilibrium is located on the opposite side of the Earth from the Moon, the opening or closing of $\mathrm{E}_3(\theta)$ does not notably modify the flow in the vicinity of the 3:1 synodic resonant NRHO orbit.

### Linear Stability Properties

The NRHO subset of the halo family is defined by its stability properties. The Lyapunov exponent, defined in Eq. (4.12), is a convenient metric to assess the stability of a periodic solution. Recall that a periodic orbit in the CR3BP possesses six Lyapunov exponents, including two always equal to zero. An orbit is stable in the linear sense if all six Lyapunov exponents are equal to zero, otherwise, the periodic solution is unstable. The Lyapunov exponents along a portion of the CR3BP $\mathrm{L}_2$ halo family are plotted in Figure 4.34. The NRHO subset is highlighted in orange, the NRHO+ subset in green, and the previously investigated synodic resonant orbits are indicated by colored dots. The NRHO subset is comprised of orbits with perilune radii between $1,800$ and $17,300$ km. Halo orbits with perilune radii lesser than $1,800$ km are labeled NRHO+ orbits. Note that the Lyapunov exponent corresponding to the unstable mode for the unstable part of the NRHO subset

ranges from 0 to 0.62. Thus, the instability, in the linear sense, of the members in this part of the family is quite limited. Two of the synodic orbits constructed previously in the CR3BP are linearly stable: the 5:1 synodic resonant NRHO+ and the 3:1 synodic resonant NRHO. The other two, the 4:1 and the 9:2 synodic resonant NRHOs, are linearly unstable. However, as observed previously, the magnitude of the eigenvalue associated with the unstable mode is very low for the unstable NRHOs.

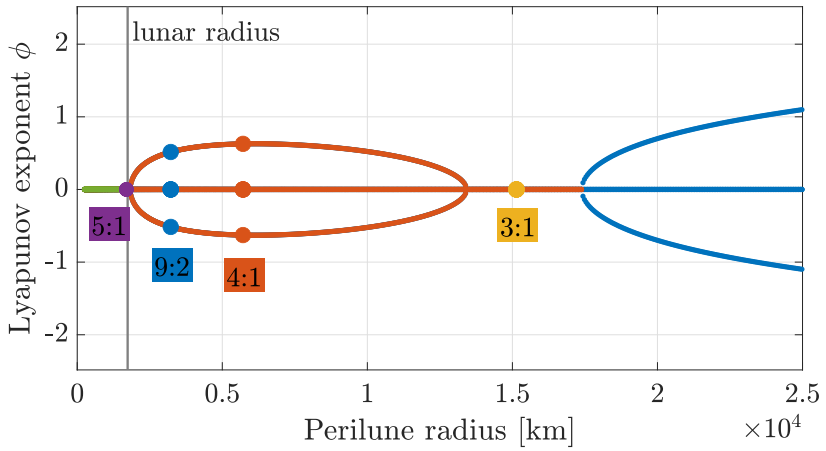


**Figure 4.34.** Lyapunov exponents across a subset of the CR3BP $L_2$ halo family. Members of the NRHO subset are colored in orange and NRHO+ orbits are colored in green. Synodic resonant orbits of interest are denoted by colored dots.

Given the stability properties from the CR3BP, the stability of the periodic solutions in the BCR4BP is explored. The six eigenvalues associated with the position and velocity states for a periodic orbit in the BCR4BP occur in pairs, as the Lyapunov theorem still applies in this model. The Lyapunov exponents associated with the resonant NRHOs in the CR3BP and the BCR4BP are presented in Table 4.5. One advantage of the Lyapunov exponents, as defined in Eq. (4.12), is that they are not influenced by the orbital period. Thus, a comparison of the stability characteristics between orbits with very different orbital periods, for instance the 9:2 NRHO in the CR3BP and its BCR4BP counterpart, is immediately available.

The stability characteristics for the synodic resonant 4:1 NRHO and the 9:2 NRHO are generally consistent between the CR3BP and the BCR4BP. Both orbits are linearly

**Table 4.5**. Lyapunov exponents for the sampled synodic resonant NRHOs as computed in the CR3BP and the BCR4BP

| Orbit | CR3BP, 1 period | BCR4BP, 1 period |
|---|---|---|
| 3:1 NRHO | 0<br>0<br>0 | 0<br>0<br>±0.6223 |
| 4:1 NRHO | 0<br>0<br>±0.6277 | 0<br>0<br>±0.6364 |
| 9:2 NRHO | 0<br>0<br>±0.5157 | 0<br>±0.0013<br>±0.5208 |
| 5:1 NRHO | 0<br>0<br>0 | 0<br>0<br>±0.0322 |

unstable, but the magnitude of the Lyapunov exponent associated with the unstable mode is small. For the 4:1 NRHO, the Lyapunov exponent associated with the unstable mode is equal to 0.6277 when computed in the CR3BP, and equal to 0.6364 in the BCR4BP. Similarly, the Lyapunov exponents for the synodic resonant 9:2 NRHO is consistent between the CR3BP and the BCR4BP. As noted previously, the pair of unit eigenvalues associated with the autonomous nature of the CR3BP is not conserved in the BCR4BP. However, the corresponding eigenvalues for the BCR4BP periodic orbit are located on the unit circle in the complex plane, i.e., the norm of each eigenvalue is equal to unity, or on the real axis in the immediate vicinity of one. Either case yields two Lyapunov exponents equal to zero or very close to zero. The stability properties of the synodic resonant 4:1 and 9:2 NRHOs are apparently maintained when the orbits are transitioned to the BCR4BP.

Some differences in the stability characteristics between the CR3BP and the BCR4BP models are present for the 3:1 and the 5:1 NRHOs. Both synodic resonant orbits are linearly stable in the CR3BP, and linearly unstable in the BCR4BP. In Table 4.5, the magnitude of the Lyapunov exponent associated with the unstable mode along the 5:1 BCR4BP NRHO is very close to zero (0.0322). Thus, perturbed motion in the vicinity of the 5:1 NRHO+ remains close to the periodic orbit for an extensive length of time, despite the linearly

unstable nature of the solution, as expected for such a low magnitude of the Lyapunov exponent, since the associated time constant for the unstable mode is large. The stability characteristics vary more significantly between models for the synodic resonant 3:1 NRHO. In the CR3BP, the periodic orbit is stable, in the linear sense. The solution constructed in the BCR4BP from this periodic, linearly stable initial guess is unstable. The Lyapunov exponent associated with the unstable mode is equal to 0.6223. The stability differences for certain synodic resonant periodic orbits signal a need for further verification that the BCR4BP periodic solutions are the true analogs of the CR3BP synodic NRHOs.

Recall that construction of the periodic orbits in the BCR4BP requires a continuation process. The Lyapunov exponents along the NRHO continuation in solar mass are investigated. Discontinuities as the Lyapunov exponents evolve suggest that the type of solutions, in terms of the stability characteristics, might have also shifted during the corrections and continuation process and that the periodic orbit is not the true counterpart of the CR3BP orbit. If no discontinuity is observed but the stability properties for the periodic orbits are different between the CR3BP and BCR4BP, a bifurcation occurs along the evolution of the family in Sun mass. To explore this possibility, the Lyapunov exponents along the continuation process for the four synodic resonant NRHOs and NRHO+ are plotted in Figure 4.35. In all four plots, the horizontal axis reflects the value of the Lyapunov exponents, that is, $\phi_{\mathrm{i}}$, and the vertical axis describes the percentage of the Sun mass that is assumed at each step in the continuation process. Thus, when the assumed mass of the Sun is 0% of the actual solar mass, the Lyapunov exponents correspond to the values for the Earth-Moon CR3BP NRHOs and with an assumed mass equal to 100% of the true solar mass, they correspond to the Lyapunov exponents for the synodic resonant orbits in the BCR4BP. Note that the intermediate steps in assumed mass between 0% and 100% possess periodic solutions that satisfy the equations of the motion for the BCR4BP at the specified given assumed mass of the Sun. However, the BCR4BP systems for these intermediate values of the solar mass do not have any physical meaning and only serve to facilitate the transition between the CR3BP and the BCR4BP. Six colored lines are plotted on each plot in Figure 4.35—one for each Lyapunov exponent. Recall that eigenvalues associated with linear stability yield Lyapunov exponents equal to zero. The evolution of the Lyapunov exponents along the continuation in assumed

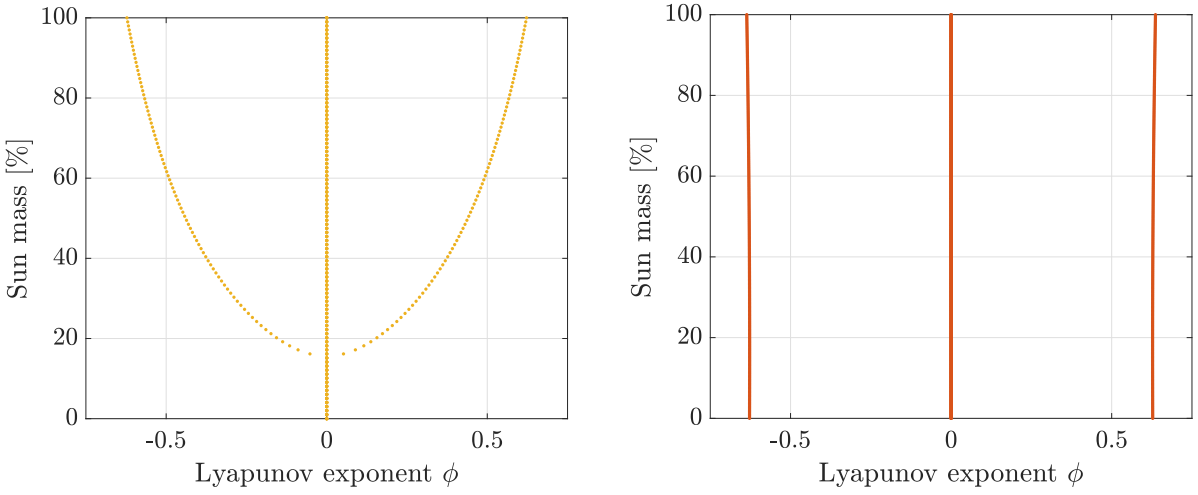


(a) CR3BP 3:1 to BCR4BP $T_{\text{syn}}$-periodic




(b) CR3BP 4:1 to BCR4BP $T_{\text{syn}}$-periodic

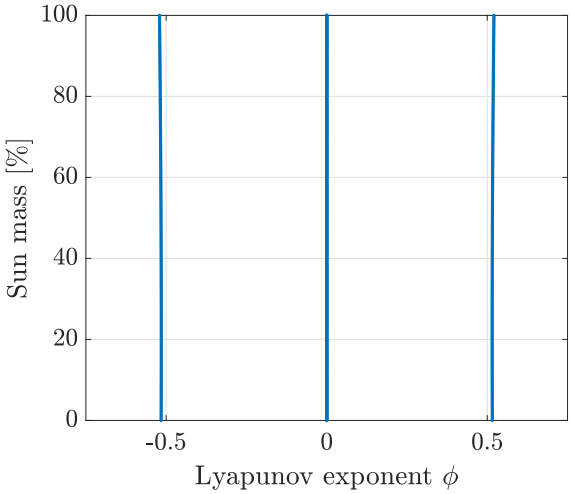


(c) CR3BP 9:2 to BCR4BP 2 $T_{\text{syn}}$-periodic

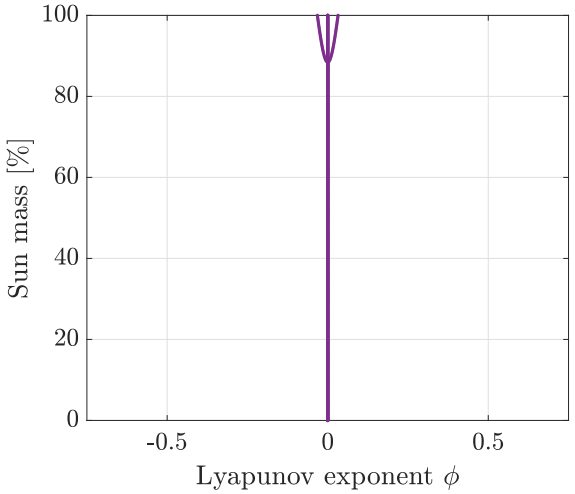


(d) CR3BP 5:1 to BCR4BP $T_{\text{syn}}$-periodic

**Figure 4.35.** Lyapunov exponents values for synodic resonant NRHOs along the continuation from CR3BP to BCR4BP.

solar mass for the Earth-Moon CR3BP 3:1 NRHO is plotted in Figure 4.35(a). Four of the six Lyapunov exponents remain equal to zero. The remaining two lines originate at a value of $\phi$ corresponding to the linear stability bounds—recall that all six Lyapunov exponents for the 3:1 NRHO in the CR3BP are such that $\phi = 0$. With increasing solar mass, the curves cross the linear stability boundary when assumed mass is near 15% of the true mass of the Sun and grow larger in magnitude. The curves representing the evolving Lyapunov exponent values correspond to the 'mismatch' in stability observed between the CR3BP 3:1 synodic

resonant NRHO and the corresponding BCR4BP $T_{\text{syn}}$-periodic orbit. However, there is no discontinuity in the stability index lines in Figure 4.35(a). Thus, a bifurcation occurs in the continuation process when the assumed mass is approximately 15% of the true solar mass, and the $T_{\text{syn}}$-periodic in the BCR4BP that corresponds to the 3:1 NRHO in the CR3BP is unstable in the linear sense. This difference in stability is likely one aspect that contributes to the numerical challenges in transitioning the 3:1 NRHO in the CR3BP to the higher-fidelity, ephemeris model [88]. Similarly, the 'mismatch' in stability for the synodic periodic orbit corresponding to the 5:1 resonant orbit is explored in Figure 4.35(d). Four of the Lyapunov exponents in Figure 4.35(d) remain along the $\phi = 0$ linear stability line throughout the continuation in assumed mass, while the remaining two lines both reflect nonzero values of $\phi$ and leave the stability boundary when the assumed mass is approximately equal to 90% of the Sun's true mass. Since the evolution of all six Lyapunov exponents are smooth, it is deduced that a bifurcation occurs at an assumed mass around 90% of the Sun's true mass along the continuation process. The $T_{\text{syn}}$-periodic solution in the BCR4BP introduces a small unstable mode, while the 5:1 synodic resonant orbit in the CR3BP is stable in the linear sense. The Lyapunov exponents for the synodic resonant solutions corresponding to the 4:1 and the 9:2 NRHOs are consistent in both models, as apparent in Table 4.5. Therefore, it is not surprising that the Lyapunov exponent evolutions in Figures (b) and (c) are nearly vertical lines. By examination of the evolution of the Lyapunov exponents over the continuation in Sun mass, it is determined that the NRHOs, as constructed in the BCR4BP, are the counterparts of the CR3BP orbits, but the linear stability characteristics are not necessarily the same in both models.

### Epoch Considerations

Periodic orbits in the BCR4BP model are defined for a specific epoch. In this investigation, the initial epoch is specified by the Sun angle at perilune. Recall that the $T_{\text{syn}}$-periodic and $2T_{\text{syn}}$-periodic orbits in the BCR4BP include multiple revolutions around the Moon and, thus, multiple perilunes are recorded. During the continuation of a synodic periodic orbit from the CR3BP, an autonomous model, to the BCR4BP, a periodic time-dependent

model, an initial epoch is introduced. To explore the impact of this initial epoch selection on the final BCR4BP synodic resonant orbit, solar mass exclusion plots are exploited. Solar mass exclusion plots relate the initial epoch to the convergence of a BCR4BP periodic orbit. For instance, consider the solar mass exclusion plot associated with the 3:1 NRHO in Figure 4.36. The horizontal axis represents the Sun angle at each perilune from 0° to 360°, while the vertical axis identifies the percentage of the assumed solar mass. The continuation process from the CR3BP periodic orbit to its BCR4BP counterpart is initialized for a perilune occurring over a range of Sun angles from 0° to 360°, as illustrated by the blue and red dots at 0% in Figure 4.36. Each set of initial conditions is continued in solar mass, and the intermediate steps are recorded as the assumed solar mass is increased from 0 to 100% of the true solar mass. The dots in Figure 4.36 are colored according to the outcome of the continuation process: blue dots corresponds to initial conditions that reach 100% of the actual solar mass, that is, initial conditions that successfully yield a periodic solution in the Earth-Moon-Sun BCR4BP. Red dots correspond to solutions that only converge for assumed masses smaller than 100% of the true solar mass; that is, red dots are associated with initial Sun angles that do not produce a periodic solution in the Earth-Moon-Sun BCR4BP. Three nearly vertical blue lines are apparent in Figure 4.36. These blue lines reflect to the range of initial conditions that yield an Earth-Moon-Sun BCR4BP periodic orbit. Note that the three lines, associated with Sun angles approximately equal to 0°, 120° and 240°, all correspond to the same orbit. The $T_{\text{syn}}$-periodic orbit in the BCR4BP corresponding to the 3:1 NRHO in the CR3BP includes three lobes around the Moon, and, thus, three distinct perilunes, as plotted in Figure 4.29(b). Each vertical line thus corresponds to the Sun angle at one perilune passage. Note that the lines are separated by approximately 120°, or, equivalently, approximately one third of the synodic period. The three lobes along the BCR4BP orbit in Figure 4.29(b) have slightly different sizes, and thus, slightly different revolution times.

The unicity of BCR4BP counterparts to a synodic resonant orbit in the CR3BP is explored with the solar mass exclusion plots. It is apparent in Figure 4.36 that the continuous range of initial Sun angles in the CR3BP all converge to one of two solutions as the assumed solar mass is increased. Most of the initial conditions, marked in blue, immediately converge to the BCR4BP periodic orbit when the Sun is introduced, i.e., for an assumed mass greater

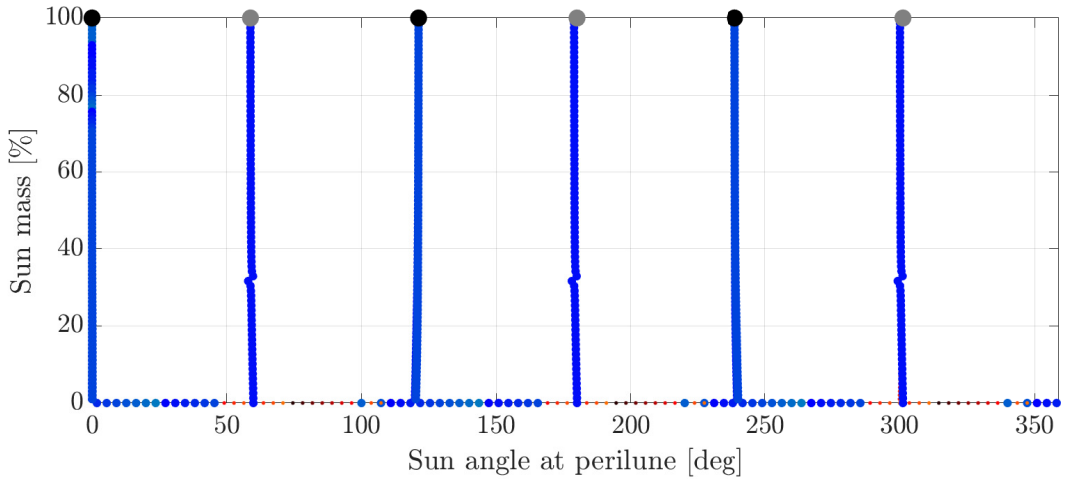


**Figure 4.36.** Solar mass exclusion plot for the synodic resonant 3:1 NRHO continuation from the CR3BP to the BCR4BP. The BCR4BP counterpart A is denoted by a black dot, and the BCR4BP counterpart B by a gray dot.

than or equal to 1% of the actual solar mass. Two counterparts, or analogs, of the 3:1 NRHOs are obtained in the BCR4BP. The counterpart denoted 'A' corresponds to the three black dots in Figure 4.36; the three perilunes have an associated Sun angle of approximately 0°, 120°, and 240°. The remaining initial conditions yield a periodic orbit offset by 60° denoted by gray dots in Figure 4.36. This second analog[5] to the CR3BP 3:1 NRHO possesses perilunes for Sun angles approximately equal to 60°, 180°, and 300°. The CR3BP synodic resonant 3:1 NRHO has thus two BCR4BP counterparts, identified by the black and gray dots in Figure 4.36. The periodic solutions corresponding to the two configurations overlap when the orbits are plotted in the Earth-Moon rotating frames; both solutions coincide with the orbit plotted in black in Figure 4.37(a). The differences between the two counterparts becomes apparent when the two orbits are plotted as viewed in the Sun-$B_1$ rotating frame in Figure 4.37(b). The lunar orbit is represented by the dashed black line, and perilune and apolunes are denoted by triangles and inverted triangles, respectively. Due to the symmetric nature of the BCR4BP, the apolune associated with the center lobe (C), colored in gray, is located along the Sun-$B_1$ rotating $\hat{x}$ direction for each analog. However, in the Sun-$B_1$ rotating frame, the apolune C is located on the right of the Earth for counterpart A, and

[5]↑The author incorrectly states in [44] convergence for assumed solar mass greater than 17% is not achieved.

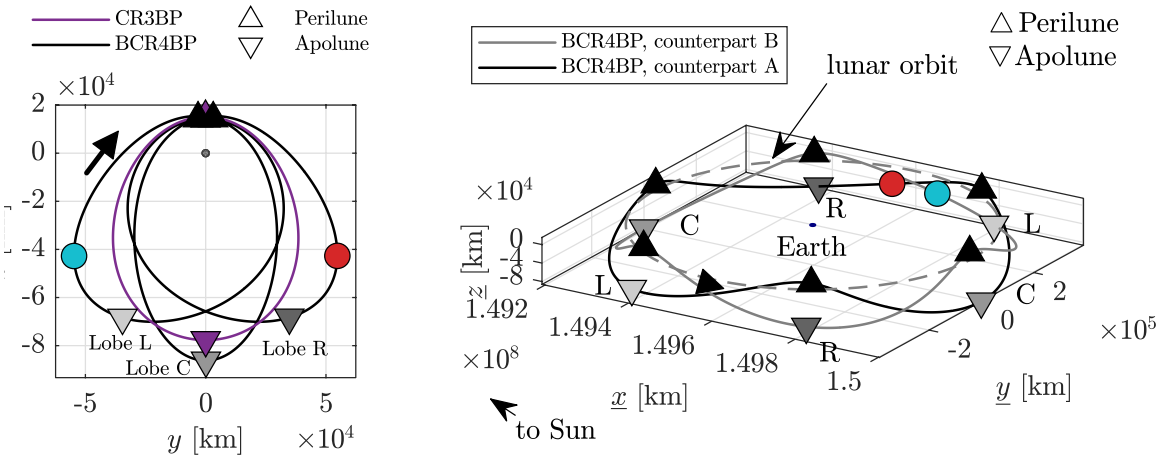


(a) Earth-Moon rotating frame, looking toward the Earth

(b) Sun-$B_1$ rotating frame

**Figure 4.37.** Geometry of the 3:1 NRHO computed in the BCR4BP, as viewed in the Earth-Moon rotating frame (a) and in the Sun-$B_1$ rotating frame (b). Perilunes are denoted by a triangle, apolunes are denoted by an upside-down triangle. For the BCR4BP orbit, the apolunes are colored according to their lobe: 'L' in light gray, 'C' in gray, 'R' in dark gray. Two spacecraft, identified by the cyan and red circles in Figures 4.37(a) and 4.37(b) are concurrently flying in the BCR4BP 3:1 NRHO, one in each configuration.

on the left of the Earth for counterpart B. The apolunes associated with the remaining two lobes are colored in dark gray for the right (R) lobe and light gray for the left (L) lobe in Figure 4.37(b). From the view in the Sun-$B_1$ rotating frame, it is apparent that the solutions from the two different configurations are rotated from each other by 180° around the rotating $\hat{\underline{z}}$ axis. Note that two spacecraft can fly concurrently in the BCR4BP 3:1 NRHO: one spacecraft along the orbit associated with configuration 1, and the other along the orbit given configuration 2. As an illustration, consider the red and cyan circles in Figures 4.37(a) and 4.37(b). The red circle represents a spacecraft flying in the 3:1 NRHO in configuration 1 while the blue circle represents a spacecraft flying in the 3:1 NRHO in configuration 2 *at the same instant in time*. While the spacecraft denoted by the red circle is approaching apolune along the R lobe, the blue dot spacecraft is approaching perilune along the L lobe, as apparent in Figure 4.37(a). Note that the two 3:1 NRHOs at different configurations do not

intersect when viewed in the Sun-$B_1$ rotating frame, as Figure 4.37(b) might suggest. The 'intersection' point corresponds to the closest approach between the gray and black curves in Figure 4.37(b): the two spacecraft are then located at the same $z$ coordinate, but on different sides of the Earth-Moon rotating $\hat{x}$ axis in Figure 4.37(a). The 3:1 NRHO as computed in the BCR4BP exists at two different epochs; two spacecraft can contemporaneously fly along the 3:1 NRHO without encountering each other

Now consider the solar mass exclusion plot for the 4:1 synodic resonant NRHO, presented in Figure 4.38. The $T_{\text{syn}}$-periodic orbit in the BCR4BP corresponding to the 4:1 NRHO possess four lobes, and, thus, four perilunes. Therefore, Sun angles corresponding to four perilunes are associated with this orbit, separated by approximately by a phase of 90°. However, 8 blue lines, separated by approximately 45°, are apparent in Figure 4.38. Thus, two $T_{\text{syn}}$-periodic counterparts in the BCR4BP of the 4:1 synodic resonant CR3BP NRHO are obtained. One counterpart, labeled orbit A and denoted by a green dot in Figure 4.38, presents the following Sun angle at perilune combination: 45°, 135°, 225° and 315°. The second analog's apolunes occur for Sun angles equal to 0°, 90°, 180° and 270°, and is indicated by the purple dot in Figure 4.38. The resulting counterparts in the Earth-

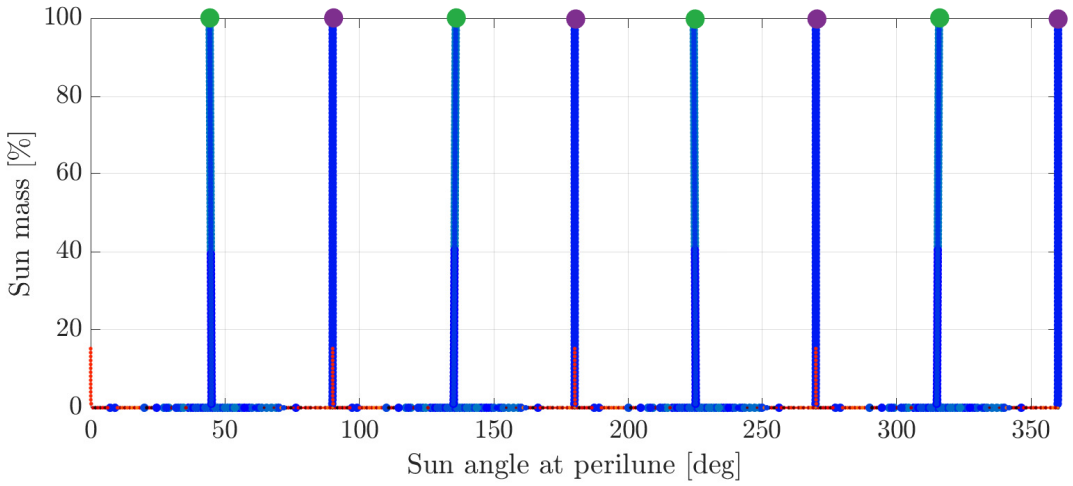


**Figure 4.38.** Solar mass exclusion plot for the synodic resonant 4:1 NRHO continuation from the CR3BP to the BCR4BP. The BCR4BP counterpart A is denoted by a green dot, and the BCR4BP counterpart B by a purple dot.

Moon-Sun BCR4BP appear in Figure 4.39. The two orbits are plotted in the Earth-Moon

rotating frame in Figure 4.39(a). Recall that the $T_{\text{syn}}$-periodic orbit corresponding to the 4:1 NRHO includes four lobes around the Moon grouped in pairs. The difference in geometry between counterpart A (green) and the counterpart B (purple) is small, but noticeable in Figure 4.39(a). The four perilunes associated with orbit A lie approximately the same distance from the Moon at a distance of $5,940$ km. The perilunes of orbit B exist in two groups: a lower pair of perilunes with radii approximately equal to $4,970$ km and a higher pair with radii about $7,100$ km from the center of the Moon. Note the difference in the spread of lobes in Figure 4.39(a). The four apolunes associated with orbit A, marked with green asterisks, lie along $y = 0$ axis with a pair of two distinct $x$ values. In contrast, the four apolunes of orbit B, denoted with purple asterisks, share a single $x$ coordinate and are offset in two symmetric pairs about $y = 0$. The differences in geometry between the two counterparts become clear when the orbits are viewed in the Sun-$B_1$ rotating frame, as in Figure 4.39(b). The phase shift of 45° in Sun angle at perilune, revealed in the solar mass exclusion plot in Figure 4.38, is apparent in Figure 4.39(b). Note the consistency in the placement of apsides within the Sun-$B_1$ quadrants. The perilunes associated with orbit A, marked by green dots, lie in the middle of each quadrant, while the apolunes, marked by green asterisks, are located at the edge between adjoining quadrants. Plotted in purple, orbit B demonstrates the reverse configuration. Note the difference between Figure 4.31(b), where two spacecraft phased differently fly simultaneously in a single periodic orbit in the BCR4BP, and Figure 4.39(b), in which two different periodic orbits in the BCR4BP are plotted.

The number of BCR4BP counterparts to a synodic resonant CR3BP orbit is not limited to two. Consider the solar mass exclusion plot for the 9:2 synodic resonant NRHO in Figure 4.40. Many lines are apparent, and the information is difficult to extract from this plot. First, recall that the BCR4BP counterpart to the CR3BP 9:2 NRHO presents nine lobes around the Moon, thus, nine Sun angle values at perilune are expected (the BCR4BP is a 2 $T_{\text{syn}}$-periodic orbit, but the Sun angles range from 0 to 360° in the solar mass exclusion plots). Secondly, notice the repeating vertical pattern every 40° or so. Two consecutive perilunes along a 2 $T_{\text{syn}}$-periodic orbit in the BCR4BP lie approximately 80° apart. However, since the nine perilunes along the BCR4BP counterpart to the 9:2 NRHO occur along

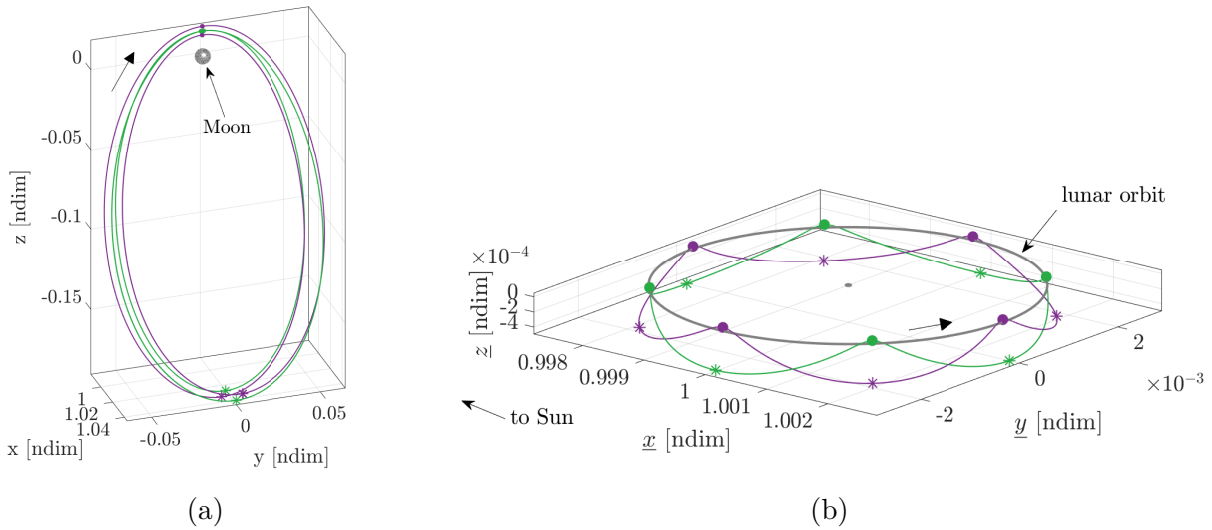


(a) (b)

**Figure 4.39.** BCR4BP counterpart A (in green) and counterpart B (in purple) of the synodic resonant 4:1 NRHO, as seen in Earth-Moon rotating frame (a) and in the Sun-$B_1$ rotating frame (b). Perilunes are denoted by colored dots and apolunes by colored asterisks.

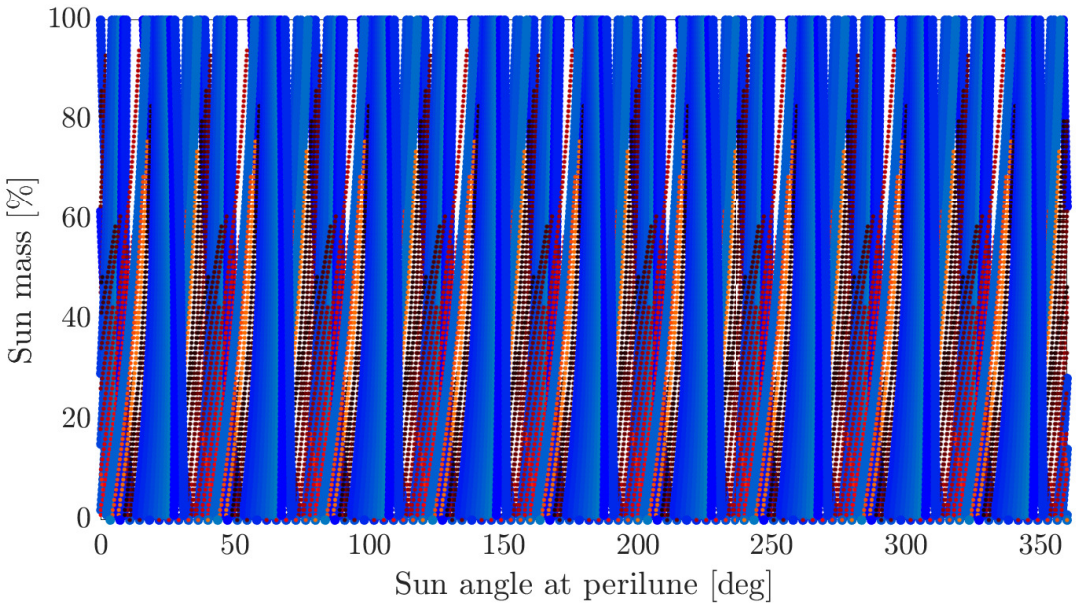


**Figure 4.40.** Solar mass exclusion plot for the synodic resonant 9:2 NRHO continuation from the CR3BP to the BCR4BP.

two synodic periods, i.e., two revolutions of the Sun, the smallest angle difference between two non-consecutive perilunes is 40°. Therefore, a zoomed version of Figure 4.40 between the Sun angles of 0° and 40° appears in Figure 4.41. Further insights are apparent at this

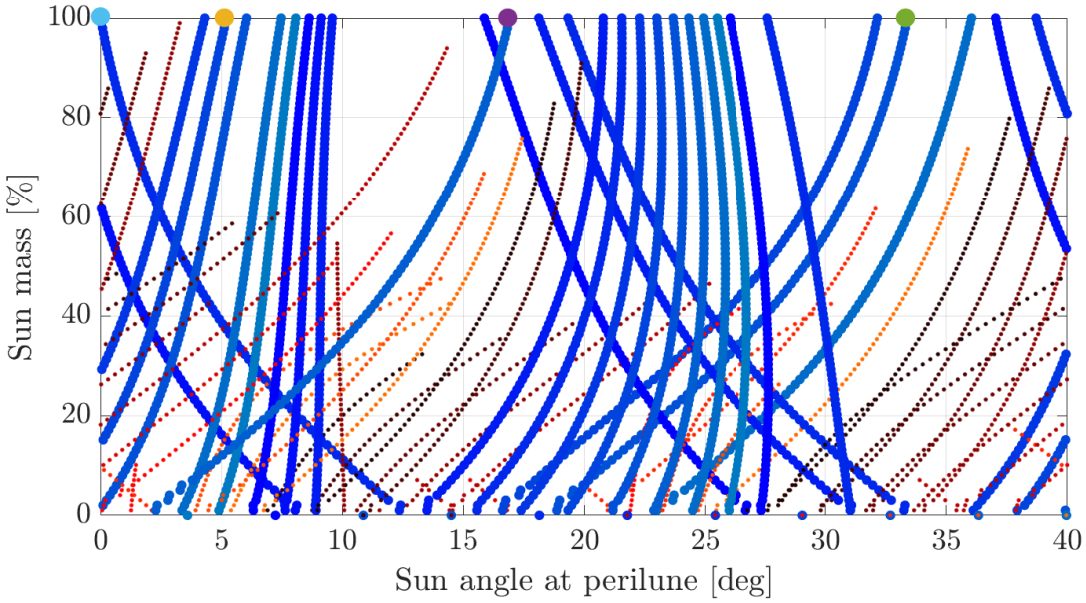


**Figure 4.41.** Zoom between 0 and 40° in the solar mass exclusion plot for the synodic resonant 9:2 NRHO continuation from the CR3BP to the BCR4BP. Selected Earth-Moon-Sun BCR4BP initial conditions are denoted by colored dots.

scale. First, note the shift in the Sun angle at perilune as the assumed mass of the Sun is increased. Some perilunes are shifted toward smaller Sun angles while others are shifted to larger Sun angles, creating the woven pattern in Figure 4.41. Secondly, note the orange and red lines that experience similar evolution to the blue lines as the assumed mass of the Sun is increased, but do not reach 100% of the true solar mass. Further experience is required to establish whether adjustments to the numerical corrections and continuation scheme could extend the convergence or whether these sets of initial conditions do not yield a periodic orbit in the Earth-Moon-Sun BCR4BP. Four converged Earth-Moon-Sun BCR4BP orbits are denoted by colored dots in Figure 4.41 and plotted in Figure 4.42. The different orientations of the nine lobes along each orbit are apparent when plotted in the Earth-Moon rotating frame, in Figure 4.42(a). The differences in phasing are more apparent when the orbits are

plotted in the Sun-$B_1$ rotating frame, in Figure 4.42(b). This range of possibilities for the Sun angle at perilune, and thus this range in possible epochs, may contribute to the ease of transitioning the synodic resonant 9:2 orbit from the CR3BP to the higher-fidelity, time-dependent ephemeris model. Numerous counterparts of the CR3BP 9:2 NRHO are available in the BCR4BP.

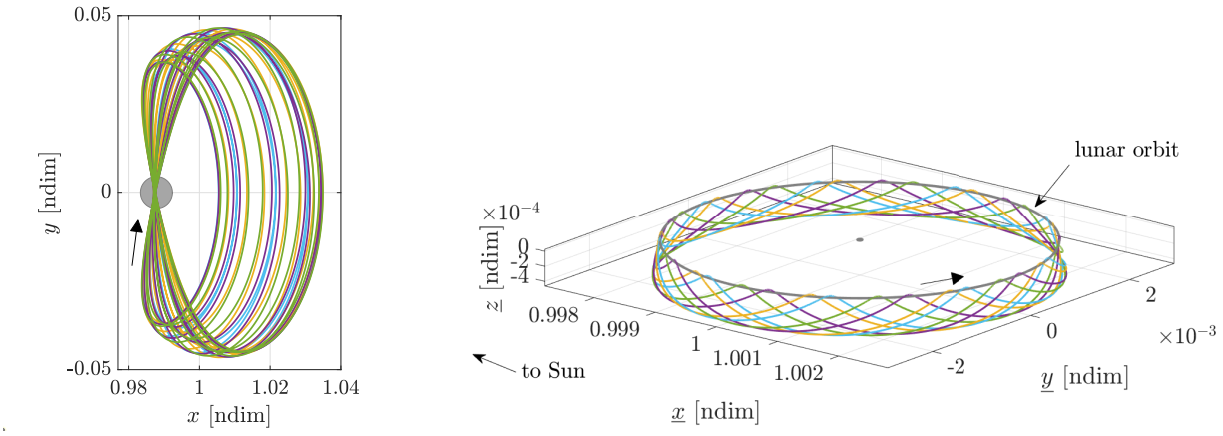


**Figure 4.42.** Selected Earth-Moon-Sun BCR4BP counterparts of the 9:2 synodic resonant NRHO, as viewed in the Earth-Moon rotating frame (a) and in the Sun-$B_1$ rotating frame (b).

### 4.3.4 Sun-$B_1$ Lagrange Orbits

The Sun-$B_1$ Lagrange orbits are the dynamical counterparts in the BCR4BP of the Sun-$B_1$ Lagrange points. Recall from Table 4.4 that only the $\underline{L}_1$ and $L_2$ libration are distinctly affected by the motions of the Earth and Moon along their respective orbits; the other points are too far. Thus, the Lagrange periodic orbits corresponding to the $\underline{L}_1$ and $L_2$ points are explored in the BCR4BP. Recall that these synodic resonant periodic orbits are constructed using the CR3BP Lagrange point as the initial guess for the natural parameter continuation in Earth-Moon distance described in Section 3.4.2. The results of the continuation scheme for $\underline{L}_1$ and $\underline{L}_2$ are presented in Figure 4.43. Each curve is a periodic orbit as viewed in the Sun-$B_1$ rotating frame, constructed in a BCR4BP with an artificial Earth-Moon distance that is generally not equal to Earth-Moon distance employed in the Earth-Moon-Sun BCR4BP; these

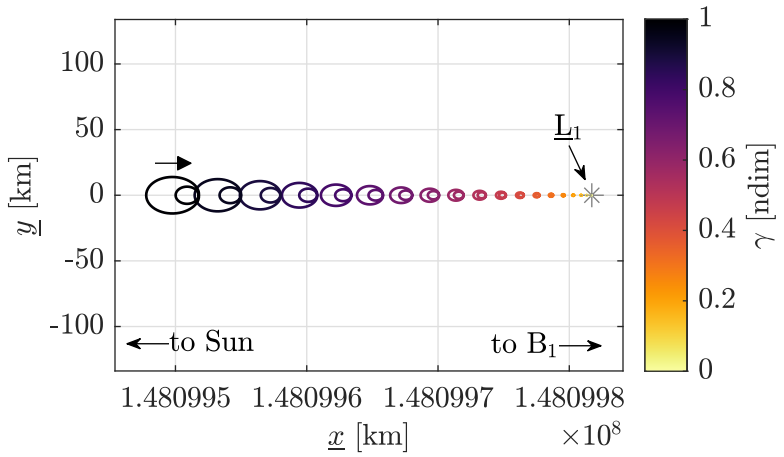


(a) $\underline{L}_1$

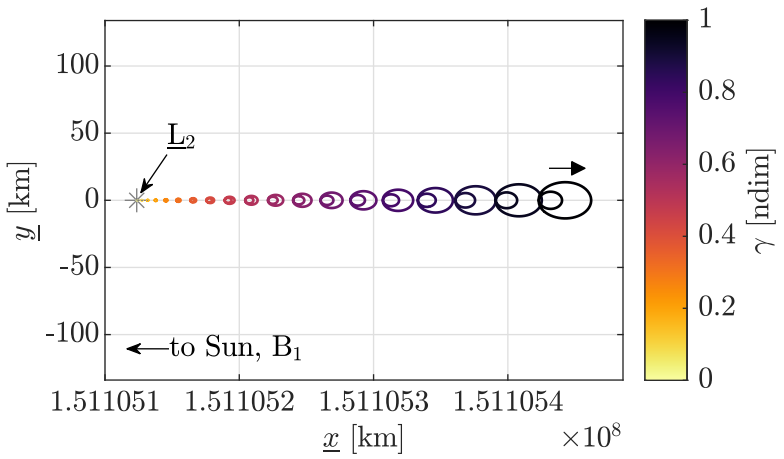


(b) $\underline{L}_2$

**Figure 4.43.** Continuation in Earth-Moon radius parameter $\gamma$ of the Sun-$B_1$ $\underline{L}_1$ (a) and $\underline{L}_2$ Lagrange points. The Lagrange points are denoted by gray asterisks.

periodic orbits are used as steps along the continuation process between the Sun-$B_1$ CR3BP, i.e., $\gamma = 0$, and the Earth-Moon-Sun BCR4BP, i.e., $\gamma = 1$. As intuitively expected, the size of the periodic orbit increases as the Earth-Moon distance is increased. However, unlike the Earth-Moon Lagrange orbits presented in Figures 4.19(a), 4.20(a), 4.21(a) and 4.21(c), the Lagrange point from the Sun-$B_1$ CR3BP is not the center of the curvature of the periodic orbits. For the $\underline{L}_1$ periodic orbits, the centers of the curvature of the periodic orbits evolve in

the negative $\hat{x}$ direction as the continuation parameter $\gamma$ increases. Conversely, the centers of the curvature of the periodic orbits associated with $L_2$ evolves in the positive $\hat{x}$ along the family of solution parametrized by $\gamma$. A continuation scheme in the Earth-Moon distance is employed to construct the Lagrange orbits in the BCR4BP corresponding to the Sun-$B_1$ $L_1$ and $L_2$ libration points.

Lagrange orbits associated with the Sun-$B_1$ $L_1$ and $L_2$ libration points are obtained for $\gamma = 1$, i.e., for the $l^*$ value that is consistent with the Sun-Earth-Moon BCR4BP. The resulting orbits appear as the blue curves in Figure 4.44. The Zero Acceleration Contours

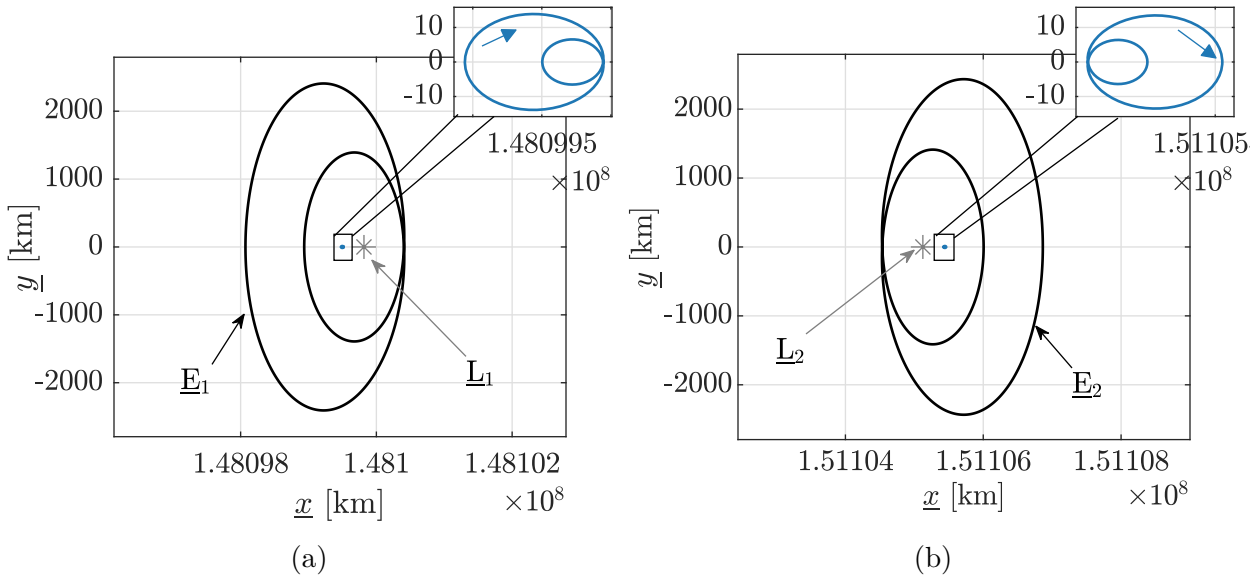


**Figure 4.44.** BCR4BP Lagrange periodic orbit, in blue, and instantaneous equilibrium solutions, in black, associated with the $L_1$ (a) and $L_2$ (b) Lagrange points.

(ZACs) are plotted in black, and the libration points in the Sun-$B_1$ CR3BP are denoted by the gray asterisks. Note the difference in sizes between the ZACs and the Lagrange periodic orbits; while the dimensions of the periodic orbits are in the order of kilometers, the ZACs associated with $L_1$ and $L_2$ span thousands of kilometers. Thus, both the CR3BP libration point and its associated Lagrange periodic orbit in the BCR4BP are encircled by their corresponding ZACs, as apparent from Figure 4.44. However, unlike the Zero Acceleration Contours, the Lagrange periodic orbits are trajectories, that is, they satisfy the differential equations of motion in Equation (2.8). The $L_1$ and $L_2$ Lagrange periodic orbits in

the BCR4BP possess small dimensions relatively to the characteristic length of the Sun-$B_1$ system.

The linear stability properties associated with the Lagrange periodic orbits are explored. Similar to the Earth-Moon libration points, the $\underline{\mathrm{L}}_1$ and $\underline{\mathrm{L}}_2$ Lagrange points in the Sun-$B_1$ possess a two-dimensional saddle mode and a four-dimensional center mode. The dimensions of these linear modes are examined as the $\gamma$ continuation parameter evolves from 0 to 1, the results are plotted in Figure 4.45. The horizontal axes represent the maximum distance from the Lagrange point along the periodic orbit (note the different scales for each plot); the vertical axis represent the nondimensional mass continuation parameter $\gamma$ employed to construct each periodic orbit. The curves are colored as a function of the modes associated with the periodic orbits. For the $\underline{\mathrm{L}}_1$ and $\underline{\mathrm{L}}_2$ periodic orbits in Figure 4.43, the $S^2 \times C^4$ characteristics of the CR3BP Lagrange points are preserved along the continuation scheme. Note that the curves in Figures 4.45(a) and 4.45(b) are not identical; the differences are indistinguishable at this scale. The $\underline{\mathrm{L}}_1$ and $\underline{\mathrm{L}}_2$ Lagrange periodic possess the same stability properties (in the linear sense) as their respective underlying libration points.

### 4.3.5 Sun-$B_1$ Halo Orbits

Similar to the Earth-Moon halo orbits, the $\underline{\mathrm{L}}_1$, $\underline{\mathrm{L}}_2$, and $\underline{\mathrm{L}}_3$ halo families are comprised of three-dimensional periodic orbits in the Sun-$B_1$ CR3BP [36]. The halo family of orbits bifurcates from each family of planar Lyapunov orbits associated with the collinear libration points. The halo orbits are mirrored across the $\underline{x}$-$\underline{y}$ plane; a northern family member possesses a positive $\underline{z}$ component over the majority of each orbit, while the southern family members are defined by a negative $\underline{z}$ component. For instance, consider the $\underline{\mathrm{L}}_2$ halo family in the Sun-$B_1$ CR3BP, as plotted in the Sun-$B_1$ rotating frame in Figure 4.46(a). The color scale denotes the orbital period, and the darker shades of gray represent the orbits with larger periods. The halo family originates in the $\underline{x}$-$\underline{y}$ plane from the bifurcating orbit in the planar Lyapunov family and evolves out of plane as the family of orbits approaches the secondary body. Recall that in the Sun-$B_1$ CR3BP, the smaller primary is a fictitious body with mass equal to the sum of the masses of the Earth and the Moon. Thus, the position of the Earth

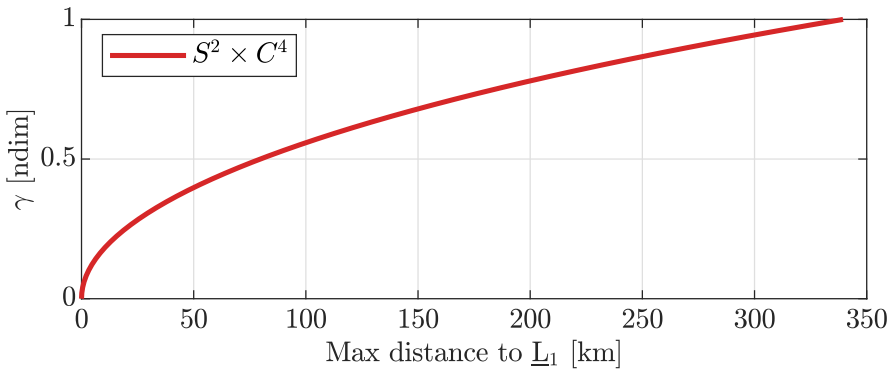


(a) $\underline{L}_1$ periodic orbit from Figure 4.43(a)

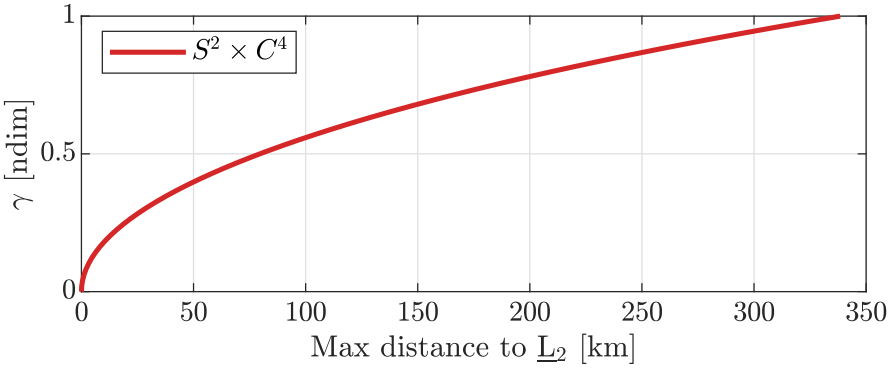


(b) $\underline{L}_2$ periodic orbits from Figure 4.43(b)

**Figure 4.45.** Stability characteristics associated with the periodic orbits along the continuation in Earth-Moon radius parameter of the Sun-$B_1$ $\underline{L}_1$ (a) and $\underline{L}_2$ Lagrange points. Red points denote periodic orbits with $S^2 \times C^4$ modes.

and the orbit of the Moon are indicated for reference in Figure 4.46(a). Synodic resonant $\underline{L}_2$ halo orbits are selected in the Sun-$B_1$ CR3BP using a resonance plot[38], [46]. A resonance plot, as in Figure 4.47, represents the ratio of the orbital period to the synodic period versus another parameter, such as the maximum $\underline{z}$ excursion, across a family of periodic orbits. Simple resonance ratios, for instance 1:3 or 2:11 are easily identified in the resonance plot in Figure 4.47. However, less intuitive ratios, such as 12:73, also yield valid synodic resonant orbits and are identifiable from a resonance plot. The resonance quotients identified in Figure 4.47 are colored as functions of the type of resonance; 1:$\alpha$ resonances are colored in orange, 2:$\alpha$ resonances in blue, 4:$\alpha$ resonances in green, and other types of resonance, such as 12:73, in purple. Synodic resonant periodic orbits are selected in the Sun-$B_1$ CR3BP

and are then employed as initial guess for the computation of the periodic solutions in the BCR4BP.

The synodic resonant $\underline{L}_2$ halo orbits that are selected from Figure 4.47 are transitioned from the Sun-$B_1$ CR3BP to the BCR4BP as formulated in the Sun-$B_1$ rotating frame [6]. The resulting orbits are plotted along with their CR3BP counterparts in Figure 4.46(b). Orbits near the $\underline{L}_2$ equilibrium point, for instance the 1:6 or the 12:73 synodic resonant orbits are not significantly perturbed by the actual Earth and the Moon on their respective planetary orbits. In contrast, the $\underline{L}_2$ resonant orbits that pass closer to the Earth and the Moon orbits, such as the 1:3 or the 2:7 synodic resonant halos, visibly differ from the periodic orbits as computed in the Sun-$B_1$ CR3BP. Note the multiple lobes that are apparent on some of the orbits as computed in the BCR4BP, e.g., the 4:15 synodic resonant halo, plotted in green in Figure 4.46(b). Each lobe corresponds to $^{15}/_{4} = 3.75$ synodic periods, or equivalently 3.75 revolutions of the Moon around the Earth-Moon barycenter, $B_1$. The 12:73 synodic resonant halo orbit includes 12 lobes, but they are indistinguishable at this scale.

### 4.3.6 Non-Synodic Resonant Orbits and Bounded Motion

The requirement of synodic resonance considerably restricts the availability of periodic orbits in the BCR4BP. For instance, consider the resonance ratio plots for the CR3BP Earth-Moon $L_2$ NRHOs in Figure 4.28(b) and the Sun-$B_1$ $\underline{L}_2$ halo family of periodic orbits in Figure 4.47. The majority of the available orbits have an irrational resonance ratio, or possess rational but non-intuitive synodic resonance ratios, such as 776:127. Thus, a different approach is employed to construct quasi-periodic, or *bounded* motion in the BCR4BP.

#### Definition

A strategy is developed to transition orbits that do not present a simple resonance ratio with the synodic period. Periodic orbits in the CR3BP are transitioned to reflect simply bounded motion, rather than periodic motion, in the BCR4BP. Multiple revolutions of periodic orbits from the CR3BP are 'stacked', discretized, and corrected for continuity in the

[6]↑Initial conditions for some of these orbits are produced in Appendix E.2.

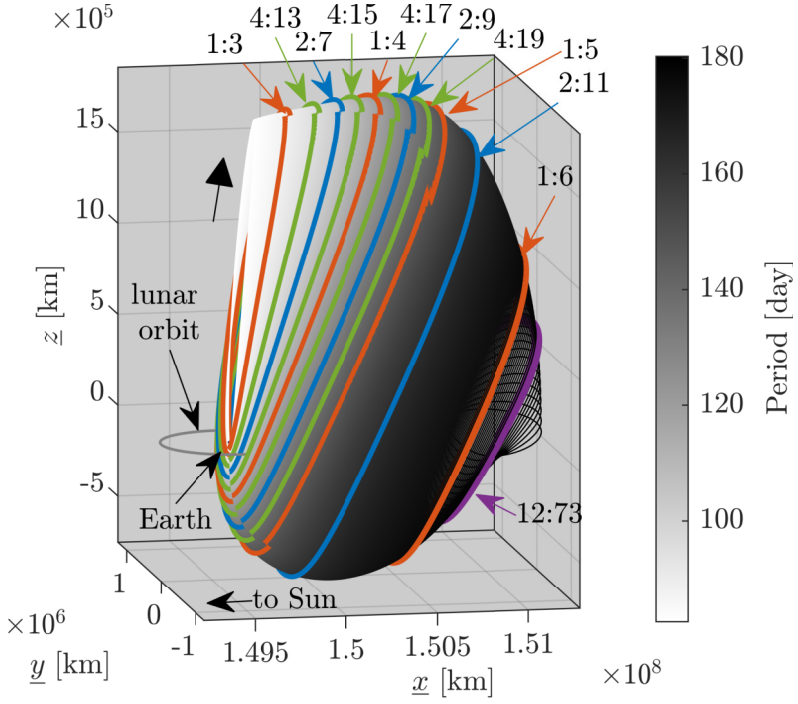


(a)

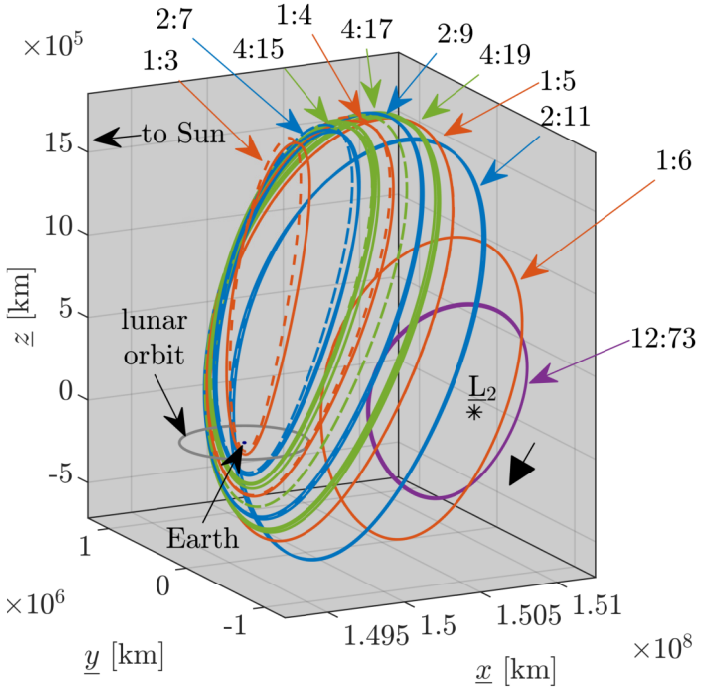


(b)

**Figure 4.46.** Representative $\underline{L}_2$ halo orbits, as seen in the Sun-$B_1$ rotating frame. Selected synodic resonant members are plotted in color. (a) Selected synodic resonant members as computed in the CR3BP, in dashed lines, and in the BCR4BP, in solid lines (b).

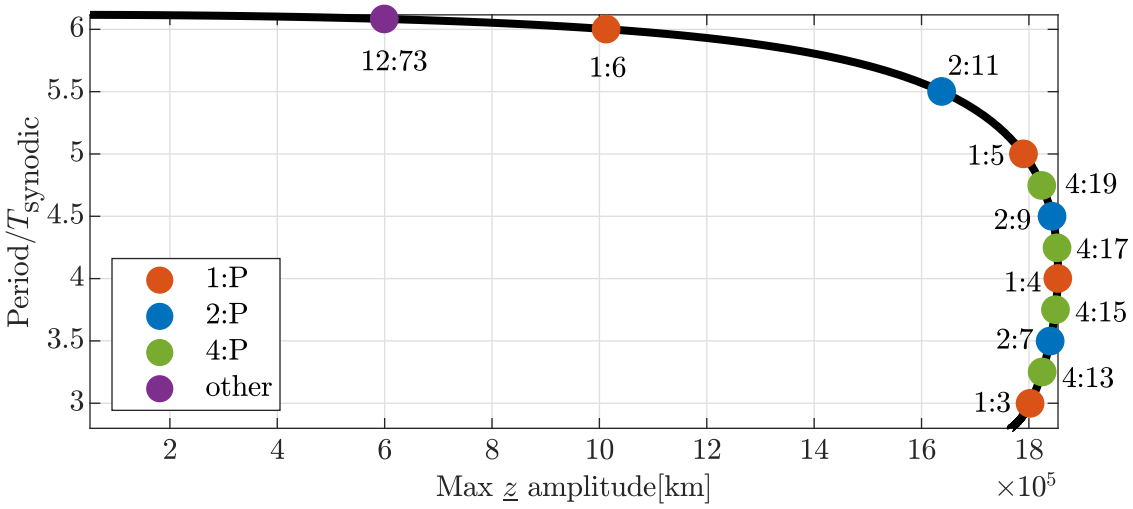


**Figure 4.47.** Synodic resonance across a representative subset of the CR3BP Sun-$B_1$ $\underline{L}_2$ halo family. The $\underline{z}$ amplitude corresponds to the dimension of the orbit when represented in the Sun-$B_1$ rotating frame.

BCR4BP using a differential corrections scheme a continuation method. However, periodicity is not enforced: the initial and final states along the corrected trajectory in the BCR4BP do not necessarily match. The differences between the methods for constructing periodic orbits and bounded methods in the BCR4BP are presented in Figure 4.48. When multiple revolutions from the same orbit are stacked together, the strategy is labeled a 'homogeneous stacking' method. This strategy is employed for constructing either periodic orbits (when the orbits stacked are synodic resonant) or quasi-periodic orbits. Previous contributions offer details for the development of 'non-homogeneous stacking' strategies, where different orbits from the CR3BP are stacked to create the initial guess in the higher-fidelity model, that is, to adjust certain characteristics of the converged final orbit, such as the perilune epoch [45] or the perilune radius [21]. This approach is typically more suitable to construct bounded motion. Bounded motion is successfully produced in the BCR4BP for both Earth-Moon and Sun-$B_1$ structures.

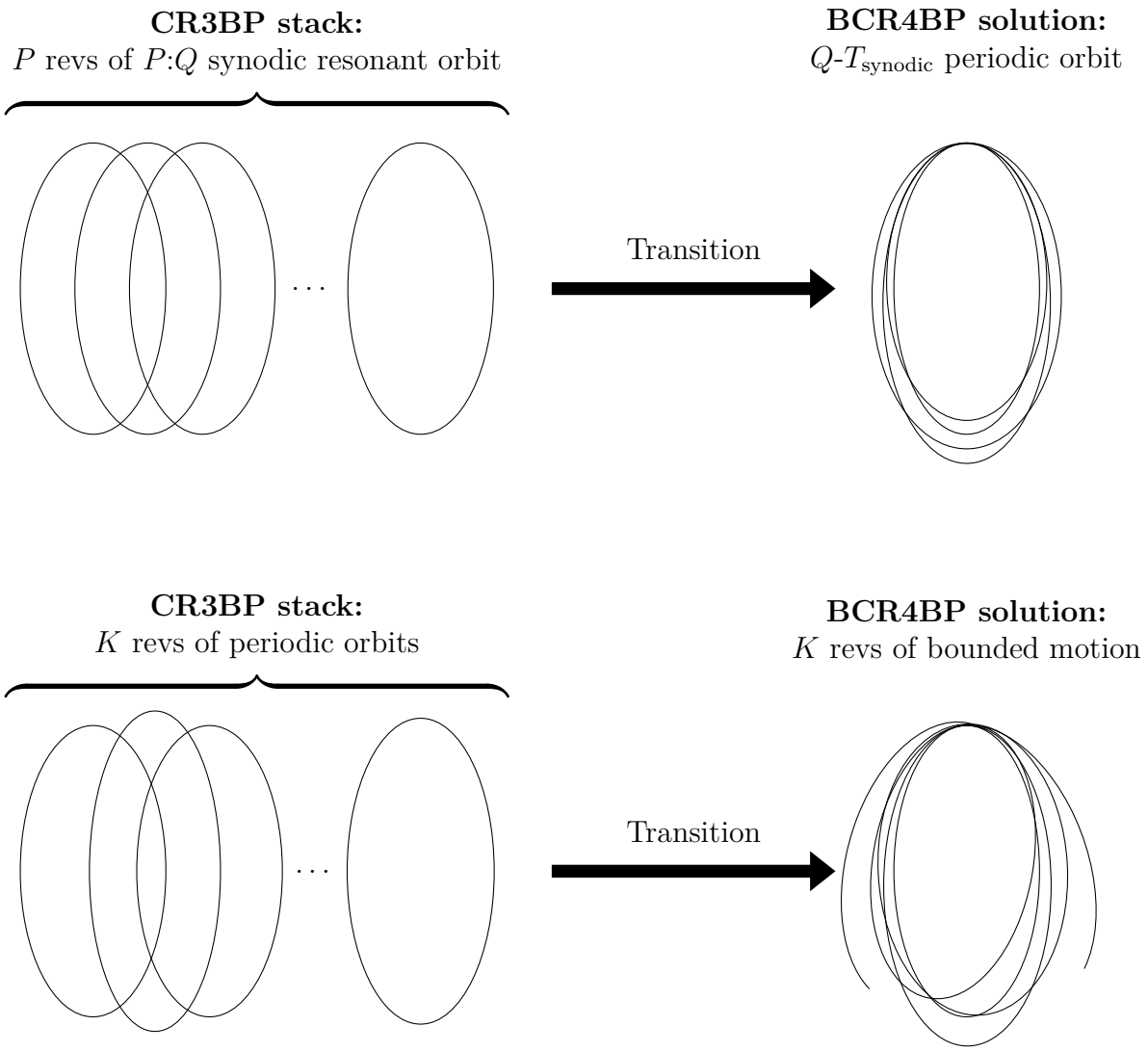


**Figure 4.48.** Methodology for constructing periodic orbits (top) and bounded motion (b) in the BCR4BP, employing a stack of orbits from the CR3BP as the initial guess

### Examples of Bounded Motions

Two illustrations of bounded motion as constructed in the BCR4BP are presented. First, an *NRHO-like* bounded motion is produced in the Earth-Moon rotating frame leveraging a non-homogeneous stacking strategy. In this investigation, a non-homogeneous stack is used to maintain the perilune radius within a specified range over multiple revolutions. An example of non-homogeneous stacking delivers the required characteristics. The goal is to

construct three revolutions of *NRHO-like* motion in the BCR4BP, with each perilune altitude within the $3,250$ to $3,575$ kilometers range. The periodicity of the solution is not strictly required in this scenario. Three orbits in the vicinity of the 9:2 synodic resonant NRHO, are selected from the CR3BP NRHOs subset, as viewed in Figure 4.49(a). The process to select the NRHOs is very dependent on the initial Sun angle. For instance, for the epoch considered, that is, $\theta = 0$ at the first apolune, the gravitational influence from the Sun tends to decrease the altitude of the next perilune. Thus, to counterbalance this effect, the second NRHO in the stack is selected such that its periapse altitude is higher than the altitude of the first orbit in the stack. The process is repeated for the subsequent orbits in the stack. The three selected orbits are then discretized, and each arc is propagated in the BCR4BP, as apparent in Figure 4.49(b). Note that the propagated trajectory is discontinuous, as expected in the BCR4BP. A differential correction process reduces position and velocity discontinuities between consecutive arcs to within an acceptable tolerance. The resulting, converged trajectory is plotted in Figure 4.50. The initial and end points along the trajectory are not co-incident, since the periodicity is not constrained. The evolution of the perilune radius along the converged solution is presented in Figure 4.51. The acceptable perilune radius region, colored in blue, is defined by the range of periapse radii from $3,250$ and

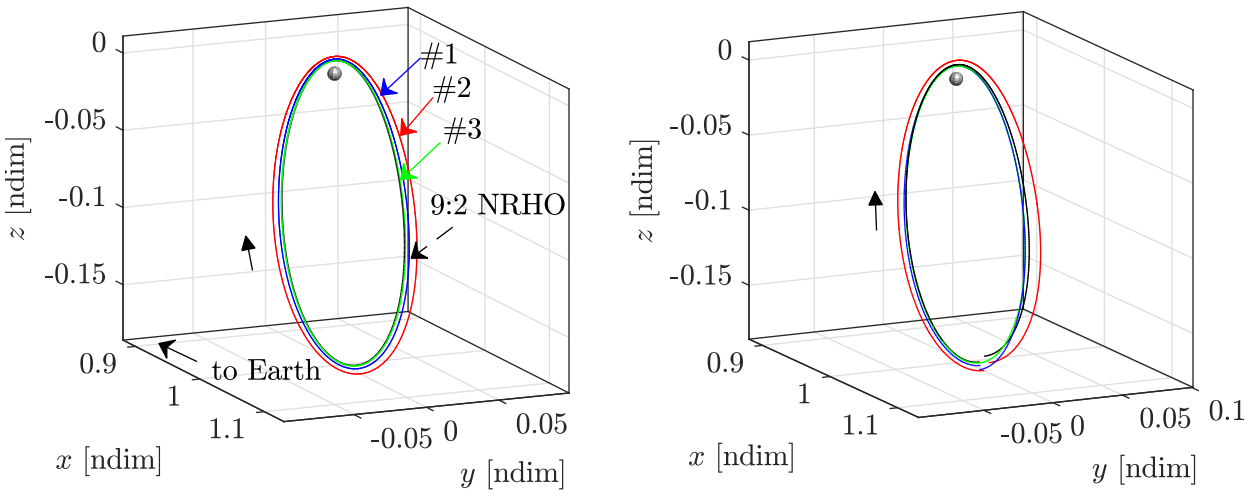


(a) CR3BP propagation

(b) BCR4BP propagation

**Figure 4.49.** Stack of three orbits of an NRHO in the CR3BP (a) and the BCR4BP (b).

3, 575 kilometers. Then, the perilune distances along each solution are denoted by markers in Figure 4.51. Using a homogeneous stack, i.e., a stack of three identical NRHOs with perilune radius equal to 3, 400 km, results in lunar periapsis radii outside of the acceptable region, as in Figure 4.51(a). However, this information is useful to help select the NRHOs in the non-homogeneous stack. The converged solution, using the non-homogeneous stack, results in three periapses within the acceptable region, as seen in Figure 4.51(b). Non-homogeneous stacking is, thus, a convenient method to produce *NRHO-like* motion with specific characteristics in the BCR4BP.

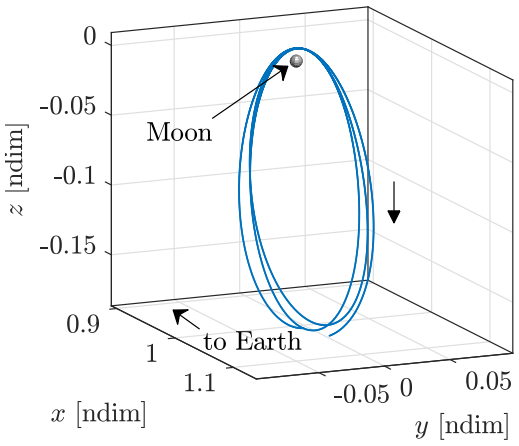


**Figure 4.50.** Converged trajectory in the Earth-Moon-Sun BCR4BP for $\theta_0 = 0°$

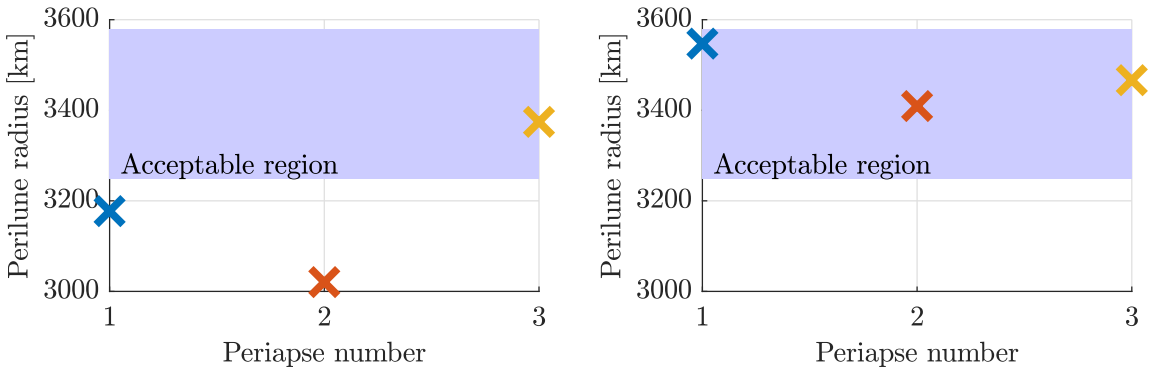


(a) Homogeneous stacking

(b) Non-homogeneous stacking

**Figure 4.51.** Radius from the Moon for the periapses of the converged trajectory using a homogeneous stacking method (a) and a non-homogeneous stacking method (b).

The second example of a quasi-periodic orbit constructed in the BCR4BP consists of bounded motion in the vicinity of Sun-$B_1$ $L_2$ halo orbits. For instance, potential orbits for upcoming space telescopes include a subset of $L_2$ Sun-$B_1$ halo orbits with maximum $z$ amplitudes less than 250,000 km. From Figure 4.47, the resonance ratio along this portion of the family is approximately equal to 6.11; no simple resonance ratio exists in this subset of the $L_2$ family of periodic orbits. Bounded motion in the BCR4BP is constructed using a homogeneous stack of thirty revolutions of a CR3BP $L_2$ halo orbit of maximum $z$ amplitude equal to $125,000$. The resulting bounded motion spans approximately 15 years and is plotted in Figure 4.52. Note that this bounded motion may be leveraging structures from a BCR4BP periodic orbit at a higher resonance ratio or from a BCR4BP quasiperiodic orbit [19], [89]. The $L_2$ equilibrium point and the $\mathbb{E}_2$ ZAC in the BCR4BP are denoted by red dots and are indistinguishable at this scale. Non-synodic resonant periodic orbits from the CR3BP are successfully transitioned as bounded motion to the BCR4BP.

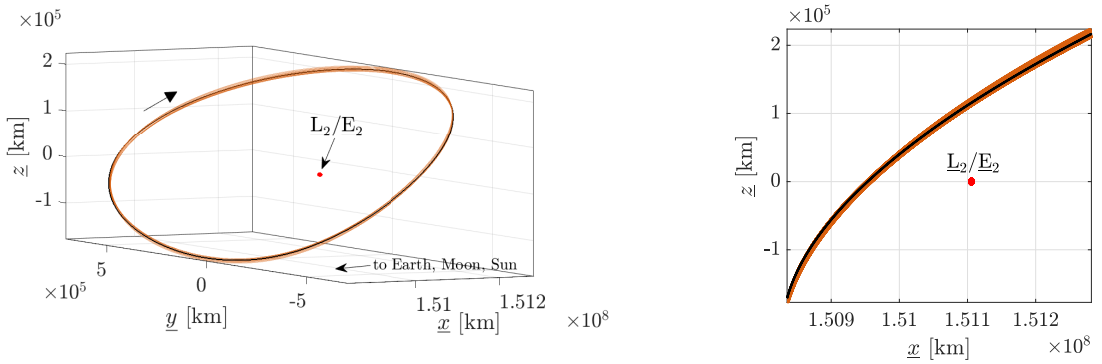


**Figure 4.52.** Isometric (a) and side (b) views of the bounded BCR4BP motion (in orange) in the vicinity of the $L_2$ CR3BP halo orbit (in black) with max. $z$ amplitude equal to 125,000 km

## 4.4 Hyperbolic Manifolds

Invariant manifolds provide a useful approximation to the nonlinear dynamical behavior in the vicinity of a reference solution. Specifically, the stable and unstable invariant manifolds associated with a periodic orbit are employed to determine flow toward and away from a

reference solution. The existence of these invariant manifolds is examined, and strategies to compute global invariant manifolds associated with periodic orbits and bounded motion are introduced.

### 4.4.1 Existence

Fixed points, i.e., equilibrium solutions or periodic orbits when examined on a stroboscopic map, possess hyperbolic manifolds of dimension equal to the dimension of the saddle mode [90]. The hyperbolic manifold includes that asymptotically approach and depart from the fixed point. The *unstable* manifold represents motion that departs from the fixed point in forward time, while the *stable* manifold reflects motion that departs from the fixed point in negative time. Flow that asymptotically departs from and arrives at a periodic orbit is available for saddle points.

While the eigenvalues associated with the matrix $\mathbf{A}$ for an equilibrium point or the monodromy matrix $\mathbf{\Phi}(t_0 + \mathbb{P}, t_0)$ for a periodic orbit of period $\mathbb{P}$ reflect the linear stability properties of the structure in question, the eigenvectors of $\mathbf{A}$ or $\mathbf{\Phi}(t_0 + \mathbb{P}, t_0)$ span the subspace of each mode. However, the span of the eigenvectors defines *local* manifolds, as they are computed for the linearized dynamics with respect to the fixed point. While the local manifolds provide a useful approximation of the motion near a fixed point, they may only be representative of the nonlinear dynamical flow in a small region around the fixed point. Thus, the linear solutions are 'globalized', i.e., transitioned to the nonlinear regime. As an illustration, consider the local and global manifolds associated with the $L_1$ equilibrium point of the Earth-Moon CR3BP in Figure 4.53. A frame centered at $L_1$ is defined in position space in Figure 4.53(a) and in velocity space in Figure 4.53(b); the fixed point is located at the origin and is denoted by the grey asterisk. The local manifolds, $W_{loc}$, are computed using the $\mathbf{A}$ matrix associated with $L_1$, and are denoted by the thin arrows in Figure 4.53. A superscript indicates whether the stable manifold $s$, or the unstable manifold $u$ is considered, as well as the side of the manifold[7]: $+$ for flow on the positive $x$ side and $-$ for flow on the negative $x$ side. The global manifolds $W$ are also considered; an

[7]↑If $\bar{\nu}$ is an eigenvector of the $\mathbf{A}$ matrix, then $(-\bar{\nu})$ is also an eigenvector.

initial state is first computed along the local manifold close to the equilibrium point and propagated using the nonlinear dynamics. The resulting trajectories along the global red manifold, $W^{u-}$ and $Wu+$, and along the stable manifold, $Ws-$ and $Ws+$, appear as the thick red and blue lines, respectively, in Figure 4.53. The local and global manifolds are than at the equilibrium point in both position space in Figure 4.53(a) and velocity space in Figure 4.53(b). However, as the distance to the equilibrium point along the trajectories increases, the global and local manifolds begin to diverge. This divergence is expected, as the approximation of the dynamical flow provided by the linearized dynamics tends to break away from the linearization point. Global manifolds in the nonlinear dynamical model are straightforwardly transitioned from the local manifolds provided by the linearization of the dynamics about a fixed point.

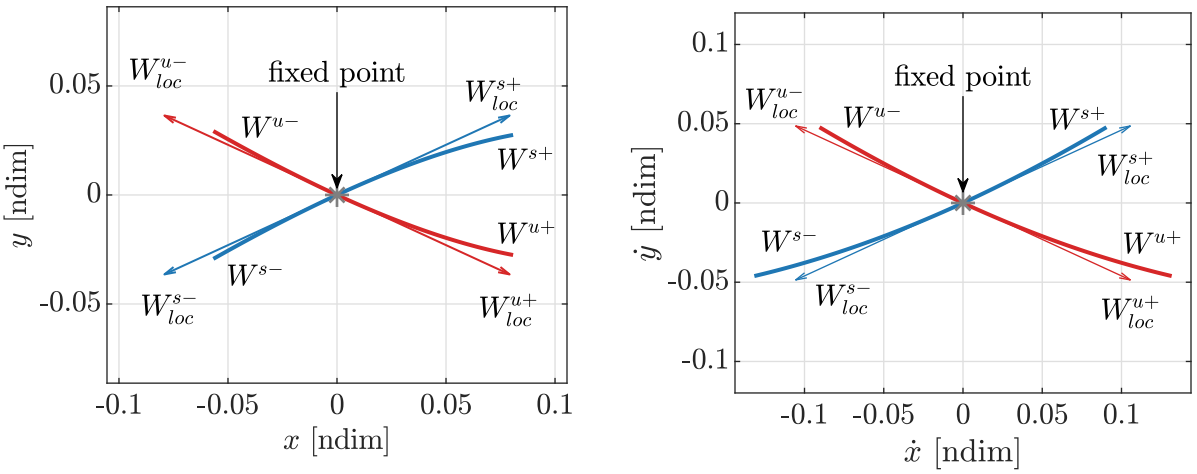


(a) Position space

(b) Velocity space

**Figure 4.53.** Local and global manifolds associated with a fixed point of the CR3BP in position (a) and velocity (b) spaces. Red lines correspond to the unstable manifold and forward time propagation. Blue lines correspond to the stable manifold and backward time propagation.

The evolution of the global manifolds is explored within the context of a time-dependent dynamical model, the BCR4BP. Recall that the Lagrange points of the CR3BP are transitioned to either instantaneous equilibrium solutions or periodic orbits in the BCR4BP. The global manifolds associated with the collection of $\mathrm{E}_1(\theta)$ instantaneous equilibrium points are

investigated in Figure 4.54. The ZAC is discretized into a set of points and the hyperbolic local manifolds are computed using the **A** matrix at each point. Initial states relative to the set of discretized equilibrium point are generated along these local manifolds and are propagated using the nonlinear equations of motion from Equation (2.4). The resulting trajectories appear in Figure 4.54(a); trajectories along the stable manifold are colored in blue while trajectories along the unstable manifold are plotted in red. Thick lines denote the global stable and unstable manifold associated with the $L_2$ equilibrium point in the Earth-Moon CR3BP. Note that the local manifolds at computed at snapshot in time; the computation of each manifold includes information about the *location* of the Sun, but not its *motion* within the Earth-Moon rotating frame. The perturbing effects of the motion of the Sun becomes apparent when comparing Figure 4.54(a) with the Figure 4.54(b). In the Figure 4.54(b), the Sun angle is maintained constant along each propagated arc, that is, a fictitious and time-independent version BCR4BP where the Sun is fixed within the Earth-Moon rotating frame is created for each instantaneous equilibrium point along the ZAC. Using this fictitious dynamical model, the boundedness of each of the manifold 'tubes' is apparent in Figure 4.54(b). By comparison, the trajectories along the manifolds computed in the BCR4BP accounting for the motion of the Sun are visibly more disturbed, as apparent in Figure 4.54(a). Note that such distortion does not appear for the global manifold associated with periodic orbit. While the dynamics of local manifolds associated equilibrium points are described by the constant **A** matrix from Equations (3.6) and (3.7), the local manifolds of periodic orbits are computed using the $\mathbf{\Phi}(t_0 + \mathbb{P}, t_0)$ monodromy matrix. The monodromy matrix a linearization of the dynamical flow that maps perturbation in the initial state to perturbation after one period $\mathbb{P}$ of the orbit. Since this map includes first-order information about the motion of the Sun in the Earth-Moon frame, the global manifolds are not significantly distorted (although they do diverge from the local manifolds at a certain distance from the periodic orbits). Figure 4.54 illustrates some particularities associated with the computation of global manifolds for certain structures in the time-dependent, periodic BCR4BP.

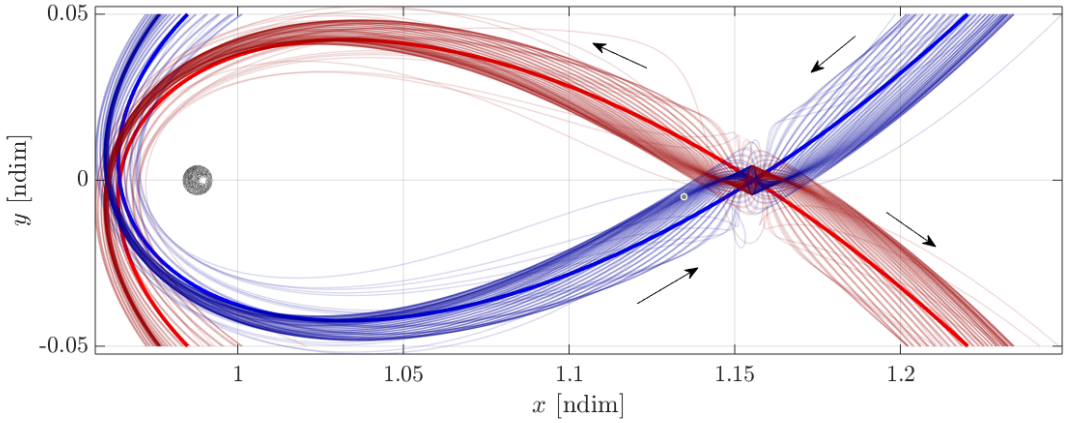


(a) BCR4BP

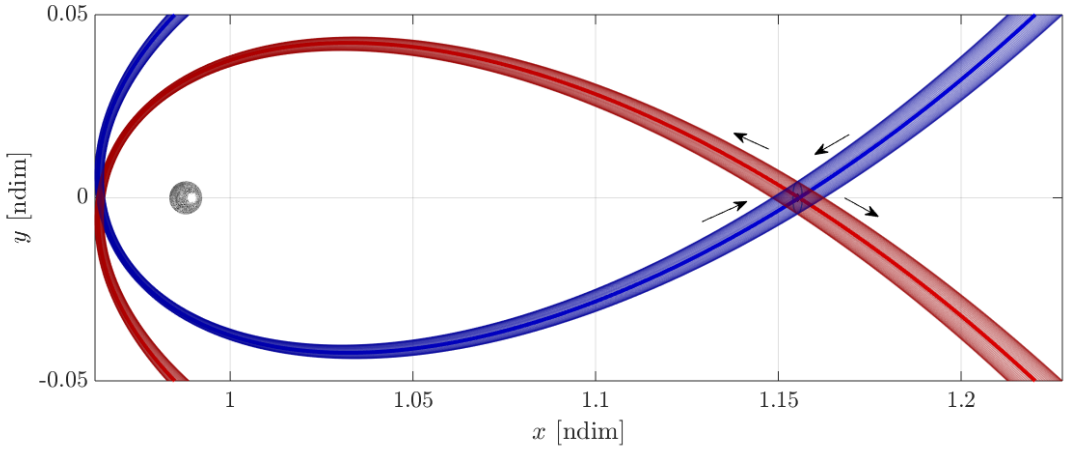


(b) BCR4BP, fixing the Sun at $t = 0$ in the Earth-Moon rotating frame.

**Figure 4.54.** Stable and unstable manifold associated with the $\mathbb{E}_2$ ZAC in the BCR4BP (a), and in the BCR4BP with the Sun fixed in the Earth-Moon rotating frame (b). The thick lines denote the global manifolds associated with $L_2$ in the Earth-Moon CR3BP.

### 4.4.2 Computation for Periodic Orbits

A method to compute trajectories along the global manifolds of periodic orbits in the BCR4BP is presented. The stable and unstable manifolds associated with a periodic orbit form surfaces that asymptotically approach and depart every point along the period orbit, respectively. Thus, a 'mesh' of trajectories along each of the manifolds is typically computed

to approximate this surface. The following steps are employed to create the mesh of trajectories along the manifold. First, the linearly unstable periodic orbit is discretized into a set of points. The monodromy matrix, $\mathbf{\Phi}(t_0 + \mathbb{P}, t_0)$, is computed for each of these points, and the eigenvectors, $\bar{\nu}_s$ and $\bar{\nu}_u$, associated with the stable and unstable subspaces are identified. Then, for each state $\bar{q}^*$ along the discretized periodic orbit, an initial guess along the local stable manifold, $\bar{q}$, is computed as

$$\bar{q} = \bar{q}^* + \kappa \frac{\bar{\nu}_s}{\|\bar{\nu}_s\|} \tag{4.13}$$

where $\kappa$ is a scaling factor, or 'step' size. The size of $\kappa$ must be chose appropriately; a value too large results in a state $\bar{q}$ for which the assumption of tangency between the local and global manifolds is not true. However, a value too small of $\kappa$ yields a state $\bar{q}$ that is departs (or arrives, for backward time propagations) the fixed point after a large propagation time; for such cases, the numerical error buildup needs to be considered as well. In this analysis, a value of $\kappa = 10^{-7}$ is employed to compute trajectories along the manifolds of Sun-$B_1$ orbits, and a value of $\kappa = 10^{-4}$ for the manifolds associated with Earth-Moon orbits. Note that the value of $\kappa$ depends on the system, as the characteristic length and mass ratios affect the scaling. For each point along the discretized periodic orbit, the initial state along the *local* stable manifold computed in Equation (4.13) is propagated in negative time using the nonlinear set of equations of motion in Equation (2.4) or Equation (2.8), yielding a trajectory along the *global* manifold. Similar, the unstable manifold is globalized by computing an initial step along discretized local manifold,

$$\bar{q} = \bar{q}^* + \kappa \frac{\bar{\nu}_u}{\|\bar{\nu}_u\|} \tag{4.14}$$

and propagated using the nonlinear equations of motion in Equation (2.4) or Equation (2.8). Additionally, recall that if $\bar{\nu}$ is an eigenvector of an eigenvalue problem, then any vector $c\,\bar{\nu}$, where $c$ is a scalar, is also an eigenvector. Selecting $c = -1$, the other 'side' of the manifold surface is obtained. The global manifolds associated with a periodic solution are

approximated using a discrete set of initial conditions along the local manifolds, as well as numerical integrations of the nonlinear equations of motion.

To illustrate this method, the stable and unstable manifolds associated with the 2:1 synodic resonant $L_2$ Lyapunov orbit in the BCR4BP are constructed. Trajectories along the global manifolds are computed for a discrete set of points along the periodic orbits. The resulting trajectories are plotted as viewed in configuration space in the Earth-Moon rotating frame in Figure 4.55(a). Trajectories along the stable and unstable manifolds are plotted in shades of blue and red, respectively; the underlying periodic orbit appears in black. The trajectories are propagated until they intercept one of two defined hypersurfaces. Trajectories along the global manifold on the 'left' side, i.e., arriving from or departing toward the Earth, are propagated until they intercept a hyperplane located at $x = 0.7$ ndim; this hyperplane appears as a vertical line in configuration space in Figure 4.55(a). Trajectories along this half-manifold are colored in dark blue and red. The second hypersurface is defined for the

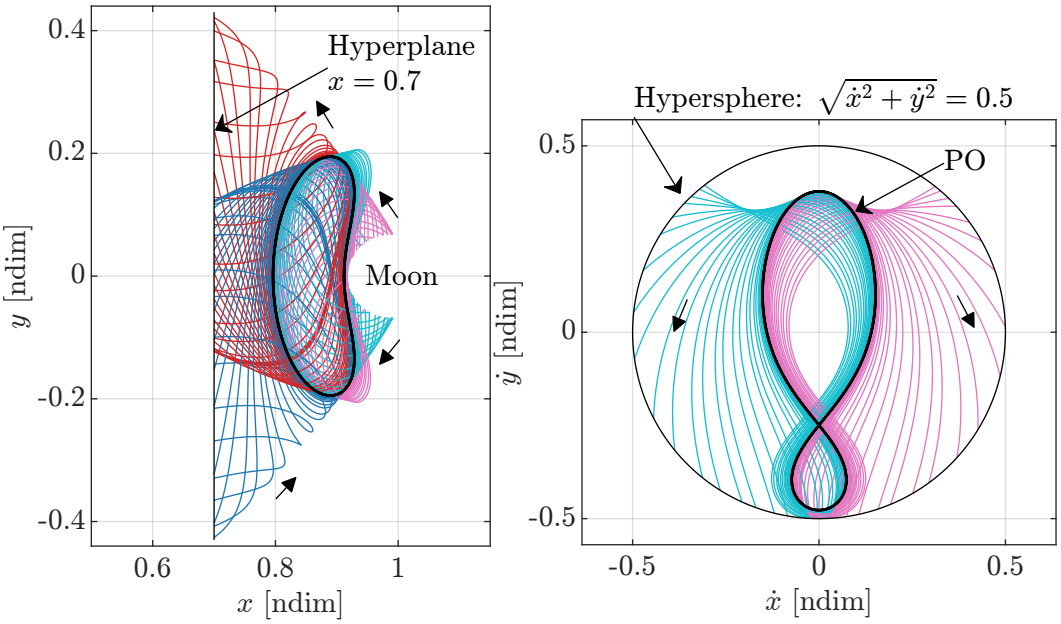


(a) Position space (b) Velocity space

**Figure 4.55.** Stable (blue hues) and unstable (red hues) manifolds associated with the $L_2$ 2:1 synodic resonant Lyapunov orbit in the BCR4BP. The manifolds are propagated to two arbitrary hypersurfaces located at $x = 0.7$ ndim and $\sqrt{\dot{x}^2 + \dot{y}^2} = 0.5$ ndim.

trajectories along the manifolds on the 'right' side of the periodic orbit, i.e., the manifolds flowing towards or away from the Moon. This hypersurface is defined as $\sqrt{\dot{x}^2 + \dot{y}^2} = 0.5$, i.e., the trajectories along the global manifolds are propagated in backward and forward time until the magnitude of their rotating velocity reaches the value of 0.5. In Figure 4.55(a), trajectories on the right side of the periodic orbit, colored in cyan and pink, all appear to intercept an ellipse around the Moon. The dimensions of this ellipse are determined by the energy-like relationship in Equation (2.7). However, the defined hypersphere is directly visible when the motion is represented in the rotating velocity space, as in Figure 4.55(b). The periodic orbit is denoted by the thick black curve, and the trajectories along the stable and unstable manifold are colored in cyan and pink, respectively. The trajectories are propagated until they intercept the hypersphere, which appears as a circle centered at the origin with radius equal 0.5 ndim in velocity space. The 'mesh' approximation of the manifold surfaces is apparent in Figure 4.55. When selecting a larger set of points along the periodic orbit, the resulting trajectories fill the space between the existing trajectories in Figures 4.55(a) and 4.55(b); as the number of point tends to infinity, the manifold complete surface is obtained. An approximation of the manifold surfaces is constructed by computing trajectories along the global manifolds for a range of states along the periodic orbit.

### 4.4.3 Computation for Bounded Motion

A method for computing the global manifolds associated with unstable bounded motion as constructed in Section 4.3.6 is introduced. First, note that the concepts of linear stability, and thus, of local and global manifolds, are defined in this document within the context of precisely periodic orbits. The monodromy matrix, that is, the state transition matrix for one orbital period, is not defined for bounded motions as the period is undefined too. However, for bounded motion in the vicinity of a precisely periodic, each revolution along the quasi-periodic orbit may be approximated as periodic. Thus, an approximate state transition is computed, approximate manifolds are constructed to estimate the flow arriving and departing from the bounded motion.

The computation of the local approximate manifold directions, i.e., the eigenvectors associated with the approximate monodromy matrix, differs from the computation performed for periodic orbits. For a periodic orbit of period $\mathbb{P}$, as the blue orbit in Figure 4.56(a), the monodromy matrix is defined as the state-transition $\mathbf{\Phi}$ between the initial time, $t_0$, and one orbital period downstream, $t_0 + \mathbb{P}$. The directions of the local manifolds are then evaluated as the right eigenvectors associated with the monodromy matrix, that is, $\bar{\nu}_S$ and $\bar{\nu}_U$.

A different method is employed for computing the approximate manifolds associated with $K$ revolutions of bounded motion, as in Figure 4.56(b). First, the bounded is divided into multiple arcs that may be approximated as periodic. This partition is typically accomplishing by using the orbital period of the underlying orbit employed for the homogeneous stack to separate the trajectories into arcs. (Note that this process is extendable to bounded motions constructed with a non-homogeneous stacking method; rather than a unique value, a range of periods is considered for the partition.) In Figure 4.56(b), the converged bounded motion is divided into revolutions of different colors. For each of these non-periodic revolution, an approximate monodromy matrix $\tilde{\mathbf{\Phi}}_{\mathrm{i}}(t_{\mathrm{i}}, t_{\mathrm{i}-1})$ is computed. Assuming that a homogeneous stack of the underlying $\mathbb{P}$-periodic orbit, represented by the black dashed line in Figure 4.56(b), is employed, the propagation time for the approximate monodromy matrix is $t_{\mathrm{i}} - t_{\mathrm{i}-1} = \mathbb{P}$. The local manifolds are then approximated by computing the eigenvectors $\tilde{\bar{\nu}}_S$ and $\tilde{\bar{\nu}}_U$ associated

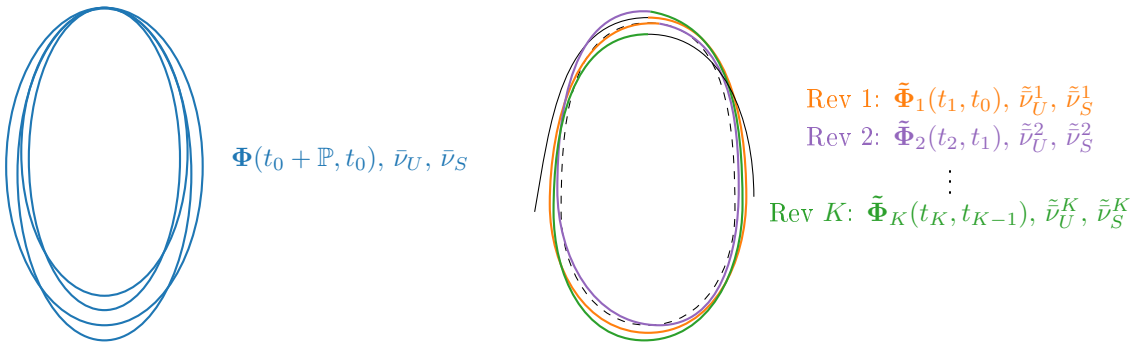


(a) Periodic orbit (b) $K$ revolutions of bounded motion

**Figure 4.56.** Differences between the computation of the monodromy matrix $\mathbf{\Phi}$ and eigenvectors $\bar{\nu}$ for a periodic orbit of period $\mathbb{P}$ (a), and the computation of the approximate monodromy matrices $\tilde{\mathbf{\Phi}}$ and approximate eigenvectors $\tilde{\bar{\nu}}$ for a $K$ revolutions of bounded motion.

with the $\mathbf{\Phi}(t_{\mathrm{i}}, t_{\mathrm{i}-1})$ matrix. The departing and arriving flow into bounded motion associated with unstable periodic orbits is approximated on a revolution-to-revolution, employed the orbital period of the underlying periodic orbit to perform the partition.

# 5. CISLUNAR-TO-HELIOCENTRIC TRANSFERS

## 5.1 Problem Formulation

A comprehensive knowledge of the dynamical structures identified in the BCR4BP simplifies the preliminary design process for transfers between the Earth-Moon system and the Sun-$B_1$ system. To illustrate the use of the dynamical structures from the BCR4BP to design transfers, consider a servicing mission from the 9:2 synodic resonant $L_2$ NRHO to various $\underline{L}_1$ and $\underline{L}_2$ halo orbits. With the recently launched James Webb Space Telescope [91] and the upcoming Nancy Roman Space Telescope [92], opportunities for missions between cislunar space and heliocentric space will arise in the near future. In this investigation, the round-trip servicing trajectories are required to originate and end in the Earth-Moon 9:2 NRHO. Recall that the 9:2 synodic resonant $L_2$ NRHO is the candidate baseline orbit for the Gateway facility [41] and is intended to serve as a stepping location to destinations beyond the Earth-Moon vicinity. The intermediate destination for the round-trip trajectory is a $\underline{L}_1$ or $\underline{L}_2$ Sun-$B_1$ halo orbit. A flowchart detailing the phases of the trajectory construction procedure appears in Figure 5.1. The trajectory arc from the Earth-Moon NRHO to the Sun-$B_1$ halo orbit is denoted the 'outbound leg', while the arc from the heliocentric halo to the 9:2 synodic resonant $L_2$ NRHO is labeled the 'inbound leg'.

The parameters along each phase of the transfer are detailed. The phasing of the cislunar orbit, that is, the 9:2 synodic resonant $L_2$ NRHO, is fixed for both the outbound and inbound parts of the transfer. Consistent with the baseline NRHO for the Gateway facility, the phase of the 9:2 NRHO is selected such that the distance to the Earth shadow is maximized, providing an entirely Earth eclipse-free trajectory. By fixing the phase of the NRHO for both the outbound and inbound legs, returning to the same phase as the Gateway vehicle facilitates an eventual rendezvous after arrival. The departure and arrival locations along the NRHO are free variables in the design process. However, it is necessary that certain regions likely are excluded, such as the region near perilune due to the high relative velocity magnitudes with respect to the Moon. The phasing of the Sun-$B_1$ halo orbit is free in the initial development of the design process. Allowing the phasing and thus, the epoch, of the heliocentric orbit to vary increases the number of potential connections between heliocentric arcs and the lunar

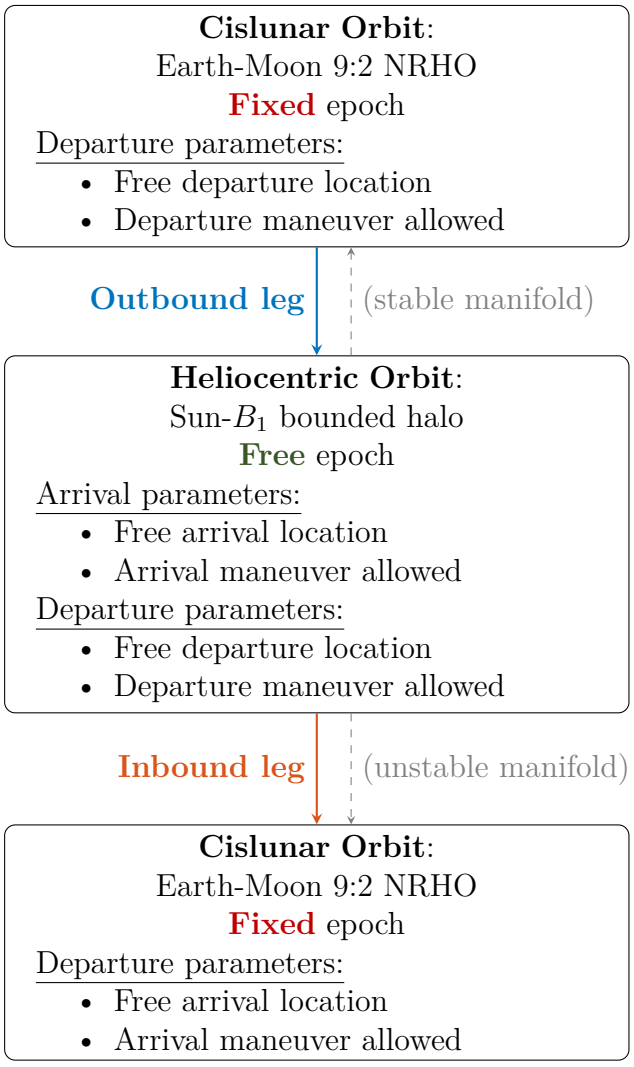


**Figure 5.1.** Flowchart for the round-trip trajectory design framework. Fixed and free parameters along each of part of the transfer are labeled. The underlying natural motion for each leg is identified in gray.

vicinity. The phasing of the heliocentric orbit may eventually be constrained if the objective is a rendezvous with an object, for instance, a specific solar observatory or space telescope in orbit. Similar to the cislunar orbit, the departure and arrival locations are free. The options for the maneuvers are noted in Figure 5.1: maneuvers are allowed for departure and arrival along both the cislunar and heliocentric orbits. Finally, the grey dashed arrows in the figure detail the underlying natural motions that are leveraged for the initial guess generation.

## 5.2 Reference Orbits

Reference motions are defined in the cislunar and heliocentric spaces. In the lunar vicinity, the 9:2 synodic resonant $L_2$ NRHO that is consistent with the candidate orbit for Gateway [41], is identified as the baseline cislunar orbit. In heliocentric space, ranges of Sun-$B_1$ $\underline{L}_1$ and $\underline{L}_2$ halo orbits are selected consistently with space telescope [2]–[4] and observatories [5]. While the 9:2 synodic resonant $L_2$ NRHO exists as a precisely periodic in the BCR4BP, most of the Sun-$B_1$ CR3BP halo orbits considered are not synodic resonant; they are thus transitioned as bounded or quasi-periodic motion in the BCR4BP.

### 5.2.1 Cislunar Orbit

The selected cislunar orbit in this investigation is the Earth-Moon 9:2 synodic resonant $L_2$ NRHO as computed in the BCR4BP. The 9:2 synodic resonant $L_2$ NRHO is a potential candidate baseline trajectory for a long-term facility near the Moon due its favorable eclipse-avoidance and stability properties[41]. The 9:2 synodic resonant $L_2$ NRHO as computed in the CR3BP, plotted in black in Figure 5.2, is transitioned to the BCR4BP using continuation in the Sun mass parameter described in Section 4.3.3.

Multiple 9:2 NRHOs exist in the BCR4BP [44]; the orbit selected in this investigation is the NRHO that allows the largest relative distance with respect to the Earth shadow and is colored in blue in Figure 5.2. The position of the NRHO relative to the Earth's shadow is apparent when the motion is plotted in the Sun-$B_1$ rotating frame, in Figure 5.2(b). The period of the 9:2 synodic resonant $L_2$ NRHO in the BCR4BP is equal to exactly two synodic periods, or 9 orbital periods along the 9:2 synodic resonant $L_2$ NRHO in the CR3BP. The radius ranges corresponding to its nine perilunes (between 3,100 and 3,900 km) and apolunes (between 69,900 and 71,700 km) are consistent with the values of the CR3BP 9:2 synodic resonant $L_2$ NRHO. The Jacobi constant value remains constant along a periodic orbit in the CR3BP. Its counterpart in the BCR4BP, the Hamiltonian value, varies due to the variation of the Sun angle. For a periodic orbit in the BCR4BP, the Hamiltonian value returns to its initial value after precisely one orbital period. As a potential staging location to various

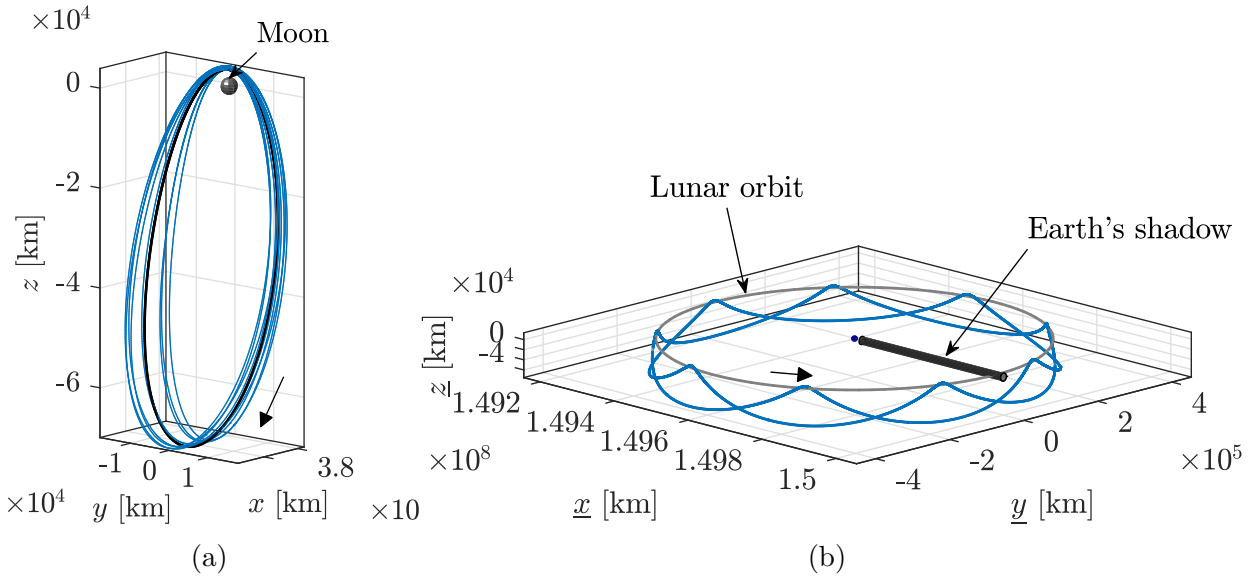


**Figure 5.2.** 9:2 synodic resonant $L_2$ as constructed in the BCR4BP in the Earth-Moon rotating frame (a) and the Sun-$B_1$ rotating frame (b). The 9:2 NRHO as computed in the Earth-Moon CR3BP is plotted in black in (b). The Earth's shadow is denoted by the gray cone in (b).

destinations from the lunar vicinity, the 9:2 NRHO as computed in the BCR4BP is selected as the reference cislunar orbit in this investigation.

Locations along the 9:2 synodic resonant $L_2$ NRHO are defined in terms of the osculating True Anomaly (TA) with respect to the Moon, as plotted in Figure 5.3(a). The osculating true anomaly is an intuitive and geometric approach in the Earth-Moon rotating frame: a true anomaly of 0° corresponds to perilune, 90°and 270°are the locations where the orbit crosses the $x$-$y$ plane, and 180°corresponds to apolune. As a comparison, the 9:2 NRHO colored in terms of time along the orbit is plotted in Figure 5.3(b). The time along the orbit is not an intuitive metric to determine a location in the NRHO due to the significant variations in velocity. The velocity is much larger near perilune than apolune. Zimovan-Spreen [43] demonstrate that visibility of the north pole of the Moon is achieved for 1.52 hours per revolution, that is, per 6.5 days. The osculating true anomaly is the metric leveraged in this investigation to identify locations along the NRHO.

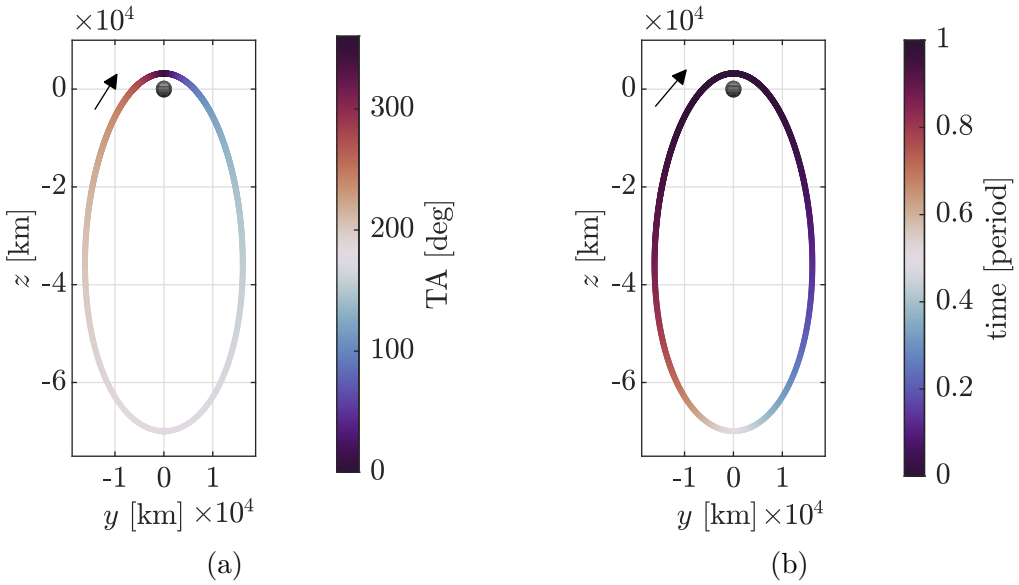


**Figure 5.3.** Osculating true anomaly (a) and time (b) along the Earth-Moon CR3BP 9:2 NRHO, as viewed in the Earth-Moon rotating frame.

### 5.2.2 Heliocentric Orbits

Two subsets of the Sun-Earth $\underline{L}_1$ and $\underline{L}_2$ halo orbit families serve as the baseline Sun-$B_1$ libration point orbits (LPOs) for this analysis. This investigation focuses on transit to and from Sun-$B_1$ northern halo orbits that reflect a limited range of $\underline{z}$ component magnitudes, as plotted in Figure 5.4. In addition to a higher associated value of an energy-like quantity, i.e., a lower Jacobi constant in the CR3BP or a lower Hamiltonian value in the BCR4BP, halo orbits with a larger maximum $\underline{z}$ component magnitude possess a higher inclination relative to the Sun-Earth-Moon plane and are, thus, more challenging to access from the Earth-Moon vicinity.

Representative orbits from each of the subsets defined in Figure 5.4 are transitioned from the CR3BP to the BCR4BP. An infinite number of periodic solutions, i.e., solutions that precisely repeat in all six position and velocity states over every revolution, exist in the CR3BP[75]. The BCR4BP is formulated to represent a time-dependent, periodic system. Therefore, only isolated periodic orbits with specific orbital periods equal to a multiple of the lunar synodic period exist rather than families with continuously varying periods[76]. Gómez et al.[20] and Boudad[44] use a continuation method to transition synodic resonant orbits

from the CR3BP to the BCR4BP. While this approach offers many advantages, it greatly restricts the number of periodic orbits available. Consider the resonance plot in Figure 5.5. The horizontal axis represents the maximum $\underline{z}$ component magnitudes for two subsets of

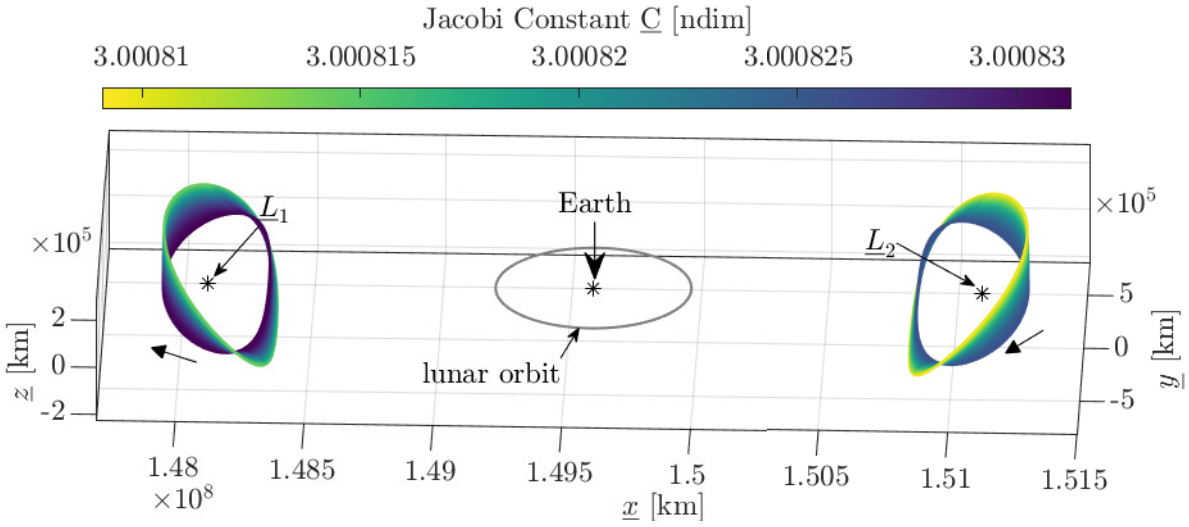


**Figure 5.4.** Representative $\underline{L}_1$ and $\underline{L}_2$ halo orbits as computed in the CR3BP with maximum $\underline{z}$ amplitude values between 0 and 250,000 km, colored as a function of the Jacobi constant value

the Sun-$B_1$ $\underline{L}_1$ and $\underline{L}_2$ halo families. The vertical axis reflects the synodic resonance ratio, that is, the ratio between the orbital period and the synodic period. The low-amplitude halo orbits of interest for this investigation are highlighted by the green box, and the dashed line identifies the resonance ratio, i.e., one orbital period per six synodic periods. Thus, the halo orbits selected in this investigation evidently do not possess a simple resonance ratio. Note that less intuitive resonance ratios, such as $^{1699}/_{278}$, may be available, but the orbits associated with such resonance ratios usually possess a large number of revolutions and are, therefore, numerically challenging to converge. In the BCR4BP, only isolated, synodic resonant orbits are exactly periodic. To overcome a lack of sufficient synodic resonant orbits in the region of interest, the alternative approach described in Section 4.3.6 is employed to leverage non-synodic resonant periodic halo orbits. Leveraging this strategy, baseline bounded motions representative of the range of orbits described in Figures 5.4 and 5.5 are successfully constructed for various epochs. Note that the halo orbits leveraged in this

investigation are linearly unstable[49], thus, discretization of the trajectory and a numerical corrections scheme are necessary to produce these long, bounded trajectories.

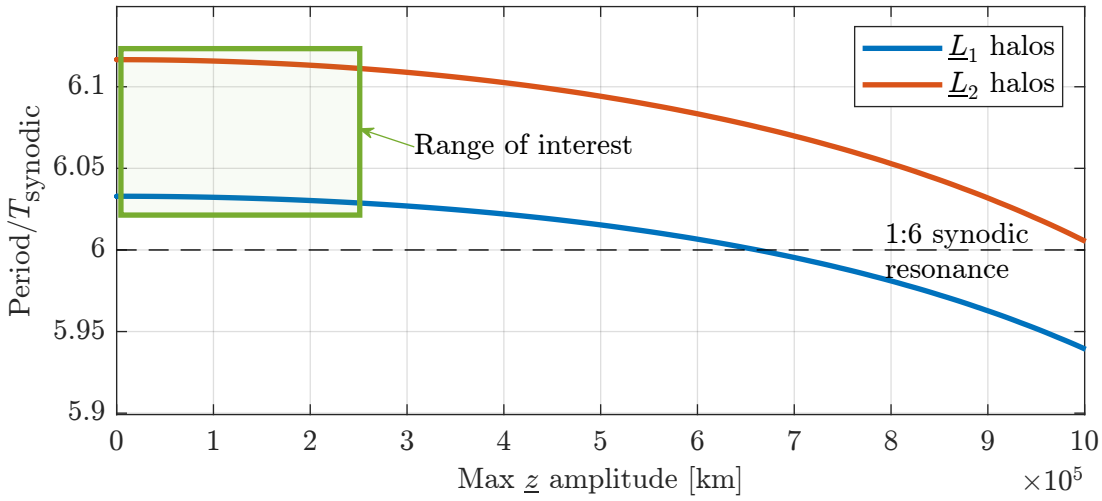


**Figure 5.5.** Synodic resonance ratio plots for a subset of the Sun-$B_1$ $\underline{\text{L}}_1$ and $\underline{\text{L}}_2$ halo families as computed in the CR3BP

### 5.2.3 Challenges

Two challenges emerge from the selection of reference motions. The first challenge is associated with the *nearly stable* nature of the 9:2 synodic resonant $\text{L}_2$ NRHO. Periodic orbits that exhibit one or multiple saddle mode possess invariant manifolds that offer low-cost transfers options to and from the periodic solutions. However, the stable and unstable manifolds associated with the orbits are not suitable for examining the flow into and out of the NRHO. The second challenge is associated with the absence of simple resonance ratios between the cislunar and heliocentric reference trajectories. Recurring, predictable transfers between two periodic orbits exists when the ratio of their orbital periods is an intuitive rational number. Since the cislunar 9:2 synodic resonant $\text{L}_2$ NRHO and the range of Sun-$B_1$ halo orbits are not in orbital resonance, a variety of paths must be constructed to allow regular transfers between the selected cislunar and heliocentric orbits with specific phases.

### Departure and Arrival Dynamics from the Earth-Moon NRHO

The departure dynamics from the 9:2 synodic resonant $L_2$ NRHO are investigated using tools from dynamical systems theory in the CR3BP and the BCR4BP. Although described as a 'nearly stable orbit', the 9:2 synodic resonant $L_2$ NRHO possesses a saddle mode and, thus, stable and unstable eigenvectors. A saddle mode exists for each non-zero Lyapunov exponent associated with the monodromy matrix of a precisely periodic orbit or, equivalently, for each pair of eigenvalues with terms that possess a magnitude other than one. The Lyapunov exponents and the pairs of eigenvalues associated with the 9:2 synodic resonant $L_2$ NRHO in the CR3BP and the BCR4BP are presented in Table 5.1. The NRHOs in both models present a saddle mode with associated Lyapunov exponents equal to approximately $\pm 0.5$. This saddle mode is unique in the CR3BP. Recall that this pair of unit eigenvalues in the CR3BP corresponds to the time-autonomous nature of the model [6]. In the BCR4BP, there is no pair of unit eigenvalues; for the 9:2 NRHO, a second pair of eigenvalues off the unit circle exists, as evident in Table 5.1. Thus, there is a second saddle mode associated with the 9:2 synodic resonant $L_2$ NRHO in the BCR4BP. However, the magnitude of the Lyapunov exponent associated with this saddle mode is very small (approximately 0.001). Thus, this saddle mode is neglected in this analysis, and the saddle mode with the larger magnitude of the corresponding Lyapunov exponent is labeled the dominant saddle mode.

**Table 5.1**. Lyapunov exponents and pairs of eigenvalues associated with the 9:2 synodic resonant $L_2$ NRHO in the CR3BP and the BCR4BP. Values corresponding to the dominant saddle mode are marked in bold.

| | **CR3BP** | **BCR4BP** |
|---|---|---|
| **Lyapunov exponents** | 0<br>0<br>$\mathbf{\pm 0.5157}$ | 0<br>$\pm 0.0013$<br>$\mathbf{\pm 0.5208}$ |
| **Eigenvalue pairs** | $0.6846 + \mathrm{i}\ 0.7289$<br>$0.6846 - \mathrm{i}\ 0.7289$<br>1.0000<br>1.0000<br>$\mathbf{-2.1774}$<br>$\mathbf{-0.4593}$ | $0.3581 + \mathrm{i}\ 0.9337$<br>$0.3581 - \mathrm{i}\ 0.9337$<br>1.0183<br>0.9820<br>$\mathbf{-1178.9}$<br>$\mathbf{-0.0008}$ |

The relationship between the dynamical flow near the Moon and the eigenvectors associated with the dominant saddle mode of the 9:2 synodic resonant $L_2$ NRHO is explored. The eigenvectors offer insights into the dynamical flow in the local vicinity under the assumptions of the linearized motion. The six-dimensional angle between the stable and unstable eigenvector is computed as

$$\alpha_{s/u} = \cos^{-1}\left(\bar{x}_s \cdot \bar{x}_u\right) \tag{5.1}$$

where $\bar{x}_s$ and $\bar{x}_u$ are respectively the stable and unstable unit vector associated with the 9:2 synodic resonant $L_2$ NRHO. Recall that while the eigenvalues associated with the monodromy matrix of a periodic orbit are constant, the eigenvector directions are a function of the location along the orbit at which the monodromy matrix is evaluated. Thus, this six-dimensional angle is computed along the 9:2 synodic resonant $L_2$ NRHO in the CR3BP and the BCR4BP and is plotted in Figure 5.6 as a function of the true anomaly. Near apolune, i.e., TA = 180°, the eigenvectors are oriented in distinct directions, and the angle reaches a maximum value of approximately 55 degrees. Close to the Moon, however, the angle between the stable and unstable eigenvectors is small, with a minimum value of less than 4 degrees at perilune, that is, TA = 0. The small angle indicates that the eigenvectors (and, thus, manifolds) are not well defined near perilune; for example, a numerical step along the

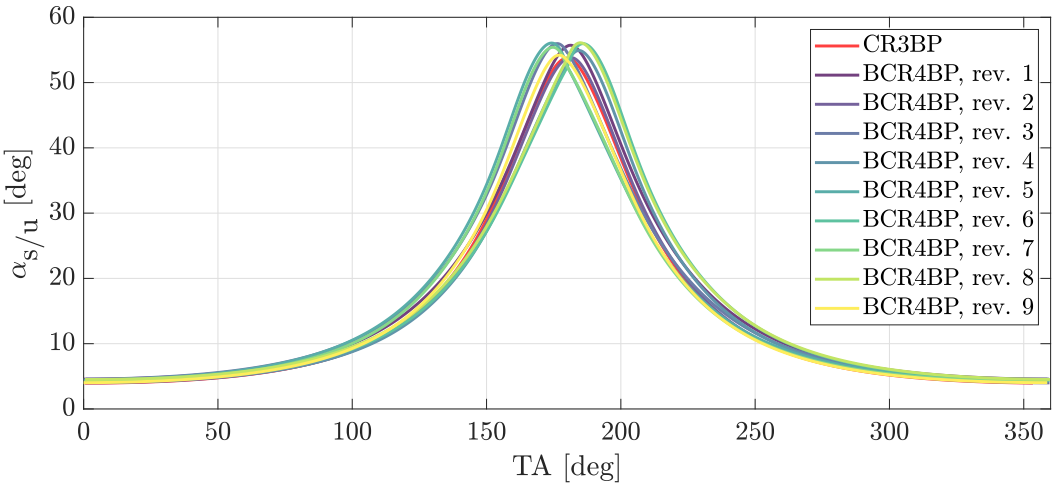


**Figure 5.6.** Six-dimensional angle between the stable and the unstable eigenvectors as a function of osculating true anomaly.

unstable eigenvector can result in a propagated step close to the unstable manifold, a step near the stable manifold, or a combination of both modes. The proximity of the eigenvector spaces represents an additional challenge in the near vicinity of the Moon, along with strong nonlinear effects and numerical challenges in both the CR3BP and the BCR4BP. Invariant manifolds associated with 9:2 synodic resonant $L_2$ NRHO do not reliably yield flow into and out of the orbit, and are, thus, not employed in the trajectory design process.

### Non-Resonance between the Selected Cislunar and Heliocentric Orbits

Recurring transfers between the cislunar and heliocentric space are sought in this analysis. In general, predictable, recurring transfers between two spacecraft along their respective orbits are available when the orbits are in orbital resonance, i.e., when there exists an intuitive ratio between their orbital periods. Consider the example in Figure 5.7. In each of the schematics, a transfer with time-of-flight $\mathcal{T}$, is colored in blue and connects two periodic orbits colored in black. In Figures 5.7(a) and 5.7(b), the two orbits are assumed to be in $^K/_L$ orbital resonance with each other; the period of final orbit is $(^K/_L)\mathcal{A}$, where $\mathcal{A}$ is the orbital period of the initial orbit. The *phase* associated with each orbit is also considered. Thus, transfers between a green spacecraft A, for instance, the Gateway in cislunar space, and a red spacecraft B, the James Webb Space Telescope for example, are depicted in Figure 5.7. An initial transfer is constructed, departing the green spacecraft in the initial orbit at $t_0$ and arriving at the red spacecraft in the final orbit at $t_0 + \mathcal{T}$. This transfer is plotted in blue in Figures 5.7(a) and 5.7(c). When the initial and final orbits are in $^K/_L$ orbital resonance, transfers between spacecraft A and B are then available at every $L\mathcal{A}$ interval, as apparent in Figure 5.7(b). However, when the initial and final orbits are not in orbital resonance, subsequent transfers, for instance at each revolution of the initial orbits, do not allow the spacecraft to rendezvous with spacecraft B on the destination orbit, as in Figure 5.7(d). The subsequent transfers in Figure 5.7(d) connect the initial and final orbits at different phases. For the spacecraft to transit between A and B, a new transfer arc must be generated for each subsequent transfer or, alternatively, or an additional transfer must be constructed along the arrival orbit to allow rendezvous with spacecraft B after insertion into the final

orbit. The ratio between the orbital periodic of two orbits provides insight into the existence of repeatable, recurring transfers.

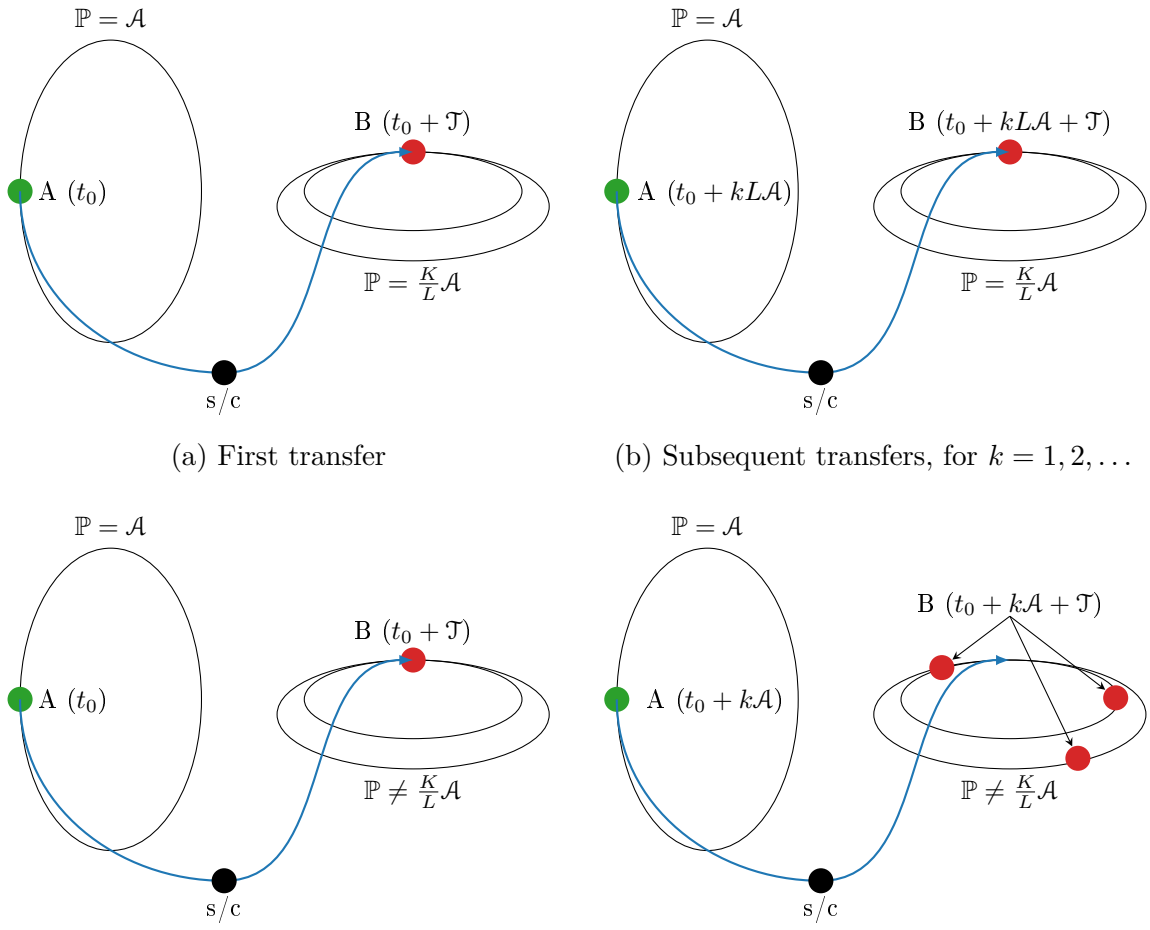


(a) First transfer

(b) Subsequent transfers, for $k = 1, 2, \ldots$

(c) First transfer

(d) Subsequent transfers, for $k = 1, 2, \ldots$

**Figure 5.7.** Transfers between two orbits that are in orbital resonance with each other (a, b) and between two orbits that are not (c, d). Predictable, recurring transfers between objects A and B are available for when the two orbits are in orbital resonance with each other.

The orbital resonance ratio between the 9:2 synodic resonant $L_2$ NRHO and the selected range of Sun-$B_1$ halo orbits is investigated. Recall that the orbital period of the 9:2 NRHO as constructed in the BCR4BP is equal to two synodic months or, equivalently, nine revolutions of the 9:2 NRHO as computed in the Earth-Moon CR3BP. Conversely, the orbital period for the $\underline{L}_1$ and $\underline{L}_2$ halo orbits as computed in the Sun-$B_1$ CR3BP ranges from 80 to 180 days. The ratio between the orbital periods of the 9:2 NRHO and the Sun-$B_1$ halo orbits

is presented as a function of the maximum $\underline{z}$ amplitude along the families of halo orbits in Figure 5.8. This ratio ranges from approximately 1.5 to 3; the horizontal dashed lines in Figure 5.8(a) indicate the 2-resonance and the 3-resonance, that is, the Sun-$B_1$ halo orbits that present an orbital period equal to precisely four and six synodic months, respectively. Note that only a small subset of Sun-$B_1$ halo orbits is considered in this investigation: the subset of halo orbits with maximum $\underline{z}$ less than or equal to 250,000 km. This subset is highlighted by the green box in Figure 5.8(a); the orbital resonance ratio computed for this range of orbits appear in Figure 5.8(b). The ratio between the periods of the selected Sun-$B_1$ halo orbits and the 9:2 NRHO as computed in the BCR4BP is approximately equal to 3.02 for the $\underline{L}_1$ orbits and 3.06 for the $\underline{L}_2$ orbits. Thus, there are no intuitive resonance ratios between the selected cislunar and heliocentric orbits; constructed trajectories are generally not extended to recurring, repeatable transfers between two orbits at specified phases.

The geometry of the Sun-$B_1$ halo orbits that present a simple orbital resonance with the Earth-Moon 9:2 NRHO is explored. The $\underline{L}_1$ and $\underline{L}_2$ halo orbits that cross the 2-resonance and 3-resonance dashed lines in Figure 5.8(a) are plotted in configuration space in Figure 5.9.

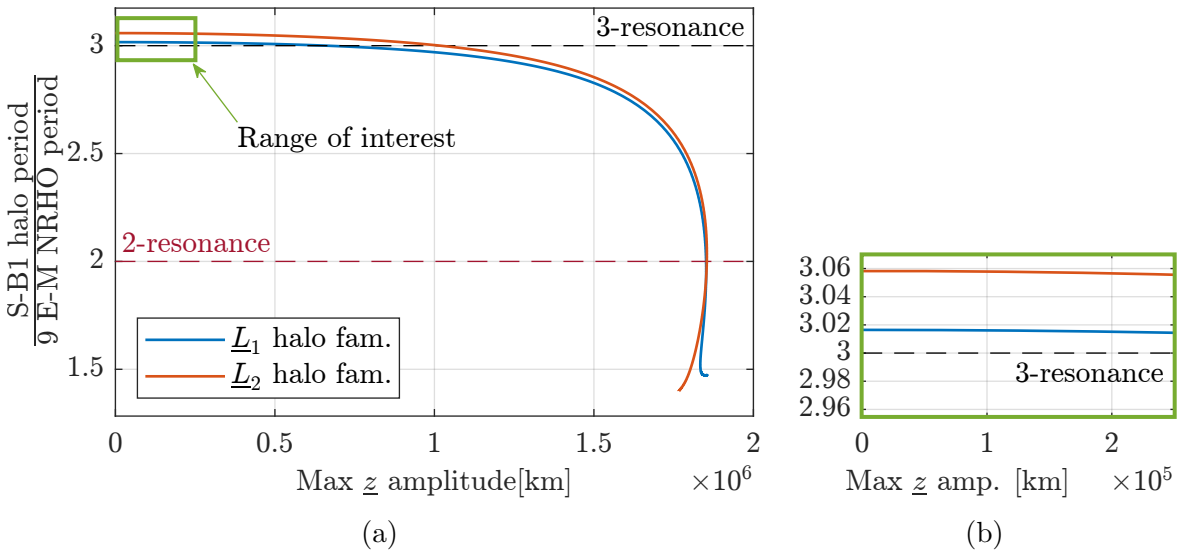


**Figure 5.8.** Resonance ratio between the Sun-$B_1$ halo orbits and the Earth-Moon 9:2 synodic resonant $L_2$ NRHO, as a function of the maximum $\underline{z}$ amplitude of the Sun-$B_1$ halo orbits (a). Zoomed view of the region of interest, i.e., Sun-$B_1$ halo orbits with maximum $\underline{z}$ amplitude less than or equal to 250,000 km (b).

The 9:2 synodic resonant $L_2$ NRHO as constructed in the BCR4BP and the lunar orbit are plotted in blue and grey, respectively. The ranges of Sun-$B_1$ halo orbits considered in this analysis are included and colored as a function of the color scheme in Figure 5.4. The Sun-$B_1$ orbits that present a 2-resonance, i.e., an orbital period precisely equal to synodic month are plotted in black in Figure 5.9. Their maximum $\underline{z}$ amplitude is approximately equal to one million kilometers, which is four times the maximum $\underline{z}$ amplitude considered for the heliocentric orbits in this analysis. The orbits with a period precisely equal to six synodic months, that is, the halo orbits presenting a 3-resonance with the Earth-Moon NRHOs are plotted in red in Figure 5.9. The maximum $\underline{z}$ component magnitude associated with these orbits is approximately equal to 1.75 million kilometers. Additionally, these two orbits interest with the rotating $\underline{x}$-$\underline{y}$ plane inside the lunar orbit, denoted by the grey circle in Figure 5.9. Note that these orbits are constructed in the Sun-$B_1$ CR3BP, in which the Moon is not included as a celestial body moving along its orbital path. The existence and geometry of these large $\underline{L}_1$ and $\underline{L}_2$ halo orbits require further analysis. The Sun-$B_1$ halo orbits that possess a 2- or a 3-resonance with the Earth-Moon 9:2 NRHO possess dimensions that are beyond the range considered in this investigation.

## 5.3 Initial Guess Generation

Initial guesses for transfers between the cislunar and heliocentric regions are generated employing the invariant manifolds on Sun-$B_1$ halo orbits as computed in the BCR4BP. Trajectories along the manifolds are propagated and perilunes within a specified to the Moon are recorded. Families of transfers from a perilune state to a specified Sun-$B_1$ halo orbits are then constructed for various parameters, such as time-of-flight and perilune radius. Perilune maps are employed to visually compile these transfers and the trajectories along the manifold. Lastly, multiple methods are introduced to select an initial guess among the collection of available arcs for a transfer to/from the 9:2 synodic resonant $L_2$ NRHO, given certain desired transfer characteristics.

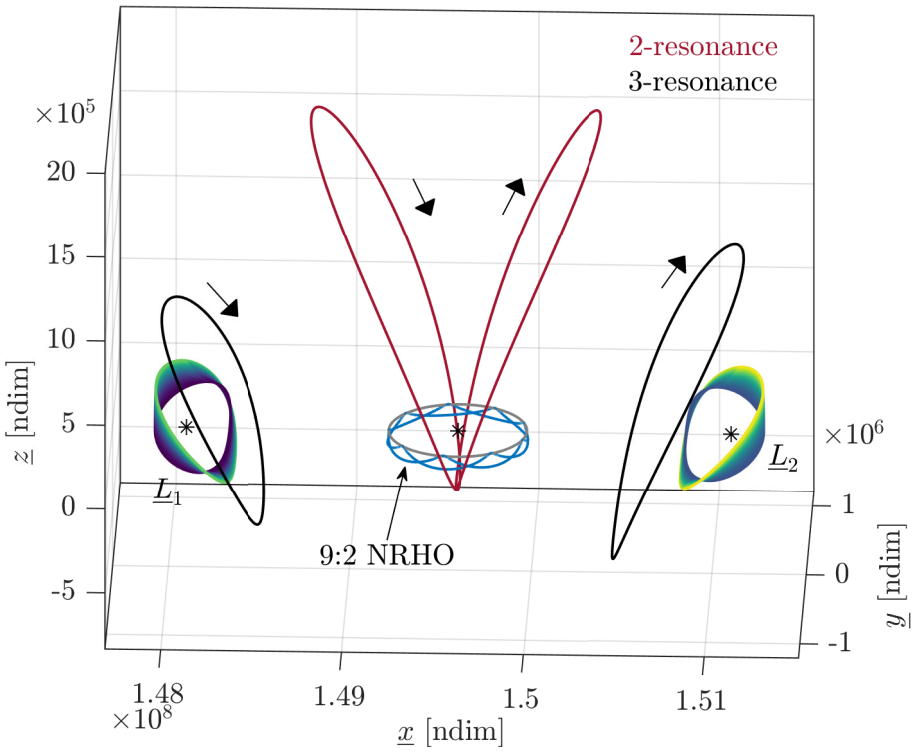


**Figure 5.9.** $\underline{L}_1$ and $\underline{L}_2$ halo orbits as constructed in the Sun-$B_1$ CR3BP that present a 2-resonance (in black) and a 3-resonance (in red) with the 9:2 NHRO (in blue), as viewed in the Sun-$B_1$ rotating frame. The range of halo orbits considered for transfers are colored following the color scheme in Figure 5.4.

### 5.3.1 Manifolds

Transfers leveraging the natural dynamics to and from the heliocentric orbits are sought. Thus, manifolds associated with the Sun-$B_1$ halo orbits are incorporated. Manifolds reflect the local ballistic flow approaching and departing an unstable periodic orbit and are frequently exploited for transfer design [27], [93]. The stability information of the range of Sun-$B_1$ halo orbits plotted in Figure 5.4. Recall that one or more nonzero Lyapunov exponents associated with a periodic solution denote instability and, thus, the existence of approaching and departing flows with respect to the orbit. All the orbits across both subsets as seen in Figure 5.4 possess one unstable mode; the range of the Lyapunov exponents for each unstable mode is summarized in Table 5.2. Note the similar range for the Lyapunov

exponents in the two subsets. Thus, approaching and departing flows from the selected orbits possess similar arrival and departure rates.

**Table 5.2**. Stability information associated with the Sun-$B_1$ CR3BP $\underline{L}_1$ and $\underline{L}_2$ halo orbits with maximum $\underline{z}$ component magnitude between 0 and 250,000 km

| Subset | Unstable mode(s) | Range of $\phi_i$ for the unstable mode(s) |
|---|---|---|
| $\underline{L}_1$ halo | 1 | $\pm 2.4207 - \pm 2.4431$ |
| $\underline{L}_2$ halo | 1 | $\pm 2.3757 - \pm 2.3961$ |

The bounded motions in the BCR4BP corresponding to the non-synodic resonant CR3BP orbits are, by definition, not periodic. Thus, there is no monodromy matrix associated with a bounded motion, and the Lyapunov exponent for the entire time-of-flight associated with a multi-revolution baseline may not be an insightful metric. However, subsequent revolutions along a bounded BCR4BP solution tend to remain close to each other, as apparent in Figure 4.52. Thus, an approximate monodromy matrix is computed for each quasi-revolution along the bounded motion, and approximate unstable and stable directions are produced. These approximate manifold directions provide adequate estimates for departing and approaching the heliocentric halo orbits for the purpose of this investigation. Note that directions other than the (approximate) unstable and stable directions, such as the maximum stretching and restoring directions [94], may offer alternative directions for the flow departing and approaching the heliocentric orbit. Approximate stable and unstable manifold directions are employed in this investigation for leveraging the natural arcs to and from the Sun-$B_1$ halo orbits.

Consider the process for the generation of an initial guess for the outbound leg, that is, the Earth-Moon NRHO to Sun-$B_1$ halo orbit transfer as defined in Figure 5.1. This process leverages the stable manifold of the Sun-$B_1$ orbit and backwards propagation. A similar strategy is employed for generating an initial guess for the inbound leg but employs the unstable manifold of the heliocentric orbit and forward propagation. The BCR4BP bounded motions, corresponding to representative Sun-$B_1$ CR3BP halo orbits from Figure 5.4, are

discretized and trajectories along the approximate stable manifold path are propagated. As these trajectories evolve toward the Earth (when propagated in negative time), a small subset of the arcs encounters the Moon. A sample of these trajectories for the heliocentric orbits on the $\underline{L}_1$ side appears in Figure 5.10. A perilune within 30,000 km of the Moon, denoted by a colored dot in Figure 5.10, occurs along each of these trajectories. The color of the lines denotes the $\underline{z}$ component magnitude of a destination orbit from among the subset of options; the out-of-plane nature of these trajectories is apparent in Figure 5.10(b). In general, multiple geometries for transfer trajectories between heliocentric orbits and the lunar vicinity are efficiently produced from back- or forward-propagation of the manifolds associated with the Sun-$B_1$ halo orbit.

Trajectories approximating the stable manifolds of the Sun-$B_1$ halo orbits offer a variety of geometries both in the heliocentric space and in the vicinity of the Moon. Sample trajectories of different geometries from the manifolds of a quasi-periodic orbit associated with a Sun-$B_1$ $\underline{L}_1$ halo orbit are plotted in Figure 5.11. Three types of geometry are identified. The first type of geometry, colored in orange in Figure 5.11, encounters an Earth flyby before departing the Earth-Moon system. Note that the Earth flyby helps accomplish part of the inclination change required to reach the Sun-$B_1$ destination orbit. The second geometry, maroon in Figure 5.11, corresponds to transfers that exit the Earth-Moon system through the Earth-Moon $L_2$ gateway. Finally, trajectories plotted in green in Figure 5.11 encounter a lunar flyby before leaving cislunar space through the Earth-Moon $L_2$ portal. In general, multiple geometries for transfer trajectories from cislunar space to the Sun-$B_1$ BCR4BP periodic orbit are efficiently produced from back-propagation of the manifolds associated with the destination orbit.

Initial guesses for transfers with a close lunar encounter are of particular interest. Dynamical structures that naturally link the vicinity of the 9:2 synodic resonant $L_2$ NRHO to the selected destination orbits are explored within the context of the BCR4BP. A sample stable manifold arc connecting a lunar flyby with the destination orbit is plotted in Figure 5.12. The 9:2 synodic resonant NRHO is transitioned from the Earth-Moon CR3BP to the BCR4BP as formulated in the Earth-Moon frame[44], [46] and is plotted in black. Proximity (in position space) between the manifold arc and the NRHO orbit is apparent.

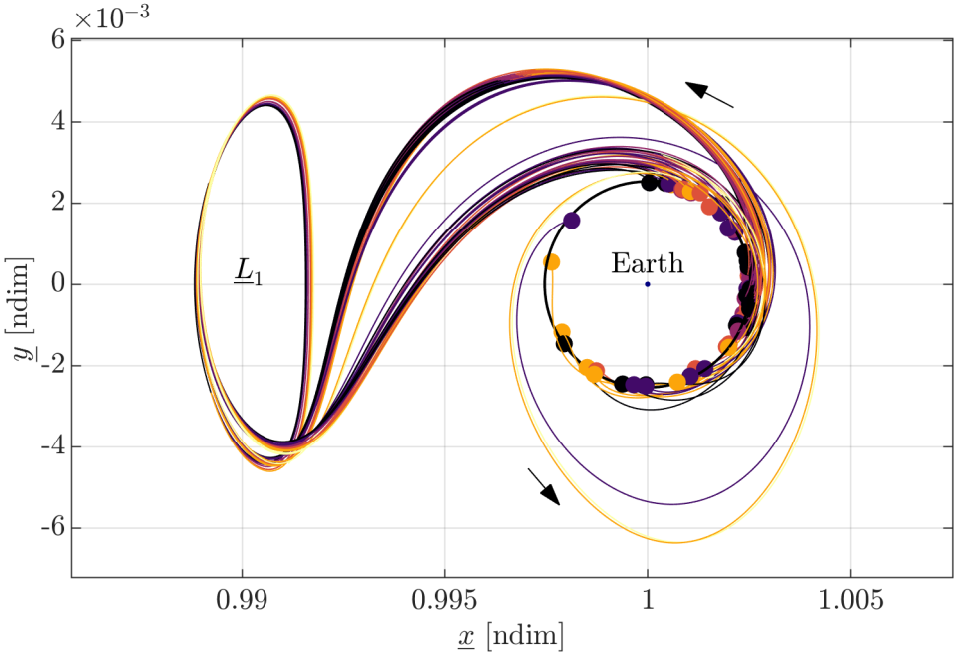


(a)

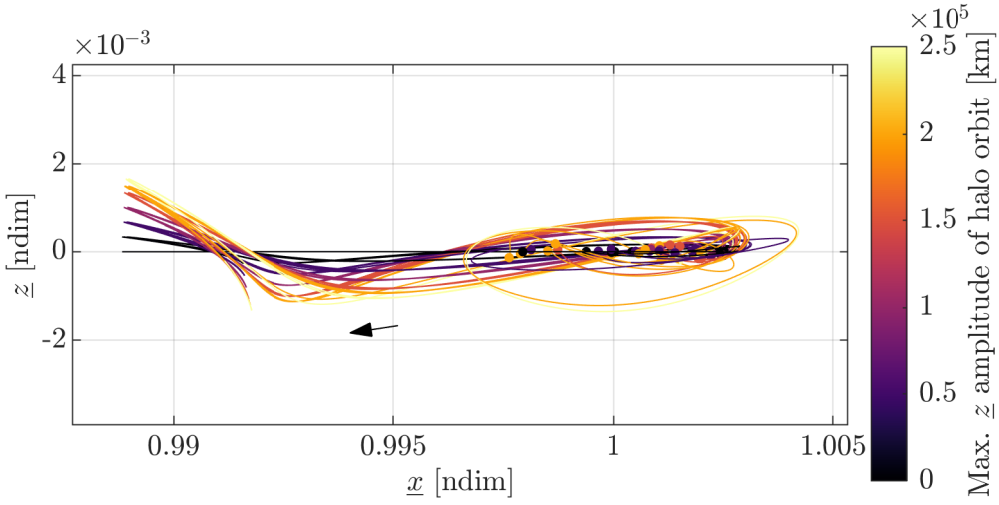


(b)

**Figure 5.10.** Trajectories along the approximate stable manifold for a various range of Sun-$B_1$ $\underline{\mathrm{L}}_1$ halo bounded motion, as computed in the BCR4BP. All the trajectories encounter a perilune within 30,000 km of the Moon; the perilunes are denoted by colored dots.

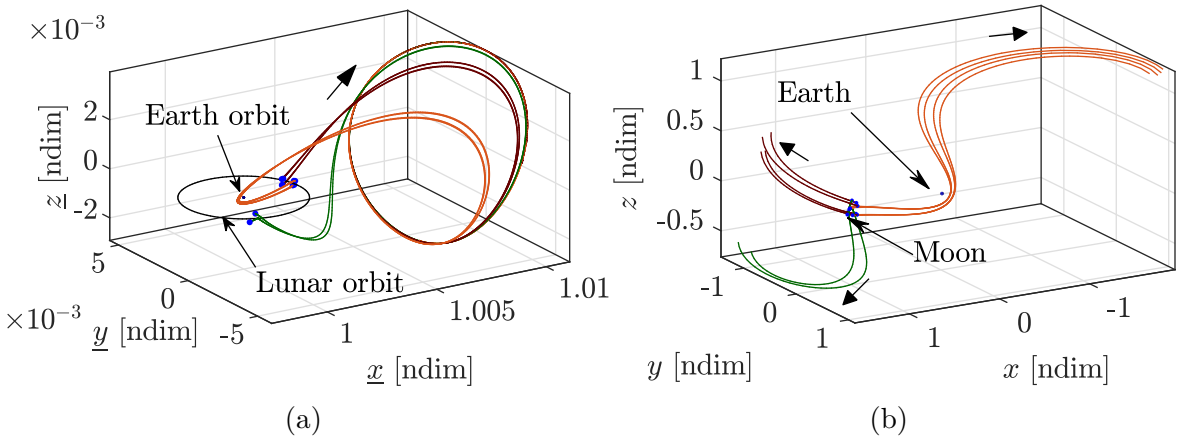


**Figure 5.11.** Various geometries of sample manifold trajectories from the lunar vicinity to a $L_1$ halo bounded motion, as viewed in the Sun-$B_1$ rotating frame (a). Zoomed-in view of the departure from the lunar vicinity, as observed in the Earth-Moon rotating frame (b).

Additionally, the geometry of the trajectory in Figure 5.12 is consistent with departure flow previously observed in the 9:2 NRHO [48]. Manifold arcs from the Sun-$B_1$ halo destination orbit, as computed in the BCR4BP, encounter the 9:2 synodic resonant NRHO and offer transfer opportunities.

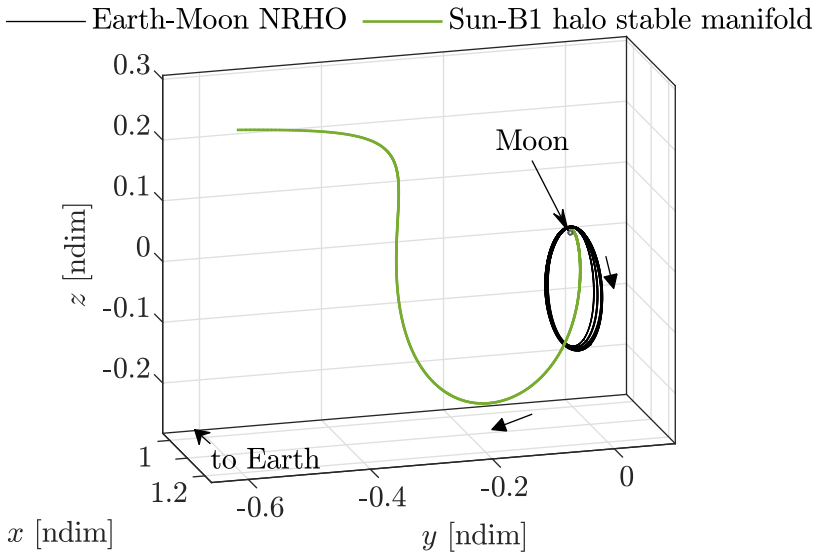


**Figure 5.12.** Stable manifold trajectory from the BCR4BP Sun-$B_1$ halo destination orbit that encounters the BCR4BP Earth-Moon NRHO, as seen in the Earth-Moon rotating frame.

### 5.3.2 Perilune Maps

Maps are generated to explore the dynamical flow between the selected range of Sun-$B_1$ orbits and the lunar vicinity. Recall that the bounded baseline motions are not precisely periodic orbits. However, they are nearly periodic when considering only a single revolution along the orbit at a time. Thus, the stable manifold directions are approximated (for flow toward the Sun-$B_1$ halo orbits) and representative trajectories are computed along each revolution. Trajectories (propagated backwards in time) that possess a perilune distance within 30,000 km of the Moon are recorded. Additional filtering of the remaining trajectories is then applied: trajectories that present a $H$ value, i.e., the energy-like quantity in the BCR4BP, that is below the block of Earth-Moon energy-like values corresponding to the $\mathrm{E}_{4/5}$ equilibrium points are excluded. This additional filter removes trajectories with a high energy value in comparison to orbits in the lunar vicinity. Representative perilunes from trajectories corresponding to both the iso-amplitude $\underline{\mathrm{L}}_1$ subset and the $\underline{\mathrm{L}}_2$ subset are plotted as viewed in the Sun-$B_1$ rotating frame in Figure 5.13(a), and colored as a function of their associated Earth-Moon energy-like values, $H$. Darker colors denote higher energy (lower $H$) values and lighter colors indicate perilunes with lower energy (higher H) values. Circle markers denote perilunes for trajectories leading to a Sun-$B_1$ $\underline{\mathrm{L}}_2$ orbit while diamond markers denote perilunes along transfers to a $\underline{\mathrm{L}}_1$ orbit. Recall that the diamond and circle markers denote state vectors along trajectories propagated backwards in time from the Sun-$B_1$ destination orbits; each point is both a perilune state and within a sphere of 30,000 km radius around the Moon. The lunar orbit is denoted by a black circle in Figure 5.13. A set of quadrants, centered at $B_1$ in the Sun-$B_1$ rotating frame and labeled in Figure 5.13, is defined in a counterclockwise manner to facilitate the investigation of the net perturbing acceleration due to the Sun, or tidal acceleration [95]. The majority of the perilunes associated with trajectories leading to the $\underline{\mathrm{L}}_1$ halo orbits are located in the right half-plane (i.e., quadrants I and IV). Transfers that present a lower energy (higher $H$ value) at perilune correspond to the diamonds markers colored in light shades of green and blue, highlighted by the red dashed circle in Figure 5.13(a) and are located close to the rotating Sun-$B_1$ $+\underline{x}$ axis. A cluster of perilunes possessing higher energy (lower $H$ value) is apparent near the rotating

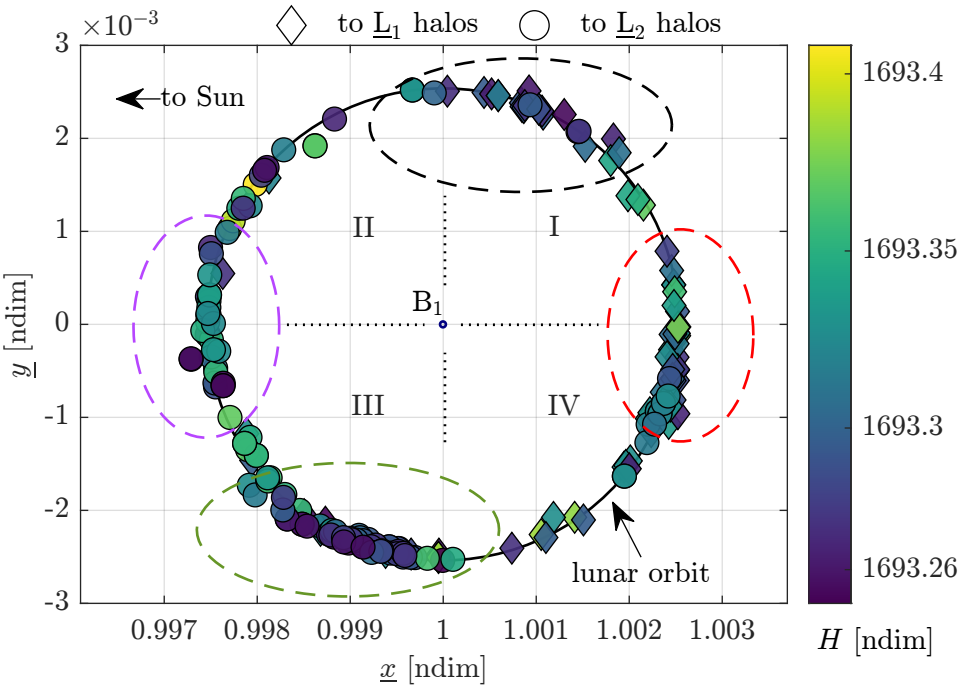


(a)

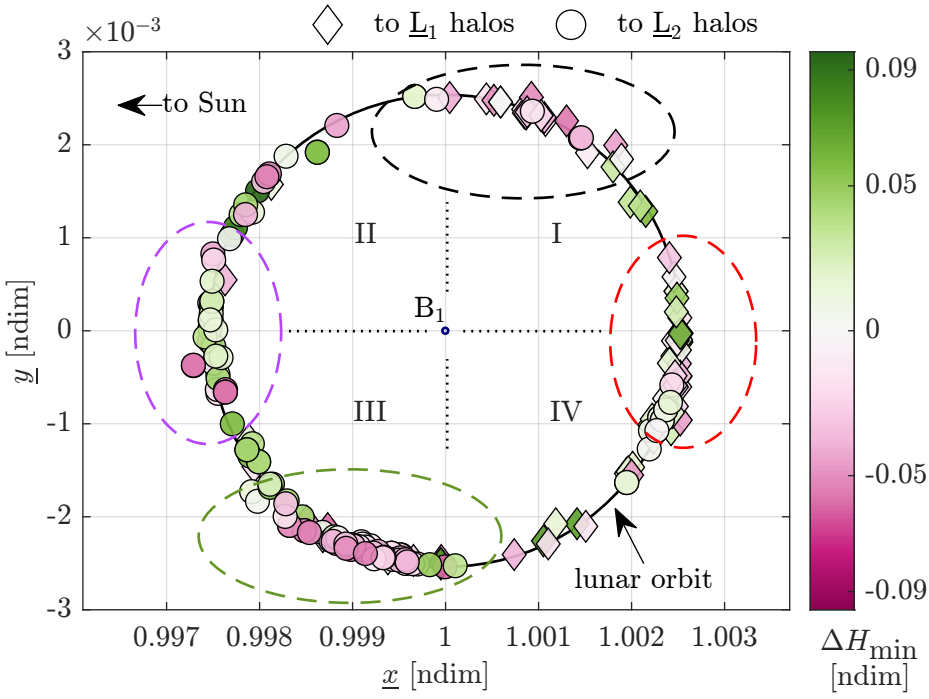


(b)

**Figure 5.13.** Perilune maps of trajectories leading to iso-amplitude Sun-$B_1$ $\underline{L}_1$ (diamond marker) and $\underline{L}_2$ halo orbits (circle marker), as viewed in the Sun-$B_1$ rotating frame. The color of the marker denotes the Earth-Moon energy-like value $H$ in (a) and the minimum isochronous $\Delta H$ with the 9:2 NRHO in (b).

$+\underline{y}$ axis, and are highlighted by the black dashed circle. In contrast, the majority of the perilunes for natural arcs that lead to the selected range of Sun-$B_1$ $\underline{\text{L}}_2$ halo orbits are located in the left half-plane, that is, quadrants II and III. Similar to the transfers reaching the $\underline{\text{L}}_1$ side, low-energy transfers, denoted by light green and light blue circles in Figure 5.13(a), are located near the rotating $-\underline{x}$ axis, and are highlighted by the purple dashed circle. However, the higher energy transfers to the $\underline{\text{L}}_2$ halo orbits are located near the rotating $-\underline{y}$ axis (dashed green circle). The perilune map in Figure 5.13(a) indicates the perilune locations for trajectories flowing toward the $\underline{\text{L}}_1$ and $\underline{\text{L}}_2$ destination orbits as oriented in the Sun-$B_1$ rotating frame (i.e., the phasing of the trajectory with respect to the Earth, the Moon, and the Sun), and the values of their associated energy-like quantities.

A map that incorporates both the energy and the phasing differences for the arcs departing the lunar vicinity with respect to the departure orbit, the 9:2 synodic resonant $\text{L}_2$ NRHO, as computed in the BCR4BP, is constructed and plotted in Figure 5.13(b). To produce this map, the minimum energy difference at a specific Sun angle, $\Delta H_{\text{min}}(\theta)$, between the departure NRHO and the perilune states that represent the departure arcs is introduced. Recall that the 9:2 synodic resonant $\text{L}_2$ NRHO as constructed in the BCR4BP possesses an orbital period equal to 2 synodic periods. Thus, for each Sun angle $\theta_{\text{i}}$, there are two distinct states along this NRHO: one at $\theta_{\text{i}}$, and one at $\theta_{\text{i}} + 2\pi$, that occur at the same Earth-Moon-Sun configuration. However, the two states are not isochronous: they occur one synodic month (or approximately 29.5 days) apart along the periodic orbit. Consider the Earth-Moon energy-like value, $H$, along the 9:2 synodic resonant $\text{L}_2$ NRHO, plotted as a function of the Sun angle, $\theta$, in Figure 5.14. The Sun angle associated with each state along the 9:2 synodic resonant $\text{L}_2$ NRHO are wrapped between 0 and $2\pi$. Thus, two separate blue curves are plotted in Figure 5.14: one line corresponds to the states along the NRHO that occur during the first synodic period ($0 \leq \theta \leq 2\pi$), and the other blue curve corresponds to the states that occur during the second synodic period ($2\pi \leq \theta \leq 4\pi$, wrapped between 0 and $2\pi$). The perilunes and apolunes along the 9:2 synodic resonant $\text{L}_2$ NRHO orbit are denoted by red triangles and inverted red triangles, respectively. Recall that the 9:2 synodic resonant $\text{L}_2$ NRHO as computed in the BCR4BP consists of 9 individual revolutions around the Moon. Apses occur at the same Earth-Moon-Sun orientation states along the orbit: i.e., for

each perilune, an apolune with the same Sun angle occurs 29.5 days apart. To compare the relative energy between the NRHO and the manifold trajectories departing from the Sun-$B_1$ halo orbits, three perilunes associated with the manifolds are selected from Figure 5.13(a) and are plotted with diamond markers in Figure 5.14. The minimum energy difference for a given Sun angle, $\Delta H_{\text{min}}$, is computed as

$$\Delta H_{\text{min}}(\theta_*) = \text{sgn}\Big(H_*(\theta_*) - H_{9:2}(\theta_*)\Big) \min \Big|H_*(\theta_*) - H_{9:2}(\theta_*)\Big| \tag{5.2}$$

where the $*$ subscript denotes quantities associated with the perilunes along the departure trajectories, i.e., the points on the map in Figure 5.13, and sgn$(\cdot)$ is the signum function. The $\Delta H_{\text{min}}$ values associated with the three selected perilunes are represented by the vertical lines in Figure 5.14. Note that this minimum energy difference quantity is signed: $\Delta H_{\text{min},1}$ is positive, while $\Delta H_{\text{min},2}$ and $\Delta H_{\text{min},3}$ are negative. The sign of $\Delta H_{\text{min}}$ determines whether energy must be gained or lost in order to connect the 9:2 synodic resonant $L_2$ NRHO and the departure arc for this specific Sun angle. Positive $\Delta H_{\text{min}}$ $(H_*(\theta_*) > H_{9:2}(\theta_*))$ implies that the perilune along the departure trajectory has a lower energy than the 9:2 synodic resonant $L_2$ NRHO state at the same Sun angle. Note the small magnitude of $\Delta H_{\text{min},2}$: its associated line in Figure 5.14 is indistinguishable at this scale. The minimum energy difference is a useful metric to measure the energy differences between departure arcs and the 9:2 synodic resonant $L_2$ NRHO, while considering their relative phasing.

The minimum energy difference for a given Sun angle is computed for all perilunes plotted in Figure 5.13(a). The perilunes are plotted in the Sun-$B_1$ rotating frame and colored as a function of the $\Delta H_{\text{min}}$, as apparent in Figure 5.13(b). Markers colored in shades of white correspond to the perilunes for transfers with an associated small magnitude for the quantity $\Delta H_{\text{min}}$. Trajectories with an associated energy higher than the value along the NRHO at the same Earth-Moon-Sun configuration, i.e., at the same Sun angle, are colored in shades of pink, while trajectories with a lower associated $\Delta H_{\text{min}}$ value are colored in shades of green. Clusters are identified as previously apparent. Perilunes presenting a low energy difference with the 9:2 NRHO states at the same Sun angle are predominantly located near the Sun-$B_1$ rotating $\pm\underline{x}$ axis (purple and red dashed circles). Perilunes with a higher associated energy

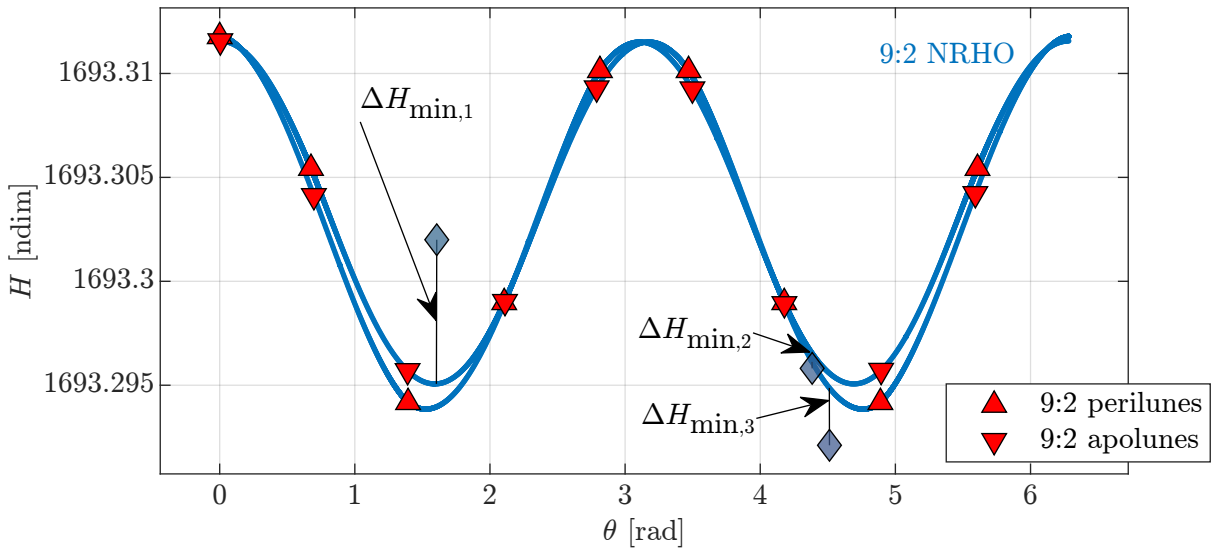


**Figure 5.14.** Earth-Moon energy-like value as a function of the Sun angle.

are primarily located off the Sun-$B_1$ rotating $\pm\underline{y}$ axis, as denoted by the pink markers in Figure 5.13(b) and are highlighted by the black and green dashed circles. Perilunes presenting a lower energy than the departure orbit state at the same Sun angle are sparser and mainly correspond to transfers to the $\underline{L}_1$ halo orbits, as evidenced by the green diamond markers in Figure 5.13(b). The perilune maps in Figure 5.13 inform the general structure of the natural flow from the lunar vicinity to the Sun-$B_1$ $\underline{L}_1$ and $\underline{L}_2$ halo orbits; these are leveraged to construct initial guesses for transfers between lunar and heliocentric spaces.

Families of transfers from the lunar vicinity to the Sun-$B_1$ libration point region are constructed using favorable stable manifolds from the Sun-$B_1$ destination halo orbit in the BCR4BP. For each member of the family, the departure state is constrained as a perilune, and an insertion maneuver into the Sun-$B_1$ arrival orbit is initially allowed. Employing a continuation process, families are then produced in two continuation parameters: departure perilune radius and time-of-flight. Maps of the resulting transfers appear in Figure 5.15. The horizontal axis represents the time of flight between the departure state at perilune and the insertion maneuver at the Sun-$B_1$ orbit. The vertical axis corresponds to the radius from the Moon to the perilune departure state. Each dot corresponds to a converged transfer and is colored by the insertion $\Delta V$ cost, using a perceptually uniform color scale [96]. The

initial guess from the stable manifold arc associated with the destination halo orbit is plotted as a green dot. Two steps are employed to continue this transfer into families of transfers. First, the time of flight is held constant while the family of transfers is continued in terms of perilune radius. This first family of transfers corresponds to the vertical dark line in Figure 5.15. Then, families of transfers are continued off this first family. For various selected

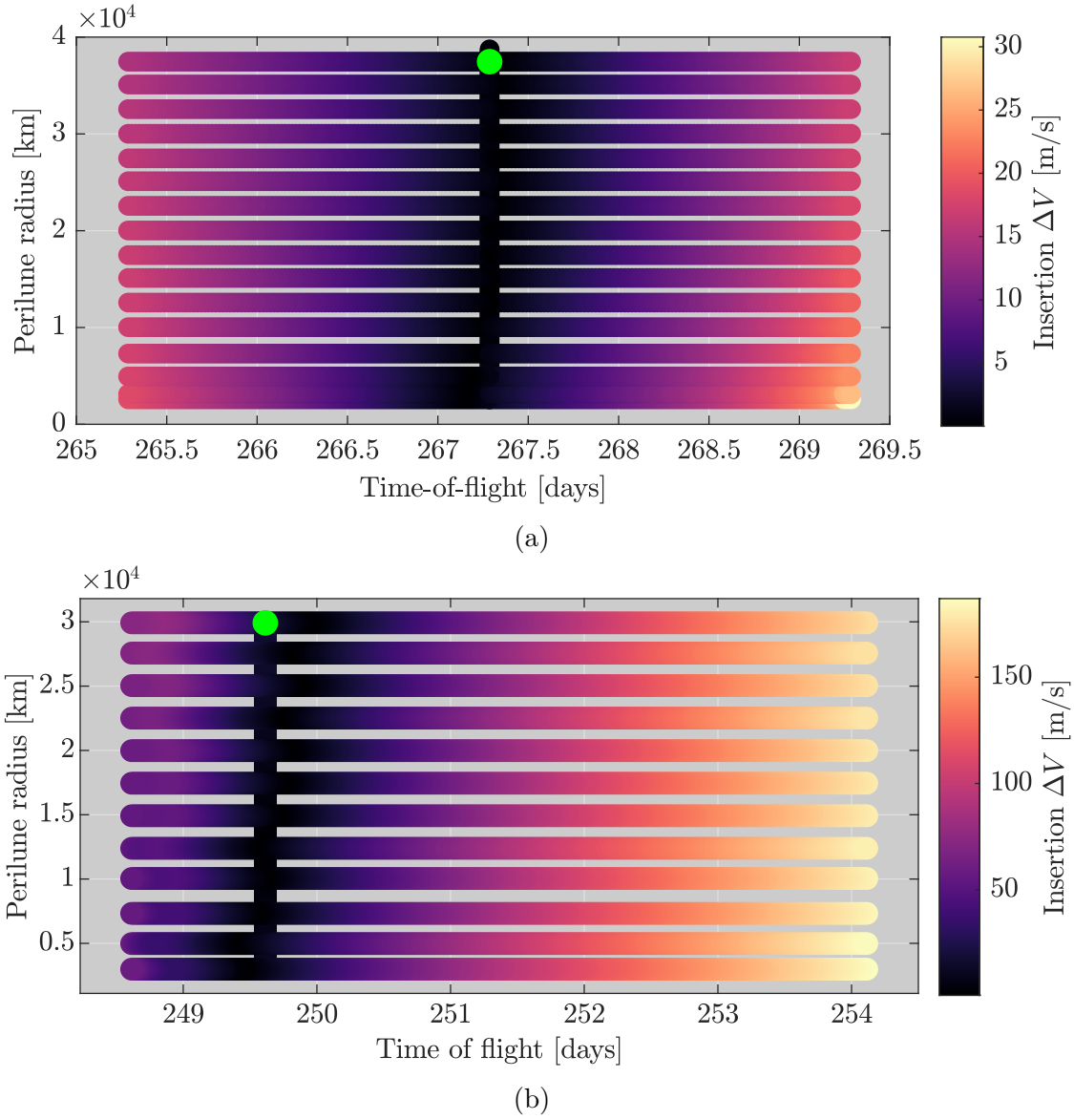


**Figure 5.15.** Map of transfers from perilune states to the Sun-$B_1$ $\underline{L}_2$ halo bounded motion with maximum $\underline{z}$ amplitude equal to 225,000 km (a) and 600,000 km (b) , colored by the magnitude of the insertion maneuver $\Delta V$. The initial guess from the manifold arc is denoted by a green dot.

perilune radii, the corresponding converged transfers in the first family are continued in time of flight, corresponding to the horizontal lines in Figure 5.15. Using this two-step continuation process, transfers are produced between perilune states and two Sun-$B_1$ $\underline{\mathrm{L}}_1$ halo bounded motion are construct. The maximum $\underline{z}$ component associated with the quasi-periodic orbit in Figure 5.15(a) is 225,000 km, while the maximum $\underline{z}$ amplitude associated with the destination orbit for the transfers in Figure 5.15(b) is approximately equal to 600,000 km. Note that this bounded motion is outside of the range of interest defined in Figures 5.4 and 5.5; perilune transfers to this orbit are constructed for comparison purposes. The perilune distances associated with the transfers in Figure 5.15(a) range from 3,000 km to 30,000 km, and from 3,000 km and 40,000 km in Figures 5.15(a) and 5.15(b), respectively. The times of flight range from approximately 248 to 254 days for transfers to the smaller halo orbit, and from 265 to 270 days for transfers to the larger halo orbit. Note the different scales along the color bars in Figure 5.15. Most of the transfers to the smaller Sun-$B_1$ halo orbit require an insertion $\Delta V$ maneuver of less than 20 m/s. Transfers to the larger Sun-$B_1$ halo with relatively low insertion maneuver cost, i.e., less than 50 m/s, are available for all the sampled perilune radii and for times of flight between 248 and 251 days. These transfers correspond to the points colored in the dark purple shades in Figure 5.15(a) and correspond to transfers that follow closely the flow into the synodic resonant orbit. As the time of flight increases, the insertion $\Delta V$ cost increases as well, as denoted by the lighter colored points between 252 and 254 days. Transfers from the lunar vicinity to the Sun-$B_1$ destination orbit are obtained for relatively low-cost insertion maneuvers.

Sample transfers are selected from the map in Figure 5.15. First, a family of perilune transfers with fixed time-of-flight equal to 266 days is selected; this collection of transfers corresponds to the vertical green line in Figure 5.16. Second, the horizontal blue line in Figure 5.16 corresponds to the family of perilune transfers with fixed initial perilune distance equal to 10,000 km. The two families are plotted in the Earth-Moon rotating frame and the Sun-$B_1$ rotating frame in Figures 5.17 and 5.18, with the remaining transfers from Figure 5.16 plotted as gray lines. Each family is colored as a function of the varying parameter; for instance, the transfers along the fixed time-of-flight family in Figure 5.17 are colored as a function of the initial perilune radius. The variation of the transfer geometry for the

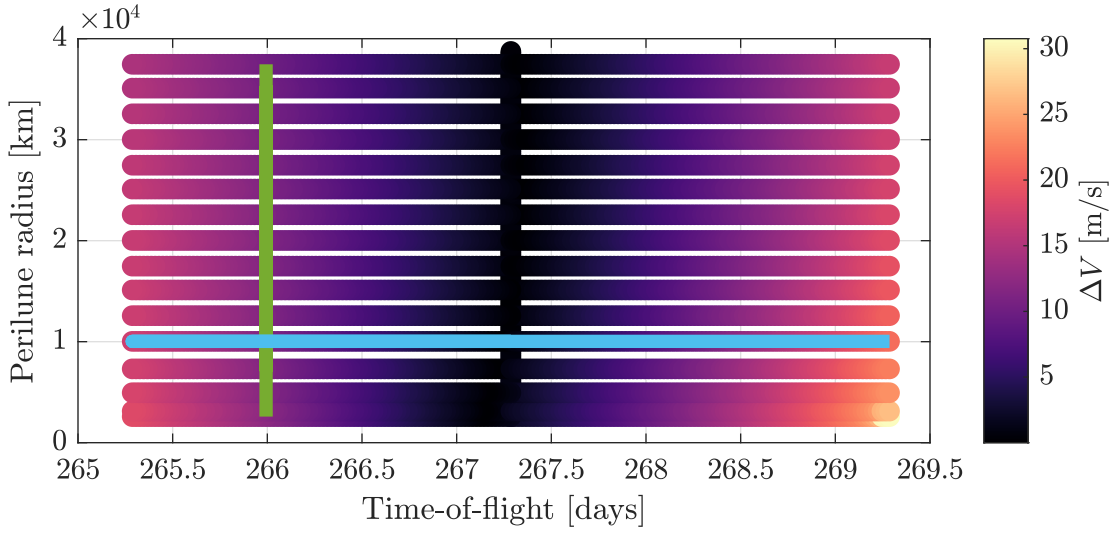


**Figure 5.16.** Family of perilune transfers with a time-of-flight equal to 266 days (in green) and family of perilune transfers with an initial perilune radius equal to 10,000 km (in blue), overlaid on the map from Figure 5.15(a).

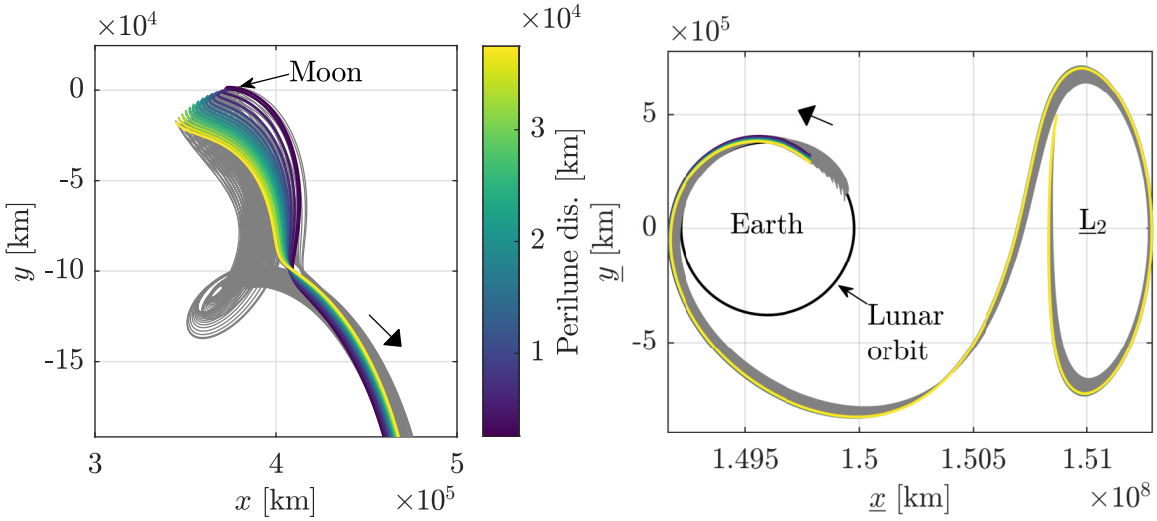


(a) Earth-Moon rotating frame

(b) Sun-$B_1$ rotating frame

**Figure 5.17.** Family of perilune transfers to a $\underline{L}_2$ halo quasi-periodic with maximum $\underline{z}$ amplitude equal to 225,000 km. The transfers have a fixed time-of-flight equal to 266 days and are colored as a function of the initial perilune radius. These transfers correspond to the vertical green line in Figure 5.16.

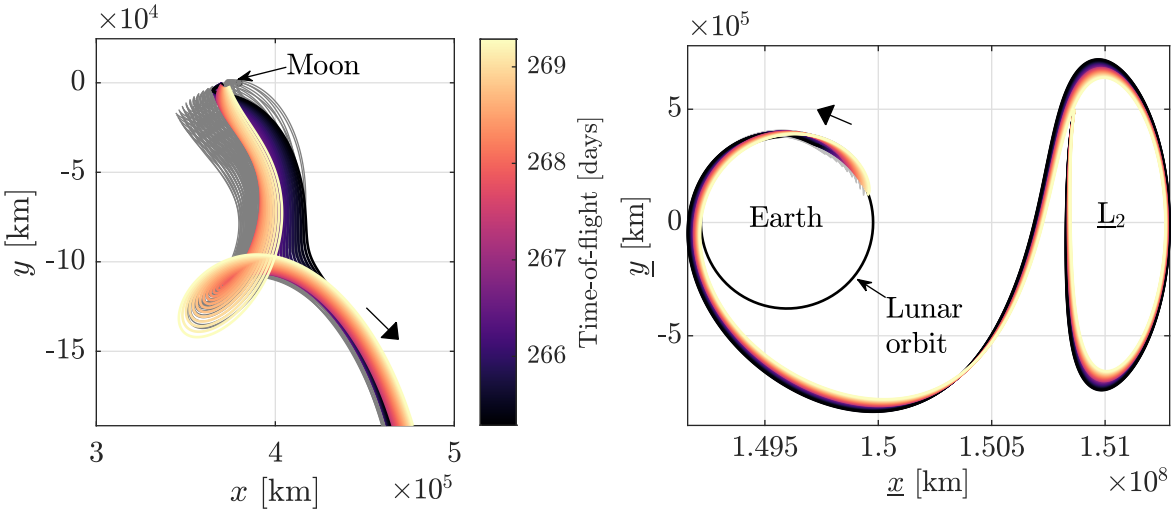


(a) Earth-Moon rotating frame

(b) Sun-$B_1$ rotating frame

**Figure 5.18.** Family of perilune transfers to a $\underline{L}_2$ halo quasi-periodic with maximum $\underline{z}$ amplitude equal to 225,000 km. The transfers have a fixed initial perilune radius equal to 10,000 km, colored as a function of the time-of-flight. These transfers correspond to the horizontal blue line in Figure 5.16.

fixed time-of-flight family is primarily apparent in the Earth-Moon rotating frame view in Figure 5.17(a), where the gradient of distances from the initial state to the Moon is visible. Note that the transfers presented in Figures 5.17 and 5.18 are spatial; thus, the trajectories in Figures 5.17(a) and 5.18(a) do not intersect the Moon. The trajectories in Figure 5.17(b) all depart at the same Moon angle value $\underline{\theta}$, since both the time-of-flight and the epoch of the insertion into the heliocentric halo orbit are fixed. The variations in geometry are more pronounced for the transfers with variable time-of-flight and fixed initial perilune distance, plotted in Figure 5.18. An extra loop near the Moon is apparent in Figure 5.18(a); this loop allows for the correct phasing of the trajectories within the Sun-$B_1$ rotating in Figure 5.18(b). When represented in the Sun-$B_1$ rotating frame, the initial states associated with the transfers in Figure 5.18 cover the majority of quadrant I and part of quadrant II. A variety of geometries within the Earth-Moon rotating frame and phasing with respect to Sun-$B_1$ rotating frame is available from the perilune transfers map.

### 5.3.3 Initial Guess Selection

A strategy to construct an initial guess for an end-to-end transfer between the 9:2 synodic resonant $L_2$ NRHO and a Sun-$B_1$ halo orbit is detailed. The first parameter is the selection of the destination orbit: in this example, an $\underline{L}_1$ halo orbit with a maximum $\underline{z}$ amplitude of 225,000 km is identified. This trajectory is consistent with orbits selected for solar weather observatory missions, such as the WIND spacecraft [97]. The perilune of a predetermined transfer to this $\underline{L}_1$ destination orbit is selected and highlighted in Figure 5.19(a). The perilune is located in quadrant III, and its associated energy is above the value associated with the state along the NRHO that possesses the same Earth-Moon-Sun orientation. The minimum energy difference for this Sun angle value, plotted in Figure (b), is approximately equal to $-0.04$.

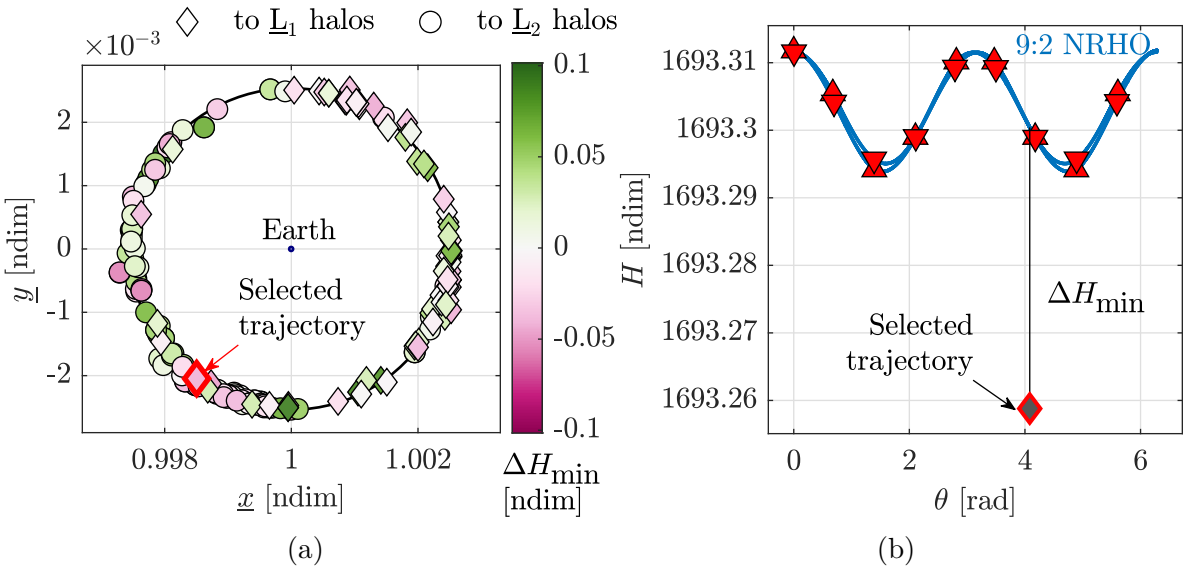


**Figure 5.19.** Perilune of the sample initial guess to the 225,000 km $\underline{z}$ amplitude $\underline{L}_1$ halo orbit, as viewed in the Sun-$B_1$ rotating frame (a). Energy-like value associated the initial guess perilune as a function of the Sun angle $\theta$ (b).

The selected transfer is examined in configuration space. The departure orbit, the arrival orbit, and the transfer are plotted as viewed in the Sun-$B_1$ rotating frame in Figure 5.20(a). The lunar orbit is plotted in gray and the perilune state from Figure 5.19(a) is denoted by a red diamond. The time of flight between the perilune and the end of the trajectory along

the $\underline{L}_1$ halo is approximately 280 days. Note that this time includes some 'winding' on the destination orbit and may not be representative of the actual transfer time of flight. A close view of the trajectory near the Moon, as viewed in the Earth-Moon rotating frame, appears in Figure 5.20(b). The departure orbit, the 9:2 synodic resonant $L_2$ NRHO, is plotted in blue. Note the generally close alignment of the trajectory in black and the NRHO as viewed in the lunar-centered, Earth-Moon rotating frame. However, it is apparent from Figures 5.19(b) and 5.20(a) that the perilune along the transfer and the closest perilune along the 9:2 synodic resonant $L_2$ NRHO are not at the same Sun-Earth-Moon orientation. Thus, this difference in epoch is rectified during the differential corrections scheme or, alternatively, an additional arc is leveraged to connect the two components of the transfers (see Section 5.4.1).

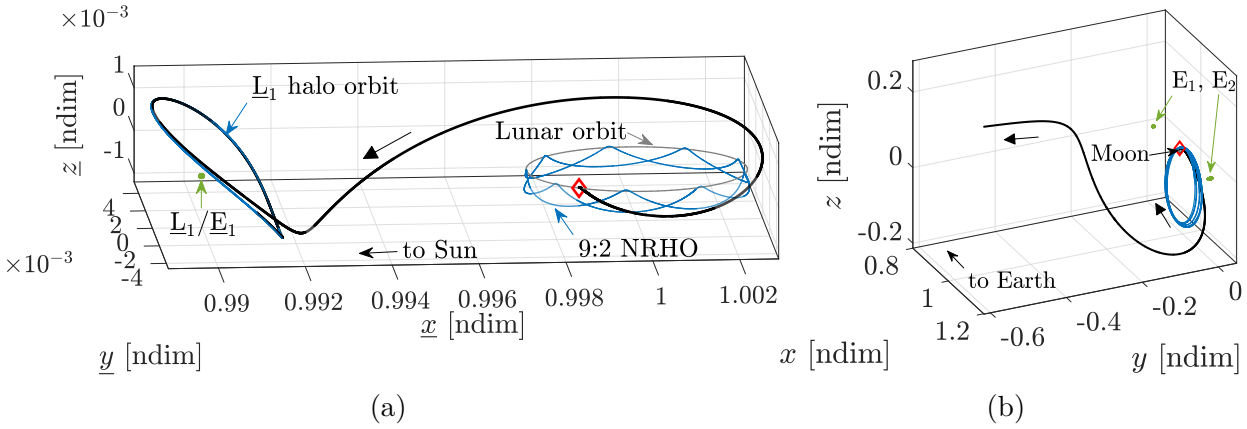


**Figure 5.20.** Sample initial guess in the BCR4BP to the 225,000 km amplitude $\underline{L}_1$ halo orbit, as viewed in the Sun-$B_1$ rotating frame (a) and the Moon-centered Earth-Moon rotating frame (b). The departure orbit, that is, the 9:2 synodic resonant $L_2$ NRHO, and the destination heliocentric halo orbit, are colored in blue. The perilune is denoted by the red diamond.

Alternatively, initial guesses for the end-to-end transfer are selected from the map of perilune transfers, in Figure 5.15, given certain parameters. Recall that the perilune maps in Figure 5.15 corresponds to families of transfers from a perilune state to two $\underline{L}_2$ halo orbits. In addition to the insertion $\Delta V$ into the destination orbit, the Earth-Moon energy-like values, $H$, corresponding to the departure states are compared to the values along the Earth-Moon periodic orbit. Initial guess trajectories that represent the smallest difference in the energy-like value values are sought, as they generally yield transfers with small departure

maneuvers. For instance, consider the initial guesses for the end-to-end transfers plotted in Figure 5.21, as viewed in the Earth-Moon rotating frame. Perilune states with Earth-Moon energy-like values that are similar to the 9:2 NRHO are selected from Figure 5.15(a) and plotted as the colored dots. The transfers associated with these perilune states are plotted in gray. The energy-like values along the 9:2 synodic resonant orbit range from 1693.29 to 1693.31; this range is slightly above the color bar used in Figure 5.21. The perilunes along transfers with departure energy levels that are similar to the departure NRHO orbit correspond to the darkest dots in Figure 5.21. In addition to the energy-like value, multiple parameters are relevant when selecting potential transfer from the maps in Figure 5.15 to seed an initial guess for an end-to-end transfer.

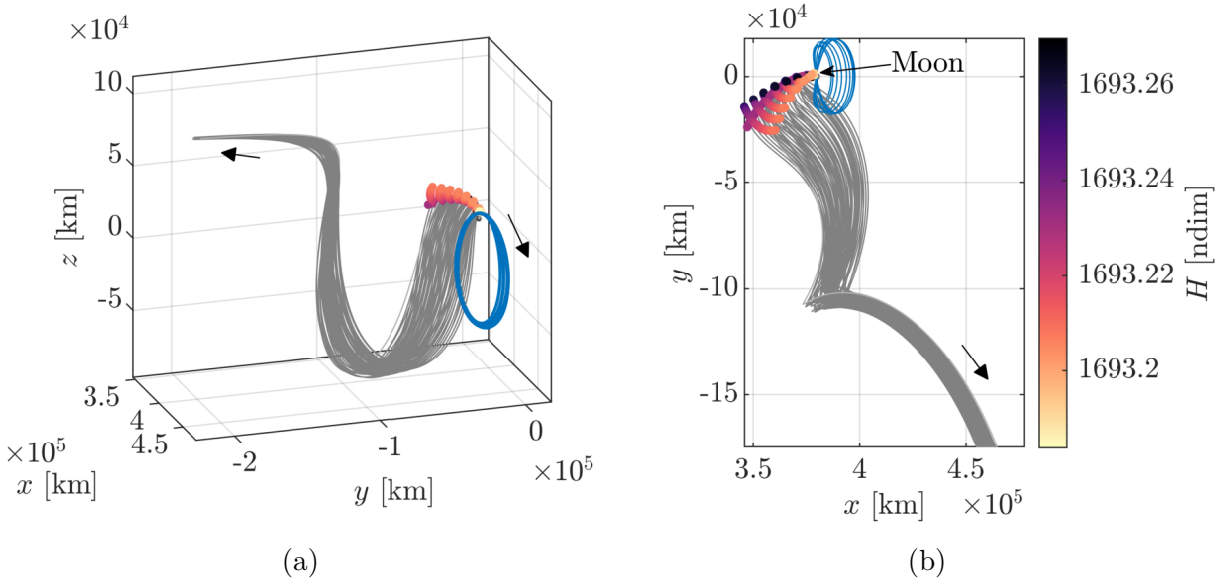


**Figure 5.21.** Selected initial guesses for transfers from the 9:2 synodic resonant NRHO to the Sun-$B_1$ halo orbit, as viewed in the Earth-Moon rotating frame. Perilune states are colored by their associated Earth-Moon Hamiltonian values.

## 5.4 End-to-End Transfers

Continuous end-to-end transfers in the BCR4BP between the 9:2 synodic resonant $L_2$ NRHO and a Sun-$B_1$ halo orbit are constructed using a numerical scheme. The initial guess is selected employing one of the methods in Section 5.3.3. A maneuver departure

location along the 9:2 synodic resonant $L_2$ NRHO is selected; a bridge arc is leveraged if the phasing between the departure state and the perilune is not consistent with the selected perilune state. In this investigation, the differential correction schemes for the transfer generation are applied for states as represented in the Earth-Moon rotating frame. However, recall that the dynamics in the BCR4BP as described by the equations of motion in the Earth-Moon frame (Equations (2.4) and (2.5)) are identical to the behavior modeled by the equations of motion in the Sun-$B_1$ frame (Equations (2.8) and (2.9)). Boudad et al.[49] employ numerical corrections on states represented in the Sun-$B_1$ rotating frame; results in the current investigation are consistent within the specified numerical tolerance. The initial guess trajectory is discretized into patch points to facilitate the convergence process. While a single-shooting algorithm is an acceptable alternative in certain scenarios, it generally fails for long transfers with close passages of one or more primaries. Thus, a multiple-shooting scheme is selected for the numerical corrections. The trajectory is corrected for continuity between consecutive patch points. Maneuvers are allowed at the departure from the NRHO, at the insertion into the Sun-$B_1$ destination orbit and, when a bridge arc is used, at the connection between the bridge arc and the heliocentric part of the transfer. The arrival location and epoch in the Sun-$B_1$ halo orbit are fixed in the current implementation of the numerical scheme. The time of flight is not explicitly allowed to vary during the corrections process, but it is adjusted by modifying the departure location along the Earth-Moon NRHO. Recall that the BCR4BP is a time-dependent, periodic model. Thus, adjusting the departure state also changes the departure time and, thus, modifies the time of flight. Once a transfer satisfies the constraints within some specified numerical tolerance, families of transfers are produced by continuing the numerical corrections along some parameter, such as departure location from the NRHO.

### 5.4.1 Bridge Arcs

A technique to bridge the cislunar orbit to a preselected heliocentric arc, thus mitigating phasing discrepancies, is introduced. Recall the selected arc in Figure 5.19, connecting the vicinity of the Moon to a Sun-$B_1$ halo orbit with maximum $\underline{z}$ component approximately

equal to 225,000 km. However, it is apparent from Figures 5.19(b) and 5.20(a) that perilune along the transfer and the closest perilune along the 9:2 synodic resonant $L_2$ NRHO are not at the same Sun-Earth-Moon orientation. Thus, a direct transfer departing from the perilune along the 9:2 NRHO is not possible. Rather, a 'bridge' arc is leveraged to link the transfer trajectory and the departure state along the NRHO, as plotted in Figure 5.22. The departure location from the NRHO is selected near perilune and is labeled '1'. The time of flight along the bridge arc is approximately one and one-half revolutions along the 9:2 NRHO, that is, approximately ten days. A second maneuver, labeled '2' in Figure 5.22, allows a connection between the bridge arc and the transfer arc plotted in Figure 5.20. After a differential corrections process, the first and second $\Delta$V maneuver magnitudes are approximately 20 m/s and 74 m/s, respectively. After the second maneuver, the black arc in Figure 5.22 corresponds to a ballistic trajectory into the Sun-$B_1$ $\underline{L}_1$ halo orbit in Figure 5.20(a). Thus, a feasible guess for a transfer from the 9:2 synodic resonant $L_2$ NRHO to the selected $\underline{L}_1$ halo orbit is produced for a $\Delta$V impulsive maneuver cost under 100 m/s. Bridge arcs are successfully to overcome challenges in connecting the cislunar orbit and the heliocentric arcs.

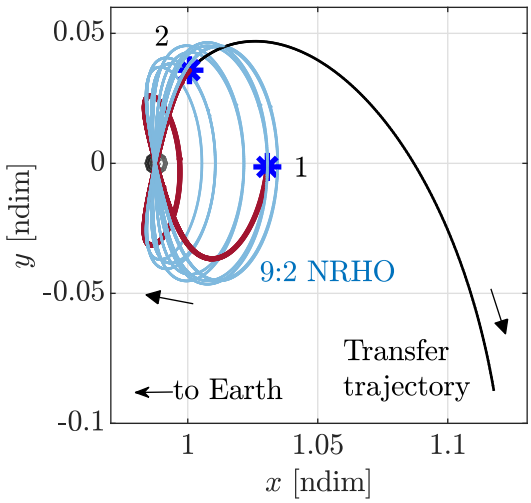


**Figure 5.22.** Bridge arc (in red) between the 9:2 synodic resonant $L_2$ NRHO (in blue) and the transfer trajectory (in black) to the Sun-$B_1$ $\underline{L}_1$ halo orbit, as viewed in the Earth-Moon rotating frame. Two maneuvers, labeled 1 and 2, are allowed.

### 5.4.2 One-Way Transfers

One-way transfers from the 9:2 synodic resonant $L_2$ NRHO to Sun-$B_1$ halo orbits associated with the $L_1$ or the $L_2$ points are constructed within the BCR4BP. A variety of geometries, both in cislunar and heliocentric spaces, are presented. The transfers represent a range of departure and arrival epochs. Characteristics, including the energy and the directions of the departure maneuvers, are explored along the families of one-way transfers.

#### Transfers to $L_1$ halos

End-to-end transfers from the NRHO to $L_1$ Sun-$B_1$ halo orbits with maximum $z$ amplitude equal to 225,000 km are computed for different epochs. Representative transfers are plotted in Figures 5.23 and 5.24. Trajectories are colored according to the total $\Delta$V, that is, the sum of the departure, arrival, and potential bridge maneuver magnitudes. Transfers in Figures 5.23(a) and 5.24(a) possess a total $\Delta$V ranging from approximately 130 to 240 m/s. The insertion $\Delta$V varies from 7 to 30 m/s, while the bridge $\Delta$V remains below 10 m/s. Transfers in Figures 5.23(b) and 5.24(b) possess a total $\Delta$V ranging between 90 and 250 m/s. No bridge arc is leveraged for constructing this family, and the insertion $\Delta$V is ranges from 20 to 30 m/s. Thus, the majority of the maneuver cost occurs at the NRHO departure for both families of transfers. The initial epoch, i.e., the Earth-Moon-Sun relative geometry at departure, is different for each group of transfers in Figures 5.23 and 5.24. Though the departure locations for both families, denoted by gray dots in Figures 5.23(a) and 5.23(b) are all located in quadrant III, the two families are separated in epoch by a synodic month. The geometry of the departure from the Earth-Moon NRHO is also explored. The close vicinity of the Moon in the Earth-Moon rotating frame is apparent in Figures 5.24(a) and 5.24(b). The departure locations along the NRHO are also denoted by gray dots in these plots. The locations for the departure maneuver are selected to occur after perilune, on the side of the NRHO with a positive rotating $y$ component for the transfers in Figure 5.24(a), and after apolune (states with a negative rotating $y$ component) in Figure 5.24(b). Note that no departure location is selected close to perilune; near this apse, higher dynamical sensi-

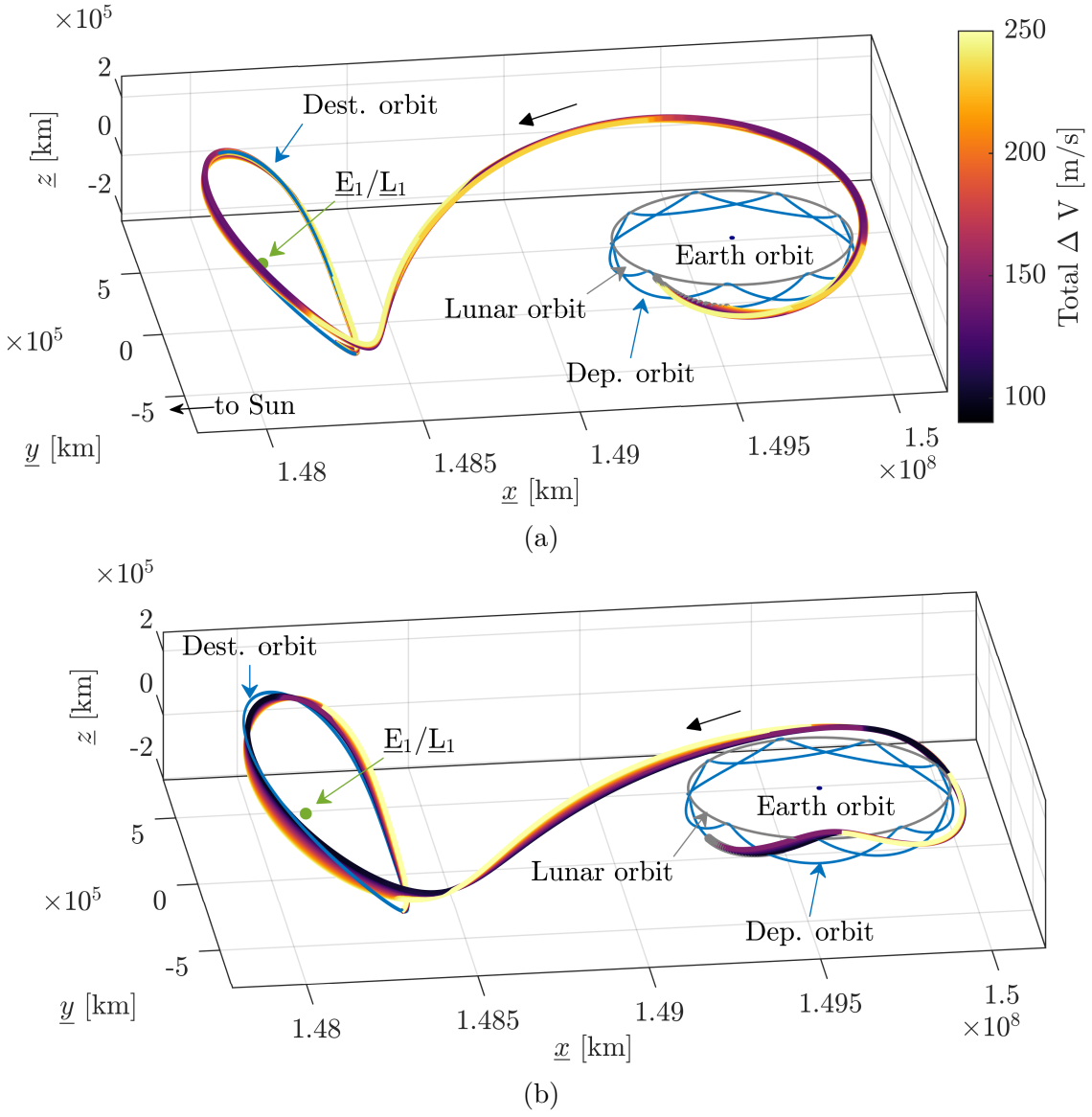


**Figure 5.23.** Two geometries of representative end-to-end transfers in the BCR4BP between the 9:2 NRHO and the Sun-$B_1$ $\underline{\text{L}}_1$ halo orbit with maximum $z$ amplitude equal to 225,000 km, as viewed in the Sun-$B_1$ rotating frame.

tivities present challenges in constructing consistent departures. The departure geometry in Figure 5.24(a) presents a sharp 'turn' after departing the NRHO; this behavior is consistent with observations from previous contributions [48], [49]. However, the departure arcs in Figure 5.24(b) do not include this turn geometry; rather, they wind off from the NRHO. The tilted lobe around the Moon could suggest some structures from a BCR4BP resonant 3:1 NRHO [44] or from a higher-period dynamical structure near the NRHO [42]. Note that

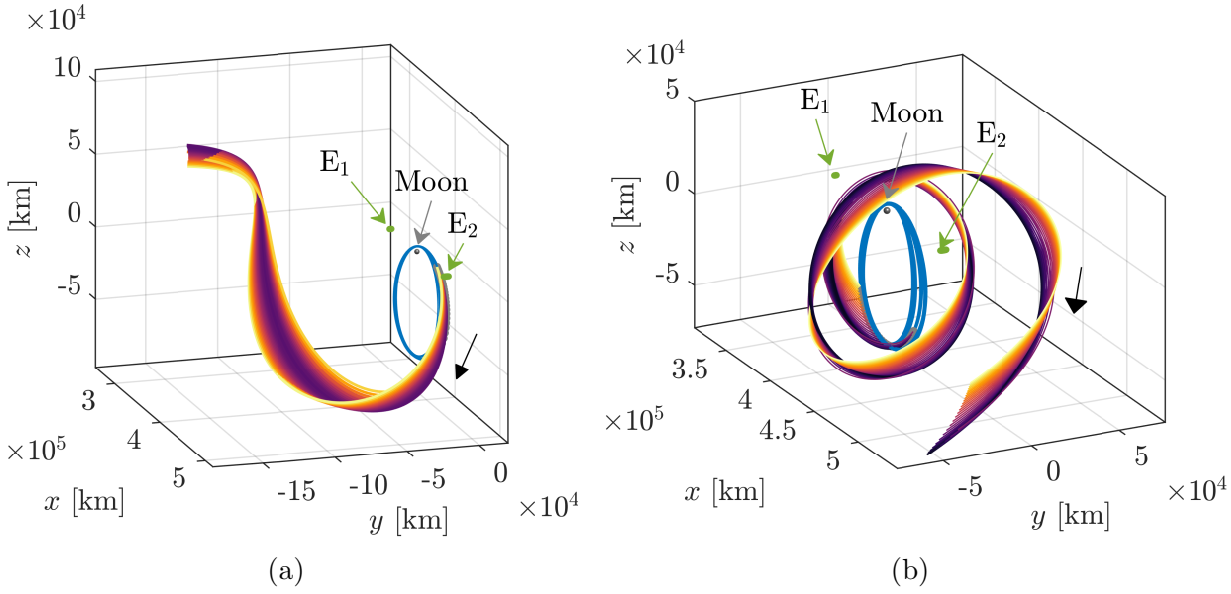


**Figure 5.24.** Two geometries of representative end-to-end transfers in the BCR4BP between the 9:2 NRHO and the Sun-$B_1$ $\underline{\text{L}}_1$ halo orbit with maximum $z$ amplitude equal to 225,000 km, as viewed in the Earth-Moon rotating frame near the Moon .

none of these transfers are optimized. Nevertheless, this investigation demonstrates that low-cost transfers leveraging natural arcs between the 9:2 synodic resonant $\text{L}_2$ NRHO and Sun-$B_1$ $\underline{\text{L}}_1$ halo orbits can be produced using dynamical systems tools in the BCR4BP.

The evolution of the energy along the NRHO-to-halo transfer families is explored. Recall that the BCR4BP does not admit an integral of the motion. Two time-dependent energy-like values, the Earth-Moon $H$ value, and the Sun-$B_1$ $\underline{H}$ value, are defined to be the energy-like quantities in the BCR4BP. The Earth-Moon energy-like values along the transfers in Figures 5.23 and 5.24 are plotted as function of time in Figure 5.25. The initial time is arbitrarily defined as the initial time along the departure orbit, that is, the 9:2 synodic resonant $\text{L}_2$ NRHO. The energy-like values associated with the departure and the arrival orbit, the $\underline{\text{L}}_1$ halo orbit with maximum $\underline{z}$ equal to 225,000 km, are plotted in blue. Note that the difference in the energy-like values oscillations between the two periodic orbits. The oscillations along the Sun-$B_1$ halo $H$ values are much larger than those along the values associated with the Earth-Moon NRHO, since the dimensions of the Sun-$B_1$ halo are larger when represented in the Earth-Moon rotating frame. The oscillations along the Sun-$B_1$ halo

energy-like values also have a lower frequency due to the longer orbital period of the orbit as compared to the 9:2 synodic resonant $L_2$ NRHO. The $H$ values associated with the transfers in Figures 5.23(a) and 5.24(a) are depicted in turquoise, and orange lines are associated with the energy-like values along the trajectories in Figures 5.23(b) and 5.24(b). The energy-like values depicted in Figure 5.25 accomplish the required change of energy naturally between the 9:2 NRHO and the Sun-$B_1$ halo orbit. Two small discontinuities in energy-like values are present, one at departure from the Earth-Moon NRHO and one at arrival in the Sun-$B_1$ halo orbit, as illustrated in the inserts in Figure 5.25. These differences in $H$ values are labeled the $\Delta H_{\text{dep}}$ and $\Delta H_{\text{arr}}$, and correspond to the minimum $\Delta$V maneuver magnitudes required to accomplish the change in energy, without considering the velocity direction. The two families of transfers in Figure 5.25 share the same departure and arrival orbit, but they differ in phasing. The transfers from Figures 5.23(a) and 5.24(a) have a longer time-of-flight than the transfers from Figures 5.23(b) and 5.24(b); they depart earlier from the NRHO and insert later into the Sun-$B_1$ halo orbit. The correct transfer phasing is accomplished differently along each family. Transfers Figure 5.24(a) included a quick departure from the

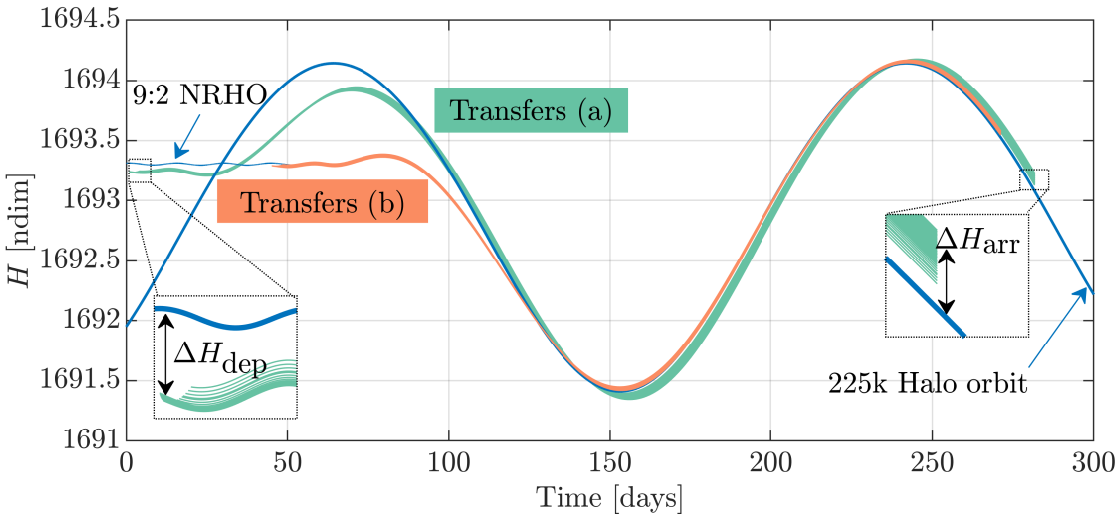


**Figure 5.25.** Earth-Moon energy-like values as a function of time along the trajectories plotted in Figures 5.23 and 5.24. The blue lines denote the Earth-Moon departure and Sun-$B_1$ arrival orbits.

NRHO, as observed in Figure 5.24(a), but spend some time in the Earth-Moon vicinity

before inserting into the Sun-$B_1$ orbit, as apparent in Figure 5.23(a). Conversely, transfers from Figures 5.23(b) and 5.24(b) present a slower departure from the lunar vicinity: note the extra lobes in Figure 5.24(b) and the longer 'flat' orange lines for the energy-like values after departure in Figure 5.25. After departure from the lunar vicinity, the trajectories in Figure 5.23(b) deliver a shorter time of flight before inserting into the Sun-$B_1$ halo. The analysis of the Earth-Moon energy-like values along the transfers trajectories offer insight into the changes in energy and phasing.

**Transfers to $\underline{\text{L}}_2$ halos**

End-to-end transfers from the NRHO to a Sun-$B_1$ $\underline{\text{L}}_2$ halo orbit with maximum $z$ amplitude equal to 225,000 km are computed for different epochs. Representative transfers in the Sun-$B_1$ rotating frame are plotted in Figures 5.26 and 5.27. Trajectories are colored according to the total $\Delta V$, that is, the sum of the departure and arrival maneuver magnitudes. Transfers in Figures 5.26(a) and 5.26(b) possess a total $\Delta V$ ranging from approximately 90 m/s to 200 m/s, while transfers in Figure 5.26(c) require a total maneuver cost between 200 m/s and 250 m/s. The insertion $\Delta V$ remains consistent across all the transfers, i.e., between 4 and 6 m/s.

The majority of the maneuver cost occurs at the NRHO departure: the minimum departure $\Delta V$ is approximately 87 m/s for a transfer in Figure 5.26(b) and the maximum $\Delta V$, about 245 m/s, is produced for a transfer in Figure 5.26(c). The range of $\Delta$V, as well of times-of-flight and initial epochs, for each family of transfers is summarized in Table 5.3. The initial epoch, i.e., the Earth-Moon-Sun relative geometry at departure, is different for each group of transfers in Figure 5.26. Recall that, in the BCR4BP, the epoch is described by the Sun angle in the Earth-Moon rotating frame, or, equivalently, the Moon angle and/or the quadrants in the Sun-$B_1$ frame. Transfers plotted in Figures 5.26(a) and 5.26(c) possess departure states from the NRHO as located in quadrant IV. The majority of departure states for the transfers in Figure 5.26(b) are located in quadrant I and incorporate Moon angles at departures that are similar to the transfers described by Folta and Webster[3]. Note that none of these transfers are optimized. Nevertheless, this investigation demonstrates that

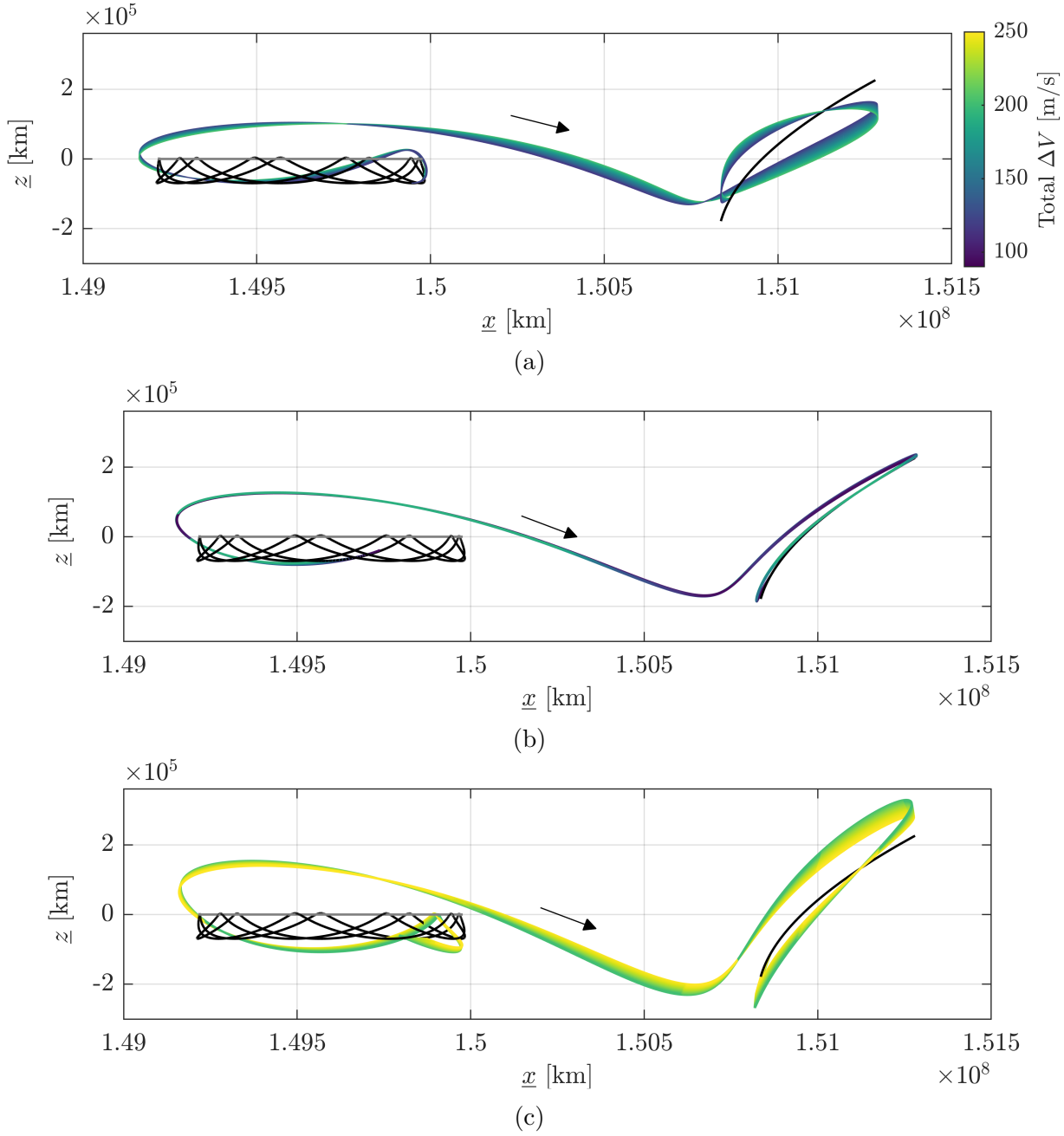


**Figure 5.26.** Representative end-to-end transfers between the 9:2 NRHO and the Sun-$B_1$ halo orbit B, as viewed in the Sun-$B_1$ rotating frame. Additional views of the transfers are available in Figure 5.27.

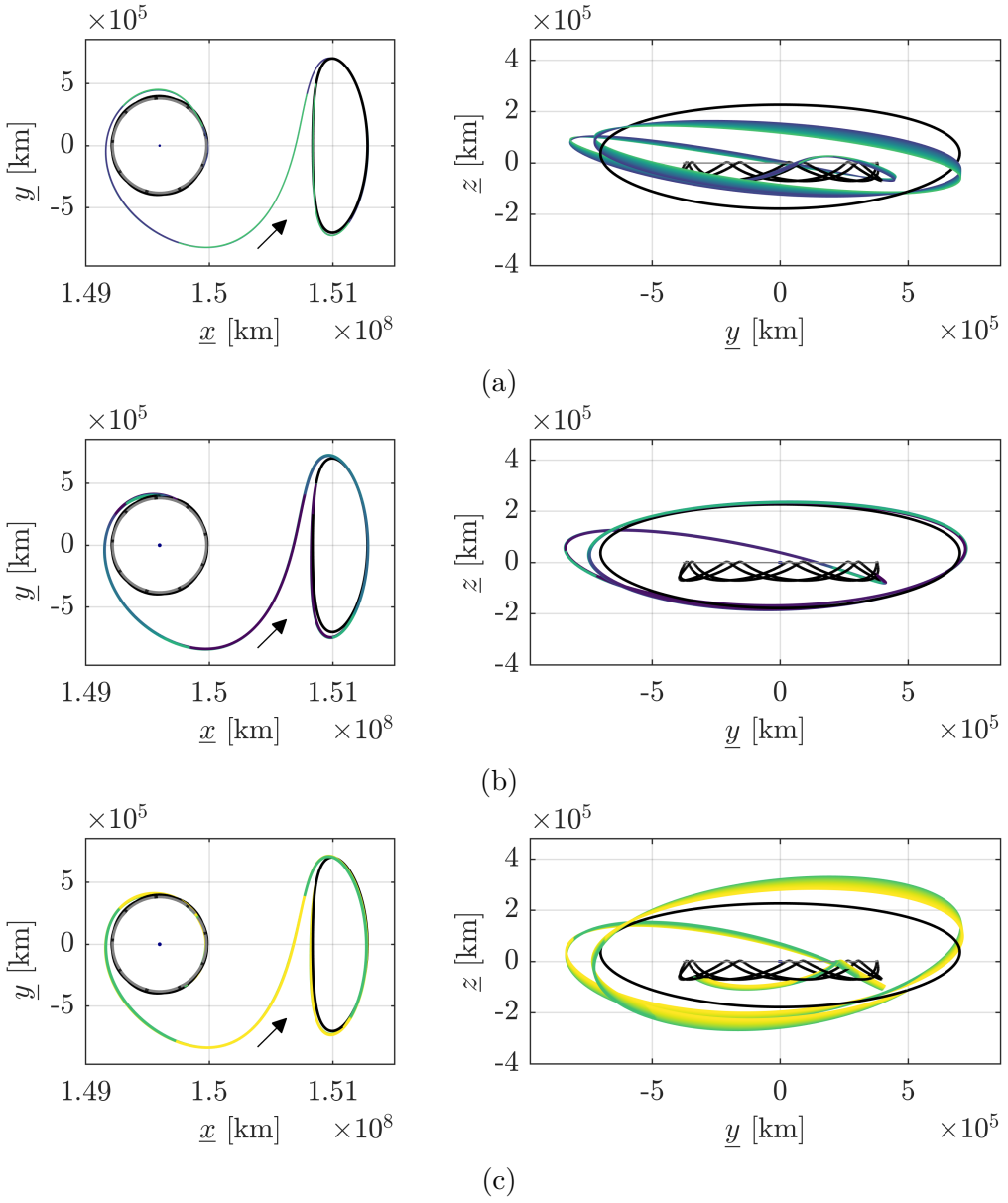


**Figure 5.27.** Additional views of the transfers from Figure 5.26.

natural/low-cost transfers between to cislunar and heliocentric space can be obtained using dynamical systems tools in the BCR4BP.

The geometry of the departure from the Earth-Moon NRHO is explored. Close views of the previous transfers in Figures 5.26 and 5.27 are now plotted in the Earth-Moon rotating frame in Figure 5.28. The maneuver to depart from the NRHO is constrained to occur to near apolune. Near perilune, higher dynamical sensitivity and higher orbit determination

errors present challenges to obtain consistent departures. However, note the difference in the departure location from the NRHO: transfers in Figures 5.28(a) and 5.28(c) include departure maneuvers prior to apolune, while transfers in Figure 5.28(b) depart from the NRHO after perilune. All transfers present this sharp 'turn', indicated by the red arrows in Figure 5.28 in space after leaving the NRHO. This geometry is consistent with observations from previous contributions[48]: departure arcs from the NRHO that do not present this 'turn' do not have sufficient energy to depart the Sun-$B_1$ portals. The numbers of loops around the Moon differ for each type of transfer plotted in Figure 5.28: no loop around the Moon for the transfers in Figure 5.28(b), one loop for the transfers in Figure 5.28(a), and two loops for the transfers in Figure 5.28(c). Note that the close lunar flybys in trajectories in Figure 5.28(c) could cause some navigation challenges, and that some of the trajectories intersect the lunar radius.

**Table 5.3**. Range of the characteristics associated with the transfers plotted in Figures 5.26 and 5.28

| | Transfers (a) | Transfers (b) | Transfers (c) |
|---|---|---|---|
| Dep. $\Delta V$ [m/s] | 117.0 : 202.2 | 87.4 : 187.4 | 196.9 : 245.1 |
| Arr. $\Delta V$ [m/s] | 5.3 : 5.4 | 4.7 : 4.8 | 4.5 : 4.6 |
| **Total $\Delta$V [m/s]** | **122.3 : 207.6** | **92.1 : 192.1** | **201.4 : 249.7** |
| Time of flight [days] | 271.2 : 273.3 | 263.0 : 265.4 | 274.5 : 275.9 |
| Dep. Moon angle [deg] | $-30.5$ : $-4.8$ | 66.2 : 95.4 | $-61.8$ : $-45.6$ |

Similar to the transfers to the $\underline{L}_1$ halo orbits, the evolution of the energy along the NRHO-to-halo transfers is also explored. Recall that the BCR4BP does not admit an integral of the motion. The Earth-Moon energy-like values, $H$, along the transfers in Figure 5.26(b) are plotted as a function of the Moon angle $\underline{\theta}$ in Figure 5.29. The energy-like values associated with the Earth-Moon 9:2 NRHO are plotted in black. The states of the Sun-$B_1$ halo orbit are rotated into the Earth-Moon rotating frame; the associated Earth-Moon energy-like values are plotted in red in Figure 5.29. Note the differences in the energy-like value oscillations between the two periodic orbits. The oscillations along the red line are much larger than those along the black line, since the dimensions of the Sun-$B_1$ halo orbit are larger when represented in the Earth-Moon rotating frame. The oscillations along the red line also have a

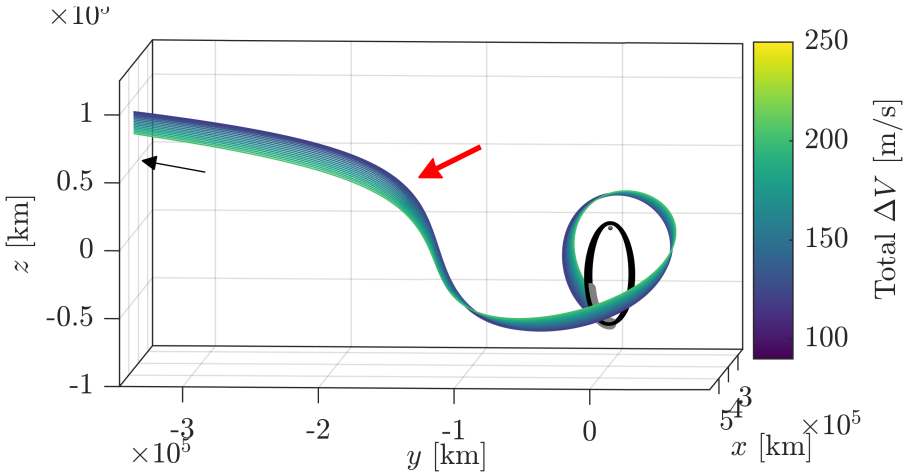


(a) Transfers from (a)

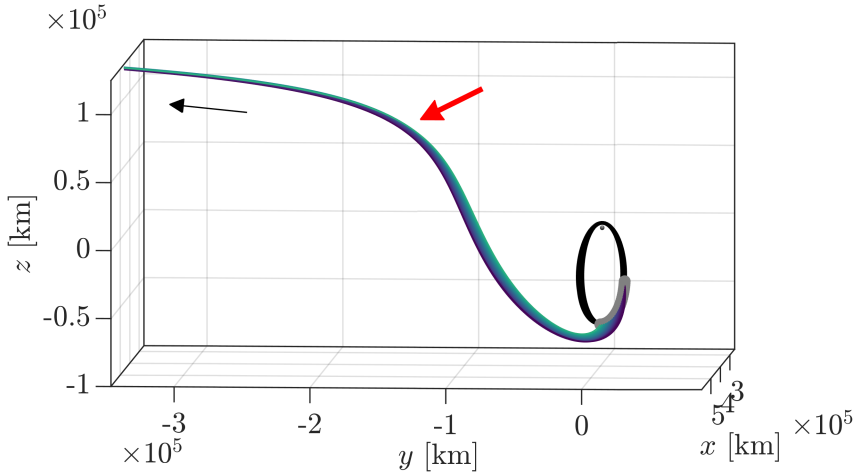


(b) Transfers from (b)

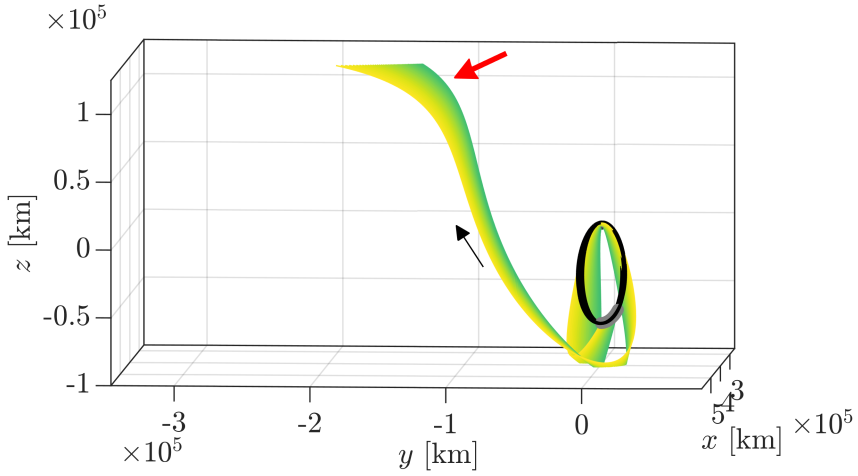


(c) Transfers from (c)

**Figure 5.28.** NRHO departure geometry from the end-to-end transfers in Figure 5.26, as viewed in the Earth-Moon rotating frame. The departure maneuver locations are denoted by gray dots.

lower frequency due to the longer orbital period of the halo orbit as compared to the NRHO, represented in black. The energy-like values associated with the transfers in Figures 5.26(b) and 5.28(b), depicted in the blue to purple colors in Figure 5.29, accomplish naturally the required change of energy between the Earth-Moon NRHO and the Sun-$B_1$ halo orbit. Small discontinuities in energy-like values are present at departure between the transfer arc and the NRHO, and at arrival between the transfer arc and the Sun-$B_1$ halo orbit, as illustrated in the insets in Figure 5.29. These differences are labeled the departure $\Delta H$ and the arrival $\Delta H$, and correspond to the minimum $\Delta V$ maneuver required to achieve this change of energy, assuming the velocity vector of the incoming/outgoing transfer arc and the velocity vector of the insertion/departure location in the periodic orbit are aligned. A larger maneuver is required if the directions of the velocity vectors are not aligned. The angle between the transfer arc velocity vector and the velocity vector along the periodic orbit, $\Lambda$, is defined

$$\Lambda = \arccos \frac{\bar{v}_{\mathrm{t}} \cdot \bar{v}_{\mathrm{p.o.}}}{\|\bar{v}_{\mathrm{t}}\| \|\bar{v}_{\mathrm{p.o.}}\|} \tag{5.3}$$

where $\bar{v}_{\mathrm{t}}$ and $\bar{v}_{\mathrm{p.o.}}$ are the velocity vectors along the transfer arcs and the periodic orbit, respectively. For $\Lambda$ equal 0°, the maneuver is tangential to the periodic orbit velocity vector and maximizes the change in energy. Conversely, for $\Lambda$ equal 90°, the maneuver direction

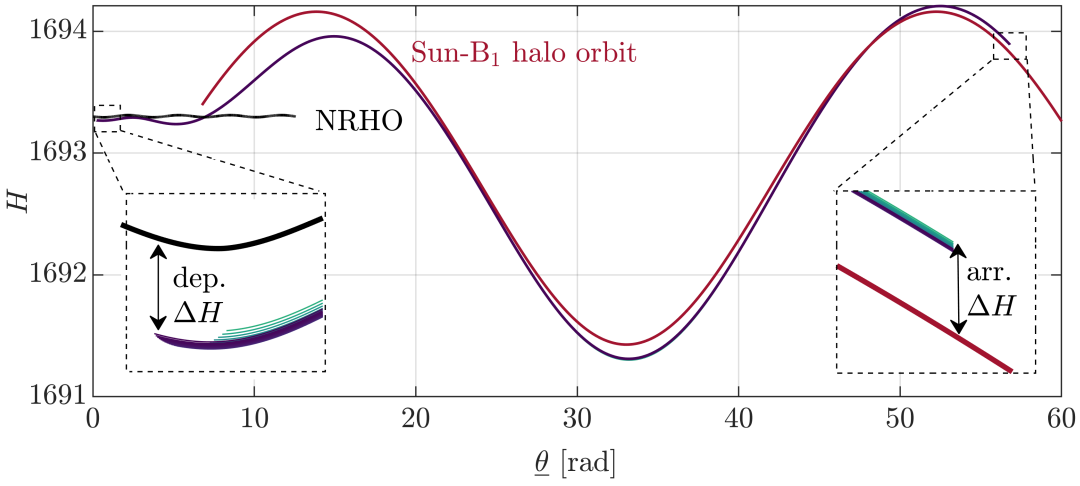


**Figure 5.29.** Earth-Moon energy-like values along the transfers in Figure 5.26(b); energy-like values associated with the Earth-Moon NRHO and the Sun-$B_1$ halo orbit B are plotted in black and in red, respectively.

and the velocity vector along the periodic orbit are perpendicular, the maneuver minimizes the change in energy. The $\Lambda$ angles at the departure from the NRHO for transfers in Figures 5.26(b) and 5.28(b) are plotted as a function of the $z$ component of the departure location in Figure 5.30(a). Transfers near apolune possess a $\Lambda$ angle between 50° and 70°, and thus, the associated maneuvers do not efficiently change the energy-like value. As a consequence, the total $\Delta V$ for these transfers is relatively high, between 160 and 190 m/s. In contrast, the $\Lambda$ angle for departure locations with $z$ component between -55,000 km and -38,000 km possess a $\Lambda$ angle between 10° and 15°. The maneuvers from these locations are close to tangential to the periodic orbit, and the total $\Delta V$ is between 90 and 110 m/s. Note that the theoretical minimum $\Delta V$ [98] maneuvers between the Earth-Moon NRHO and the stable manifold of the Sun-B1 halo orbit range from 40 m/s to 85 m/s, depending on the departure location along the NRHO. Additional numerical corrections processes could potentially further decrease the value of $\Lambda$ and thus, the total $\Delta V$s associated with the transfers. The majority of the energy change required in the transfer between the Earth-Moon NRHO and the Sun-$B_1$ halo orbit occurs with the natural dynamics of the Earth-Moon-

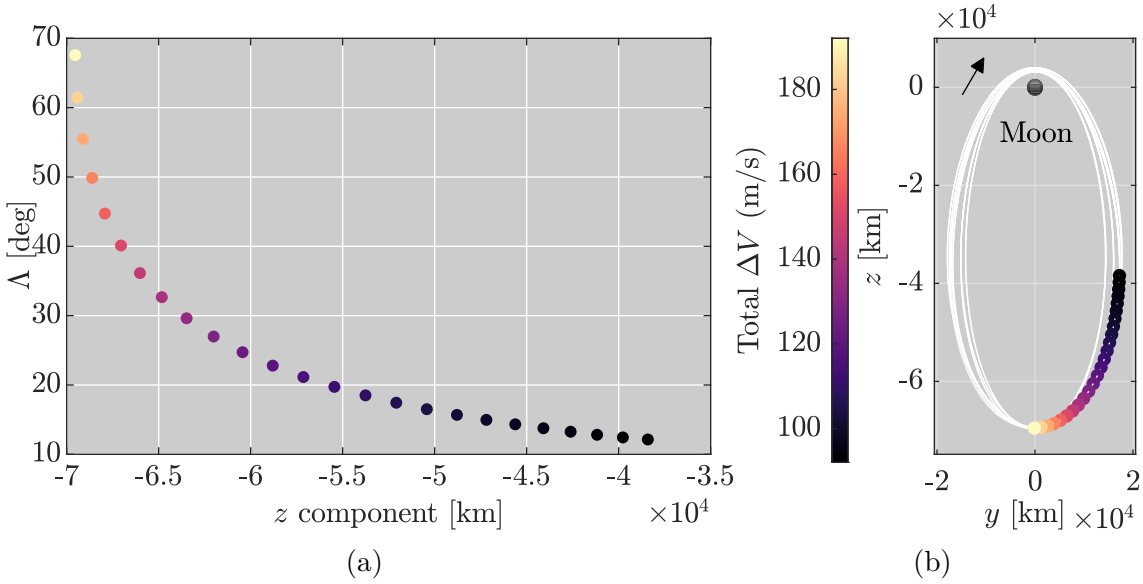


**Figure 5.30.** $\Lambda$ angle at departure from the Earth-Moon NRHO associated with the transfers in Figures 5.26(b) and 5.28(b) (a). Departure locations along the Earth-Moon NRHO, as viewed in the Earth-Moon rotating frame (b).

Sun system, and the effectiveness of the departure and insertion maneuvers is assessed using the $\Lambda$ angle.

### 5.4.3 Round-Trip Transfers

A sampling of round-trip transfer families to heliocentric orbits near the $\underline{L}_1$ and $\underline{L}_2$ Lagrange points are examined. To construct a family of inbound or outbound transfers, an initial guess is first select using of the methods presented in Section 5.3.3. The time-of-flight along this initial guess is adjusted to be continuous in epoch with the selected departure or arrival state along the 9:2 synodic resonant $L_2$ NRHO. In cases where the epoch discontinuity between the initial guess and the NRHO state is significant, additional trajectory arcs, labelled 'bridge arcs' and described in Section 5.4.1, are employed to facilitate the process. A numerical differential corrections scheme on the transfer trajectory is then employed to reduce the discontinuities between consecutive patch points to within a specified tolerance, while allowing the maneuvers noted in Figure 5.1. Once a continuous end-to-end transfer is obtained, it may be continued into a family of transfers by varying a parameter, such as the maneuver location and repeating the differential corrections process. Among the constructed families of outbound and inbound transfers, a round-trip trajectory that presents the lowest $\Delta$V for each leg and its characteristics are explored.

#### Round-trip Transfers to Sun-$B_1$ $\underline{L}_1$ Orbits

Families of end-to-end outbound and inbound transfers between the 9:2 synodic resonant $L_2$ NRHO and the Sun-$B_1$ halo orbits around the $\underline{L}_1$ libration point are constructed. As an illustration, consider the transfer families to and from the BCR4BP $\underline{L}_1$ halo bounded motion with maximum $\underline{z}$ component magnitude equal to 225,000 km, as produced in Figure 5.31. Two families are plotted in each figure: one corresponding to the inbound transfers and one for the outbound transfers. Each arc is colored as a function of the total $\Delta$V along the leg. For instance, the total $\Delta$V along the outbound leg is the sum of the departure maneuver from the Earth-Moon NRHO and the arrival maneuver into the Sun-$B_1$ halo orbit. The transfer families in Figure 5.31 possess a total leg $\Delta$V ranging between 98 and 300 m/s for

the outbound family, and ranging between 245 and 300 m/s. (The maximum allowable $\Delta$V magnitude for one leg of the round trip was set to 300 m/s in this analysis). The times-of-flight range from 220 to 226 days for the outbound transfers, and from 254 to 257 days for the inbound legs. The geometry of the transfers with respect to the Sun-$B_1$ rotating

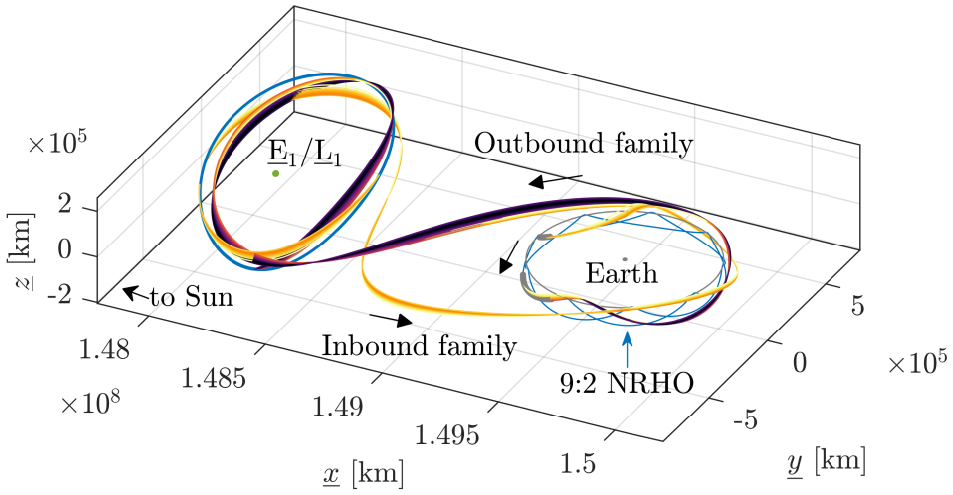


(a) Sun-$B_1$ rotating frame

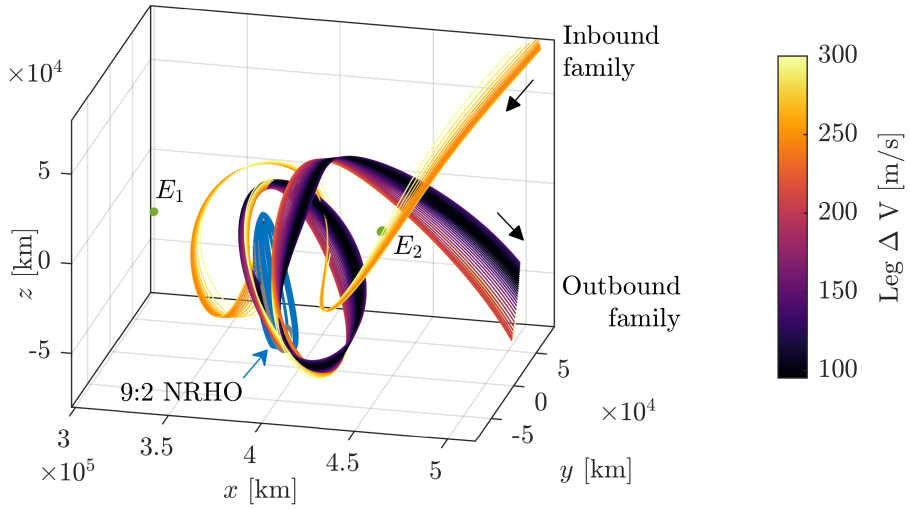


(b) Earth-Moon rotating frame

**Figure 5.31.** Outbound and inbound transfers as computed in the BCR4BP. The heliocentric orbit is the $L_1$ halo bounded motion with 225,000 km maximum $z$ component magnitude.

frame is apparent in Figure 5.31(a). The cislunar and heliocentric orbits are colored in blue, and the lunar orbit is the gray circle. The location of the CR3BP libration points and their

osculating BCR4BP counterparts are denoted by the green points and are indistinguishable at this scale. The maneuver locations along the NRHO are highlighted by white dots. The geometry of the transfers near the Moon, as viewed in the Earth-Moon rotating frame, is also explored in Figure 5.31(b). The locations for the NRHO departure and arrival maneuvers occur near an apolune, but on different revolutions along the NRHO. Note that no departure or arrival location is selected close to perilune: near this apse, higher dynamical sensitivities introduce different challenges in constructing consistent transfers and, thus, are avoided. The outbound and inbound transfer families both include additional revolutions around the Moon near the NRHO after departure and before arrival, respectively. The geometry of these extra revolutions suggests some arcs from a higher-period dynamical structures [42] are possibly leveraged to access and depart from the vicinity of the NRHO.

The round-trip transfer from the Earth-Moon 9:2 synodic resonant $L_2$ NRHO to the selected Sun-$B_1$ halo orbit that reflects the lowest total $\Delta$V cost is plotted in Figure 5.32. The associated total time-of-flight is 616 days and the total $\Delta$V cost is 412 m/s. For a round-trip transfer, the time-of-flight is defined as the sum of the time-of-flight along the outbound leg, the time spent in the heliocentric halo orbit, and the time-of-flight on the inbound leg. The location of the maneuvers is highlighted by red dots and text boxes in Figure 5.32; all four maneuvers are apparent in the Sun-$B_1$ rotating frame in Figure 5.32(a). The initial and final maneuvers along the transfer, i.e., the departure from and insertion into the Earth-Moon NRHO are visible in Figure 5.32(b). The magnitude associated with each the maneuvers is listed in Table 5.4. The majority (approximately 65%) of the total $\Delta$V cost is employed for the insertion into the Earth-Moon NRHO on the inbound leg of the transfer. This high insertion cost could potentially be reduced using a different initial guess for the inbound leg. Despite this relatively high insertion $\Delta$V maneuver magnitude, note that natural Sun-Earth-Moon dynamical flow is leveraged for the round-trip transfer. Consider the Sun-$B_1$ rotating velocity profile along the round-trip transfer as a function of the time along the trajectory in Figure 5.33. The colors are consistent with Figure 5.32: black for the cislunar and heliocentric orbits, blue for the outbound leg and orange for the inbound leg. The black spikes correspond to the rapid velocity change near perilune along the Earth-Moon 9:2 NRHO. Small discontinuities are apparent at each color transition; each discontinuity

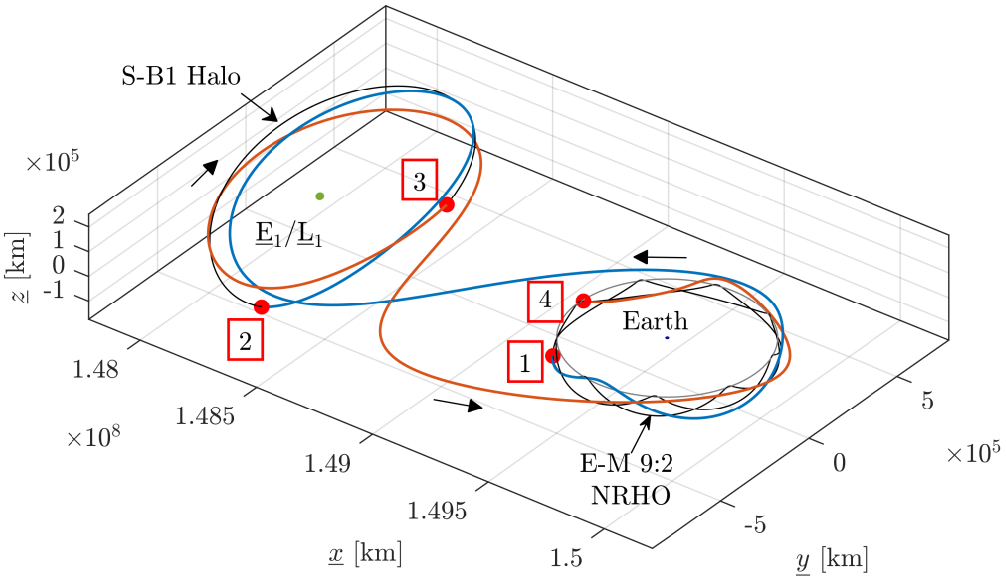


(a) Sun-$B_1$ rotating frame

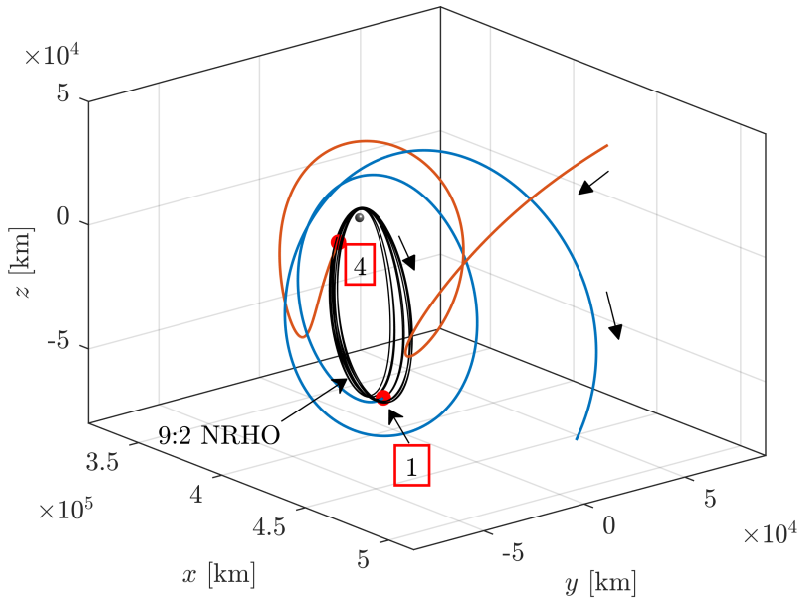


(b) Earth-Moon rotating frame

**Figure 5.32.** Round-trip transfer with the lowest total $\Delta$V cost among the transfers in Figure 5.31. The total $\Delta$V is 412 m/s and the total time-of-flight is 616 days.

**Table 5.4**. $\Delta$V maneuvers along the round-trip transfer in Figure 5.32

| **Maneuver** | **Label** | **Magnitude [m/s]** |
|---|---|---|
| E-M NRHO departure | 1 | 77.3 |
| S-B1 halo arrival | 2 | 20.6 |
| S-B1 halo departure | 3 | 43.1 |
| E-M NRHO arrival | 4 | 271.5 |
| **Total** | | **412.4** |

corresponds to a $\Delta$V maneuver and is identified by a red label. The small, sometimes indistinguishable, discontinuities do not significantly change the post-maneuver evolution of the velocity curve. Therefore, the round-trip transfer between the Earth-Moon NRHO and the Sun-$B_1$ libration point orbit leverages the natural Sun-Earth-Moon dynamical flow.

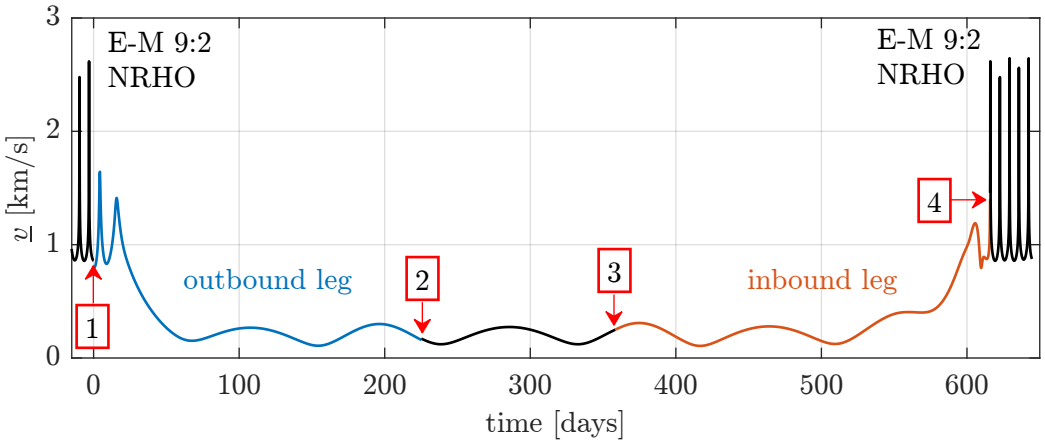


**Figure 5.33.** Sun-$B_1$ rotating velocity profile as a function of the time along the round-trip transfer in Figure 5.32

### Round-trip Transfers to Sun-$B_1$ $\underline{\text{L}}_2$ Orbits

Using this trajectory design framework, families of round-trip BCR4BP transfers to the Sun-$B_1$ $\underline{\text{L}}_2$ halo orbits are also successfully constructed. For example, consider the trajectories in Figure 5.34. The selected halo bounded motion has a maximum $\underline{z}$ component magnitude equal to 185,000 km. Recall that the cislunar orbit is the 9:2 synodic resonant $\text{L}_2$

NRHO with a phase consistent with the Gateway baseline orbit. Similar to the transfers in Figure 5.31, the trajectories are colored as a function of the $\Delta$V along each leg. A round-trip transfer involves an outbound (NRHO to Halo) leg and an inbound (Halo to NRHO) leg. Thus, the total $\Delta$V for a round-trip transfer is the sum of the $\Delta$V's for each leg. The $\Delta$V for the transfers along the family in Figure 5.34 range from 144 to 255 m/s for the outbound transfers and from 178 to 255 m/s for the inbound legs. The time-of-flight varies between 232 and 236 days, and between 307 and 312 days for the outbound and inbound trajectories, respectively. The times-of-flight between outbound and inbound legs may differ for a variety of reasons. First, the departure/arrival motion from the Sun-$B_1$ LPO leverages the approximate manifold associated with the orbit. Thus, the spacecraft may be in close proximity to the heliocentric orbit over a significant amount of time before the insertion maneuver (in the case of the outbound trajectories) and the end of the transfer leg. This 'winding' onto the LPO, apparent in Figure 5.34(a), is generally different for the outbound and inbound transfers and thus, results in different ranges for times-of-flight for the two parts of the transfer. Second, the geometry of the outbound and inbound transfers themselves are in general different. There is no resonance between the Earth-Moon 9:2 synodic resonant $L_2$ NRHO and the range of Sun-$B_1$ LPOs in Figure 5.4 that can be exploited in this investigation. If a resonance exists, symmetric, repeatable round-trip transfers would be available between the Earth-Moon NRHO and the Sun-$B_1$ halo orbit. Since it is not the case here, the geometries and, thus, the times-of-flight for the outbound and inbound legs differ to accommodate the change in relative phasing between the two orbits. Note the additional lobe and apogee along the inbound transfers as viewed in the Sun-$B_1$ rotating frame in Figure 5.34. This geometry is similar to the one associated with ballistic lunar transfers[99]. Inbound and outbound transfers that possess different Sun-$B_1$ geometries and times-of-flight are constructed in the BCR4BP employing the proposed trajectory design framework.

The transfers are also examined in the vicinity of the NRHO, in the Earth-Moon rotating frame, as plotted in Figure 5.34(b). In contrast to the transfers in Figure 5.31, these transfers do not possess multiple revolutions near the NRHO after departure or before arrival. In Figure 5.34, the outbound trajectories directly depart the vicinity of the NRHO after the departure maneuver; the inbound trajectories present one large revolution near the NRHO

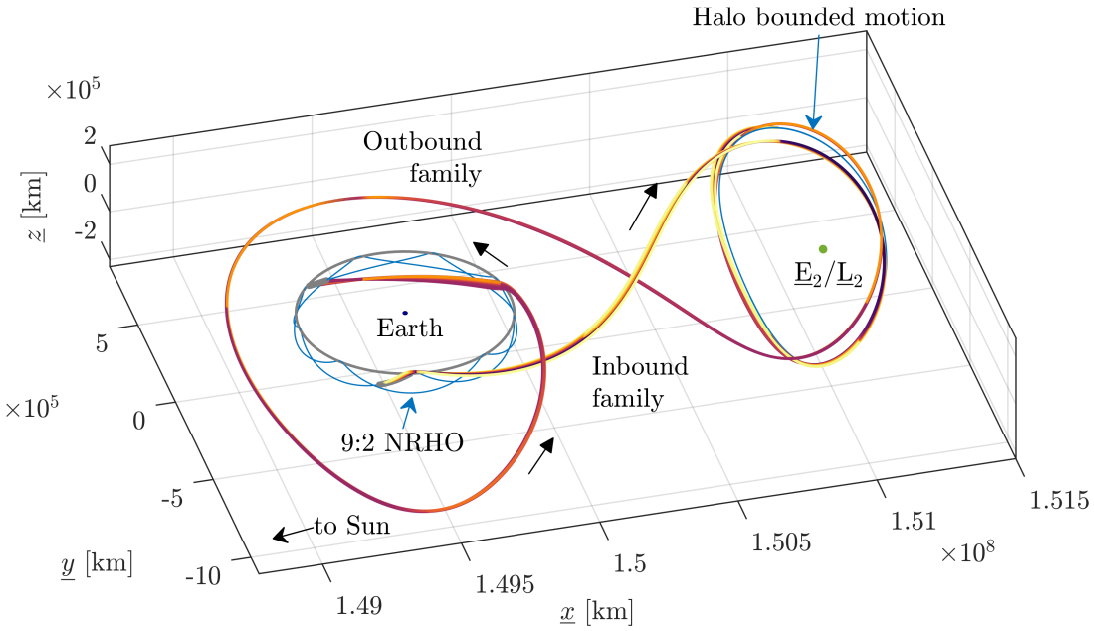


(a) Sun-$B_1$ rotating frame

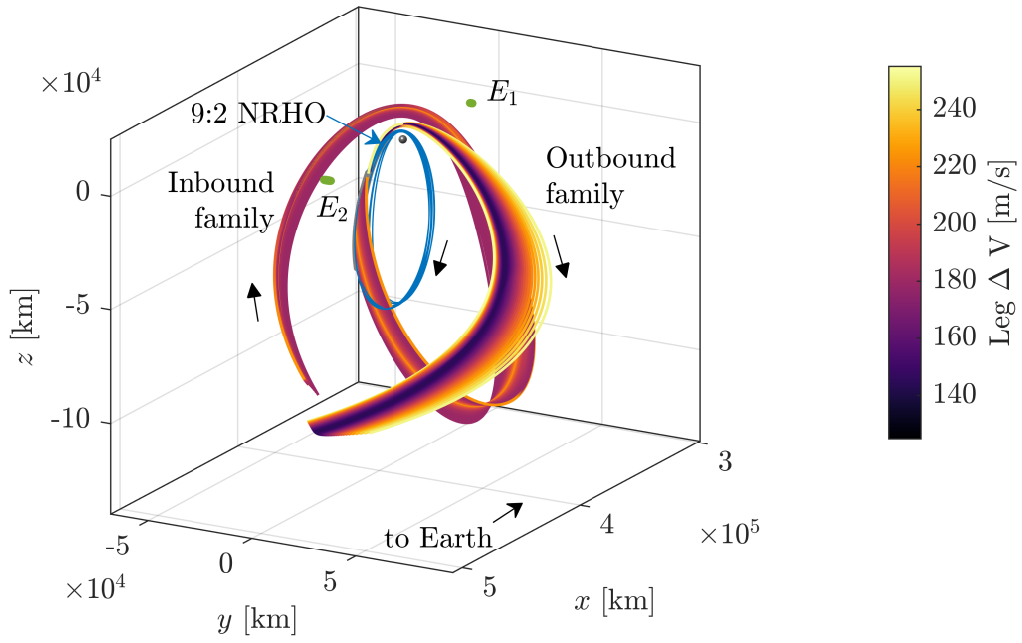


(b) Earth-Moon rotating frame

**Figure 5.34.** Families of outbound and inbound transfers, as computed in the BCR4BP. The heliocentric orbit is the $\underline{L}_2$ halo bounded motion with 185,000 km maximum $\underline{z}$ component magnitude.

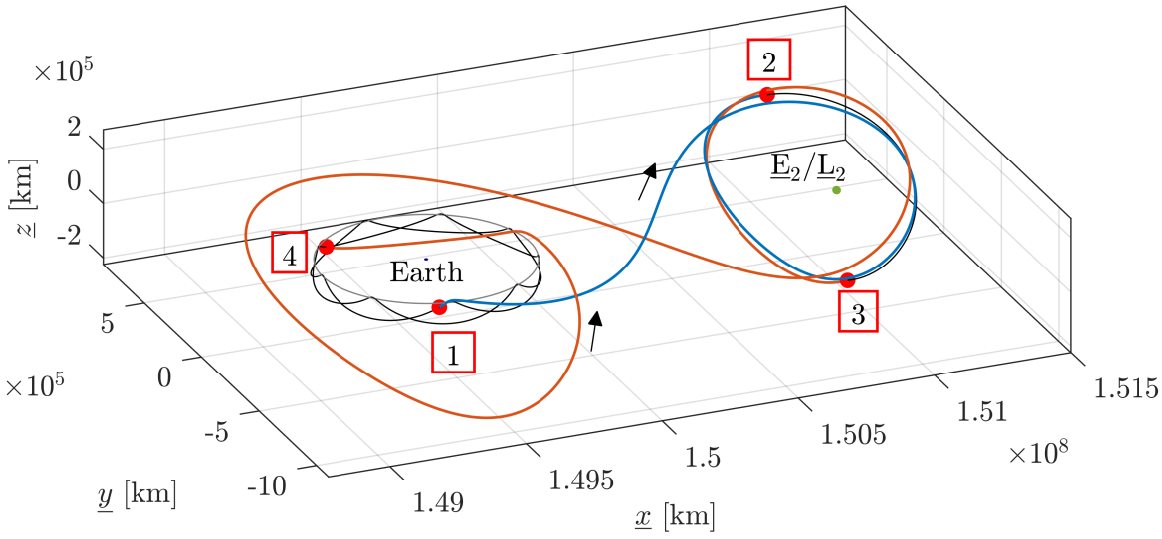


(a) Sun-$B_1$ rotating frame

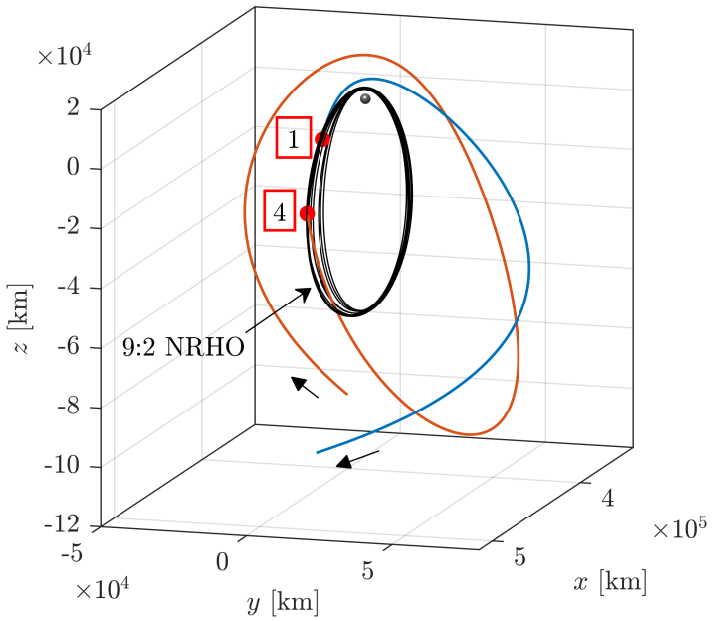


(b) Earth-Moon rotating frame

**Figure 5.35.** Round-trip transfer with the lowest total $\Delta$V cost among the transfers in Figure 5.34. The total $\Delta$V is 323 m/s and the total time-of-flight is 638 days.

before the insertion $\Delta$V maneuver. The location of the maneuvers along the NRHO are denoted by the white dots. Both departure and arrival maneuvers occur after an apolune state, that is, on the side of the NRHO with a negative rotating $\underline{y}$ component. Note that such as a location is not a requirement for constructing transfers: transfer families departing (or arriving) to a state prior to an apolune have been successfully constructed using this framework.

The round-trip transfer from the Earth-Moon NRHO to the Sun-Earth $\underline{L}_2$ LPO that offers the lowest total $\Delta$V cost is extracted from Figure 5.34 and plotted in Figure 5.35. The color along each arc is consistent with Figure 5.1 and each maneuver is located by a red dot and a label. Note that only the initial and final maneuvers are visible in the Earth-Moon rotating frame view in Figure 5.35(b). The total $\Delta$V value associated with this transfer is 323 m/s and the associated time-of-flight is 638 days. Recall that the time-of-flight along a round-trip is comprised of the times-of-flight along the outbound and inbound legs, as well as the time-of-flight along the heliocentric LPO, between the arrival and departure maneuvers. The magnitude for each of the four maneuvers along the transfer is summarized in Table 5.5. As compared to the transfer to the $\underline{L}_1$ region in Figures 5.32 and 5.33, the $\Delta$V budget is relatively balanced between the two parts of the transfers. The $\Delta$V cost for the outbound leg (i.e., maneuvers 1 and 2) is 144.3 m/s while the maneuvers (3 and 4) for the inbound leg amount to 179 m/s. The Sun-$B_1$ rotating velocity profile along the transfer is presented as a function of time along the trajectory in Figure 5.36. The small discontinuities at each color transition represents the $\Delta$V maneuver and is indicated by a

**Table 5.5**. $\Delta$V maneuvers along the round-trip transfer in Figure 5.35

| **Maneuver** | **Label** | **Magnitude [m/s]** |
|---|---|---|
| E-M NRHO departure | 1 | 124.5 |
| S-B1 halo arrival | 2 | 19.8 |
| S-B1 halo departure | 3 | 23.6 |
| E-M NRHO arrival | 4 | 155.2 |
| **Total** | | **323.1** |

red arrow and label. Similar to the velocity profile for the round-trip transfer to the $\underline{L}_1$ LPO in Figure 5.33, the velocity profile in Figure 5.36 is nearly continuous; the maneuvers do not significantly affect the downstream evolution of the velocity profile. Thus, the round-trip

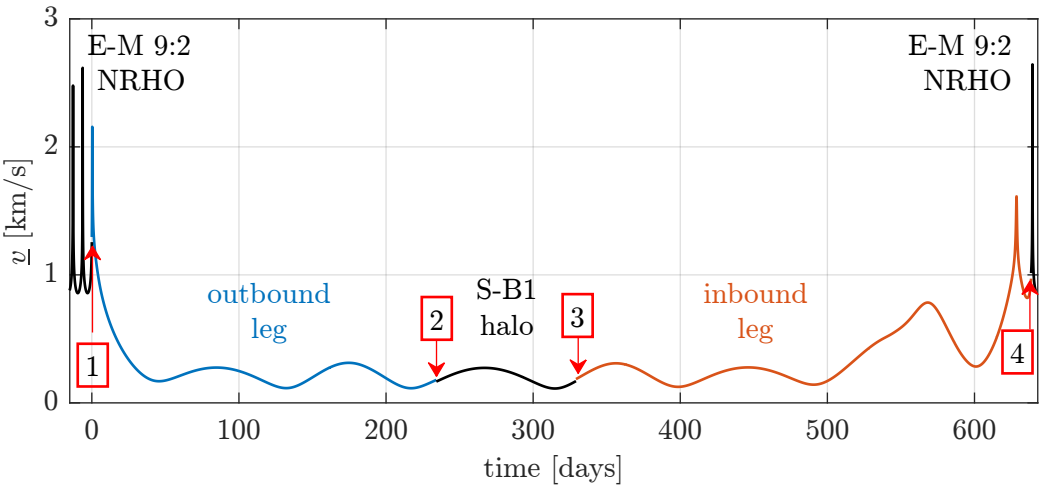


**Figure 5.36.** Sun-$B_1$ rotating velocity profile as a function of the time along the round-trip transfer in Figure 5.35

transfer that is constructed between the Earth-Moon 9:2 synodic resonant $L_2$ NRHO and the selected heliocentric $\underline{L}_2$ LPO leverages the natural dynamics of the blended Earth-Moon-Sun system.

## 5.5 Validation in the Ephemeris Model

The round-trip trajectories between the Earth-Moon NRHO and selected Sun-$B_1$ halo orbits are transitioned to the higher-fidelity ephemeris model for validation. First, a method to transform an epoch between the BCR4BP and the ephemeris model, that is, to convert a Sun angle to a calendar date, is introduced. Second, the reference cislunar and heliocentric orbits are transitioned. Reconstructing the departure and arrival motion in ephemeris model a priori typically facilitate the convergence of the end-to-end transfer. Third, the two formulations of the BCR4BP, i.e., the Earth-Moon frame and the Sun-$B_1$ frame formulations, are leveraged to construct an initial guess for the end-to-end transfers in the Earth centered inertial frame associated with the ephemeris model. Lastly, sample round-trip transfers are

transitioned from the BCR4BP to the ephemeris model, and characteristics of the transfers in the two dynamical models are compared.

### 5.5.1 Epoch Transformation between the BCR4BP and the Ephemeris Model

The process employed in this investigation to convert between a BCR4BP epoch, that is, a specific value of Sun angle, and the epoch employed in the ephemeris force model is detailed. Recall that the BCR4BP is a time-dependent model, as is the ephemeris model. However, the BCR4BP is a periodic model, of period equal to the lunar synodic month. Thus, a Sun-Earth-Moon configuration represented by a certain Sun angle corresponds to an infinite number of epochs in the higher-fidelity ephemeris model. For instance, a Sun angle equal to 180° corresponds to an alignment of the Sun, the Earth, and the Moon, in this order. This configuration also corresponds to the first phase of the lunar cycle, that is, a new Moon. Thus, the Sun angle $\theta = 180°$ corresponds to all possible new Moon epochs. Since the BCR4BP is a periodic dynamical model, the conversion of the epoch from the BCR4BP to the ephemeris force model is not unique.

For practical reasons, the Sun angle in the BCR4BP is matched to an epoch given a specific month and a specific year. For instance, the Sun angle $\theta = 180°$ is mapped to a unique epoch for the month of February 2020. The month and year are selected to be as close as possible to the desired epoch in the ephemeris model. To determine the day within the month and year that corresponds to the BCR4BP configuration, the osculating Sun angle is computed over this range as

$$\hat{\theta} = \arccos\left(\frac{\bar{\rho}^R_{\text{B1-Moon}} \cdot \bar{\rho}^R_{\text{B1-Sun}}}{\|\bar{\rho}^R_{\text{B1-Moon}}\|\|\bar{\rho}^R_{\text{B1-Sun}}\|}\right) \tag{5.4}$$

where $\bar{\rho}^R_{\text{B1-i}}$ is the position vector from the Earth-Moon barycenter to the body i, obtained from ephemerides and rotated to the Earth-Moon rotating frame. Then the corresponding epoch is determined in the ephemeris by locating the epoch corresponding the minimum

error between the Sun angle in the BCR4BP and the osculating Sun angle as computed in the ephemeris model, that is,

$$\text{equivalent epoch} = \arg \min_{\substack{\text{month,} \\ \text{year}}} \left( \|\theta - \hat{\theta}\| \right) \tag{5.5}$$

Some assumptions are incorporated when employing this conversion process between epochs in the ephemeris and the BCR4BP. First, the Sun position vector employed in Equation (5.4) to compute the osculating Sun angle is generally not in the Earth-Moon plane, since the Earth, Moon, and Sun are not located in the same plane in the ephemeris model. Thus, the equivalent epoch in Equation (5.5) is computed by comparing angles defined in two different planes. However, note that this approximation is acceptable for the Earth-Moon-Sun system, as the mean inclination of the lunar orbit with respect to the ecliptic plane is approximately 5.14°. For instance, the conversion method, described in Equations (5.4) and (5.5) and tested for the month of February 2020, predicts a new Moon ($\theta = 180°$) on the 09th at 07:47 UTC. According to the NASA GSFC Sky Events Calendar [100], a new Moon occurred on February 09th at 07:33 UTC. Thus, the simplified scheme is a suitable approximation for converting between ephemeris and BCR4BP epochs. The second assumption maps each Sun angle to one epoch for a given month and year. In reality, this mapping is not always unique, since the lunar synodic month (approximately 29.5 days) is shorter than the mean month-length (30.4 days). Thus, for certain months, a specific Sun angle corresponds to two different days. For instance, a new Moon ($\theta = 180°$) occurs on both the 1st and the 30th day in April 2022. In such instances, the strategy in Equations (5.4) and (5.5) returns the epoch that is numerically the closest to the selected Sun angle $\theta$. The equivalent epochs for the apolunes in the BCR4BP 3:1 NRHO as plotted in Figure 4.37 are computed for the month of May 2023 using the technique described in Equations (5.4) and (5.5) and are included in Table 5.6. The method procedure in this investigation maps an epoch as defined in the BCR4BP, that is, a Sun angle value, to an epoch in the ephemeris model given a certain month and year.

**Table 5.6**. Sun angle and equivalent epochs for the month of May 2023 for the two configurations of BCR4BP 3:1 NRHOs plotted in Figure 4.37(b).

| **Configuration** | **A** | | **B** | |
|---|---|---|---|---|
| Lobe | $\theta$, deg | Equivalent Epoch | $\theta$, deg | Equivalent Epoch |
| **L** | $-64$ | 2023 MAY 25 05:44:30 | 116 | 2023 MAY 10 15:18:11 |
| **C** | 180 | 2023 MAY 05 17:33:41 | 0 | 2023 MAY 19 15:16:45 |
| **R** | 64 | 2023 MAY 14 14:03:14 | $-116$ | 2023 MAY 29 23:18:11 |

### 5.5.2 Reference Cislunar and Heliocentric Orbits

To facilitate the convergence of the numerical corrections scheme in the ephemeris, the cislunar 9:2 NRHO and the Sun-$B_1$ halo orbits are converged are first reconstructed in the higher-fidelity model separately from the end-to-end transfers. Recall that precisely periodic motion generally does not exist in the ephemeris. Thus, periodic orbits from the lower-fidelity are transitioned to quasi-periodic orbits in the higher-fidelity model, similarly to the bounded motions in the BCR4BP in Section 4.3.6.

The process for transitioning a solution from the CR3BP or the BCR4BP to the ephemeris is not unique, that is, there are multiple processes that generate converged solutions with different characteristics in the ephemeris model. Recall that the ephemeris model relies on ephemerides for the position, velocity, and epoch states of the celestial bodies. Consequently, the ephemeris model is not time-autonomous, like the CR3BP; nor is it time-dependent and periodic like the BCR4BP. Periodic orbits from lower-fidelity models, that is, the CR3BP or the BCR4BP, are thus transitioned to a bounded or, at best, quasi-periodic motion in the ephemeris model. As such, without careful consideration of the details of the transitioning process, an infinite variety of trajectories may emerge. One transition approach to shift a periodic orbit between models involves a stacking process [101]. Multiple revolutions of the periodic orbit from the CR3BP (or the BCR4BP) are stacked, discretized, and corrected for continuity in the ephemeris model using a differential corrections scheme. However, periodicity is not enforced: the initial and final states along the corrected ephemeris trajectory do not necessarily match. The present investigation leverages a homogeneous stacking method

to transition periodic orbits in the CR3BP/BCR4BP to bounded motions in the ephemeris model.

As an illustration of the transition process between lower- and higher-fidelity models, consider the trajectories in Figure 5.37. Four $L_2$ halo orbits are transitioned from the Earth-Moon CR3BP to the Earth-Moon-Sun-Jupiter ephemeris model. Recall that in this formulation of the ephemeris model, the celestial bodies are included as point masses. The four selected halo orbits are characterized by synodic resonant periods; each period is a rational multiple of the synodic period, that is, approximately 29.5 days. In this example, the 2:1, 3:1, 9:2, and 5:1 synodic resonant $L_2$ halo orbits are selected. Their associated orbital periods are equal to $1/2$, $1/3$, $2/9$, and $1/5$ of the synodic period, respectively. For each orbit, 12 revolutions are stacked and the epoch for the initial state is set to May 15th, 2023. The resulting trajectories are discretized; patch points are selected every 2 days and propagated without corrections in the ephemeris model. The resulting initial guesses that are not converged in the ephemeris are plotted as viewed in the Earth-Moon rotating frame in Figure 5.37(a). The trajectories are discontinuous, as highlighted by the insert in Figure 5.37(a). Thus, a differential corrections scheme is employed to enforce continuity in position, velocity, and epoch between consecutive arcs. The resulting converged bounded motions are plotted in Figure 5.37(b). For the 2:1 halo orbit, the 9:2 NRHO, and the 5:1 halo orbit, the ballistic trajectories as constructed in the ephemeris model remain in close vicinity in configuration space of the CR3BP periodic orbits, plotted as the black dashed lines in Figure 5.37(b). (Note the CR3BP periodic orbits are also plotted for reference in Figure 5.37(a), but are indistinguishable given the initial guesses propagated in the ephemeris model.) However, the geometry of the 3:1 NRHO is not maintained in the ephemeris model. The trajectory that results from the differential corrections scheme, plotted in red in Figure 5.37(b), does not resemble the 3:1 NRHO from the Earth-Moon CR3BP, denoted by the black dashed line, or even the initial guess in the ephemeris model, plotted in red in Figure 5.37(a). The ephemeris trajectory from the differential corrections scheme is continuous in position, velocity, and epoch, and remains in the vicinity of the Moon, but does not follow any bounded pattern. In this example, at this epoch, the 3:1 $L_2$ NRHO is not successfully transitioned from the Earth-Moon CR3BP to the Earth-Moon-Sun-Jupiter ephemeris model. Thus, Boudad et al.

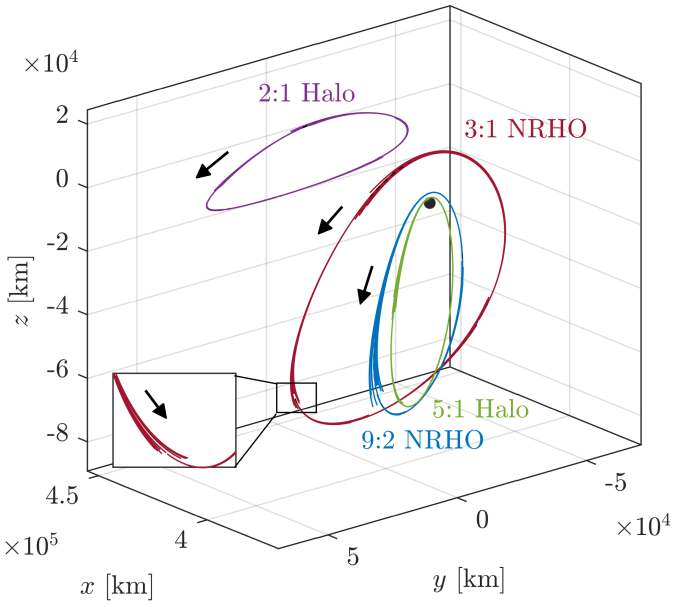


(a) Initial guesses

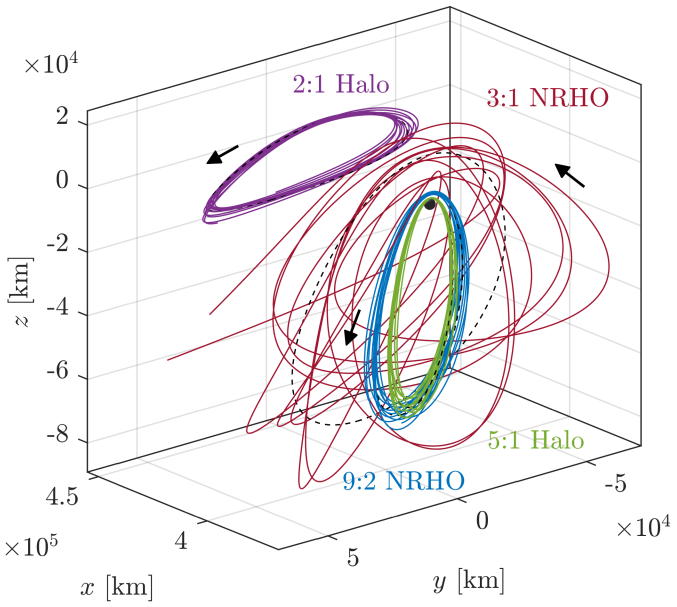


(b) Converged trajectories

**Figure 5.37.** Initial arcs (a) and converged trajectories (b) for various Earth-Moon $L_2$ halo orbits, as computed in the Earth-Moon-Sun-Jupiter ephemeris model and plotted in the Earth-Moon rotating frame. The initial guesses are constructed leveraging CR3BP periodic orbits.

[52] employ the BCR4BP as an intermediate step along the transition process to further maintain boundedness and repeatability in the ephemeris model. While it does not guarantee convergence or a preserved geometry, the transition employed in this analysis between lower- and higher-fidelity models generally yield continuous, repeatable motion.

The cislunar reference orbit, the 9:2 synodic resonant $L_2$ NRHO is transitioned from the Earth-Moon-Sun BCR4BP to the Earth-Moon-Sun-Jupiter ephemeris model. A stack of multiple 9:2 synodic resonant NRHOs as computed in the BCR4BP is assembled, and the resulting trajectory is discretized. The initial epoch associated with the trajectory is computed using the method introduced in Section 5.5.1. A differential corrections scheme is then employed to create a continuous trajectory in the ephemeris model, under the dynamics from Equation (2.16). The result of this differential correction process is plotted in Figure 5.38 for a stack of two BCR4BP 9:2 NRHOs, i.e., approximately 120 days of times-of-flight. In Figure 5.38(a), the trajectory is represented in the Earth-Moon rotating-pulsating frame; the similarity with the underlying periodic orbit from Figure 5.2(a) is apparent. The initial epoch associated with this solution is May 7th, 2024. The trajectory is also represented in the Sun-Earth rotating-pulsating frame in Figure 5.38(b). The lunar orbit is obtained from

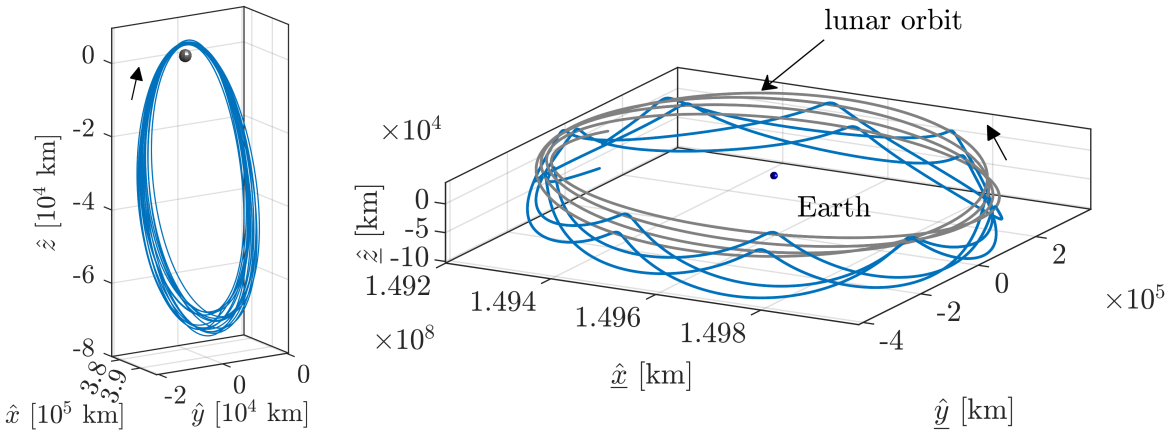


(a) Earth-Moon rotating pulsating frame

(b) Sun-Earth rotating-pulsating frame

**Figure 5.38.** 120 days of the 9:2 synodic resonant $L_2$ NRHO as computed in the Earth-Moon-Sun-Jupiter ephemeris model. The initial guess for this converged trajectory is a stack of 2 9:2 NRHO as constructed in the Earth-Moon-Sun BCR4BP, from Figure 5.2.

ephemerides [39], [54]; the trajectory is not periodic as the true eccentricity of the lunar orbit and its inclination with respect to the Earth ecliptic plane are considered. The characteristics, including the avoidance of the shadow of the Earth, associated the 9:2 synodic resonant $L_2$ NRHO in the BCR4BP, from Figure 5.2(b) are maintained. The cislunar reference orbit, the 9:2 synodic resonant $L_2$ NRHO as constructed in the BCR4BP, is successfully transitioned to the Earth-Moon-Sun-Jupiter ephemeris model.

The Sun-$B_1$ reference orbits, the bounded motions around selected $\underline{L}_1$ and $L_2$ orbits are also transitioned to the ephemeris model. Recall that bounded motion in the BCR4BP is constructed for non-synodic resonant orbits, such as the range of Sun-$B_1$ halo orbits in Figure 5.5. For such cases, the stack of orbits is first corrected in the BCR4BP, as in Figure 4.52, then discretized for the transition to the ephemeris model. As an illustration, consider the transition process in Figure 5.39(b). Three and half years (7 revolutions) of bounded motion associated with the $\underline{L}_2$ halo orbit with 185,000 km maximum $\underline{z}$ amplitude are constructed in the BCR4BP and appear in blue in Figure 5.39(a). Note that this trajectory is not periodic, but the discontinuity between the final and initial states is imperceptible at the scale of Figure 5.39(a). This trajectory is discretized, and the patch points are employed as the initial guess for a continuous trajectory in the ephemeris model. A differential corrections scheme is employed to reduce position, velocity, and epoch discontinuities between consecutive arcs to within an acceptable tolerance. The result of this differential corrections scheme is the blue trajectory in Figure 5.39(b). While this trajectory still closely resembles the bounded motion from the BCR4BP, the influence of the perturbations from the true motions of the celestial bodies, here Earth, the Moon, the Sun, and Jupiter, is apparent. The non-periodicity of the solution is also evidenced by the disconnected start of the trajectory near the rotating-pulsating $\hat{\underline{x}}$ axis. Note the lunar orbit, colored in gray in Figure 5.39. In the BCR4BP, in Figure 5.39(a), the lunar orbit is assumed to be circular and coplanar with the Sun-Earth plane. In the ephemeris model, the lunar orbit is obtained from ephemerides; the eccentricity and inclination with respect to the ecliptic plane are considered. In Figure 5.39(b), the lunar orbit is included for the same epochs as the blue trajectory, i.e., three and a half years starting on May 1$^{\text{st}}$, 2024. This span of time corresponds to approximately 43 revolutions of the Moon in the Sun-Earth rotating-pulsating frame; the lunar orbit thus appears as a torus

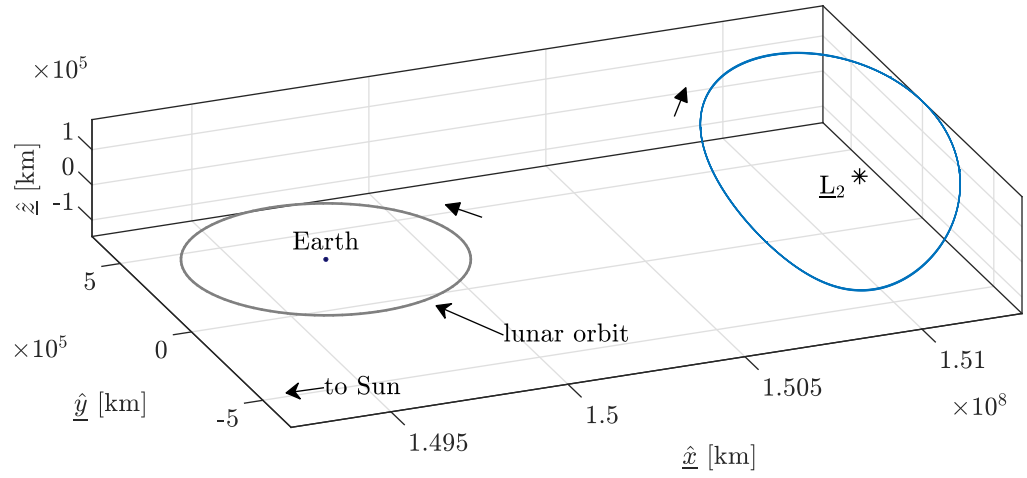


(a) BCR4BP, Sun-$B_1$ rotating frame

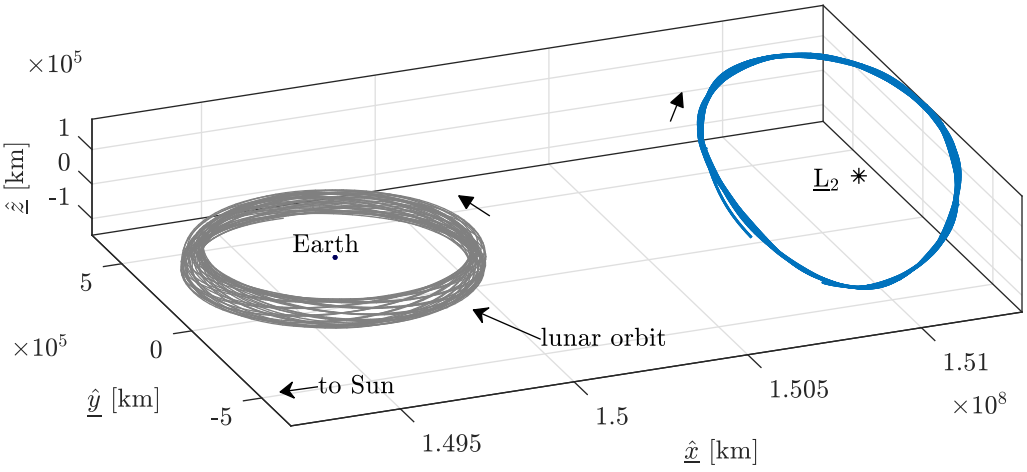


(b) Earth-Moon-Sun-Jupiter Ephemeris Model, Sun-Earth rotating frame

**Figure 5.39.** 3.5 years around the $\underline{\mathrm{L}}_1$ halo orbit with maximum $\underline{z}$ amplitude equal to 185,000 km, as computed in the Earth-Moon-Sun BCR4BP (a) and the Earth-Moon-Sun-Jupiter ephemeris model (b). The lunar orbit is denoted by the gray curves.

around the Earth. The differences in scale for the characteristics length, time, and masses between the Earth-Moon and Sun-$B_1$ systems are summarized in Chapter B. Bounded motion around the Sun-$B_1$ libration points is successfully transitioned from the BCR4BP to the higher-fidelity model.

### 5.5.3 Transformation Considerations for the Ephemeris Initial Guess

The end-to-end, round-trip transfers between the NRHO in cislunar space and the halo orbit in heliocentric space are transitioned to the higher-fidelity ephemeris model for validation. Recall that the equations of motion for the ephemeris model in Equation (2.16) are defined in an inertial frame and with respect to a central body. In this analysis, the Earth is selected as the central body, as it is a primary in both the Earth-Moon and the Sun-Earth[1] frames. Additionally, recall that the equations of motion for the BCR4BP are defined in two frames: the Earth-Moon rotating frame in Equation (2.4) and the Sun-$B_1$ rotating frame in Equation (2.8). Thus, the initial guess for the end-to-end transfers is rotated from either the Earth-Moon rotating frame or the Sun-$B_1$ rotating frame, to an inertial Earth-centered ephemeris frame.

The influence of the selection of the transformation scheme on the initial guess in the higher-fidelity model is non-negligible. For instance, consider the round-trip transfer to a $\underline{\mathrm{L}}_2$ halo orbit as converged in the BCR4BP in Figure 5.35. All the states along the trajectory are rotated to the J2000 Earth-Centered Inertial (ECI) frame in Figure 5.40 using the method detailed in [98], [102], [103]. The differences between the results of the two transformation schemes are evident. While the two trajectories remain relatively close to each other at the beginning and end, the rotated ECI trajectory from the Earth-Moon rotating states presents loops when away from the Earth. These loops are an artifact of the scaling factor employed in the transformation scheme. As detailed by Ocampo [102], this scaling factor is employed to incorporate the variations, or pulsations, between the primaries in the higher-fidelity model. For transformation from the Earth-Moon rotating frame, the scaling factor corresponds to the change of Earth-Moon distance due to the eccentricity of the lunar orbit. Similarly, the eccentricity of the Earth orbit around the Sun is incorporated in the scaling factor when transforming states from the Sun-$B_1$ frame to the J2000 ECI frame. Since the characteristic lengths (presented in Appendix B) and the eccentricities of the Earth's and the Moon's orbits (0.0167 and 0.0549 on average, respectively), the scaling factors affects differently the

[1]↑Due to the data available from ephemerides, the Sun-Earth rotating frame, rather than the Sun-$B_1$ rotating frame is considered is considered in the ephemeris model.

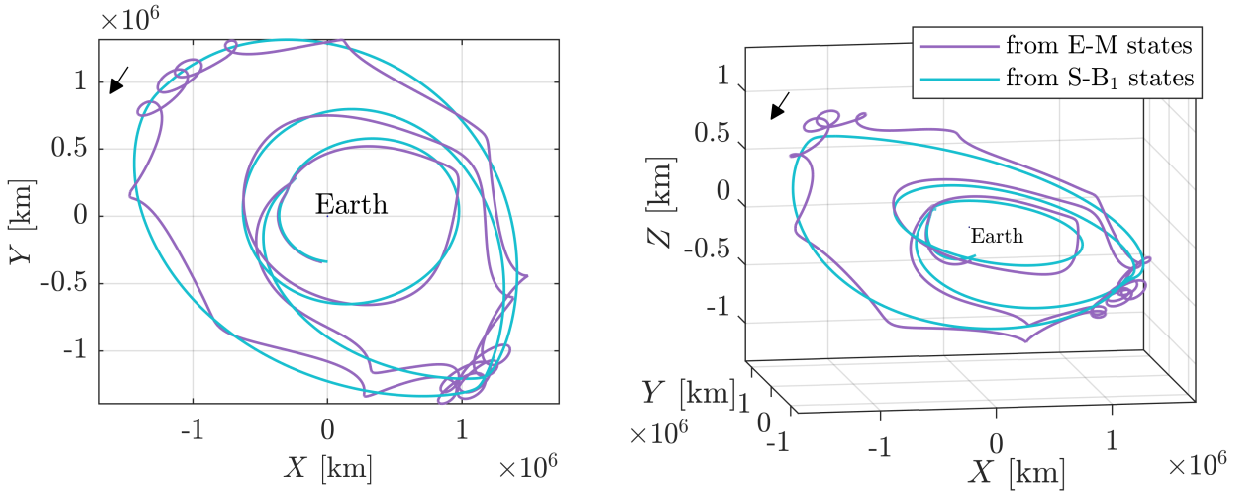


**Figure 5.40.** BCR4BP round-trip trajectory from Figure 5.35 rotated to the J2000 ECI from Earth-Moon rotating states (in purple) and Sun-$B_1$ rotating states (in cyan).

transformation to the ECI frame. The influence of each scaling factor distinctively appears in Figure 5.41. The distance to Earth is plotted as a function of time for both rotated transfers from Figure 5.40. Both curves follow the same trend. However, the purple curve, correspond to states transformed from the Earth-Moon rotating frame, appears to oscillate around the cyan curve. The period of the oscillations is approximately 28 days, that is, the sidereal period of the Moon around the Earth. The second, longer period apparent in Figure 5.41 is approximately equal to six months. This variation is not associated with either of the scaling factors; rather, it is associated with the period of the Sun-$B_1$ halo orbit. Thus, these oscillations correspond to the part of the trajectory where the spacecraft is flying along the Sun-$B_1$ halo orbit. The choice of the original frame for the transformation of a transfer to the J2000 ECI frame presents decisive implications.

The selection of the initial frame for the transformation bears implication for the quality of the propagation of the initial guess in the ephemeris model. Following the transformation from the selected rotated frame to the ECI frame, the BCR4BP trajectory is discretized. The resulting patch points are then propagated using the ephemeris dynamics from Equation (2.16). For instance, consider the propagated arcs in Figure 5.42. The black lines

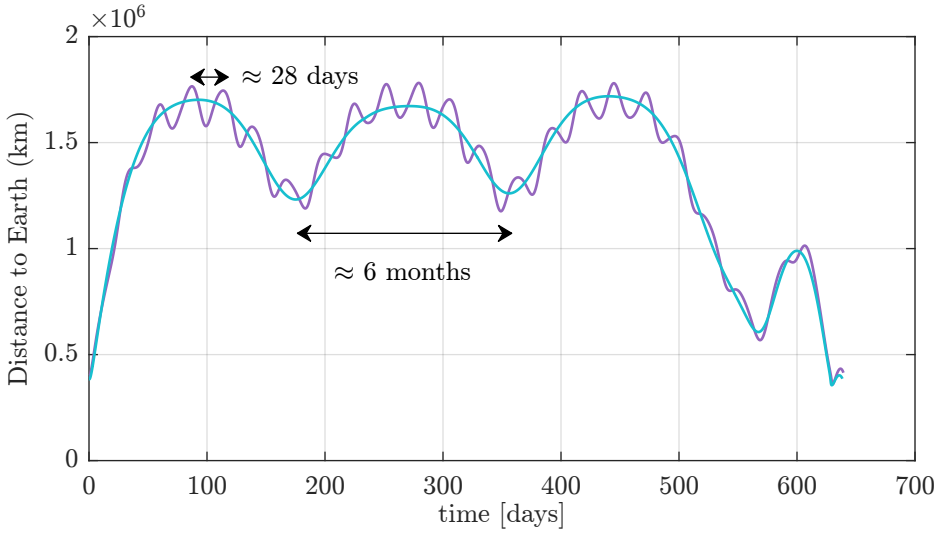


**Figure 5.41.** Distance to Earth as a function of time along each rotated transfer in Figure 5.40. The cyan line corresponds to J2000 ECI states transformed from the Sun-$B_1$ rotating frame, while the purple curve denotes J2000 ECI states transformed from the Earth-Moon rotating frame.

correspond to the rotated BCR4BP trajectories from Figure 5.40. Patch points are selected every 300,000 km along the black curves and propagated in using the Earth-centered ephemeris equations of motion from Equation (2.16). The included celestial bodies are Earth, the Moon, the Sun, and Jupiter. The propagated arcs plotted in color in Figure 5.42. Propagated arcs that employ initial states transformed from the Sun-$B_1$ rotating states, in Figure 5.42(a), appear to follow more closely the lower-fidelity trajectory (in configuration space), plotted in black, than propagated arcs employing transformed Earth-Moon rotating states in Figure 5.42(b). Proximity between the propagated lower- and higher-fidelity models is an insightful measure of the quality of the estimation from the lower-fidelity model. For instance, the Sun-$B_1$ rotating states from the BCR4BP seem to appropriately capture the dynamics of the Earth-Moon-Sun-Jupiter ephemeris model in heliocentric space, as the cyan arcs closely align the with the black trajectory away from the Earth in Figure 5.42(a). Unsurprisingly, the states transformed from the BCR4BP Earth-Moon rotating frame do not reflect the higher-fidelity dynamical environment away from the Earth-Moon vicinity. Recall that the loops observed in Figure 5.42(b) are a consequence of a scaling factor in the transformation scheme; they are not caused by the dynamics. Thus, the arcs in Fig-

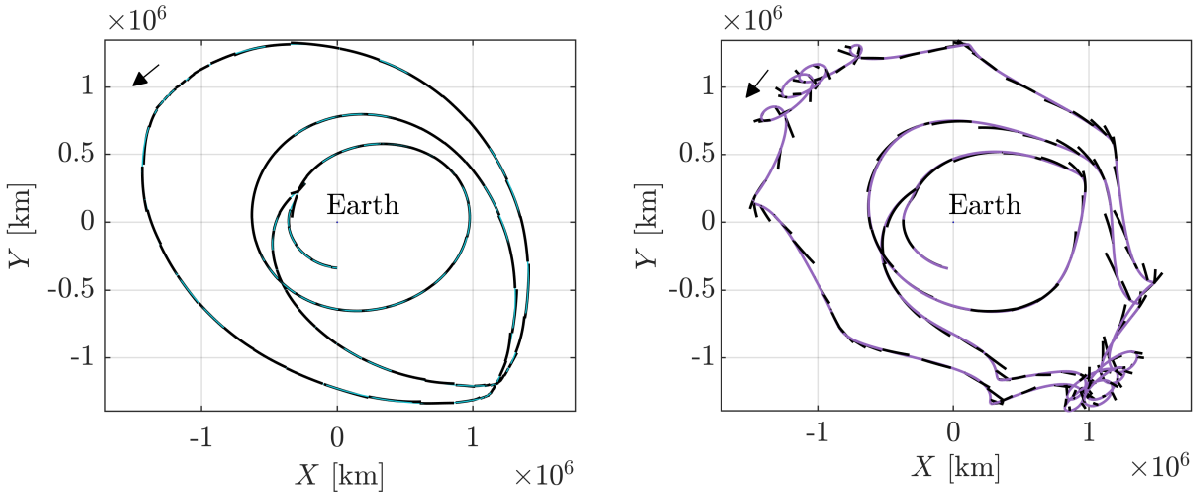


(a) From Sun-$B_1$ rotating states

(b) From Earth-Moon rotating states

**Figure 5.42.** Trajectories propagated using the ephemeris equations of motion (colored) employing patch points along the rotated BCR4BP transfer (black). The celestial bodies included for the ephemeris are Earth, the Moon, the Sun, and Jupiter.

ure 5.42(b), propagated using the dynamics of the ephemeris model, do not follow these loops. Although states in the Earth-Moon and Sun-$B_1$ rotating frames reflect the same dynamics in the BCR4BP, the transformation scheme between rotating frame impacts the quality of the initial guess for the ephemeris model.

While they do not provide a suitable initial guess for the ephemeris dynamics in heliocentric space, the ECI states obtained from the Earth-Moon rotating frame adequately reflect the higher-fidelity dynamics in the lunar vicinity. The propagated arcs from Figure 5.42 are transformed from the J2000 ECI frame to a Sun-Earth rotating-pulsating frame, in Figure 5.43(a), and to an Earth-Moon rotating-pulsating frame, in Figure 5.43(b). In heliocentric space, the poor quality of the initial guess from Earth-Moon rotating states is demonstrated by the disconnected purple arcs around $\underline{L}_2$, in Figure 5.43(a). The arcs propagated in the ephemeris model with initial guesses transformed from the Sun-$B_1$ rotating frame, colored in cyan in Figure 5.43, closely align with the expected $\underline{L}_2$ halo motion. However, these cyan propagated arcs do not appropriately reflect the desired motion in the vicinity of the Moon, as apparent from the Earth-Moon rotating-pulsating view in Figure 5.43(b).

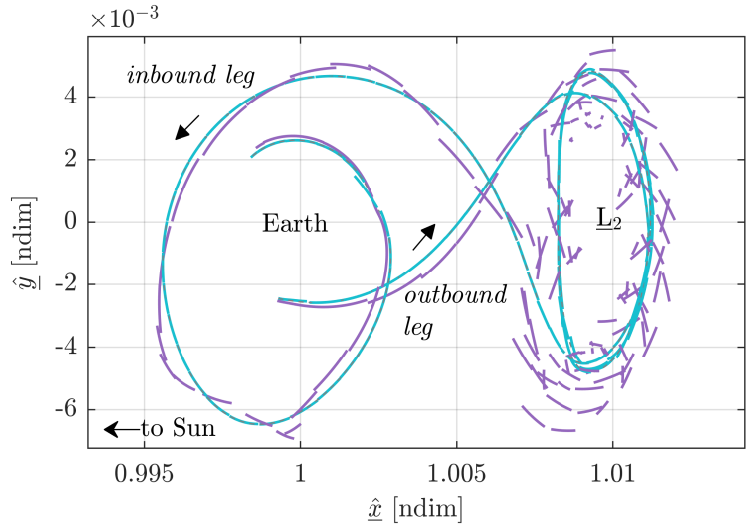


(a) Sun-Earth rotating-pulsating frame

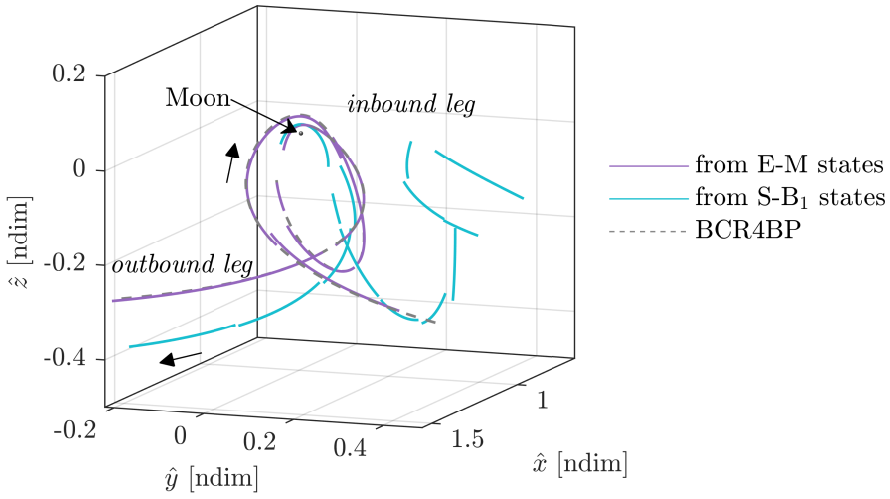


(b) Earth-Moon rotating-pulsating frame

**Figure 5.43.** Propagated ephemeris arcs from Figure 5.42, as viewed in two rotating-pulsating frames. The initial guess from the BCR4BP is denoted by the grey dashed line.

Moreover, the purple arcs corresponding to the inbound leg of the transfer do not return to an NRHO-like motion; these propagated arcs appear to 'miss' the Moon. Recall that the scaling factor in the transformation between Sun-$B_1$ rotating and ECI does not explicitly account for the eccentricity of the Moon and, thus, the variations in the Earth-Moon distance. The purple arcs are trajectories propagated in the Earth-Moon-Sun-Jupiter ephemeris model in the J2000 ECI frame using initial states transformed from Earth-Moon rotating

BCR4BP states. These propagated arcs are closely aligned with the BCR4BP, plotted as the grey dashed line, in Figure 5.43(b). While the scaling factor in the transformation from the Earth-Moon rotating frame distorts trajectories in heliocentric space, it allows for the accurate incorporation of the Earth-Moon pulsation in cislunar space, including in the vicinity of NRHO.

An alternative method for transforming a cislunar-to-heliocentric transfer from BCR4BP to an initial guess in the J2000 ECI frame for the ephemeris model. This alternative method blends the transformations from the Earth-Moon rotating frame and the Sun-$B_1$ rotating frame, to exploit the benefits of each transformation. The transformation is varied along the transfer; in the lunar vicinity, states from the Earth-Moon rotating frame are leveraged since their associated transformation accurately represent the eccentricity of the lunar orbit in the ephemeris model. Conversely, in heliocentric space, the process that transforms the Sun-$B_1$ states is employed, as it adequately renders the dynamics of the ephemeris model in this region. In this analysis, the instantaneous distance to the Moon along the trajectory is employed to determine which transformation to use for each state. For states within one Earth-Moon characteristic length, that is, $l^* \approx 384,000$ km, the Earth-Moon states are transformed to the J2000 ECI frame. For states outside this sphere, the transformation that leverages the Sun-$B_1$ frame states is employed. Note that the cutoff parameters are a function of the applications; this combination of switching conditions yield adequate results for this analysis. As an illustration, return to the round-trip transfer to a $\underline{\mathrm{L}}_2$ halo constructed in the BCR4BP and examined in Figures 5.35 and 5.40–5.42. This transfer is plotted in the Sun-$B_1$ and Earth-Moon rotating frames and colored as a function of the distance to the Moon in Figure 5.44. Purple states are located within one $l^*$ of the Moon, while cyan states are outside this boundary. Thus, these states are rotated to the J2000 ECI frame leveraging the Sun-$B_1$ rotating states, represented by the cyan curve in Figure 5.44(a). Conversely, points within the defined lunar distance are rotated to the J2000 ECI frame employing Earth-Moon rotating states, i.e., the purple points in Figure 5.44(b). The blended transformation method developed in this investigation employs the distance to the Moon along the trajectory to determine the set of states to employ for the transformation to the J2000 ECI.

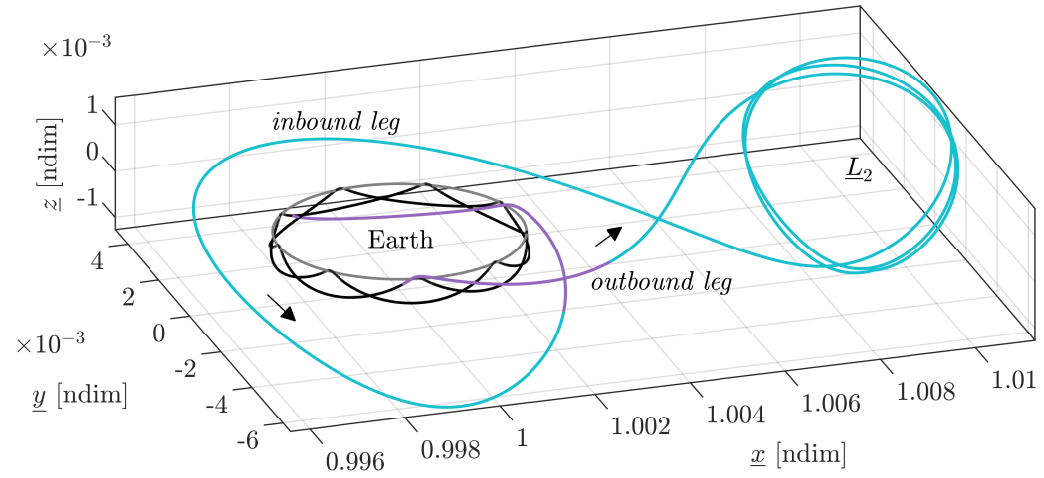


(a) Sun-$B_1$ rotating frame

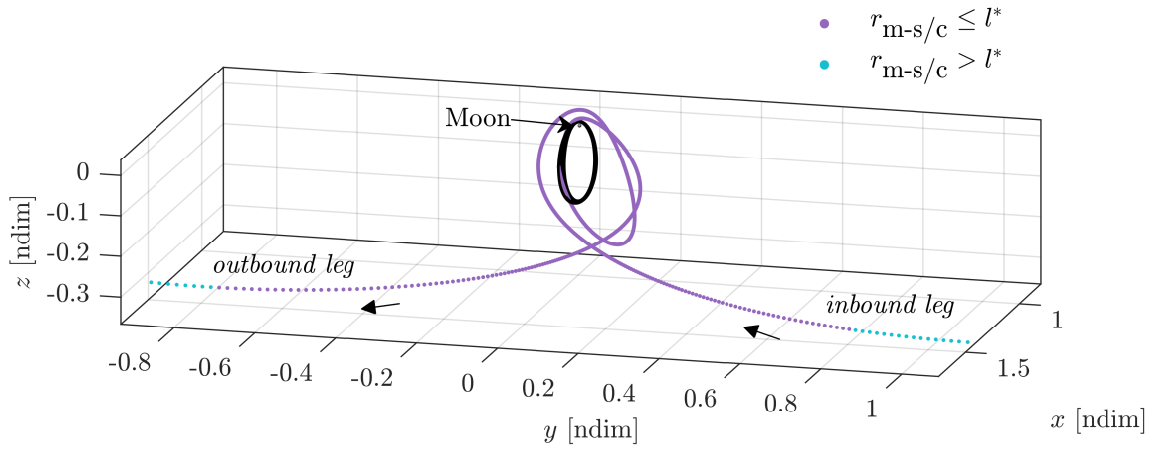


(b) Earth-Moon rotating frame

**Figure 5.44.** BCR4BP round-trip trajectory from Figure 5.35, colored as a function of the distance to the Moon. Purple states are located within one $l^* \approx 384,000$ km of the Moon, cyan states are outside this region.

Employing this proposed transition method, initial guesses for the differential corrections scheme in the ephemeris model are constructed. The transfer from Figure 5.44 is transformed to the J2000 ECI frame with the blended method; the resulting trajectory is presented in Figure 5.45(a). Purple and cyan states are transformed using the Earth-Moon and Sun-$B_1$ states, respectively. Note that the purple and cyan curves in Figure 5.45(a) are not connected; the small discontinuities at the interface between the two transformation

schemes are due to the different scaling factors. Patch points are distributed every 300,000 km along the cyan and purple trajectories in Figure 5.45(a). These patch points are then propagated in the Earth-Moon-Sun-Jupiter ephemeris model using the equations of motion from Equation (2.16). The resulting trajectories appear in Figure 5.45(b). Although the trajectory is not continuous, it closely follows the transfer constructed in the lower-fidelity model in Figure 5.45(a). Thus, the trajectory in Figure 5.45(b) is an adequate initial guess for the reconstructing the round-trip transfer in the ephemeris model. A differential corrections scheme is employed to reduce position, velocity, and epoch discontinuities between the consecutive black arcs to within an acceptable tolerance. The blended transition method improves the quality of the initial guess for the numerical corrections in the higher-fidelity model, thus increasing the likelihood of smooth and quick convergence.

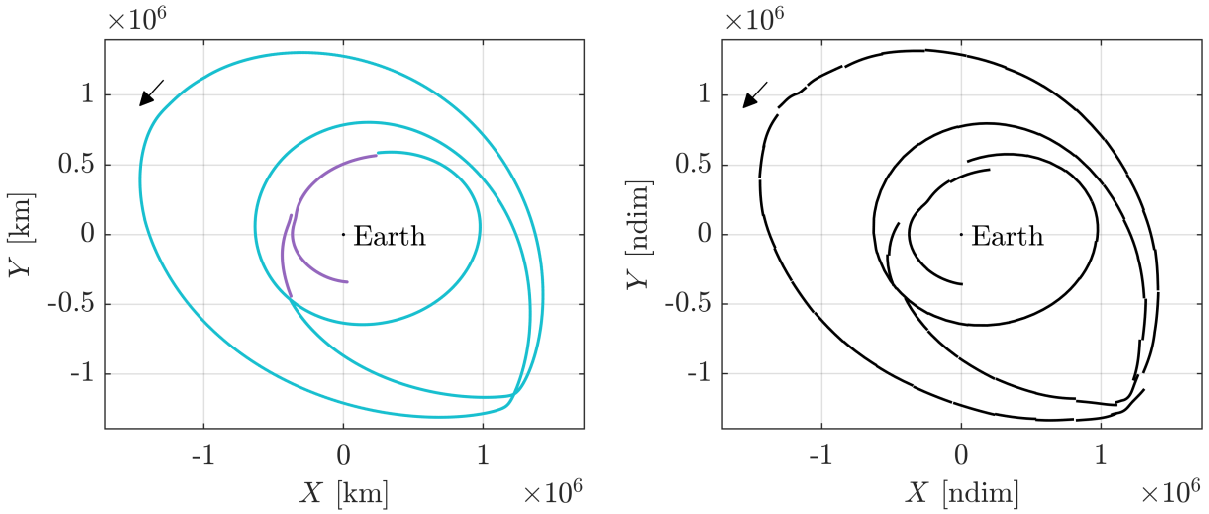


(a) Rotated states from the BCR4BP (b) Propagated states in the ephemeris model

**Figure 5.45.** Result of the blended transformation of the converged transfer constructed in the BCR4BP to the J2000 ECI frame (a). The propagated arcs in (b) form a suitable initial guess for a differential corrections scheme to reconstruct the transfer in the higher-fidelity ephemeris.

### 5.5.4 Converged Transfers

Round-trip transfers between the cislunar NRHOs and selected Sun-$B_1$ bounded halo motions are transitioned to the ephemeris force model. Initial guesses from the higher-

fidelity transfers are constructed using the end-to-end transfers generated in the BCR4BP in Section 5.4.3 and the blended transformation method from Section 5.5.3. The discontinuous initial guesses are passed to a differential corrections scheme that is employed to reduce discontinuities between the consecutive arcs to within an acceptable tolerance set to $10^{-12}$. The phases associated with the cislunar and heliocentric are not allowed to vary. This targeting scheme is implemented in the J2000 ECI frame and the celestial bodies included in the ephemeris model are Earth, the Moon, the Sun, and Jupiter. The constraints associated with the targeting scheme include continuity in position, velocity, and epoch between consecutive arcs; velocity discontinuities are allowed in four locations to represent the NRHO and halo insertion and departure $\Delta$V maneuvers. The converged trajectories are then transformed back to the Earth-Moon and Sun-Earth rotating-pulsating frames for visualizations purposes. Round-trip transfers between cislunar and heliocentric space are transitioned to the ephemeris model leveraging a blended transformation of the BCR4BP states and a differential corrections scheme.

As an illustration, the round-trip transfer between the 9:2 NRHO and a $\underline{L}_1$ halo orbit with 185,000 km maximum $\underline{z}$ amplitude from Section 5.5.3 is transitioned to the ephemeris model. The resulting trajectory for a departure from the NRHO on May 14$^{\text{th}}$ 2024 is presented in the Sun-$B_1$ rotating pulsating frame in Figure 5.46 and in the Earth-Moon rotating-pulsating frame in Figure 5.47. The geometry of the ephemeris solution generally follows the lower-fidelity transfer from the BCR4BP, plotted as the dashed black line. The motion near the $\underline{L}_2$ libration point is shifted in position and inclination relative to the ecliptic plane. The geometry of the initial guess is distorted along the differential corrections process; the resulting motion in Figure 5.46 resembles revolutions along a Lissajous orbit [104], [105]. The original shape of the $\underline{L}_2$ motion may be further preserved by enforcing additional constraints on the trajectory in the differential corrections scheme, such as a cone constraint [106]. In the Earth-Moon rotating-pulsating frame, in Figure 5.47, the resemblances between lower- and higher-fidelity solutions are also apparent. The first apolune along the outbound leg is and the last apolune along the inbound leg are closer to the Moon for the ephemeris solution than they are in the BCR4BP. Additional constraints may also be implemented for the NRHO departure and arrival to further maintain desired characteristics from the BCR4BP

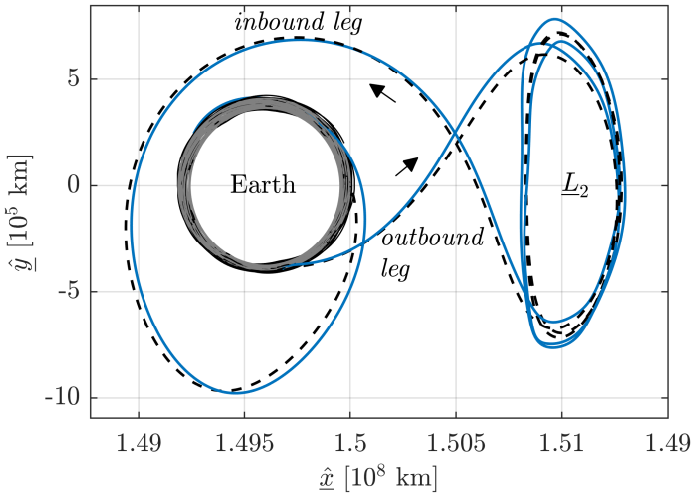


(a)

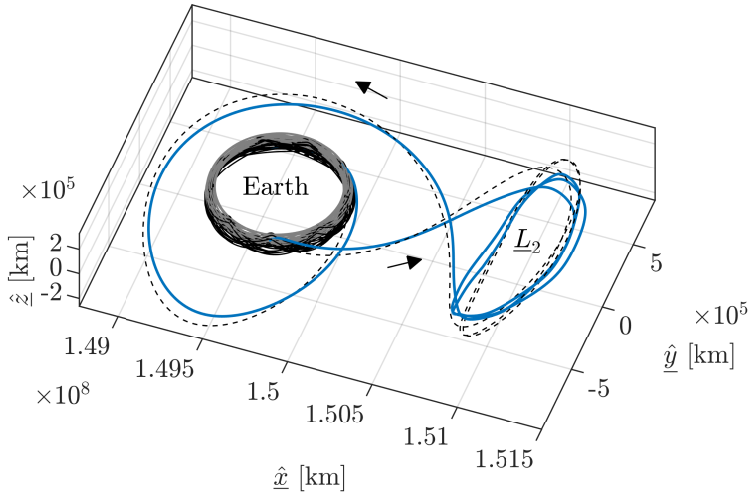


(b)

**Figure 5.46.** Round-trip ephemeris transfer (in blue) between the cislunar 9:2 NRHO and a heliocentric $\underline{L}_2$ halo orbit with maximum $\underline{z}$ amplitude equal to 185,000 km, for an initial epoch of May 14$^{\text{th}}$ 2024. After 640 days (1.75 years), the spacecraft returns to the NRHO on February 13$^{\text{th}}$ 2026. The BCR4BP transfer is denoted by the dashed black line.

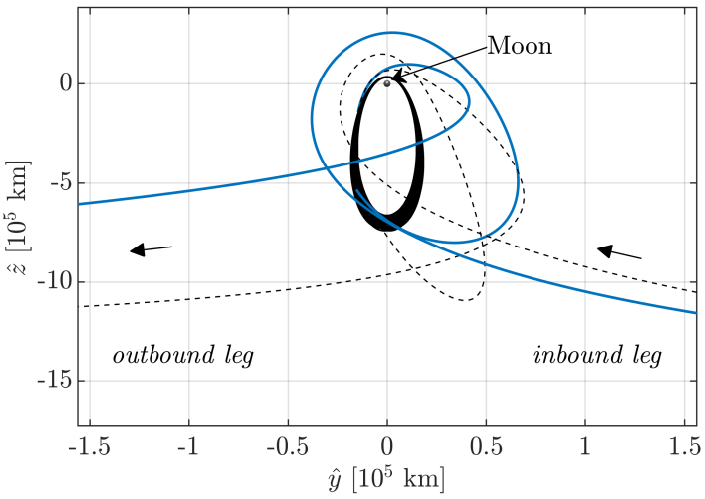


(a)

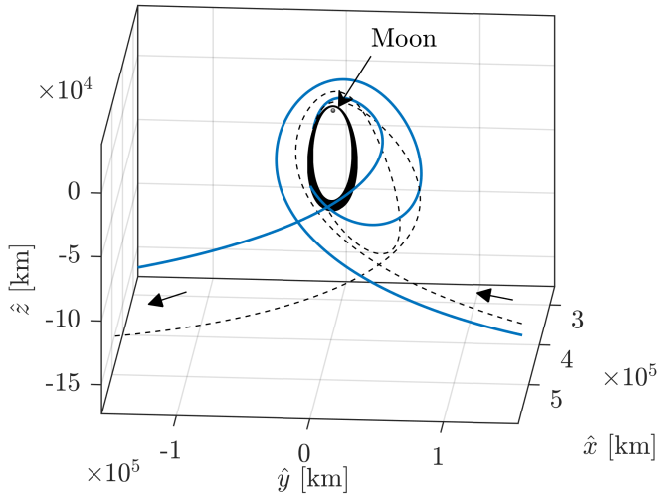


(b)

**Figure 5.47.** Earth-Moon rotating-pulsating view of the transfer from Figure 5.46, in the vicinity of the Moon.

transfer. A sample round-trip transfer between cislunar and heliocentric space is successfully transitioned to the higher-fidelity ephemeris model.

The magnitudes of the $\Delta$V maneuvers are compared between the BCR4BP and ephemeris end-to-end transfer. Recall that four maneuvers are allowed along each transfer: two for the NRHO departure and arrival near the Moon, and two for the halo insertion and departure in heliocentric space. The magnitudes associated with each maneuver in both the BCR4BP

and ephemeris model are summarized in Table 5.7. The total $\Delta$V associated with the ephemeris is 646 m/s, and 412.4 m/s for the BCR4BP transfer. However, the increase in $\Delta$V is not uniform across the four maneuvers in the ephemeris. While the order of magnitude is similar for the heliocentric maneuvers in both models, the maneuvers along the NRHO vastly differ. For the ephemeris transfer, the NRHO departure that starts the outbound leg is approximately four times larger (413.4 m/s in contrast to 77.3 m/s), while the NRHO insertion that ends the inbound leg is approximately halved (133.1 m/s vs 271.5 m/s). Both the ephemeris and BCR4BP trajectories are *feasible* transfer. The total $\Delta$V, the times-of-flight, and the geometry of the transfer may be improved upon by iterating on the corrections process or by numerical optimization. Note that these two avenues are beyond the scope of this analysis, which aims to demonstrate a framework for transfers between the cislunar to heliocentric regions. Furthermore, the end-to-end transfers presented in Section 5.4.3 present compounded numerical and dynamical challenges, including long (over one and half year) times-of-flight, at least two close (less than $5,000$ km) lunar flybys, complex dynamics in the vicinity of the 9:2 NRHO. Further investigation into the transition of such trajectories between lower- and higher-fidelity models is required. The magnitudes of the four $\Delta$V maneuvers may differ substantially between the BCR4BP and ephemeris transfer, as a consequence of the transition between the lower- and higher-fidelity models.

**Table 5.7**. $\Delta$V maneuvers along the round-trip transfers in Figures 5.46 and 5.47.

| **Maneuver** | **BCR4BP [m/s]** | **Ephemeris [m/s]** |
|---|---|---|
| E-M NRHO departure | 77.3 | 413.4 |
| S-B1 halo arrival | 20.6 | 49.6 |
| S-B1 halo departure | 43.1 | 49.9 |
| E-M NRHO arrival | 271.5 | 133.1 |
| **Total** | **412.4** | **646.0** |

# 6. CONCLUDING REMARKS

Many opportunities for frequent transit between the lunar vicinity and the heliocentric region will arise in the near future, including servicing missions to space telescopes and proposed missions to various asteroids or other destinations in the solar system. Trajectory design connecting two different dynamical environments, such as the Earth-Moon regime and the Sun-Earth regimes, is generally challenging as phasing and disparate scales for time, distances, and energy must be considered. In this analysis, the framework developed for trajectory design leverages a four-body dynamical model, the Bicircular Restricted Four-Body Problem (BCR4BP), that includes the dynamical structures that exist due to the combined influences of the Earth, the Moon, and the Sun. The capabilities of this framework are demonstrated for constructing complex end-to-end transfers between a cislunar orbit, the 9:2 synodic resonant NRHO, and various heliocentric halo orbits associated with the Sun-Earth $\underline{L}_1$ and $\underline{L}_2$ libration points. The results of the present analysis are summarized below.

## 6.1 Dynamical Structures within an Earth-Moon-Sun Model

The Bicircular Restricted Four-Body Problem (BCR4BP) is employed to describe the motion of a spacecraft in the Earth-Moon-Sun regime. Two equivalent formulations of this dynamical model are derived. The first formulation is defined in the Earth-Moon rotating frame and corresponds to a Sun-perturbed Earth-Moon CR3BP. The second formulation describes a Moon-perturbed Sun-Earth CR3BP and is defined in the Sun-$B_1$ rotating frame, where $B_1$ is the Earth-Moon barycenter. Unlike the CR3BP, the BCR4BP is explicitly a function of time. However, the assumptions for the motion of the Earth, the Moon, and the sun, yield a periodic model, thus alleviating some of the challenges associated with the time-dependency. The BCR4BP is an intermediate step between the CR3BP and a high-fidelity, time-dependent, non-periodic ephemeris model.

Dynamical structures within the Earth-Moon-Sun BCR4BP are catalogued. Instantaneous equilibrium solutions exist in the BCR4BP, as non-autonomous counterparts of the time-invariant Lagrange points in the CR3BP. Instantaneous, or pulsating, zero velocity surfaces appear in the BCR4BP to add perspective for the dynamical behavior. The in-

stantaneous equilibrium points and zero velocity surfaces are related through an energy-like quantity, defined in this analysis as the scaled Hamiltonian function associated with the BCR4BP. Both of these instantaneous dynamical structures provide insights into the allowable motion within Earth-Moon-Sun system for a given energy-like value. Various periodic orbits and bounded motion are also constructed. In the BCR4BP, precisely periodic orbits must possess orbital periods in resonance with the Earth-Moon-Sun period, i.e., the synodic period. Such orbits, available in both formulations of the BCR4BP, include the baseline orbit for the Gateway, the 9:2 synodic resonant $L_2$ NRHO. As requirement of synodic resonance considerably restricts the availability of periodic orbits in the BCR4BP, a method for constructing bounded or quasi-periodic motion is developed. Lastly, strategies to compute global invariant manifolds associated with periodic orbits and bounded motion are introduced. The invariant manifolds are an essential component of the trajectory design framework, as they offer ballistic flow into and out of linearly unstable periodic and quasi-periodic orbits.

## 6.2 Framework for Cislunar-to-Heliocentric Trajectory Design

Employing the dynamical structures catalogued in the BCR4BP, a transfer framework is developed. Natural motion to and from the lunar vicinity is explored using the global manifold associated the heliocentric halo orbits. As these trajectories evolve towards the Moon (in either forward or backward propagation), a small subset of the arcs encounters the Moon. These ballistic arcs connecting the cislunar and heliocentric regions exist due to the incorporation of all the bodies of interest, i.e., the Earth, the Moon, and the Sun, as well as the motion along their respective orbits. The dynamical structures explored in the BCR4BP are the foundations of the transfer design framework.

Point solutions along the global manifolds are extended into families of arcs connecting the lunar vicinity and halo orbits associated with the Sun-Earth libration points. The perilune transfer families extend the pool of available initial guesses for the end-to-end transfer between the cislunar and heliocentric regions and are summarized in perilune transfer maps. Filtering techniques are described to identify candidate arcs to construct an initial guess for an end-to-end transfer between an orbit in cislunar point and a Sun-Earth libration point

orbit. Tools from dynamical system theory, such as mapping techniques, differential corrections, and continuation schemes are employed such that the natural flow and low-energy pathways emerge between the catalogued structures in the cislunar space and the heliocentric region.

Multiple methods to select an initial guess among the collection of available arcs for a transfer to/from the Earth-Moon orbits, given certain desired transfer characteristics, are detailed. The selected initial guess is then corrected using a differential corrections scheme, resulting in a continuous end-to-end trajectory. The framework currently supports two types of transfers. One-way transfers are continuous solutions that connect the orbit in the lunar vicinity to the libration point orbit in heliocentric space. Round-trip transfers include a cislunar-to-heliocentric transfer, as well as a trajectory returning to the lunar orbit after completion of the objectives in heliocentric space. Round-trip trajectories are generally multi-year solutions that returns to the NRHO after completion of the objectives in heliocentric that present significant challenges in terms in phasing; such trajectories are successfully constructed employing the presented framework.

## 6.3 End-to-End Transfers between Earth-Moon NRHOs and Sun-$B_1$ Halo Orbits

To illustrate the trajectory design framework, multiple families of round-trip transfers between the Earth-Moon 9:2 synodic resonant BCR4BP NRHO and $\underline{\mathrm{L}}_1/\underline{\mathrm{L}}_2$ libration point orbits are constructed. The transfers represent a range of departure and arrival epochs along the Earth-Moon NRHO, as well as a variety of the geometries near the Moon and in heliocentric space. Round-trip transfers offering low total $\Delta$V magnitude are extracted from the transfer families and explored. The proposed trajectory design framework is successfully employed to design round-trip transfers between the Gateway facility orbit and heliocentric space, while overcoming the challenges in the phasing and energy discrepancies associated with problems involving of blended dynamical systems.

The effectiveness of the trajectory design framework is verified in the higher-fidelity ephemeris model. The validation process requires multiple steps to ensure that the characteristics of the transfers constructed in the BCR4BP are adequately transitioned to the

ephemeris model. A method to transform an epoch between the BCR4BP and the ephemeris model, that is, to convert a Sun angle to a calendar date, is introduced. The reference cislunar and heliocentric orbits are transitioned. Reconstructing the departure and arrival motion in ephemeris model a priori typically facilitate the convergence of the end-to-end transfer. Third, the two formulations of the BCR4BP, i.e., the Earth-Moon frame and the Sun-$B_1$ frame formulations, are leveraged to construct an initial guess for the end-to-end transfers in the Earth centered inertial frame associated with the ephemeris model. The round-trip trajectories between the Earth-Moon NRHO and selected heliocentric halo orbits are validated in the higher-fidelity ephemeris model for validation, and characteristics of the transfers in the two dynamical models are compared.

## 6.4 Recommendations for Future Work

As the number of opportunities for transit between the lunar vicinity and heliocentric space continues to increase, an understanding of the dynamics that govern this four-body dynamical regime becomes increasingly indispensable. Many avenues could be explored to augment the present investigation. For conciseness purposes, only a few of the areas are listed below:

**Energy analysis extension**

The energy-like quantity employed in this investigation, the scaled Hamiltonian function, provides useful insights for the identifying suitable arcs for transfers. Further analysis is required to broaden the understanding of the energy-like quantity in the Earth-Moon-Sun regime. Analytic or semi-analytic approaches may be used, including the development of normal forms for the Hamiltonian function leveraging canonical transformations that remove the time-dependency for analysis near a periodic solution [22]. Alternatively, geometric methods that relate the change in energy-location quantities to the phase space [107] may be examined to further catalog the dynamical structures in the BCR4BP.

**Inclusion of intermediate staging orbits**

One of the challenges associated with the design of transfers between cislunar and

heliocentric space is the phasing between the initial and final orbits. The inclusion of intermediate staging orbits may alleviate some of these challenges. When acting as boundaries between phases of a transfer, the staging orbit simplifies the design process and offers additional dynamical structures [101] that may be leveraged for the transfer. Candidates for the staging orbits include Earth-Moon halo orbits outside of the NRHO ranges and resonant orbits [108]. Furthermore, incorporating quasi-periodic orbits as the intermediate staging orbit may significantly expand the array of available paths for transfers between the cislunar and heliocentric regions.

**Access to destination beyond the Sun-Earth libration point regions**

The proposed framework successfully demonstrate transit between periodic orbits in the Earth-Moon and Sun-Earth regime. A natural extension of this design framework may include transfers to destination beyond the Sun-Earth libration point regions. For instance, transfer arcs from the BCR4BP may be connected interplanetary arcs to other destinations in the solar system, such as Mars or an asteroid, to construct end-to-end transfers originating at the Gateway.

**Long-term behavior of transit trajectories in heliocentric space**

An indirect application of the presented trajectory design framework is the design of reliable disposal trajectories from Gateway to heliocentric space beyond the Sun-Earth libration point. Preliminary results of disposal trajectories from the lunar to vicinity to heliocentric space suggest some orbital resonance for the long-term motion of the disposal object. Therefore, a long-term risk of return to cislunar space from the heliocentric region exists and, thus, a possibility for the disposal object to become a potential threat to other assets in the cislunar region. Further analysis of the dynamics of disposed objects and the long-term risk of reentry into the cislunar space is necessary.

**Enhancement of the transition process to the ephemeris model** Strategies were developed along this research to facilitate the transition of the constructed dynamical transfers to the higher-fidelity ephemeris model. Additional analysis is required to better address the challenges associated with validating the cislunar-to-heliocentric

transfers, such as the extensive times-of-flight or the complex dynamics associated with the proximity to the Moon, require further analysis. One avenue includes the comparison of the current 'direct' transition process to an alternative method that transitions the different phases of the transfer separately [101]. Finally, an iterative comparison of solutions in the CR3BP (lower-fidelity), the BCR4BP, and the ephemeris model (higher-fidelity) may further specify the limitations of the BCR4BP, and how it compares to other medium-fidelity models such as the Hill Restricted Four-Body Problem [24].

These recommendations offer several research avenues to further support the design of trajectories in an Earth-Moon-Sun environment.

## 6.5 Trajectory Design Mind Map

A mind map is a diagram that visually organizes or summarizes information [109]. The different aspects of the trajectory design framework developed in this analysis are summarized in the mind map in Figure 6.1.

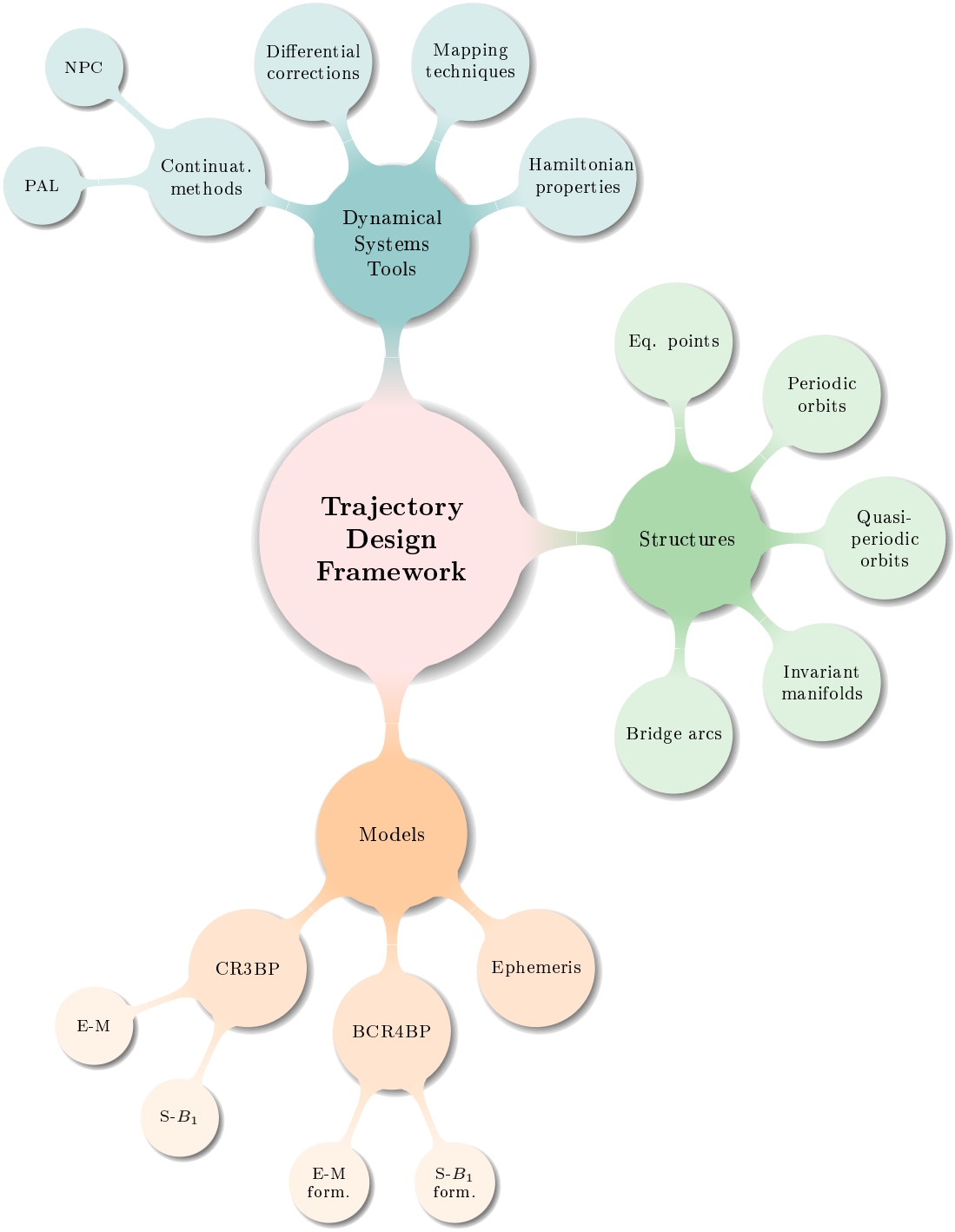


**Figure 6.1.** Mind map associated with the trajectory design framework

# REFERENCES


[1] International Space Exploration Coordination Group, *The Global Exploration Roadmap*. NASA, 2018.

[2] *James Webb Space Telescope User Documentation*, https://jwst-docs.stsci.edu/jwst-observatory-hardware/jwst-orbit, May 2017.

[3] D. C. Folta and C. Webster, "Transfer Trajectory Options for Servicing Sun-Earth-Moon Libration Point Missions," in *AAS/AIAA Astrodynamics Specialist Conference*, Portland, Maine, 2019.

[4] J. Laureijs, S. Amiaux, J. Arduini, and J. Augueres, "Euclid Definition Study Report," ESA, Tech. Rep., 2011.

[5] S. Seetha and S. Megala, "Aditya-L1 mission," *Current Science*, vol. 113, no. 4, pp. 610–612, 2017.

[6] V. G. Szebehely, *Theory of Orbits, the Restricted Problem of Three Bodies*. Academic Press, 1967.

[7] V. Domingo, B. Fleck, and A. Poland, "The SOHO Mission: an Overview," *Solar Physics*, vol. 162, no. 1-2, pp. 1–37, Dec. 1995. DOI: 10.1007/BF00733425.

[8] D. S. Burnett, B. L. Barraclough, R. Bennett, *et al.*, "The Genesis Discovery Mission: Return of Solar Matter to Earth," *Space Science Reviews*, vol. 105, no. 3, pp. 509–534, Jan. 2003. DOI: 10.1023/A:1024425810605.

[9] L. Lindegren, C. Babusiaux, C. Bailer-Jones, *et al.*, "The Gaia Mission: Science, Organization and Present Status," *Proceedings of the International Astronomical Union*, vol. 3, no. S248, pp. 217–223, 2007. DOI: 10.1017/S1743921308019133.

[10] M. Woodard, D. Folta, and D. Woodfork, "ARTEMIS: The First Mission to the Lunar Libration Orbits," in *International Symposium on Space Flight Dynamics*, Jan. 2009.

[11] Q. Wang and J. Liu, "A Chang'e-4 mission concept and vision of future Chinese lunar exploration activities," *Acta Astronautica*, vol. 127, pp. 678–683, 2016, ISSN: 0094-5765. DOI: https://doi.org/10.1016/j.actaastro.2016.06.024. [Online]. Available: https://www.sciencedirect.com/science/article/pii/S0094576515302770.

[12] S.-S. Huang, *Very Restricted Four-Body Problem* (NASA technical note). National Aeronautics and Space Administration, 1960.

[13] D. J. Scheeres, "The Restricted Hill Four-Body Problem with Applications to the Earth-Moon-Sun System," *Celestial Mechanics and Dynamical Astronomy*, vol. 11, no. 70, pp. 75–98, 1998. DOI: 10.1039/b100048i.

[14] Z. P. Olikara, G. Gómez, and J. J. Masdemont, "A Note on Dynamics About the Coherent Sun-Earth-Moon Collinear Libration Points," in *Astrodynamics Network AstroNet-II*, G. Gómez and J. J. Masdemont, Eds., Cham: Springer International Publishing, 2016, pp. 183–192, ISBN: 978-3-319-23986-6.

[15] M. A. Andreu, "The Quasi-Bicircular Problem," Ph.D. Dissertation, Universitat de Barcelona, Barcelona, Spain, 1998.

[16] J. Guzman, "Spacecraft trajectory design in the context of a coherent restricted four-body problem," Ph.D. dissertation, Purdue University, West Lafayette, Indiana, Jan. 2001.

[17] M. Jorba-Cuscó, A. Farrés, and À. Jorba, "Two Periodic Models for the Earth-Moon System," *Frontiers in Applied Mathematics and Statistics*, vol. 4, p. 32, 2018, ISSN: 2297-4687.

[18] M. Jorba-Cuscó, "Periodic Time Dependent Hamiltonian Systems and Applications," Ph.D. dissertation, Universitat de Barcelona, Barcelona, Spain, 2018.

[19] J. Rosales, "On the effect of the Sun's gravity around the Earth-Moon L1 and L2 libration points," Ph.D. dissertation, Universitat de Barcelona, Barcelona, Spain, Jun. 2020.

[20] G. Gómez, J. Llibre, R. Martínez, and C. Simó, *Dynamics and Mission Design Near Libration Points - Vol II: Fundamentals: The Case of Triangular Libration Points* (World Scientific Monograph Series in Mathematics). World Scientific Publishing Company, 2001. DOI: 10.1142/4402.

[21] K. K. Boudad, "Disposal Dynamics from the Vicinity of Near Rectilinear Halo Orbits in the Earth-Moon-Sun System," M.S. Thesis, Purdue University, West Lafayette, Indiana, 2018.

[22] A. Jorba, J. Rosales, and M. Jorba, "The vicinity of the Earth-Moon L 1 point in the Bicircular Problem," Pre-print, Nov. 2019.

[23] E. Castellà and A. Jorba, "On the vertical families of two-dimensional tori near the triangular points of the Bicircular problem," *Celestial Mechanics and Dynamical Astronomy*, vol. 76, Feb. 2000. DOI: 10.1023/A:1008321605028.

[24] D. J. Scheeres and J. Bellerose, "The Restricted Hill Full 4-Body problem: Application to spacecraft motion about binary asteroids," *Dynamical Systems*, vol. 20, no. 1, pp. 23–44, 2005, ISSN: 1468-9367. DOI: 10.1080/14689360420002813 21.

[25] E. A. Belbruno and J. K. Miller, "Sun-perturbed earth-to-moon transfers with ballistic capture," *Journal of Guidance, Control, and Dynamics*, vol. 16, no. 4, pp. 770–775, 1993. DOI: 10.2514/3.21079. eprint: https://doi.org/10.2514/3.21079. [Online]. Available: https://doi.org/10.2514/3.21079.

[26] K. Yagasaki, "Sun-perturbed earth-to-moon transfers with low energy and moderate flight time," *Celestial Mechanics and Dynamical Astronomy*, vol. 90, no. 3-4, pp. 197–212, Nov. 2004. DOI: 10.1007/s10569-004-0406-8.

[27] W. Koon, M. Lo, J. Marsden, and S. Ross, *Dynamical Systems, the Three-Body Problem and Space Mission Design* (Interdisciplinary Applied Mathematics). Springer New York, 2006, ISBN: 9780387564678.

[28] K. Onozaki, H. Yoshimura, and S. D. Ross, "Tube dynamics and low energy Earth–Moon transfers in the 4-body system," *Advances in Space Research*, vol. 60, no. 10, pp. 2117–2132, 2017, ISSN: 1879-1948. DOI: 10.1016/j.asr.2017.07.046.

[29] F. Topputo, "On Optimal Two-Impulse Earth–Moon Transfers in a Four-Body Model," *Celestial Mechanics and Dynamical Astronomy*, 2013.

[30] Y. Qi, S. Xu, and R. Qi, "Gravitational lunar capture based on bicircular model in restricted four body problem," *Celestial Mechanics and Dynamical Astronomy*, vol. 120, no. 1, pp. 1–17, 2014, ISSN: 1572-9478. DOI: 10.1007/s10569-014-9554-7.

[31] Y. Qi and S. Xu, "Study of lunar gravity assist orbits in the restricted four-body problem," *Celestial Mechanics and Dynamical Astronomy*, vol. 125, no. 3, pp. 333–361, 2016, ISSN: 1572-9478. DOI: 10.1007/s10569-016-9686-z.

[32] K. Oshima and T. Yanao, "Applications of gravity assists in the bicircular and bielliptic restricted four-body problem," vol. 152, Jan. 2014, pp. 503–522.

[33] G. Mingotti, F. Topputo, and F. Bernelli-Zazzera, "Low-energy, low-thrust transfers to the Moon," *Celestial Mechanics and Dynamical Astronomy*, vol. 105, no. 1, pp. 61–74, 2009, ISSN: 0923-2958. DOI: 10.1007/s10569-009-9220-7.

[34] G. Mingotti, F. Topputo, and F. Bernelli-Zazzera, "Efficient invariant-manifold, low-thrust planar trajectories to the Moon," *Communications in Nonlinear Science and Numerical Simulation*, vol. 17, no. 2, pp. 817–831, 2012, ISSN: 1007-5704. DOI: https://doi.org/10.1016/j.cnsns.2011.06.033. [Online]. Available: https://www.sciencedirect.com/science/article/pii/S1007570411003480.

[35] D. Pérez-Palau and R. Epenoy, "Fuel Optimization for Low-Thrust Earth–Moon Transfer via Indirect Optimal Control," *Celestial Mechanics and Dynamical Astronomy*, vol. 130, no. 2, pp. 1–29, 2018, ISSN: 1572-9478. DOI: 10.1007/s10569-017-9808-2.

[36] K. C. Howell, "Three-Dimensional, Periodic, 'Halo' Orbits," *Celestial Mechanics*, vol. 21, no. 1, pp. 53–71, 1984.

[37] D. J. Grebow, "Generating Periodic Orbits in the Circular Restricted Three-Body Problem with Applications to Lunar South Pole Coverage," M.S. Thesis, Purdue University, West Lafayette, Indiana, 2006.

[38] E. M. Zimovan, K. C. Howell, and D. C. Davis, "Near Rectilinear Halo Orbits and their Application in Cis-Lunar Space," in *3rd International Academy of Astronautics Conference on Dynamics and Control of Space Systems*, Moscow, Russia, 2017.

[39] C. Acton, "Ancillary Data Services of NASA's Navigation and Ancillary Information Facility," *Planetary and Space Science*, vol. 44, no. 1, pp. 65–70, 1996.

[40] D. E. Lee, R. J. Whitley, and C. Acton, *Sample Deep Space Gateway Orbit, NAIF Planetary Data System Navigation Node"*, https://naif.jpl.nasa.gov/pub/naif/misc/MORE_PROJECTS/DSG/, 2018.

[41] D. E. Lee, "White Paper: Gateway Destination Orbit Model: A Continuous 15 Year NRHO Reference Trajectory," NASA, Tech. Rep., 2019.

[42] E. M. Zimovan-Spreen, K. C. Howell, and D. C. Davis, "Near Rectilinear Halo Orbits and Nearby Higher-Period Dynamical Structures: Orbital Stability and Resonance Properties," *Celestial Mechanics and Dynamical Astronomy*, 2020.

[43] E. Zimovan-Spreen, "Trajectory Design and Targeting for Applications to the Exploration Program in Cislunar Space," Ph.D. Dissertation, Purdue University, West Lafayette, Indiana, 2021.

[44] K. K. Boudad, K. C. Howell, and D. C. Davis, "Dynamics of Synodic Resonant Near Rectilinear Halo Orbits in the Bicircular Four-Body Problem," *Advances in Space Research*, vol. 66, no. 9, pp. 2194–2214, Nov. 2020. DOI: https://doi.org/10.1016/j.asr.2020.07.044.

[45] S. Vutukuri, "Spacecraft Trajectory Design Techniques Using Resonant Orbits," M.S. Thesis, Purdue University, West Lafayette, Indiana, 2018.

[46] K. K. Boudad, D. C. Davis, and K. C. Howell, "Near Rectilinear Halo Orbits in Cislunar Space within the Context of the Bicircular Four-Body Problem," in *2nd IAA/AAS SciTech Forum*, Moscow, Russia, 2019.

[47] D. C. Davis, K. K. Boudad, S. M. Phillips, and K. C. Howell, "Disposal, Deployment, and Debris in Near Rectilinear Halo Orbits," in *AAS/AIAA Astrodynamics Specialist Conference*, 2019.

[48] D. C. Davis, K. K. Boudad, R. J. Power, K. C. Howell, and D. J. Sweeney, "Heliocentric Escape and Lunar Impact from Near Rectilinear Halo Orbits," in *AAS/AIAA Astrodynamics Specialist Conference*, Portland, Maine, 2019.

[49] K. K. Boudad, K. C. Howell, and D. C. Davis, "Heliocentric Access from Cislunar Space within the Context of the Bicircular Restricted Four-Body Problem," in *AAS/AIAA Astrodynamics Specialist Conference*, Lake Tahoe, California (Virtual), Aug. 2020.

[50] K. K. Boudad, K. C. Howell, and D. C. Davis, "Energy and Phasing Considerations for Low-Energy Transfers from Cislunar to Heliocentric Space," in *31st AAS/AIAA Spaceflight Mechanics Meeting*, Charlotte, North Carolina (Virtual), Feb. 2021.

[51] K. K. Boudad, D. C. Davis, and K. C. Howell, "Round-Trip Trajectories Between Earth-Moon NRHOs and Heliocentric Space in the Earth-Moon-Sun System," in *72nd International Astronautical Congress*, Dubai, United Arab Emirates, 2021.

[52] K. K. Boudad, K. C. Howell, and D. C. Davis, "Analogs for Earth-Moon Halo Orbits and their Evolving Characteristics in Higher-Fidelity Force Models," in *AIAA SciTech Forum*, San Diego, California, 2022.

[53] A. Roy, *Orbital Motion, Fourth Edition*. CRC Press, 2004, ISBN: 9781420056884.

[54] Jet Propulsion Laboratory, *SPICE Toolkit*, https://naif.jpl.nasa.gov/naif/aboutspice.html, 2000.

[55] S. H. Strogatz, *Nonlinear Dynamics and Chaos: With Applications to Physics, Biology, Chemistry, and Engineering*, 2nd ed. CRC Press, 2015. DOI: ttps://doi.org/10.1201/9780429492563.

[56] H. Keller, *Numerical Solution of Two Point Boundary Value Problems*. Philadelphia: Society for Industrial and Applied Mathematics, 1976.

[57] Å. Björck, *Numerical methods for least squares problems*. Philadelphia, Pennsylvania: Society for Industrial and Applied Mathematics, 1996.

[58] J. Nocedal and S. Wright, *Numerical Optimization*. New York: Springer, 1999.

[59] U. Ascher and C. Greif, *A First Course in Numerical Methods* (Computational Science and Engineering). Society for Industrial and Applied Mathematics, 2011, ISBN: 9780898719970.

[60] H. B. Keller, *Lectures on Numerical Methods in Bifurcation Problems*. Heidelberg: Springer-Verlag, 1986.

[61] N. Bosanac, "Leveraging Natural Dynamical Structures to Explore Multi-Body Systems," Ph.D. Dissertation, Purdue University, 2016.

[62] H. J. Pernicka, "The Numerical Determination of Nominal Libration Point Trajectories and Development of a Station-Keeping Strategy," Ph.D. Dissertation, Purdue University, West Lafayette, Indiana, 1990.

[63] *Boost C++ Library*, https://www.boost.org/.

[64] *Boost C++ Class Template* ***runge_kutta_fehlberg78***, https://www.boost.org/doc/libs/1_78_0/libs/numeric/odeint/doc/html/boost/numeric/odeint/runge_kutta_fehlberg78.html.

[65] MathWorks, *MATLAB 9.11.0.1837725 (R2021b)*, Natick, Massachusetts, 2021.

[66] MathWorks, *MATLAB MEX File Functions*, https://www.mathworks.com/help/matlab/call-mex-file-functions.html, Natick, Massachusetts.

[67] *General Mission Analysis Tool (GMAT*, https://software.nasa.gov/software/GSC-17177-1.

[68] A. Haapala, M. Vaquero, T. Pavlak, K. Howell, and D. Folta, "Trajectory Selection Strategy for Tours in the Earth-Moon System," in *AAS/AIAA Astrodynamics Specialist Conference*, Hilton Head, South Caroline, 2013.

[69] A. D. Cox, "A Dynamical Systems Perspective for Preliminary Low-Thrust Trajectory Design in Multi-Body Regimes," Ph.D. Dissertation, Purdue University, West Lafayette, Indiana, 2020.

[70] C. R. McInnes, A. J. C. McDonald, J. F. L. Simmons, and E. W. MacDonald, "Solar Sail Parking in Restricted Three-Body Systems," *Journal of Guidance, Control, and Dynamics*, vol. 17, no. 2, pp. 399–406, 1994. DOI: 10.2514/3.21211. eprint: https://doi.org/10.2514/3.21211. [Online]. Available: https://doi.org/10.2514/3.21211.

[71] A. D. Cox, K. Howell, and D. C. Folta, "Trajectory Design Leveraging Low-Thrust, Multi-Body Equilibria and their Manifolds," *The Journal of Astronautical Sciences*, 2020. DOI: https://doi.org/10.1007/s40295-020-00211-6.

[72] S. Wiggins, *Introduction to Applied Nonlinear Dynamical Systems and Chaos* (Texts in Applied Mathematics), eng, 2nd. Springer New York, 2003.

[73] L. Perko, *Differential Equations and Dynamical Systems* (Texts in Applied Mathematics). Springer New York, 1996.

[74] L. R. Irrgang, "Investigation of Transfer Trajectories to and from the Equilateral Libration Points L4 and L5 in the Earth-Moon System," M.S. Thesis, Purdue University, 2008.

[75] K. C. Howell, "Families of Orbits in the Vicinity of the Collinear Libration Points," *Journal of the Astronautical Sciences*, vol. 49, 1998. DOI: 10.2514/6.1998-4465.

[76] R. A. Broucke, "Stability of Periodic Orbits in the Elliptic, Restricted Three-Body Problem," *AIAA Journal*, 1969, ISSN: 0001-1452. DOI: 10.2514/3.5267.

[77] H. Freeman, *Discrete-Time Systems*. New York: John Wiley & Sons, 1965.

[78] V. Yakubovich and V. Starzhinskii, *Linear Differential Equations with Periodic Coefficients*. New York: John Wiley and Sons, 1975, vol. 1.

[79] N. Bosanac, "Exploring the Influence of a Three-Body Interaction Added to the Gravitational Potential Function in the Circular Restricted Three-Body Problem: A Numerical Frequency Analysis," M.S. Thesis, Purdue University, 2012.

[80] E. M. Zimovan-Spreen and K. C. Howell, "Dynamical Structures Nearby NRHOs with Applications in Cislunar Space," in *AAS/AIAA Astrodynamics Specialist Conference*, Portland, Maine, Aug. 2019.

[81] K. Meyer and G. Hall, *Introduction to Hamiltonian Dynamical Systems and the N-Body Problem* (Applied Mathematical Sciences). Springer New York, 2013, ISBN: 9781475740738.

[82] A. H. Nayfeh and B. Balachandran, *Applied Nonlinear Dynamics - Analytical, Computational, and Experimental Methods* (Wiley series in nonlinear science), eng. New York: Wiley, 1995, ISBN: 1-282-01051-4.

[83] J. Hale, H. Buttanri, and H. Kocak, *Dynamics and Bifurcations* (Texts in Applied Mathematics). Springer New York, 1996, ISBN: 9780387971414.

[84] K. Hambleton, *Deep Space Gateway to Open Opportunities for Distant Destinations*, https://www.nasa.gov/feature/deep-space-gateway-to-open-opportunities-for-distant-destinations, 2017.

[85] C. Warner, *NASA's Lunar Outpost will Extend Human Presence in Deep Space*, https://www.nasa.gov/feature/nasa-s-lunar-outpost-will-extend-human-presence-in-deep-space, 2018.

[86] J. Williams, D. E. Lee, R. J. Whitley, K. A. Bokelmann, D. C. Davis, and C. F. Berry, "Targeting Cislunar Near Rectilinear Halo Orbits for Human Space Exploration," in *AAS/AIAA Astrodynamics Specialist Conference*, 2017.

[87] C. R. Ortiz Longo and S. L. Rickman, "Method for the Calculation of Spacecraft Umbra and Penumbra Shadow Terminator Points," NASA Johnson Space Center, Tech. Rep., 1995.

[88] D. C. Davis, S. M. Phillips, K. C. Howell, S. Vutukuri, and B. P. McCarthy, "Station-keeping and Transfer Trajectory Design for Spacecraft in Cislunar Space," in *AAS/AIAA Astrodynamics Specialist Conference*, Columbia River Gorge, Stevenson, Washington, 2017, ISBN: 9780877036456.

[89] B. P. McCarthy and K. C. Howell, "Quasi-Periodic Orbits in the Sun-Earth-Moon Bicircular Restricted Four-Body Problem," in *31st AAS/AIAA Spaceflight Mechanics Meeting*, 2021.

[90] J. Guckenheimer and P. Holmes, *Nonlinear Oscillations, Dynamical Systems, and Bifurcations of Vector Fields* (Applied Mathematical Sciences). Springer New York, 2013, ISBN: 9781461270201.

[91] *NASA's Webb Telescope Launches to See First Galaxies, Distant Worlds*, https://webbtelescope.org/contents/news-releases/2021/news-2021-068, Webb Space Telescope Press Release, 2021.

[92] A. Balzer, *NASA Confirms Roman Mission's Flight Design in Milestone Review*, https://www.nasa.gov/feature/goddard/2021/nasa-confirms-roman-missions-flight-design-in-milestone-review, NASA Press Release, 2021.

[93] M. Kakoi, "Design of Transfers from Earth-Moon L1/L2 libration point orbits to a destination object," M.S. Thesis, Purdue University, West Lafayette, Indiana, 2015.

[94] V. Muralidharan, "Stretching Directions in Cislunar Space: Stationkeeping and an Application to Transfer Trajectory Design," Ph.D. dissertation, Purdue University, West Lafayette, Indiana, 2021.

[95] D. C. Davis, "Multi-Body Trajectory Design Strategies Based on Periapsis Poincaré Maps," Ph.D. Dissertation, Purdue University, West Lafayette, Indiana, 2011.

[96] S. v. d. Walt and N. Smith, "A Better Default Colormap for Matplotlib," in *SciPy 2015*, https://bids.github.io/colormap/, Jul. 2015.

[97] H. Franz, P. Sharer, K. Ogilvie, and M. Desch, "WIND Nominal Mission Performance and Extended Mission Design," *Journal of Astronautical Sciences*, 2001.

[98] A. D. Cox, "Transfers to a Gravitational Saddle Point: An Extended Mission Design Option for LISA Pathfinder," M.S. Thesis, Purdue University, West Lafayette, Indiana, 2016.

[99] J. Parker and R. Anderson, *Low-Energy Lunar Trajectory Design* (JPL Deep-Space Communications and Navigation Series). Wiley, 2014, ISBN: 9781118853870.

[100] F. Espenak and S. Dutta, *SKYCAL (Sky Events Calendar)*, https://eclipse.gsfc.nasa.gov/SKYCAL/SKYCAL.html, NASA GSFC, 2007.

[101] R. Pritchett, "Strategies for Low-Thrust Transfer Design Based on Direct Collocation Techniques," Ph.D. dissertation, Purdue University, West Lafayette, Indiana, 2020.

[102] C. Ocampo, "An Architecture for a Generalized Spacecraft Trajectory Design and Optimization System," in *Libration Point Orbits and Applications*, 2003. DOI: 10.1142/9789812704849_0023.

[103] B. Park, "Low-Thrust Trajectory Design for Tours of the Martian Moons," M.S. Thesis, Purdue University, West Lafayette, Indiana, 2021.

[104] H. Pernicka and K. Howell, "Numerical Determination of Lissajous Trajectories in the Restricted Three-Body Problem," *Celestial Mechanics and Dynamical Astronomy*, 1987.

[105] R. L. Restrepo, R. P. Russell, M. W. Lo, and T. P. McElarth, "Europa Lander Trajectory Design Using Lissajous Staging Orbits," in *AAS/AIAA Astrodynamics Specialist Conference*, Snowbird, Utah, 2018.

[106] J. Ojeda Romero and K. Howell, "Transfers from Geosynchronous Transfer Orbits to Sun-Earth Libration Point Trajectories," *The Journal of the Astronautical Sciences*, 2022.

[107] S. T. Scheuerle, B. P. McCarthy, and K. C. Howell, "Construction of Ballistic Lunar Transfers Leveraging Dynamical Systems Techniques," in *AAS/AIAA Astrodynamics Specialist Conference*, Lake Tahoe, California, 2020.

[108] M. Vaquero and K. Howell, ""Leveraging Resonant Orbit Manifolds to Design Transfers between Libration Point Orbits," *Journal of Guidance, Control, and Dynamics*, vol. 37, no. 4, 2014.

[109] J. D. Novak, *Learning, creating, and using knowledge: Concept maps® as facilitative tools in schools and corporations*. Lawrence Erlbaum Associates Publishers, 1998.

[110] I. Newton, *Philosophiæ Naturalis Principia Mathematica*. 1687.

[111] T. Pavlak, "Trajectory Design and Orbit Maintenance Strategies in Multi-Body Dynamical Regimes," Ph.D. Dissertation, Purdue University, West Lafayette, Indiana, May 2013.

# A. MULTI-BODY REGIMES

A body moves through space under the gravitational influence of infinitely many other bodies. To predict the behavior, a mathematical framework of differential equations of motion is required to represent the dynamical environment. The first general approach to modeling the behavior via equations of motion was introduced by Newton the in *PhilosophiæNaturalis Principia Mathematica* [110], published in 1687. As expressed in modern terminology, Newton's second law, in particular, relates the vector sum of forces acting on a particle in an inertial frame to its rate of change of momentum. Newton's laws serve as the foundations of classical mechanics and are used to describe the motions of objects throughout the solar system.

If the number of bodies is limited to $\mathcal{N}$, the motion of any of these bodies through space is subjected to the action of the remaining $\mathcal{N}-1$ bodies; such a scenario is termed the $\mathcal{N}$-Body problem. A vector definition of the problem is depicted on Figure A.1. The position vectors $\bar{\mathcal{R}}_{\mathrm{i}}$ are all defined with respect to an inertially fixed basepoint $O$. If each body $\mathcal{P}_{\mathrm{i}}$, of mass $\mathcal{M}_{\mathrm{i}}$, is assumed centrobaric, Newton's second law yields

$$\mathcal{M}_{\mathrm{i}}\ddot{\bar{\mathcal{R}}}_{\mathrm{i}} = -G\sum_{\substack{\mathrm{j}=1\\ \mathrm{j}\neq\mathrm{i}}}^{\mathcal{N}} \frac{\mathcal{M}_{\mathrm{i}}\mathcal{M}_{\mathrm{j}}}{\|\bar{\mathcal{R}}_{\mathrm{ji}}\|^3}\bar{\mathcal{R}}_{\mathrm{ji}} \tag{A.1}$$

where

$$\bar{\mathcal{R}}_{\mathrm{ji}} = \bar{\mathcal{R}}_{\mathrm{i}} - \bar{\mathcal{R}}_{\mathrm{j}} \tag{A.2}$$

and time is the independent variable. Here, a prime indicates a derivative with respect to the dimensional time as viewed by an inertial observer. Then, $G$, the gravitational constant, is approximately $6.674 \cdot 10^{-11}$ N·kg$^{-2}$·m$^2$. Vectors are indicated by an overbar and dimensional quantities are expressed with upper case letters or symbols. The $\mathcal{N}$-body problem does not admit a closed-form solution. Equation (A.1) is equivalent to six first-order differential equations: three for position and three for velocity. Because the motion of the particle $\mathcal{P}_{\mathrm{i}}$ influences the motion of all the other particles, the $6\mathcal{N}$ scalar first-order differential equations are solved simultaneously. Since only ten integrals of the motion are available for the $\mathcal{N}$-body

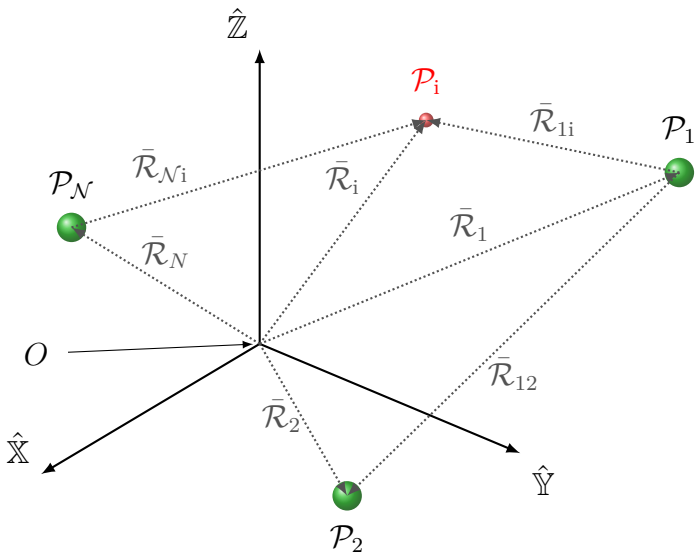


**Figure A.1.** $\mathcal{N}$-body problem

problem as formulated in the inertial frame, a closed-form solution of the $\mathcal{N}$-body problem does not exist, even for $\mathcal{N} = 2$. However, the two-body problem does possess an analytical solution when formulated in terms of relative motion. Because the number of variables generally exceeds the number of known integrals of the motion, additional simplifications allow an improved understanding of the motion of a particle in space.

# B. CHARACTERISTIC QUANTITIES

**Table B.1**. Characteristic quantities of the Earth-Moon CR3BP

| Quantity | Value | Unit | Comment |
|---|---|---|---|
| $l^*$ | $3.8440 \cdot 10^5$ | km | |
| $m_{\mathrm{m}}$ | $4.9028 \cdot 10^3$ | $\mathrm{kg}^3 \cdot \mathrm{s}^{-2}$ | |
| $m_{\mathrm{e}}$ | $3.9860 \cdot 10^5$ | $\mathrm{kg}^3 \cdot \mathrm{s}^{-2}$ | |
| $m^*$ | $4.0350 \cdot 10^5$ | $\mathrm{kg}^3 \cdot \mathrm{s}^{-2}$ | $m_{\mathrm{e}} + m_{\mathrm{m}}$ |
| $\mu$ | $1.2151 \cdot 10^{-2}$ | ndim | $m_{\mathrm{e}}/m^*$ |
| $t^*$ | 4.3425 | days | $1/86400 \cdot \sqrt{(l^*)^3/m^*}$ |

**Table B.2**. Characteristic quantities of the Sun-$B_1$ CR3BP

| Quantity | Value | Unit | Comment |
|---|---|---|---|
| $\underline{l}^*$ | $1.4960 \cdot 10^8$ | km | |
| $m_{B_1}$ | $4.0350 \cdot 10^5$ | $\mathrm{kg}^3 \cdot \mathrm{s}^{-2}$ | $m^*$ |
| $m_{\mathrm{s}}$ | $1.3271 \cdot 10^{11}$ | $\mathrm{kg}^3 \cdot \mathrm{s}^{-2}$ | |
| $\underline{m}^*$ | $4.0350 \cdot 10^5$ | $\mathrm{kg}^3 \cdot \mathrm{s}^{-2}$ | $m_{\mathrm{s}} + m_{B_1}$ |
| $\underline{\mu}$ | $3.0404 \cdot 10^{-6}$ | ndim | $m_{\mathrm{s}}/\underline{m}^*$ |
| $\underline{t}^*$ | 58.1324 | days | $1/86400 \cdot \sqrt{(\underline{l}^*)^3/\underline{m}^*}$ |

**Table B.3**. Characteristic quantities of the Earth-Moon-Sun BCR4BP

| Quantity | Value | Unit | Comment |
|---|---|---|---|
| $\mu$ | $1.2151 \cdot 10^{-2}$ | ndim | $m_{\mathrm{e}}/m^*$ |
| $a_{\mathrm{s}}$ | $3.8917 \cdot 10^2$ | ndim | $\underline{l}^*/l^*$ |
| $\mu_{\mathrm{s}}$ | $3.2889 \cdot 10^5$ | ndim | $m_{\mathrm{s}}/\underline{m}^*$ |
| $\omega$ | -0.9253 | ndim | $1 - \sqrt{1+\mu/a_{\mathrm{s}}^3}$ |
| $\underline{\omega}$ | 12.3869 | ndim | $\lvert\omega\rvert/(1-\lvert\omega\rvert)$ |

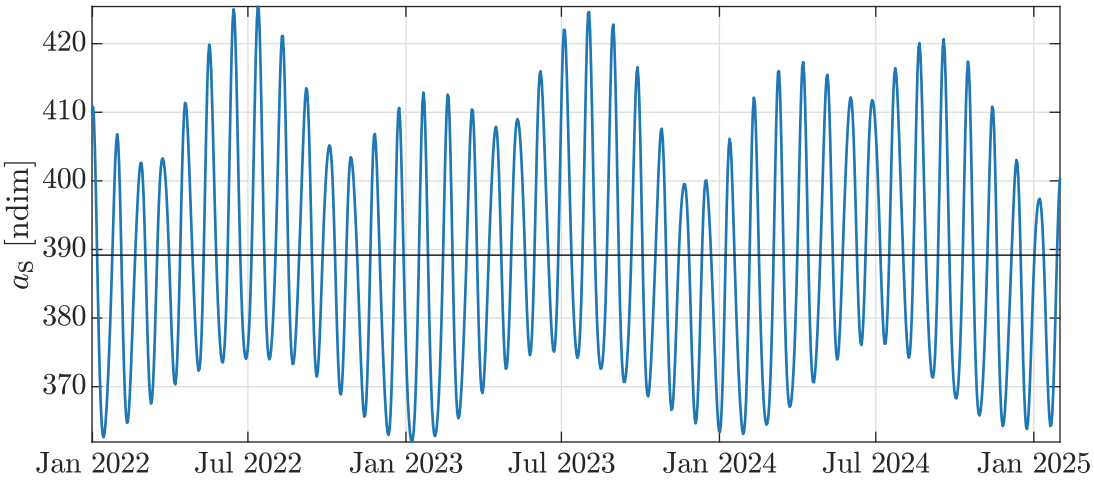


**Figure B.1.** Nondimensional Sun distance between 2022 and 2025 using ephemerides data from NAIF [39]. The black line denotes the constant value ($a_s = 389.1725$ ndim) employed in this investigation.

# C. DERIVATIONS

## C.1 Equations of Motion for the BCR4BP, Earth-Moon Formulation

In the BCR4BP, the motion of an object of negligible mass, i.e., the spacecraft, is subjected to the point-mass gravitational influences of the Earth, the Moon, and the Sun. This formulation of the BCR4BP corresponds to a *Sun-perturbed* Earth-Moon CR3BP. Similar to the Earth-Moon CR3BP, the derivation of the equations of motion for this formulation of the BCR4BP originates considering the motion of the Earth, the Moon, and the Sun in an arbitrary inertial frame centered at the Earth-Moon barycenter, $B_1$, as presented in Figure C.1. In this arbitrary inertial frame, the position of the spacecraft with respect to $B_1$ is denoted as

$$\bar{X}(t) = \begin{bmatrix} X(t) \\ Y(t) \\ Z(t) \end{bmatrix} \tag{C.1}$$

where $t$ is the independent time variable. Furthermore, the positions of the Earth, the Moon, and the Sun are described by the vectors $\bar{R}_\mathrm{e}$, $\bar{R}_\mathrm{m}$, and $\bar{R}_\mathrm{s}$, respectively,

$$\bar{R}_\mathrm{e}(t) = \begin{bmatrix} X_\mathrm{e} \\ Y_\mathrm{e} \\ Z_\mathrm{e} \end{bmatrix} = \begin{bmatrix} -\mu\cos(nt) \\ -\mu\sin(nt) \\ 0 \end{bmatrix}, \; \bar{R}_\mathrm{m}(t) = \begin{bmatrix} X_\mathrm{m} \\ Y_\mathrm{m} \\ Z_\mathrm{m} \end{bmatrix} = \begin{bmatrix} (1-\mu)\cos(nt) \\ (1-\mu)\sin(nt) \\ 0 \end{bmatrix}, \bar{R}_\mathrm{s}(t) = \begin{bmatrix} X_\mathrm{s} \\ Y_\mathrm{s} \\ Z_\mathrm{s} \end{bmatrix} = \begin{bmatrix} a_\mathrm{s}\cos(n_\mathrm{s}t) \\ a_\mathrm{s}\sin(n_\mathrm{s}t) \\ 0 \end{bmatrix} \tag{C.2}$$

where $\mu$ is the mass parameter of the Earth-Moon system, $n$ is the mean motion of the Earth and the Moon, $n_\mathrm{s}$ is the mean motion of the Sun, and $a_\mathrm{s}$ is the nondimensional distance from $B_1$ to the Sun. Note that the quantities are nondimensionalized consistent with the Earth-Moon CR3BP[1].

The position vector $\bar{X}$ for the spacecraft is defined with respect to the $\hat{\mathbb{X}}\hat{\mathbb{Y}}\hat{\mathbb{Z}}$ frame. This frame, of origin $B_1$, is not inertial because of the presence of the Sun. Thus, Newton's second law cannot be applied to the $\bar{X}$ vector. However, the barycenter of the Earth-Moon-Sun

[1]↑See the derivation of the CR3BP in [21] for more details on nondimensionalization.

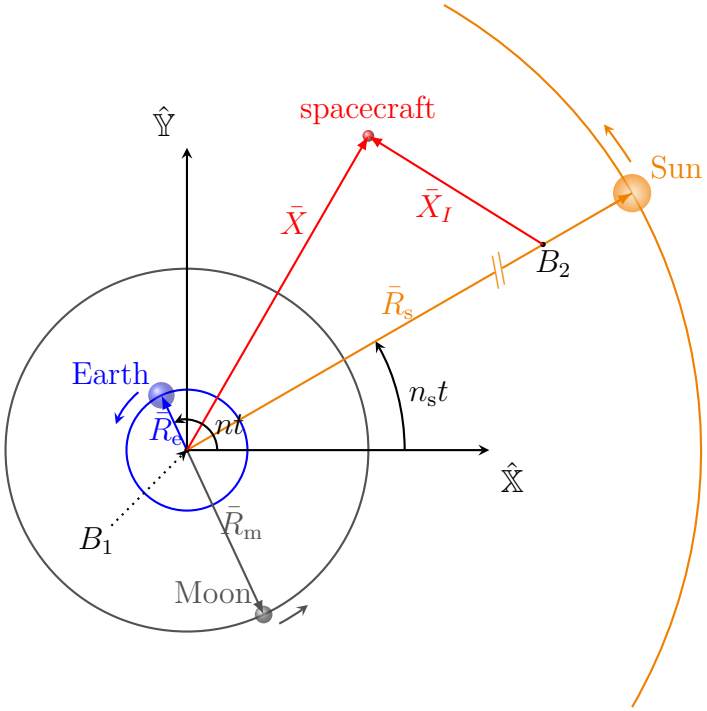


**Figure C.1.** Schematic of the BCR4BP in an arbitrary inertial frame with origin $B_1$ (adapted from [20])

system, that is, $B_2$, is by definition an inertially fixed point. The position of the spacecraft with respect to $B_2$ is defined as $\bar{X}_I$ such that

$$\begin{aligned} \bar{X}_I &= \bar{X} - (1-\mu_s)\bar{R}_s \\ \begin{bmatrix} X_I \\ Y_I \\ Z_I \end{bmatrix} &= \begin{bmatrix} X - \frac{\mu_s}{\mu_s+1} X_s \\ Y - \frac{\mu_s}{\mu_s+1} Y_s \\ Z - \frac{\mu_s}{\mu_s+1} Z_s \end{bmatrix} \end{aligned} \tag{C.3}$$

where $\mu_s = \frac{m_s}{m_e+m_m}$ is the nondimensional mass of the Sun. The second derivative of Equation (C.3) with respect to the independent time variable $t$ yields

$$\begin{bmatrix} \ddot{X}_I \\ \ddot{Y}_I \\ \ddot{Z}_I \end{bmatrix} = \begin{bmatrix} \ddot{X} + \frac{n_s^2 \mu_s}{\mu_s+1} X_s \\ \ddot{Y} + \frac{n_s^2 \mu_s}{\mu_s+1} Y_s \\ \ddot{Z} + \frac{n_s^2 \mu_s}{\mu_s+1} Z_s \end{bmatrix} \tag{C.4}$$

Employing Kepler's 3rd Law[53], the constant term multiplying the Sun position components is simplified to

$$\frac{n_{\mathrm{s}}^2 \mu_{\mathrm{s}}}{\mu_{\mathrm{s}}+1} = \frac{\mu_{\mathrm{s}}}{\mu_{\mathrm{s}}+1}\frac{\mu_{\mathrm{s}}+1}{{a_{\mathrm{s}}}^3} = \frac{\mu_{\mathrm{s}}}{{a_{\mathrm{s}}}^3} \tag{C.5}$$

Combining Equations (C.4) and (C.5) and rearranging the terms, the acceleration of the spacecraft with respect to $B_1$ is written as

$$\begin{bmatrix} \ddot{X} \\ \ddot{Y} \\ \ddot{Z} \end{bmatrix} = \begin{bmatrix} \ddot{X}_I - \frac{\mu_{\mathrm{s}}}{{a_{\mathrm{s}}}^3} X_{\mathrm{s}} \\ \ddot{Y}_I - \frac{\mu_{\mathrm{s}}}{{a_{\mathrm{s}}}^3} Y_{\mathrm{s}} \\ \ddot{Z}_I - \frac{\mu_{\mathrm{s}}}{{a_{\mathrm{s}}}^3} Z_{\mathrm{s}} \end{bmatrix} \tag{C.6}$$

The inertial acceleration $\ddot{X}_I$, $\ddot{Y}_I$, and $\ddot{Z}_I$ are obtained employing the $\mathcal{N}$-body equation from Equation (A.1):

$$\begin{aligned}
\ddot{X}_I &= -\frac{(1-\mu)(X-X_{\mathrm{e}})}{\|\bar{R}_{\text{e-sc}}\|^3} - \frac{\mu(X-X_{\mathrm{m}})}{\|\bar{R}_{\text{m-sc}}\|^3} - \frac{\mu_{\mathrm{s}}(X-X_{\mathrm{s}})}{\|\bar{R}_{\text{s-sc}}\|^3} \\
\ddot{Y}_I &= -\frac{(1-\mu)(Y-Y_{\mathrm{e}})}{\|\bar{R}_{\text{e-sc}}\|^3} - \frac{\mu(Y-Y_{\mathrm{m}})}{\|\bar{R}_{\text{m-sc}}\|^3} - \frac{\mu_{\mathrm{s}}(Y-Y_{\mathrm{s}})}{\|\bar{R}_{\text{s-sc}}\|^3} \\
\ddot{Z}_I &= -\frac{(1-\mu)(Z-Z_{\mathrm{e}})}{\|\bar{R}_{\text{e-sc}}\|^3} - \frac{\mu(Z-Z_{\mathrm{m}})}{\|\bar{R}_{\text{m-sc}}\|^3} - \frac{\mu_{\mathrm{s}}(Z-Z_{\mathrm{s}})}{\|\bar{R}_{\text{s-sc}}\|^3}
\end{aligned} \tag{C.7}$$

Then, substituting Equation (C.7) into Equation (C.6), the inertial equations of motion for the BCR4BP Restricted Four-Body with respect to $B_1$ are summarized as

$$\begin{aligned}
\ddot{X} &= -\frac{(1-\mu)(X-X_{\mathrm{e}})}{\|\bar{R}_{\text{e-sc}}\|^3} - \frac{\mu(X-X_{\mathrm{m}})}{\|\bar{R}_{\text{m-sc}}\|^3} - \frac{\mu_{\mathrm{s}}(X-X_{\mathrm{s}})}{\|\bar{R}_{\text{s-sc}}\|^3} - \frac{\mu_{\mathrm{s}}}{{a_{\mathrm{s}}}^3} X_{\mathrm{s}} \\
\ddot{Y} &= -\frac{(1-\mu)(Y-Y_{\mathrm{e}})}{\|\bar{R}_{\text{e-sc}}\|^3} - \frac{\mu(Y-Y_{\mathrm{m}})}{\|\bar{R}_{\text{m-sc}}\|^3} - \frac{\mu_{\mathrm{s}}(Y-Y_{\mathrm{s}})}{\|\bar{R}_{\text{s-sc}}\|^3} - \frac{\mu_{\mathrm{s}}}{{a_{\mathrm{s}}}^3} Y_{\mathrm{s}} \\
\ddot{Z} &= -\frac{(1-\mu)(Z-Z_{\mathrm{e}})}{\|\bar{R}_{\text{e-sc}}\|^3} - \frac{\mu(Z-Z_{\mathrm{m}})}{\|\bar{R}_{\text{m-sc}}\|^3} - \frac{\mu_{\mathrm{s}}(Z-Z_{\mathrm{s}})}{\|\bar{R}_{\text{s-sc}}\|^3} - \frac{\mu_{\mathrm{s}}}{{a_{\mathrm{s}}}^3} Z_{\mathrm{s}}
\end{aligned} \tag{C.8}$$

Observe that the scalar expressions in Equation (C.8) are components of the acceleration in the $(\hat{\mathbb{X}}\hat{\mathbb{Y}}\hat{\mathbb{Z}})$ frame, as defined in Figure C.1. A rotating frame is defined consistent with the Earth-Moon synodic frame [21] such that

$$\begin{aligned} x &= X\cos(nt) + Y\sin(nt) \\ y &= -X\sin(nt) + Y\cos(nt) \\ z &= Z \end{aligned} \tag{C.9}$$

Using the kinematic expansion [21], the nondimensional equations of motion for the BCR4BP as formulated in the Earth-Moon rotating frame are produced,

$$\begin{aligned} \ddot{x} &= 2\dot{y} + x - \frac{(1-\mu)(x+\mu)}{\|\bar{r}_{\text{e-sc}}\|^3} - \frac{\mu(x-1+\mu)}{\|\bar{r}_{\text{m-sc}}\|^3} - \frac{\mu_{\text{s}}(x-x_{\text{s}})}{\|\bar{r}_{\text{s-sc}}\|^3} - \frac{\mu_{\text{s}}}{a_{\text{s}}}x_{\text{s}} \\ \ddot{y} &= -2\dot{x} + x - \frac{(1-\mu)y}{\|\bar{r}_{\text{e-sc}}\|^3} - \frac{\mu y}{\|\bar{r}_{\text{m-sc}}\|^3} - \frac{\mu_{\text{s}}(y-y_{\text{s}})}{\|\bar{r}_{\text{s-sc}}\|^3} - \frac{\mu_{\text{s}}}{a_{\text{s}}}y_{\text{s}} \\ \ddot{z} &= -\frac{(1-\mu)z}{\|\bar{r}_{\text{e-sc}}\|^3} - \frac{\mu z}{\|\bar{r}_{\text{m-sc}}\|^3} - \frac{\mu_{\text{s}}(z-z_{\text{s}})}{\|\bar{r}_{\text{s-sc}}\|^3} - \frac{\mu_{\text{s}}}{a_{\text{s}}}z_{\text{s}} \end{aligned} \tag{C.10}$$

where the position vectors of the spacecraft relative to the primaries are

$$\bar{r}_{\text{e-sc}} = \begin{bmatrix} x+\mu \\ y \\ z \end{bmatrix}, \bar{r}_{\text{m-sc}} = \begin{bmatrix} x-1+\mu \\ y \\ z \end{bmatrix}, \bar{r}_{\text{s-sc}} = \begin{bmatrix} x-x_{\text{s}} \\ y-y_{\text{s}} \\ z-z_{\text{s}} \end{bmatrix} \tag{C.11}$$

and the position of the Sun with respect to $B_1$ in terms of Earth-Moon rotating frame components is given by

$$\bar{r}_{\text{s}} = \begin{bmatrix} x_{\text{s}} \\ y_{\text{s}} \\ z_{\text{s}} \end{bmatrix} = a_{\text{s}} \begin{bmatrix} \cos(\theta) \\ \sin(\theta) \\ 0 \end{bmatrix} \tag{C.12}$$

Then, $\theta$ is denoted the Sun angle and corresponds to the epoch in the BCR4BP. It is defined as

$$\theta = \omega t + \theta_0 = (n_{\text{s}} - n)\, t + \theta_0 \tag{C.13}$$

The planar and circular assumptions for the orbits of the Earth, the Moon, and the Sun yield constant mean motions for all three bodies in both the inertial and rotating frames. Viewed from Earth, the mean motion of the Moon is higher than the mean motion of the Sun. Therefore, in the Earth-Moon rotating frame, the Sun rotates clockwise around the Earth-Moon barycenter with an angular rate equal to $\omega = -0.9253$.

## C.2 Equations of Motion for the BCR4BP, Sun-$B_1$ Formulation

The present formulation of the BCR4BP corresponds to a *Moon-perturbed* Sun-Earth CR3BP. The Earth and the Moon are assumed to move in circular orbits around their common barycenter, $B_1$, while the Sun and $B_1$ move in circular orbits around the Earth-Moon-Sun barycenter, $B_2$, as represented in Figure C.2. All the quantities are nondimensionalized consistent with the Sun-{Earth-Moon} CR3BP. In this arbitrary inertial $\hat{\underline{\mathbb{X}}}\hat{\underline{\mathbb{Y}}}\hat{\underline{\mathbb{Z}}}$ frame, the position of the spacecraft with respect to $B_1$ is denoted as

$$\bar{\underline{X}}(\underline{t}) = \begin{bmatrix} \underline{X}(\underline{t}) \\ \underline{Y}(\underline{t}) \\ \underline{Z}(\underline{t}) \end{bmatrix} \tag{C.14}$$

where $\underline{t}$ is the independent time variable, expressed in Sun-$B_1$ nondimensional units. The positions of the Sun and the Earth-Moon barycenter $B_1$ with respect to $B_2$,

$$\bar{\underline{R}}_{\mathrm{s}}(t) = \begin{bmatrix} \underline{X}_{\mathrm{s}} \\ \underline{Y}_{\mathrm{s}} \\ \underline{Z}_{\mathrm{s}} \end{bmatrix} = \begin{bmatrix} -\frac{1}{\mu_{\mathrm{s}}+1}\cos(\underline{n}\,\underline{t}) \\ -\frac{1}{\mu_{\mathrm{s}}+1}\sin(\underline{n}\,\underline{t}) \\ 0 \end{bmatrix}, \; \bar{\underline{R}}_{B_1}(t) = \begin{bmatrix} \underline{X}_{B_1} \\ \underline{Y}_{B_1} \\ \underline{Z}_{B_1} \end{bmatrix} = \begin{bmatrix} \left(1-\frac{1}{\mu_{\mathrm{s}}+1}\right)\cos(\underline{n}\,\underline{t}) \\ \left(1-\frac{1}{\mu_{\mathrm{s}}+1}\right)\sin(\underline{n}\,\underline{t}) \\ 0 \end{bmatrix} \tag{C.15}$$

where $\underline{n}$ is the mean motion of the Sun and $B_1$ along their respective orbits. Then, the relative positions of the Earth and the Moon with respect to $B_2$ are given by

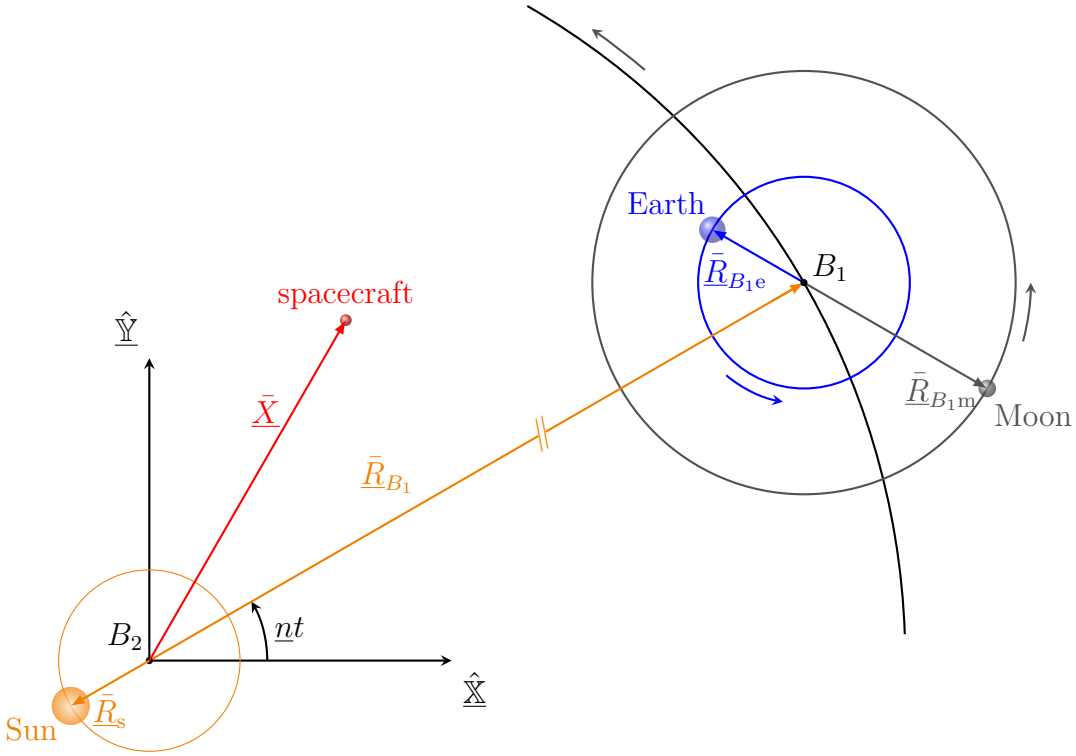


**Figure C.2.** Schematic of the BCR4BP in an arbitrary inertial frame of origin $B_2$

$$\begin{aligned}
\bar{R}_\mathrm{e} = \bar{R}_{B_1} + \bar{R}_{B_1\mathrm{e}} = \begin{bmatrix} \underline{X}_\mathrm{e} \\ \underline{Y}_\mathrm{e} \\ \underline{Z}_\mathrm{e} \end{bmatrix} &= \begin{bmatrix} -\frac{1}{\mu_\mathrm{s}+1}\cos(\underline{n}t) \\ -\frac{1}{\mu_\mathrm{s}+1}\sin(\underline{n}t) \\ 0 \end{bmatrix} + \begin{bmatrix} -\frac{\mu}{a_\mathrm{s}}\cos(\tilde{\underline{n}}t) \\ -\frac{\mu}{a_\mathrm{s}}\sin(\tilde{\underline{n}}t) \\ 0 \end{bmatrix} \\
\bar{R}_\mathrm{m} = \bar{R}_{B_1} + \bar{R}_{B_1\mathrm{m}} = \begin{bmatrix} \underline{X}_\mathrm{m} \\ \underline{Y}_\mathrm{m} \\ \underline{Z}_\mathrm{m} \end{bmatrix} &= \begin{bmatrix} \left(1-\frac{1}{\mu_\mathrm{s}+1}\right)\cos(\underline{n}t) \\ \left(1-\frac{1}{\mu_\mathrm{s}+1}\right)\sin(\underline{n}t) \\ 0 \end{bmatrix} + \begin{bmatrix} \frac{1-\mu}{a_\mathrm{s}}\cos(\tilde{\underline{n}}t) \\ \frac{1-\mu}{a_\mathrm{s}}\sin(\tilde{\underline{n}}t) \\ 0 \end{bmatrix}
\end{aligned} \tag{C.16}$$

where $a_\mathrm{s}$ is the *Earth-Moon nondimensional* distance between $B_1$ and the Sun[2], and $\tilde{\underline{n}} = {a_\mathrm{s}}^3/\sqrt{\mu_\mathrm{s}+1}$ is the *Sun-$B_1$ nondimensional* mean motions of the Earth and the Moon along their respective orbits.

The inertial acceleration acting the spacecraft, i.e., $\bar{\underline{X}}_\mathrm{i}$ is straightforwardly obtained by leveraging the $\mathcal{N}$-body differential equation in Equation (A.1), since the position vector

[2]↑Note that this value is equal to the inverse of the Sun-Earth nondimensional distance between the Earth and the Moon.

$\underline{\bar{X}}$ is defined with respect to an inertially fixed point, that is, the Earth-Moon-Sun system barycenter $B_2$. Thus, the inertial equations of motion for the BCR4BP Restricted Four-Body with respect to $B_2$ are

$$\begin{aligned}
\ddot{\underline{X}} &= -\frac{\left(1-\frac{1}{\mu_{\mathrm{s}}+1}\right)(\underline{X}-\underline{X}_{\mathrm{s}})}{\|\underline{\bar{R}}_{\text{s-sc}}\|^3} - \frac{\frac{1-\mu}{\mu_{\mathrm{s}}+1}(\underline{X}-\underline{X}_{\mathrm{e}})}{\|\underline{\bar{R}}_{\text{e-sc}}\|^3} - \frac{\frac{\mu}{\mu_{\mathrm{s}}+1}(\underline{X}-\underline{X}_{\mathrm{m}})}{\|\underline{\bar{R}}_{\text{m-sc}}\|^3} \\
\ddot{\underline{Y}} &= -\frac{\left(1-\frac{1}{\mu_{\mathrm{s}}+1}\right)(\underline{Y}-\underline{Y}_{\mathrm{s}})}{\|\underline{\bar{R}}_{\text{s-sc}}\|^3} - \frac{\frac{1-\mu}{\mu_{\mathrm{s}}+1}(\underline{Y}-\underline{Y}_{\mathrm{e}})}{\|\underline{\bar{R}}_{\text{e-sc}}\|^3} - \frac{\frac{\mu}{\mu_{\mathrm{s}}+1}(\underline{Y}-\underline{Y}_{\mathrm{m}})}{\|\underline{\bar{R}}_{\text{m-sc}}\|^3} \\
\ddot{\underline{Z}} &= -\frac{\left(1-\frac{1}{\mu_{\mathrm{s}}+1}\right)(\underline{Z}-\underline{Z}_{\mathrm{s}})}{\|\underline{\bar{R}}_{\text{s-sc}}\|^3} - \frac{\frac{1-\mu}{\mu_{\mathrm{s}}+1}(\underline{Z}-\underline{Z}_{\mathrm{e}})}{\|\underline{\bar{R}}_{\text{e-sc}}\|^3} - \frac{\frac{\mu}{\mu_{\mathrm{s}}+1}(\underline{Z}-\underline{Z}_{\mathrm{m}})}{\|\underline{\bar{R}}_{\text{m-sc}}\|^3}
\end{aligned} \tag{C.17}$$

A rotating frame consistent with the rotation of the Sun and $B_1$ is defined such that

$$\begin{aligned}
\underline{x} &= \underline{X}\cos(\underline{n}t) + \underline{Y}\sin(\underline{n}t) \\
\underline{y} &= -\underline{X}\sin(\underline{n}t) + \underline{Y}\cos(\underline{n}t) \\
\underline{z} &= \underline{Z}
\end{aligned} \tag{C.18}$$

Then, using the kinematic expansion [21] yields the nondimensional equations of motion for the BCR4BP as formulated in the Sun-$B_1$ rotating frame,

$$\begin{aligned}
\ddot{\underline{x}} &= 2\dot{\underline{y}} + \underline{x} - \frac{\left(1-\frac{1}{\mu_{\mathrm{s}}+1}\right)\left(\underline{x}-\frac{1}{\mu_{\mathrm{s}}+1}\right)}{\|\underline{\bar{r}}_{\text{s-sc}}\|^3} - \frac{\frac{1-\mu}{\mu_{\mathrm{s}}+1}(\underline{x}-\underline{x}_{\mathrm{e}})}{\|\underline{\bar{r}}_{\text{e-sc}}\|^3} - \frac{\frac{\mu}{\mu_{\mathrm{s}}+1}(\underline{x}-\underline{x}_{\mathrm{m}})}{\|\underline{\bar{r}}_{\text{m-sc}}\|^3} \\
\ddot{\underline{y}} &= -2\dot{\underline{x}} + \underline{y} - \frac{\left(1-\frac{1}{\mu_{\mathrm{s}}+1}\right)\left(\underline{y}-\frac{1}{\mu_{\mathrm{s}}+1}\right)}{\|\underline{\bar{r}}_{\text{s-sc}}\|^3} - \frac{\frac{1-\mu}{\mu_{\mathrm{s}}+1}\left(\underline{y}-\underline{y}_{\mathrm{e}}\right)}{\|\underline{\bar{r}}_{\text{e-sc}}\|^3} - \frac{\frac{\mu}{\mu_{\mathrm{s}}+1}\left(\underline{y}-\underline{y}_{\mathrm{m}}\right)}{\|\underline{\bar{r}}_{\text{m-sc}}\|^3} \\
\ddot{\underline{z}} &= -\frac{\left(1-\frac{1}{\mu_{\mathrm{s}}+1}\right)\left(\underline{z}-\frac{1}{\mu_{\mathrm{s}}+1}\right)}{\|\underline{\bar{r}}_{\text{s-sc}}\|^3} - \frac{\frac{1-\mu}{\mu_{\mathrm{s}}+1}\left(\underline{z}-\underline{z}_{\mathrm{e}}\right)}{\|\underline{\bar{r}}_{\text{e-sc}}\|^3} - \frac{\frac{\mu}{\mu_{\mathrm{s}}+1}\left(\underline{z}-\underline{z}_{\mathrm{m}}\right)}{\|\underline{\bar{r}}_{\text{m-sc}}\|^3}
\end{aligned} \tag{C.19}$$

The position vectors of the Earth and the Moon with respect to the system barycenter $B_2$ are given by

$$\begin{aligned}
\bar{\underline{r}}_{\mathrm{e}} &= \bar{\underline{r}}_{B_1} + \bar{\underline{r}}_{B_1\mathrm{e}} = \begin{bmatrix} \underline{x}_{\mathrm{e}} \\ \underline{y}_{\mathrm{e}} \\ \underline{z}_{\mathrm{e}} \end{bmatrix} = \begin{bmatrix} 1 - \frac{1}{\mu_{\mathrm{s}}+1} \\ 1 - \frac{1}{\mu_{\mathrm{s}}+1} \\ 0 \end{bmatrix} + \begin{bmatrix} -\frac{\mu}{a_{\mathrm{s}}}\cos(\underline{\theta}) \\ -\frac{\mu}{a_{\mathrm{s}}}\sin(\underline{\theta}) \\ 0 \end{bmatrix} \\
\bar{\underline{r}}_{m} &= \bar{\underline{r}}_{B_1} + \bar{\underline{r}}_{B_1\mathrm{m}} = \begin{bmatrix} \underline{x}_{\mathrm{m}} \\ \underline{y}_{\mathrm{m}} \\ \underline{z}_{\mathrm{m}} \end{bmatrix} = \begin{bmatrix} 1 - \frac{1}{\mu_{\mathrm{s}}+1} \\ 1 - \frac{1}{\mu_{\mathrm{s}}+1} + \\ 0 \end{bmatrix} + \begin{bmatrix} \frac{1-\mu}{a_{\mathrm{s}}}\cos(\underline{\theta}) \\ \frac{1-\mu}{a_{\mathrm{s}}}\sin(\underline{\theta}) \\ 0 \end{bmatrix}
\end{aligned} \tag{C.20}$$

where $\underline{\theta} = \boldsymbol{\pi} - \theta = \underline{\omega}t + \underline{\theta}_0$ is denoted the Moon angle and corresponds to the epoch of the BCR4BP, and $\underline{\omega} = \frac{|\omega|}{1-|\omega|}$ is the nondimensional angular rate of the Earth and the Moon in their motion around their common barycenter $B_1$. Alignment of the Sun, Earth, and Moon occurs every synodic period, that is, approximately 29.5 days. Similar to the BCR4BP formulated in the Earth-Moon rotating frame, the Sun-$B_1$ BCR4BP is a non-autonomous, periodic system.

# D. STATE/EPOCH DEPENDENCIES IN THE BCR4BP

The relationship between the change in initial epoch associated with a state and the change in propagated position and velocity variables is derived for the Earth-Moon formulation of the BCR4BP. A similar process is applicable for the dependencies in the Sun-$B_1$ formulation of the BCR4BP or for the $N$-body ephemeris model. See Cox [98] and Pavlak [111] for a general derivation of the explicit and implicit dependencies. Consider a state propagated from $\bar{x}_{\mathrm{i}}$ to $\bar{x}_f$ using the equations of motion in Equation (2.4). The relationship between the change in epoch associated with the initial state, that is $\theta_{\mathrm{i}}$, and the change in final position and velocity is

$$\delta\bar{x}_f = \mathcal{D}\left(\bar{x}, \theta\right)\, \delta\theta_{\mathrm{i}} = \frac{\partial \bar{x}}{\partial \theta_{\mathrm{i}}}\, \delta\theta_{\mathrm{i}} \tag{D.1}$$

where the function $\mathcal{D}$ relates the propagated state to the initial epoch. There is no straightforward analytical relation for this function. Thus, the derivative of this function with respect to the time is considered. Since the initial epoch and the time variable are independent from each other, the order of derivatives is interchangeable,

$$\begin{aligned} \frac{d}{dt}\frac{\partial \bar{x}_f}{\partial \theta_{\mathrm{i}}} &= \frac{\partial}{\partial \theta_{\mathrm{i}}}\frac{d\bar{x}}{dt\partial} \\ &= \frac{\partial}{\partial \theta_{\mathrm{i}}}\left(\dot{\bar{x}}\right) \\ &= \frac{\partial}{\partial \theta_{\mathrm{i}}}\left(\bar{f}(t, \bar{x}, \bar{r}_{\text{s-sc}})\right) \end{aligned} \tag{D.2}$$

where $\bar{f}$ represents the equations of motion of the BCR4BP. Using the chain rule,

$$\frac{\partial \bar{f}}{\partial \theta_{\mathrm{i}}} = \frac{\partial \bar{f}}{\partial t}\frac{dt}{d\theta_{\mathrm{i}}} + \frac{\partial \bar{f}}{\partial \bar{x}}\frac{d\bar{x}}{d\theta_{\mathrm{i}}} + \frac{\partial \bar{f}}{\partial \bar{r}_{\text{s-sc}}}\frac{d\bar{r}_{\text{s-sc}}}{d\theta_{\mathrm{i}}} \tag{D.3}$$

Since the initial epoch and the time variable are independent, $\frac{dt}{d\theta_{\mathrm{i}}} = 0$. Thus,

$$\begin{aligned} \frac{\partial \bar{f}}{\partial \theta_{\mathrm{i}}} &= \frac{\partial \bar{f}}{\partial \bar{x}}\frac{d\bar{x}}{d\theta_{\mathrm{i}}} + \frac{\partial \bar{f}}{\partial \bar{r}_{\text{s-sc}}}\frac{d\bar{r}_{\text{s-sc}}}{d\theta_{\mathrm{i}}} \\ &= \mathbf{A}\frac{d\bar{x}}{d\theta_{\mathrm{i}}} + \frac{\partial \bar{f}}{\partial \bar{r}_{\text{s-sc}}}\dot{\bar{r}}_S \end{aligned} \tag{D.4}$$

Where **A** is the matrix defined for the linear variational equations of motion of the BCR4BP in Equation (3.6). the second term in Equation (D.4) relates the velocity and acceleration of the state to the position of Sun

$$\frac{\partial \bar{f}}{\partial \bar{r}_{\text{s-sc}}} = \begin{bmatrix} \frac{\partial \dot{x}}{\partial x_S} & \frac{\partial \dot{x}}{\partial y_S} & \frac{\partial \dot{x}}{\partial z_S} \\ \vdots & & \vdots \\ \frac{\partial \ddot{z}}{\partial x_S} & \frac{\partial \ddot{z}}{\partial y_S} & \frac{\partial \ddot{z}}{\partial z_S} \end{bmatrix} = \begin{bmatrix} 0 & 0 & 0 \\ 0 & 0 & 0 \\ 0 & 0 & 0 \\ \frac{\partial \ddot{x}}{\partial x_S} & \frac{\partial \ddot{x}}{\partial y_S} & \frac{\partial \ddot{x}}{\partial z_S} \\ \frac{\partial \ddot{y}}{\partial x_S} & \frac{\partial \ddot{y}}{\partial y_S} & \frac{\partial \ddot{y}}{\partial z_S} \\ \frac{\partial \ddot{z}}{\partial x_S} & \frac{\partial \ddot{z}}{\partial y_S} & \frac{\partial \ddot{z}}{\partial z_S} \end{bmatrix} \tag{D.5}$$

The differential equations in $\frac{\partial \bar{x}_f}{\partial \theta_{\text{i}}}$ in Equation (D.4) are numerically integrated along the equations of motion and the STM of the BCR4BP. Since initial epoch and time are independent, the initial conditions for these differential equations are the $(6 \times 1)$ zero vector.

# E. INITIAL CONDITIONS FOR BCR4BP PERIODIC ORBITS

Initial conditions are provided for a selection of periodic orbits in the BCR4BP. The periodic solutions are discretized into patch points. The states, either in terms of Earth-Moon rotating frame or Sun-$B_1$ rotating frame components are given in the columns two through seven. The epoch is stated in column eight, either as a Sun angle $\theta$ or a Moon angle $\underline{\theta}$. Finally, the nondimensional propagation time to the next patch point is given in the last column. The periodic orbits are converged to the relative and absolute tolerances of $10^{-12}$, employing the characteristic quantities stated in Appendix B.

## E.1 Earth-Moon NRHOs

**Table E.1**. Initial conditions in the Earth-Moon rotating frame for the 3:1 NRHO (analog A) in the BCR4BP from Figures 4.29(b) and 4.37.

| pp | $x$ | $y$ | $z$ | $\dot{x}$ | $\dot{y}$ | $\dot{z}$ | $\theta$ | $T_p$ |
|---|---|---|---|---|---|---|---|---|
| 1 | 1.0868 | −0.0098 | −0.1746 | 0.0124 | −0.2349 | −0.0765 | −0.7854 | 2.2635 |
| 2 | 1.0497 | 0.0355 | −0.2086 | 0.0204 | −0.1192 | −0.1108 | −2.8797 | 2.2635 |
| 3 | 1.0511 | 0.1228 | −0.1596 | 0.1200 | −0.1283 | −0.1242 | −4.9742 | 2.2635 |

**Table E.2**. Initial conditions in the Earth-Moon rotating frame for the 4:1 NRHO (analog A) in the BCR4BP from Figures 4.29(b) and 4.39.

| pp | $x$ | $y$ | $z$ | $\dot{x}$ | $\dot{y}$ | $\dot{z}$ | $\theta$ | $T_p$ |
|---|---|---|---|---|---|---|---|---|
| 1 | 1.0272 | 0.0000 | −0.1906 | 0.0000 | −0.1259 | 0.0000 | 0.0000 | 1.6976 |
| 2 | 1.0456 | 0.0001 | −0.1879 | 0.0001 | −0.1418 | 0.0000 | −1.5707 | 1.6976 |
| 3 | 1.0272 | 0.0000 | −0.1905 | 0.0000 | −0.1260 | 0.0000 | −3.1416 | 1.6976 |
| 4 | 1.0456 | −0.0001 | −0.1879 | −0.0001 | −0.1418 | 0.0000 | −4.7124 | 1.6976 |

**Table E.3**. Initial conditions in the Earth-Moon rotating frame for the 9:2 NRHO in the BCR4BP from Figures 4.29(b) and 4.31.

| pp | $x$ | $y$ | $z$ | $\dot{x}$ | $\dot{y}$ | $\dot{z}$ | $\theta$ | $T_p$ |
|---|---|---|---|---|---|---|---|---|
| 1 | 1.0031 | 0.0181 | −0.1701 | 0.0225 | −0.0824 | −0.1109 | 0.1904 | 1.5090 |
| 2 | 1.0314 | 0.0221 | −0.1712 | 0.0295 | −0.0985 | −0.0980 | −1.2057 | 1.5090 |
| 3 | 1.0077 | 0.0205 | −0.1703 | 0.0262 | −0.0882 | −0.1081 | −2.6020 | 1.5090 |
| 4 | 1.0272 | 0.0224 | −0.1713 | 0.0307 | −0.0996 | −0.0965 | −3.9983 | 1.5090 |
| 5 | 1.0186 | 0.0225 | −0.1692 | 0.0294 | −0.0992 | −0.1095 | −5.3945 | 1.5090 |
| 6 | 1.0187 | 0.0207 | −0.1702 | 0.0280 | −0.0968 | −0.1043 | −6.7909 | 1.5090 |
| 7 | 1.0279 | 0.0225 | −0.1684 | 0.0291 | −0.1037 | −0.1112 | −8.1872 | 1.5090 |
| 8 | 1.0083 | 0.0183 | −0.1696 | 0.0233 | −0.0880 | −0.1115 | −9.5834 | 1.5090 |
| 9 | 1.0318 | 0.0217 | −0.1696 | 0.0281 | −0.1006 | −0.1062 | −10.9797 | 1.5090 |

**Table E.4**. Initial conditions in the Earth-Moon rotating frame for the 5:1 NRHO in the BCR4BP from Figure 4.29(b).

| pp | $x$ | $y$ | $z$ | $\dot{x}$ | $\dot{y}$ | $\dot{z}$ | $\theta$ | $T_p$ |
|---|---|---|---|---|---|---|---|---|
| 1 | 0.9771 | 0.0000 | −0.1686 | 0.0000 | −0.0635 | 0.0002 | 0.0000 | 1.3581 |
| 2 | 1.0356 | 0.0056 | −0.1708 | −0.0017 | −0.0838 | −0.0116 | −1.2566 | 1.3581 |
| 3 | 0.9976 | −0.0082 | −0.1698 | 0.0046 | −0.0684 | −0.0083 | −2.5132 | 1.3581 |
| 4 | 0.9976 | 0.0081 | −0.1698 | −0.0047 | −0.0684 | 0.0087 | −3.7699 | 1.3581 |
| 5 | 1.0356 | −0.0056 | −0.1708 | 0.0016 | −0.0838 | 0.0120 | −5.0265 | 1.3581 |

## E.2 Sun-$B_1$ Halo Orbits

**Table E.5**. Initial conditions in the Sun-$B_1$ rotating frame for the 12:73 $\underline{\mathrm{L}}_2$ halo orbit in the BCR4BP from Figure 4.46(b).

| pp | $\underline{x}$ | $\underline{y}$ | $\underline{z}$ | $\underline{\dot{x}}$ | $\underline{\dot{y}}$ | $\underline{\dot{z}}$ | $\underline{\theta}$ | $\mathbf{T_p}$ |
|---|---|---|---|---|---|---|---|---|
| 1 | 1.00745 | −0.00149 | −0.00278 | −0.00045 | 0.01238 | −0.00230 | 0.00 | 3.086 |
| 2 | 1.00745 | −0.00149 | −0.00278 | −0.00045 | 0.01238 | −0.00230 | 38.22 | 3.086 |
| 3 | 1.00745 | −0.00149 | −0.00278 | −0.00045 | 0.01238 | −0.00231 | 76.45 | 3.086 |
| 4 | 1.00745 | −0.00149 | −0.00278 | −0.00044 | 0.01238 | −0.00231 | 114.67 | 3.086 |
| 5 | 1.00745 | −0.00149 | −0.00278 | −0.00044 | 0.01237 | −0.00232 | 152.89 | 3.086 |
| 6 | 1.00745 | −0.00149 | −0.00278 | −0.00045 | 0.01237 | −0.00232 | 191.11 | 3.086 |
| 7 | 1.00745 | −0.00149 | −0.00278 | −0.00045 | 0.01238 | −0.00232 | 229.34 | 3.086 |
| 8 | 1.00745 | −0.00149 | −0.00278 | −0.00045 | 0.01239 | −0.00232 | 267.56 | 3.086 |
| 9 | 1.00745 | −0.00149 | −0.00278 | −0.00045 | 0.01239 | −0.00232 | 305.78 | 3.086 |
| 10 | 1.00745 | −0.00149 | −0.00278 | −0.00044 | 0.01239 | −0.00232 | 344.00 | 3.086 |
| 11 | 1.00745 | −0.00149 | −0.00278 | −0.00044 | 0.01239 | −0.00232 | 382.23 | 3.086 |
| 12 | 1.00745 | −0.00149 | −0.00278 | −0.00044 | 0.01238 | −0.00231 | 420.45 | 3.086 |

**Table E.6**. Initial conditions in the Sun-$B_1$ rotating frame for the 4:19 $\underline{L}_2$ halo orbit in the BCR4BP from Figure 4.46(b).

| pp | $\underline{x}$ | $\underline{y}$ | $\underline{z}$ | $\underline{\dot{x}}$ | $\underline{\dot{y}}$ | $\underline{\dot{z}}$ | $\underline{\theta}$ | $\mathbf{T_p}$ |
|---|---|---|---|---|---|---|---|---|
| 1 | 1.00055 | −0.00321 | −0.00249 | −0.00384 | 0.03030 | −0.01775 | 0.00 | 0.80 |
| 2 | 1.00528 | 0.00604 | 0.00922 | 0.00663 | −0.00869 | 0.01218 | 9.95 | 0.80 |
| 3 | 1.00630 | −0.00427 | 0.01096 | −0.00447 | −0.01202 | −0.00791 | 19.90 | 0.80 |
| 4 | 1.00066 | −0.00341 | −0.00251 | −0.00426 | 0.02891 | −0.01813 | 29.84 | 0.80 |
| 5 | 1.00523 | 0.00635 | 0.00879 | 0.00687 | −0.00831 | 0.01270 | 39.79 | 0.80 |
| 6 | 1.00643 | −0.00400 | 0.01102 | −0.00437 | −0.01239 | −0.00727 | 49.74 | 0.80 |
| 7 | 1.00066 | −0.00377 | −0.00212 | −0.00478 | 0.02735 | −0.01955 | 59.69 | 0.80 |
| 8 | 1.00504 | 0.00623 | 0.00906 | 0.00675 | −0.00811 | 0.01268 | 69.64 | 0.80 |
| 9 | 1.00626 | −0.00390 | 0.01117 | −0.00421 | −0.01219 | −0.00752 | 79.59 | 0.80 |
| 10 | 1.00059 | −0.00344 | −0.00229 | −0.00468 | 0.02890 | −0.01920 | 89.54 | 0.80 |
| 11 | 1.00524 | 0.00607 | 0.00907 | 0.00676 | −0.00868 | 0.01233 | 99.48 | 0.80 |
| 12 | 1.00625 | −0.00429 | 0.01092 | −0.00461 | −0.01204 | −0.00780 | 109.43 | 0.80 |

**Table E.7**. Initial conditions in the Sun-$B_1$ rotating frame for the 1:4 $\underline{L}_2$ halo orbit in the BCR4BP from Figure 4.46(b).

| pp | $\underline{x}$ | $\underline{y}$ | $\underline{z}$ | $\underline{\dot{x}}$ | $\underline{\dot{y}}$ | $\underline{\dot{z}}$ | $\underline{\theta}$ | $\mathbf{T_p}$ |
|---|---|---|---|---|---|---|---|---|
| 1 | 0.99994 | 0.00000 | −0.00207 | 0.00000 | 0.05189 | 0.00000 | 0.00 | 0.68 |
| 2 | 1.00457 | 0.00384 | 0.01063 | 0.00484 | −0.00957 | 0.00940 | 8.38 | 0.68 |
| 3 | 1.00457 | −0.00384 | 0.01063 | −0.00484 | −0.00957 | −0.00940 | 16.76 | 0.68 |

**Table E.8**. Initial conditions in the Sun-$B_1$ rotating frame for the 2:7 $\underline{L}_2$ halo orbit in the BCR4BP from Figure 4.46(b).

| pp | $\underline{x}$ | $\underline{y}$ | $\underline{z}$ | $\underline{\dot{x}}$ | $\underline{\dot{y}}$ | $\underline{\dot{z}}$ | $\underline{\theta}$ | $T_p$ |
|---|---|---|---|---|---|---|---|---|
| 1 | 0.99990 | 0.00000 | −0.00126 | 0.00000 | 0.06710 | 0.00000 | 0.00 | 0.36 |
| 2 | 1.00227 | 0.00433 | 0.00766 | 0.00651 | −0.00298 | 0.01697 | 4.40 | 0.36 |
| 3 | 1.00393 | 0.00194 | 0.01153 | 0.00258 | −0.00926 | 0.00532 | 8.80 | 0.36 |
| 4 | 1.00401 | −0.00155 | 0.01155 | −0.00218 | −0.00951 | −0.00525 | 13.19 | 0.36 |
| 5 | 1.00244 | −0.00412 | 0.00769 | −0.00645 | −0.00365 | −0.01699 | 17.59 | 0.36 |
| 6 | 0.99990 | 0.00000 | −0.00126 | 0.00000 | 0.06720 | −0.00001 | 21.99 | 0.36 |
| 7 | 1.00244 | 0.00412 | 0.00769 | 0.00645 | −0.00365 | 0.01699 | 26.39 | 0.36 |
| 8 | 1.00401 | 0.00155 | 0.01155 | 0.00218 | −0.00951 | 0.00525 | 30.79 | 0.36 |
| 9 | 1.00393 | −0.00194 | 0.01153 | −0.00258 | −0.00926 | −0.00532 | 35.19 | 0.36 |
| 10 | 1.00227 | −0.00433 | 0.00766 | −0.00651 | −0.00298 | −0.01697 | 39.58 | 0.36 |

# VITA

Kenza Katiane Boudad began her combined BS/MS degree in Aerospace Engineering in 2012 at the *École Supérieure des Techniques Aéronautiques et de Construction Automobile* (ESTACA) in France. In the fall of 2016, Kenza started her graduate studies in Aeronautical and Astronautical Engineering at Purdue University. She joined Professor Kathleen Howell's Multi-Body Dynamics Research Group in January 2017. Kenza studied disposal dynamics in the vicinity of the Near Rectilinear Halo Orbits in an Earth-Moon-Sun regime, writing her thesis on the topic and graduating with a MS degree from Purdue in December 2018. In the same month, she earned her dual BS/MS degree from ESTACA. Kenza then continued in the Multi-Body Dynamics Research Group for her doctoral degree. Her PhD research focuses on the low-energy trajectory design between the Earth-Moon and Sun-Earth libration point regions. In 2021, Kenza was awarded the Purdue Bilsland Dissertation Fellowship, a fellowship award by the Dean of the Graduate School to outstanding PhD candidates in the final year of doctoral degree completion. One of Kenza's peer-reviewed publications was awarded an Outstanding Paper Award for Young Scientists by the Committee on Space Research (COSPAR) in 2022.